Lehrstuhl für Aerodynamik
Technische Universität München

Viscous - Inviscid Interaction Methods for Flutter Calculations

Widjaja Kresna Sekar

Vollständiger Abdruck der von der Fakultät für Maschinenwesen der Technischen Universität München zur Erlangung des akademischen Grades eines

Doktor-Ingenieurs

genehmigten Dissertation.

Vorsitzender : Univ. -Prof. Dr. –Ing. habil. Nikolaus A. Adams

Prüfer der Dissertation :

1. Univ. -Prof. Dr. –Ing. Boris Laschka, em
2. Univ. -Prof. Dr. –Ing. Horst Baier
3. Prof. Dr. ir. Harijono Djojodihardjo,
   Univ. Al Azhar Indonesia

Die Dissertation wurde am 12.04.2006 bei der Technischen Universität München eingereicht und durch die Fakultät für Maschinenwesen am 21.08.2006 angenommen.

Foreword

The present work has been performed during my stay from October 1999 until April 2004 as Scholar/Guest Student at the Institute of Aerodynamics (formerly Institute of Fluid Mechanics) of the Technische Universität München. I would like to express my sincere gratitude and appreciation to all Persons and Institutions that have supported and contributed to this work, as follows:

- My especially thanks to my Doktorvater, Herrn Prof. Dr. –Ing Boris Laschka, for his guidance and advice during this research. I am grateful for his support and the given opportunity to carry out my research in his Institute. His encouragement, thoughtfulness and supervision are deeply acknowledged.
- I would like to thank Frau Dr. –Ing Caroline Weishäupl from EADS Ottobrunn for her guidance and her supervision especially in the first two years of my work.
- I would like to thank Herrn Prof. Dr.-Ing. Horst Baier from the Institute of Light Structures of the Technische Universität München for his valuable comments and his recommendation.
- I would like to thank Prof. Dr. Ir. Harijono Djojodihardjo from the Institute of Technology Bandung Indonesia for his valuable comments and his recommendation.
- I would like to thank Herrn Dr.-Ing. Ralph Voß and Herrn Dipl.-Ing. Martin Rippl from DLR Aeroelasticity in Göttingen for their valuable comments, suggestion and data exchange.
- I would like to express my deeply gratitude to Dr. ir. Bima Prananta from NLR the Netherlands for the discussions, suggestions and data exchange.
- I would like to thank Herrn Dr. –Ing. Tomislav Cvrlje from Eurocopter Deutschland for the discussions and data exchange.
- I would like to express my deeply gratitude to Dr. ir. Roul Houwink from NLR the Netherlands and also to Prof. dr. ir. H.W.M. Hoeijmakers from University of Twente the Netherlands for the suggestions and the given valuable literatures.
- I would like to thank Herrn Dr. –Ing. C. Breitsamter, Dr. –Ing M. Manhart and Dr. –Ing A. Pernpeintner from the Institute of Aerodynamics for the valuable discussions.
- I would like to thank Herrn Dr. –Ing. P. Schmid, Fr. Gärtner and Fr. Pauleweit from the Institute of Aerodynamics of the Technische Universität München for their help in administrative things during my stay.
- I would like to thank my colleagues and friends in the Institute of Aerodynamics especially to A. Pechloff, A. Allen, A. Furman, U. Sickmüller, J. Fischer, S.Eisenbach, von Vogt, M. Iatrou, L. Jiang, A. Schmid, C. Belastrada and H. Kozmar for their support, encouragement and their readiness when I needed their help.
- I also acknowledge Herrn Firmberger and Herrn Zirngibl from the Werkstatt of the Institute of Aerodynamics for their support.
- My deeply gratitude to my friends from Indonesia Circle especially I. Haryanto, M.A. Moelyadi, A. Kirdjoputro, A. Sodri and R.S. Nugraha for their support.
- I would like to acknowledge that the financial support during my stay was provided by the Deutschen Akademischen Austausch Dienst (DAAD) and the Institute of Aerodynamics of the Technische Universität München.

Finally, I would like to express my deep appreciation to my beloved wife, Evi Yulia Efiati and my beloved Son, Muhammad Fachri Gemintang for their patience and their love.

Bremen, March 2006

Widjaja Kresna Sekar

Contents

List of Figures

List of Tables

Nomenclature

Symbol	**Meaning**
α_0	Mean of Angle of Attack
α_1	Amplitude of Angle of Attack
δ	Boundary Layer Thickness
$\delta^* = \int_0^\infty \left(1 - \frac{\rho U}{\rho_e U_e}\right) dz$	Displacement thickness
$\delta^{**} = \int_0^\infty \left(1 - \frac{\rho}{\rho_e}\right) \frac{U}{U_e} dz$	Density thickness
Φ, ϕ	Velocity Potential, Disturbance Velocity Potential
φ	Sweep Angle
θ	Twist Angle
$\gamma = c_p/c_v$	Isentropic exponent (Ratio of heat capacities)
ξ, η, ζ	Components of Numerical Coordinate
$\theta = \int_0^\infty \left(1 - \frac{U}{U_e}\right) \frac{\rho U}{\rho_e U_e} dz$	Momentum Thickness
$\theta^* = \int_0^\infty \left(1 - \frac{U^2}{U_e^2}\right) \frac{\rho U}{\rho_e U_e} dz$	Kinetic Energy thickness
ρ	Fluid Density
τ	Shear Stress
μ	Dynamic Viscosity
$\nu = \mu/\rho$	kinematics Viscosity
ω	relaxation Factor
ω	Angular frequency
λ	Scale Factor of the Dissipation Length
ζ	Modal Damping Coefficient
ω_h, ω_α	Uncoupled Heaving and Pitching Angular Frequency
ω_n	Natural Frequency
$[\Phi]$	Generalised Mode Shape Matrix
$[\psi_h]$,$[\psi_{nh}]$	State Transition Matrix (in Flutter Analysis)
$\tau = \omega_\alpha t$	Dimensionless Time
$\mu = m_1/(\pi\rho b^2)$	Mass-Ratio of Airfoil to Fluid
a	Position of the Elastic Axis
a, c	Speed of Sound
a_k^l	Eigenvalue
$[A]$, $[B]$	State Matrices (in Flutter Analysis)
a, b, c	Jacobi matrices of non conservative Euler Equations
A, B, C	Jacobi matrices of the Fluxes F, G, H
b	Semi Chord
c	Chord of Airfoil of Wing
c_r	Root Chord of a Wing
c_t	Tip Chord of a Wing
$C_f = \frac{2\tau_w}{\rho_e U_e^2}$	Skin Friction Coefficient

Symbol	**Meaning**
$C_d = \dfrac{1}{\rho_e U_e^3}\int_0^\infty \tau \dfrac{dU}{dz} dz$	Dissipation Coefficient
C_τ	Shear Stress Coefficient
$C_E = \dfrac{1}{U_e}\dfrac{d}{dx}\left[U_e(\delta - \delta^*)\right]$	Entrainment Coefficient
C_L	Lift Coefficient
$\mathrm{C_D}$	Drag Coefficient
$\mathrm{C_M}$	Moment Coefficient
C_p	Pressure Coefficient
$[C]$	Generalised Damping Matrix
CFL	**C**ourant-**F**riedrich-**L**evy Number
e	Specific Total Energy (Total Energy per Density)
f, g, h	Inviscid Fluxes in Cartesian Coordinate directions
F, G, H	Inviscid Fluxes in Computational Coordinate directions
$\{F\}$, $\{Q\}$	physical and generalised Force Vector (in Flutter analysis)
$H, H^*, H_k, H^{**}, \overline{H}\ , H_1\ , H_0$	Shape Factors of Boundary Layer
$\overline{H} = \dfrac{1}{\theta}\int_0^\infty \dfrac{\rho}{\rho_e}\left(1 - \dfrac{U}{U_e}\right) dz$	incompressible Shape Factor
$H\ = \delta^*/\theta$	Displacement Shape Factor
$H_1 = (\delta - \delta^*)/\theta$	Heads Shape Factor
H_k	kinematics Shape Factor
$H^* = \theta^*/\theta$	Energy Shape Factor
$H^{**} = \delta^{**}/\ \theta$	Density Shape Factor
$[I]$	Unity matrix
$Im\{..\}$	Imaginary part of {..}
$k = \omega c/U_\infty$	reduced Frequency
k	representative symbol for ξ, η, ζ coordinate
k, l, m	Indices in direction ξ, η, ζ
$[k]$, $[K]$	physical and generalised Stiffness Matrix
L, M_{ea}	Lift and Moment in elastic Axis
m_1	Mass of Airfoil
$[m]$, $[M]$	physical and generalised Mass Matrix
M	Mach number
M_e	Mach number at boundary layer's edge
$\overline{m}$	Mass flux in the displacement thickness
n	disturbance amplification factor (laminar-turbulent Transition)
p	static pressure
Pr	Prandtl number
$\{\mathrm{q}\}$	physical conservative State Vector
$\{\mathrm{Q}\}$	numerical conservative State Vector
$r = Pr^{\ 1/3}$	heat recovery factor
R_1, R_2	Scale Factor of Compressibility
R_3	Transition Factor from attached to separated flow
Re	Reynolds number
Re_θ	Reynolds number based on the momentum thickness
$\mathrm{Re}\{..\}$	Real part of {..}
r_α	radius of gyration

Symbol	**Meaning**
s	Half span of a wing
T	Temperature
t	Time
$\{u\}$	State aerodynamic Vector
U	Tangential velocity component
u, v, w	Velocity components in Cartesian Coordinate
U,V,W	contravariant Velocities
U_m	Velocity of backward flow
U_e	Velocity at boundary layer's edge
V_f,	Flutter speed
$V^* = V_\mathrm{f}/(b\varpi_\alpha\sqrt{\mu})$	Flutter speed index
W	Vector of characteristic Variables
x_α	Static unbalance
$\{X\}$	State displacement Vector
Z_0	stationary part of variable Z
Z_1	Unsteady part of Variable Z
x, y, z	Components of physical Coordinate
$\{z\}$, $\{q\}$	Physical and generalised displacement Vector

Subscript :

t	Derivative in Time
x, y, z	Derivative in x, y, z directions
ξ, η, ζ	Derivative in ξ, η, ζ directions
∞	Undisturbed condition
le	Leading edge
te	Trailing edge
e	Edge of Boundary layer
EQ	Equilibrium condition
$EQ0$	Equilibrium condition without influence of 2nd turbulence structure
w	Wall

Superscripts

+ , -	upper, lower surface
n	time level
T	transpose

1. Introduction

Flutter analysis is one of the most important tasks in the design process of a new aircraft. To a lesser extent flutter analysis is also important during the operation of an aircraft, for example after structural modifications, changes of operational spectrum, introduction of new external stores, etc. Flutter analysis concerns with oscillations of aircraft components (or the whole aircraft) caused by interaction of the mass and stiffness of the aircraft structure with the aerodynamic forces. Beyond a certain speed, the so-called flutter speed, the structural oscillation induced by aerodynamic forces becomes unstable, i.e. with growing amplitude, which can lead to a catastrophic failure of the aircraft structure. Therefore, the flutter speed of an aircraft has to be determined accurately, in order to ensure that the aircraft is free from flutter during its operation. According to the safety regulations, it is mandatory that the determination of the flutter speed should be carried out using both numerical and experimental means.

To predict the flutter speed various activities have to be carried out, amongst other the normal mode analysis of the structure, prediction of unsteady aerodynamic force due to the structural motions, coupling of the aerodynamic with structural parts, etc. For an aircraft, which has operational envelope in subsonic or supersonic flow, a computer code based on the linear potential flow theory has been proved to be a very useful and sufficient tool for unsteady aerodynamic calculations. In this linear approach the unsteady part of the aerodynamic forces is assumed to be independent from the steady part and its calculations are carried out efficiently in the frequency domain. Examples of calculation methods of unsteady aerodynamic forces based on the linear potential flow theory, are the Lifting Surface Method [1] and the Doublet Lattice Method [2]. The first one gives the most accurate solution achievable up-to-day. The Doublet Lattice Method has been the default method for the computation of unsteady aerodynamic force during flutter analysis for years since it has been introduced into the commercial NASTRAN program. It seems the situation would not change.

For flight speeds with significant compressible effects, such as in transonic and also hypersonic flow, the linear potential flow theory is no longer useful. In particular significant interactions between the shear layer near the body surface and compression shocks arise which have to be carefully taken into account in the analysis model. At these flow conditions the unsteady part of the aerodynamic forces is no longer independent from the steady part. Therefore the steady and unsteady parts of the aerodynamic forces have to be computed simultaneously and usually are performed in the time domain. The method to handle this type of flow is the one that incorporates compressibility and viscous effects in its analysis model. Formally such a method would be based on the solution of the Navier-Stokes equations. However, computing time, turn around time and costs would penalize this type of method for industrial applications. Instead, in the last decades simplification is sought to have a balance between costs and performance. This includes methods based on the Euler equations, Full Potential (FP) equation and Transonic Small Disturbance (TSD) equation.

The most important disadvantage of methods based on the flow equations other than the Navier-Stokes equations is the inability to model the effect of viscosity. As it has been mentioned before this effect is important for some types of flows.

A way, that was established in the steady aerodynamics, to include the viscous influences succeeds through a so-called ‘Viscous - Inviscid Interaction (VII)’ method, i.e. combination of the boundary layer theory with frictionless theories, which are used to represent the inner viscous flow and the outer inviscid flow respectively [3, 4]. This VII method is expanded in the present work to cope unsteady flows and is also applied for flutter analysis, in order to answer the following questions:

- How far improves the VII Method inviscid calculations ?
- How far influences the VII Method aeroelastic calculations ?

1.1. Objectives and General Approach

The major aim of this work is to study the coupling techniques between viscous and inviscid flow and also the coupling between structural oscillation and aerodynamic forces. The objective is to develop a code based on VII method for calculating aerodynamic forces and its application for flutter analysis. The developed code should be fast, accurate and particularly suitable for industrial applications. The high-Reynolds number flow about airfoils and wings in transonic speed regime is the flow case of practical interest and have been the primary target in the present investigation.

In order to be able to calculate shock-dominating flows, the boundary layer theory is coupled with non-linear, frictionless theories for the outer flow, which can capture a shock wave. For this purpose the TSD equation, the non-linear Euler equations and the Small Disturbance Euler (SDEu) equations will be employed under the following considerations:

- By using the TSD and Euler equations one can observe the influence of the viscous aerodynamic model for weak and strong shocks.
- In order to validate and to proof a VII concept, it is easier to apply the concept to the inviscid TSD equation because of its relatively low computational time. The TSD equation is the lowest equation in the hierarchy of the non-linear, inviscid flow equations. TSD equation can be solved relatively faster than the Euler equations. Moreover, grid generation for methods based on TSD equation is relatively simpler than that based on the Euler equations.
- Since the Euler equations are the highest equations in the hierarchy of the non-linear, inviscid flow equation, one can expect the best results from the VII method when the Euler equations are used for the inviscid flow model.
- As continuation of the research at the Institute of Aerodynamics (formerly Institute of Fluid Mechanics -FLM-) of the Technical University of Munich (TUM) under the guidance of Prof. Dr. –Ing. Boris Laschka, the VII method is also developed by using the SDEu equations, which was developed based on the non-linear Euler equations particularly under small disturbance time-linearized assumption.

The calculation of the boundary layer in this present work is mainly based on the integral boundary layer equation because of its simplicity in implementation and less computational time, but a differential equation - based calculation method is also described. A laminar-turbulent transition prediction is also presented.

The results obtained using the present method are compared and validated with those obtained using the Navier-Stokes equations and also with some experimental data. It is shown that the method proposed in this thesis produces very encouraging results. This is especially true as far as its application for calculating the unsteady aerodynamic forces for flutter analysis. This proposed approach is therefore a valuable alternative to methods based on the Navier-Stokes equations particularly when a large number of computations have to be carried out involving large number parameter variation.

1.2. Scope of the Work

The scope of the present work consists of the following sections:

- Description and discussion of some VII methods.
- Description and discussion of the selected viscous aerodynamic models (boundary layer models).
- Description and discussion of the selected inviscid aerodynamic models (TSD, Euler and SDEu equations).
- Validation of each aerodynamic models used in the present study.
- Application of the VII method for flutter analysis.

The steps of the implementation works are described below:

- Development of a TSD-based computational code. For applications of the proposed VII method with the Euler equations, the available Euler and the Small Disturbance Euler Codes – so-called as FLMEu and FLMSDEu codes - in the Institute of Aerodynamics of the Technische Universität München are used.
- Development of boundary layer computational codes based on the integral equations and the differential equation that include a laminar-turbulent transition prediction.
- Development of coupling schemes between the viscous and the inviscid aerodynamic models.
- Development of a computational code for flutter analysis in time domain.

All computational codes are developed using FORTRAN programming language.

1.3. Outline of the Thesis

In order to organise the description of the present work, this thesis is divided into theoretical and results part. The theoretical part describes the viscous aerodynamic models (boundary layer) and the inviscid aerodynamic models (TSD, Euler and Small Disturbance Euler) and the coupling between both. The results section describes the validation of the developed calculation program for steady and unsteady aerodynamic test cases and its application for flutter calculation of airfoils and wings.

The outline of this thesis may be summarised as follows:

- Chapter 1 describes the background, objective, scope and outline of the present work.
- Theory of viscous - inviscid interaction and an overview of researches in this field are described in Chapter 2.
- Chapter 3 concerns with the selected viscous aerodynamic models, i.e. the calculation method of the boundary layer for incompressible and compressible flows, laminar and turbulent flows including the laminar-turbulent transition.
- Chapter 4 describes the selected inviscid aerodynamic models, i.e. the TSD equation, the Euler equations and the Small Disturbance Euler equations. The form of the equations and their numerical solutions are presented in this chapter, followed by the description of the coupling between the viscous and the inviscid model.
- Theory of the fluid - structure interaction (flutter analysis) is presented in Chapter 5.
- Some selected results will be presented in Chapter 6. Validation of the developed methods for steady and unsteady aerodynamic test cases for flat plate, airfoils and wings are presented by different flow parameters, with and without consideration of the boundary layer.
- In Chapter 7 the application of VII method in flutter analysis is presented in form of the prediction of the transonic dip of an airfoil as well as of a wing.
- Chapter 8 closes the discussion with the summary of the work and recommendation for further work.

In order to explain some details of the numerical solutions and equations, some appendices follow.

2. Theory of Viscous – Inviscid Interaction (VII)

In this chapter the theory of viscous - inviscid interaction (VII) with its historical background and an overview of researches in this field are presented.
The presentation will be organised in the following details:

- Historical Background
- Overview of researches in VII
- Basic VII Methods

2.1. Historical Background

The existence of a small viscous flow region in flows with small viscosity was recognized one hundred years ago at the beginning of the last century pioneered by Prandtl with his publication on boundary layers in Mathematical Congress in Heidelberg 1904 (see [5]). Prandtl showed how it was possible to analyze viscous flows precisely in cases which had great practical importance. He proved that the flow about a solid body can be divided into two regions, namely a thin layer around the body (boundary layer), where friction plays important role and the inviscid region outside the boundary layer, where friction may be neglected.

The boundary layer problem is solved by imposing the no-slip boundary condition at the solid surface and imposing at a location far away from the solid surface a prescribed pressure or velocity distribution, which follows from a known inviscid flow solution. At the beginning, the boundary layer theory was developed mainly for laminar flow case in an incompressible fluid. Important development of the boundary layer theory was reached by Blasius, von Karman, Pohlhausen and Thwaites among others. The theory was extended to include the turbulent, incompressible boundary layers which are more important for practical applications. Some researchers contributed in this development are Dryden, Schubauer and Klebanoff among others. The phenomenon of transition from laminar to turbulent flow was investigated among others by Reynolds, Rotta, Tollmien and Schlichting. The extension of the boundary layer theory in compressible flow was carried out among others by Ackeret, van Driest and Young. As compared to incompressible flow there are at least four additional quantities which must be taken into account in the calculation of compressible boundary layers, i.e. Mach number, Prandtl number, viscosity function and boundary condition for temperature distribution. The velocity boundary layer may interact with the thermal boundary layer and shock wave in compressible flow, which increase the degree of complexity.

Later on it was attempted to solve the combination of the boundary layer equations with an inviscid flow model numerically. This is performed by iterative calculation process, which is generally organised as follows: an inviscid flow calculation around the body, using a slip boundary condition, determines the pressure distribution over the body surface. This pressure distribution will be used to solve the boundary layer equations. An essential parameter following from the boundary layer solution is the so-called displacement thickness, which represents the displacement of the inviscid flow from the body surface due to the presence of the boundary layer. This displacement thickness value will be added to the body surface to form a so-called displacement body. The inviscid flow calculation will be carried out again subject to this displacement body. This form of iterative calculation process, which combines the boundary layer and an inviscid flow equation is known as a kind of viscous – inviscid interaction.

2.2. Overview of Researches in Viscous - Inviscid Interaction

The research within the area of VII can be generally divided into two different approximations, i.e. the Zonal and the Thin Layer approximation [6, 7]. In the Zonal approximation the inner viscous region is governed by the Navier Stokes (NS) equations and the outer inviscid region is represented either by the TSD, the Full Potential (FP) or the Euler equations. The flow parameters must be adapted at the transition of the two regions (matching of the solution from inner and outer region). The advantages of this approximation are less computational time compared to that if all regions were simulated with NS equations and the computation of the viscous layers in the proximity of the body is ensured by the NS equations. Therefore one can expect accurate results by using this kind of approximation. Two things must be considered in the Zonal approximation, i.e. the switching process between the NS equations and the inviscid equations, and the matching process within the transition area, particularly if the inviscid region is solved with TSD or FP equation. The state of variables at the outer edge of the inner region, which is solved by NS equations, serves as input for the inviscid region. Therefore the state of variables must be transformed into the potential terms. This Zonal approximation is more simply performed if the inviscid region was governed by Euler equations because one can switch the viscous terms in the NS equations off, if the calculation process enters the outer region. Figure 2.1. illustrates the Zonal approximation. Su [6] has used the Zonal approximation for the solution of an airfoil in a steady flow by using the NS equations and the FP equation to represent the inner and outer flow region respectively.

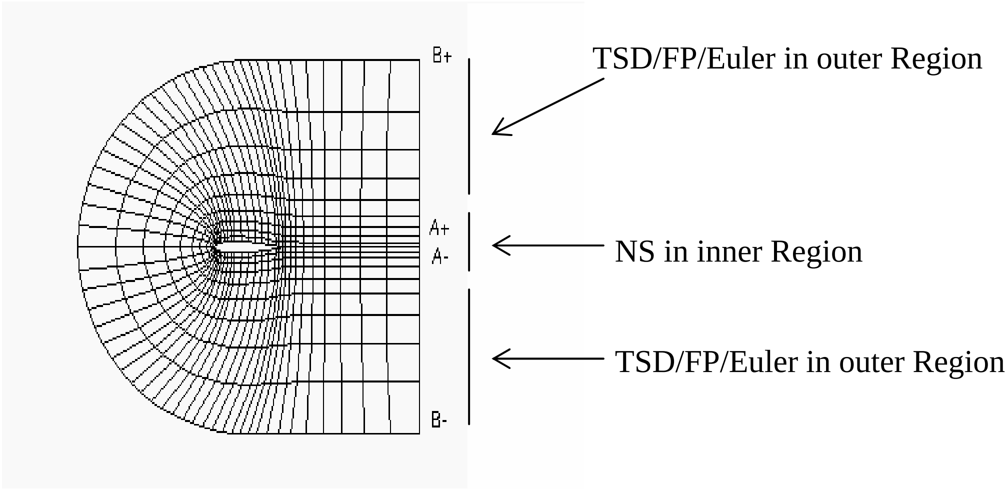

Figure 2.1. Zonal Approximation

The Thin Layer approximation is the most popular approximation used by many scientists. The inner region is simulated by the boundary layer equations (mostly by integral boundary layer equations), i.e. the viscous region is assumed only in the boundary layer and the computation of the inviscid outer region with the TSD, FP equation or Euler equations. The coupling between the boundary layer and the inviscid solution takes place at the boundary condition of the inviscid flow by means of the displacement thickness in form of transpiration velocity or modification of the surface slope. As long as the boundary layer thickness is thin, the thin layer approximation is sufficient and can supply the best results. It is best to be applied for high Reynolds number flows, because the boundary layer thickness is thin enough in order of $O(Re^{-1/2})$. The acceptance of the thin layer approximation is broken off, if the boundary layer thickness is large. The advantages of this approximation are less computational time and it can be simply constructed. The accuracy of the results depends on the quality of the boundary layer calculation method and the coupling scheme. Figure 2.2 illustrates the thin layer approximation. The interaction method or the coupling scheme in the thin layer approximation can generally be classified in six types, i.e. direct, inverse, semi inverse, quasi simultaneous, simultaneous and the combination of direct and semi inverse interaction.

In the direct interaction method the solution of the inviscid equation (velocity or pressure) serves as input for boundary layer calculation. The displacement thickness as output of the boundary layer calculation will update the boundary condition of the inviscid region.

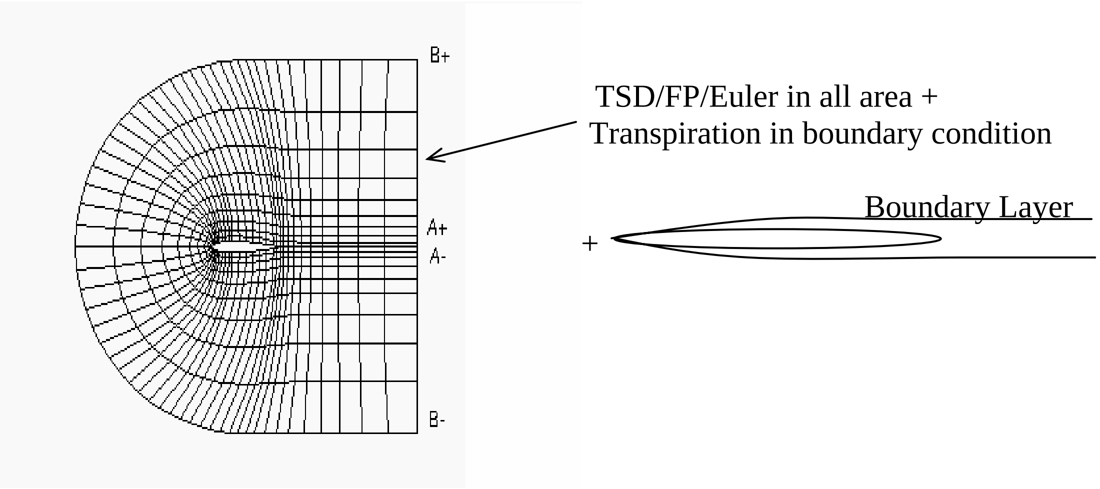

Figure 2.2. Thin Layer Approximation

The works from Rizzetta [8], Houwink [9] and Rizzetta & Borland [10] are based on the direct interaction method. They used the TSD equation coupled with the integral boundary layer equations – the Lag Entrainment method from Green et. al. [11] - to simulate an airfoil and a wing in unsteady turbulent flow without separation. The advantage of the direct interaction method is the straightforward computation of the displacement thickness and velocity or pressure. The disadvantage is that the separated flow cannot be simulated because of the appearance of a singularity in the boundary layer parameters, the so-called Goldstein Singularity [12], as the flow is separating.

In the inverse interaction method, both of the equations are solved in a reverse input output relationship. The boundary layer equations are solved not subject to a given pressure distribution, but subject to a given displacement thickness distribution. The output of the boundary layer calculation is therefore the pressure distribution. The inverse method for the solution of the boundary layer equations was probably introduced at the first time by Chaterall & Mangler [13]. The inviscid equation is solved with the given pressure from the result of the boundary layer equations. The output of the inviscid equation is the displacement thickness, which serves as input for the boundary layer equations. With this method the singularity of the boundary layer parameters can be eliminated. The inverse interaction method was not developed further because of the difficulties in the inverse solution of the inviscid equation.
The inviscid equation is more simply solved with the geometry input (straightforward as in the direct method) than with pressure distribution input (as in the inverse method).

For this reason one introduces alternative method, the so-called semi inverse method. In the semi inverse method the inviscid equation is solved as in the direct method and the boundary layer equations as in the inverse method. The input for the two equations is the displacement thickness and the output from the two equations are two velocity distributions, one from the inviscid equation (U_i) and the other one from the boundary layer equations (U_v). A relaxation method is additionally needed, until the converged solution ($U_v \approx U_i$) is achieved. Carter [14], Melnik & Brook [15] and Le Balleur & Lavigne [16] developed the semi inverse method among others. They coupled the TSD equation with Lag Entrainment integral boundary layer equations, in order to compute the two-dimensional flow with separation. Zhilliang & Voss [17] developed a similar method with FP equation plus Lag Entrainment integral boundary layer equations for solution of two- and three-dimensional problems.

The quasi simultaneous method was developed by Veldman [18] and Houwink & Veldman [19], in which an Interaction Law, deduced from the asymptotic theory, was used to compute the displacement thickness and the viscous velocity (U_v) simultaneously. The procedure of the quasi simultaneous method is similar to the direct method.

The simultaneous method was developed among others by Drela & Giles [3] and Wolles [4]. Both of the inviscid and the boundary layer equations are solved as a set of simultaneous equations. Drela & Giles used the Euler equations plus integral boundary layer equations, based on kinetic energy equation. Wolles used the FP equation coupled with the same integral boundary layer equations for the solution of two-dimensional steady problem.

The combination method of the direct and semi inverse method was developed among others by Howlett [20] and Edwards [21]. They calculated the boundary layer in attached flow by the direct method and the boundary layer in separated flow by the semi inverse method. The transition (switch) between the direct and the semi inverse method was controlled by a certain value of the shape factor (displacement to momentum thickness ratio). They used the TSD equation coupled with Lag Entrainment integral boundary layer equations. Edwards called his code as CAP TSDV (Computational Aeroelastic Program using TSD with interactive boundary layer method). He introduced a block control system, in order to control/adjust the interaction between the boundary layer and the TSD equation.

The application of the VII in the aircraft industry was carried out among others by Galpin from the British Aerospace [22] and Haase from the Daimler Benz Aerospace AG [23]. Both of them coupled the Euler equations plus integral boundary layer equations for the computation of the steady and unsteady aerodynamics of airfoil and wing.

Most of VII methods use the steady two-dimensional integral boundary layer equations as the viscous model. For three-dimensional problems one uses the strip theory approach, in which the boundary layer at a specified 3D section is assumed as purely two dimensional. The search of the three-dimensional integral boundary layer equations was published among others by Drela & Mughal [24]. They performed calculations of the atmospheric boundary layer. But its application in VII method has not yet been further developed. This is probably because the influence of the boundary layer in circumferential/span direction is smaller than in normal direction, so it can be ignored (except if the cross flow velocity is significant). Also, the computation time for solving three-dimensional boundary layer equations is longer than for solving two-dimensional ones.

The VII method with differential boundary layer equations as viscous model has been developed by Van Dalsem & Steger [25] among others. They coupled the differential boundary layer equations with the FP equation and solved both of the aerodynamic models using the finite differences method. Hamilton et. al. [26] solved the differential boundary layer equations, in order to obtain the boundary layer parameters of the flow with different fluids (ideal gas, CF4 and equilibrium air chemistry). But they did not make the interaction between the boundary layer and the inviscid flow. These VII method is not so far developed, because the effort and the cost to solve the differential boundary layer equations are more than those of the integral boundary layer equations. In order to solve the differential equation, one needs a grid system and a turbulence model, which are not needed by solving the integral boundary layer equations.

Most of VII methods use the integral boundary layer equations either for pure laminar or turbulent flow. The application of laminar-turbulent transition in VII method has been carried out by Drela & Giles [3] and Wolles [4] among others. The transition prediction was carried out by the e^n method, which has been developed by Smith, Gamberoni & van Ingen [3]. It is assumed that the transition from laminar to turbulent flow takes place if the value of spatial disturbance amplification n is equal to 9 at a certain location .

Application of VII method for calculating of aerodynamic forces and flutter analysis was also developed by Henke [27] recently and has been used at the Airbus Company as an alternative calculation method, which is more favourable compared to the Navier-Stokes equations - based calculation method.

2.3. Basic VII Methods

The following methods can be used to perform the interaction between the viscous and the inviscid flow equation: direct, inverse, semi inverse, quasi simultaneous and simultaneous method. Each method will be described in the following section.

2.3.1. Direct Method

In this interaction the outer flow region (inviscid model) is computed first subject to the slip boundary conditions, e.g. body contour without displacement thickness (δ_0^* = 0). The solution from this step is a velocity distribution along the body (U_{eOF}^1). This velocity distribution is used as the input for the inner region (viscous model). Afterwards the inner region is computed. The solution from this step is the displacement thickness (δ_1^*) among others, that change the effective body contour. With the new body contour as the input for the outer region, the velocity distribution (U_{eOF}^2) is computed again. This mechanism runs, until the two solutions - displacement thickness (δ_n^*) and velocity distribution (U_{eOF}^n) - are convergent. The iteration scheme of the direct method can be seen in Figure 2.3.

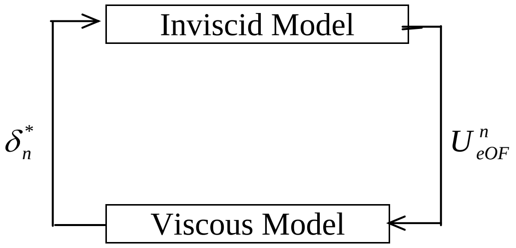

Figure 2.3. Iteration Scheme of the Direct Method

The interaction of the two models and the boundary conditions can be represented by the following functional relationship:

$$\begin{Bmatrix} OF\left(In:\delta_n^*(I_n);Out:O^{n+1},U_{eOF}^{n+1}(O^{n+1})\right)=0 \\ IF\left(In:U_{eOF}^{n+1}(O^{n+1});Out:I_{n+1},\delta_{n+1}^*(I_{n+1})\right)=0 \end{Bmatrix}$$

OF and *IF* are the functional relations for the outer and inner regions. *In* and *Out* denote the input and output. *I* and *O* are the unknowns of the viscous and the inviscid model. *n* is the iteration number. The iterative mechanism of the direct method can also be analyzed graphically. In order to accomplish this representation, the outer and inner region are transformed into the relationship between the gradient of the velocity and the gradient of the displacement thickness, as in the following [4, 28]:

$$OF \ : \ \frac{dU_e}{dx}(O^{n+1}) = E_1 + E_2\frac{d\delta^*}{dx}(O^n, I_n)$$

$$IF \ : \ \frac{d\delta^*}{dx}(O^{n+1}, I_{n+1}) = F_1 + F_2\frac{dU_e}{dx}(O^{n+1})$$

The graphical illustration of the Direct Method can be seen in Fig. 2.4. for several flow conditions.

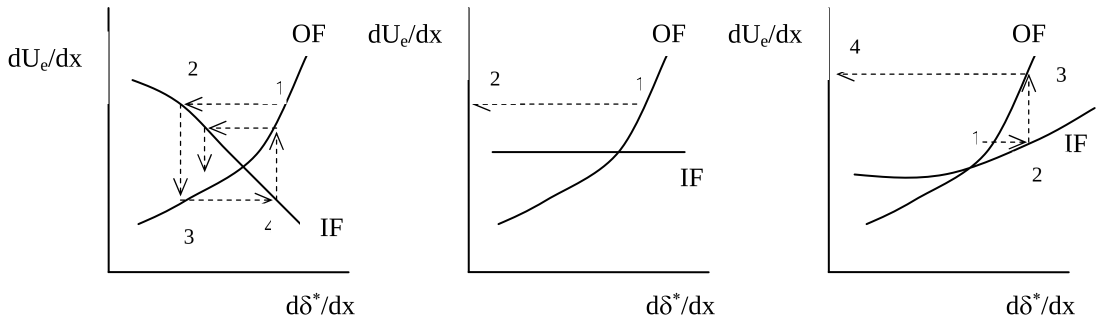

a) Attached Flow b) Separating c) Separated Flow

Figure 2.4. Graphical Illustration of the Direct Method

The line *OF* and *IF* in Figure 2.4. show the functional relationship of the outer and inner regions respectively. The form of the line depends on the value of the function E_1, E_2, F_1 and F_2. The sequence of iteration runs according to the number. For attached flows the iteration is convergent into the point of intersection between the *OF* and *IF* lines (Fig. 2.4.a). But this mechanism fails, if there is a separation point on the surface (Fig. 2.2.b and c). Computation of the displacement thickness becomes singular for separated flows (referred to as the Goldstein Singularity, see Appendix 4).

The advantage of the direct method are:

- Simple to construct (in sense of programming)
- The solutions of the outer and inner regions, U^n_{eOF} and δ^*_n, are supplied immediately, because the equations are solved straightforward.

The disadvantage of the direct method is that it cannot simulate separated flows. The direct method is also well-known as '*weak interaction*', because the interaction is dominated by the outer region.

2.3.2. Inverse Method

In this method the velocity distribution is computed from the inner region (by solving the viscous flow model) and the displacement thickness is computed from the outer region (by solving the inviscid flow model). With the velocity of the inner region U^1_{eIF} as the initial value, the computation of δ^*_2 is accomplished from the outer region. With the value of δ^*_2 one computes the new velocity distribution U^2_{eIF}. This mechanism runs, until the two solutions - displacement thickness (δ^*_{n+1}) and velocity distribution (U^n_{eIF}) - are convergent. The iteration scheme can be seen in Figure 2.5.

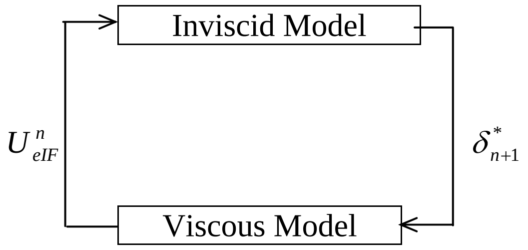

Figure 2.5. Iteration Scheme of the Inverse Method

The interaction of the two models and the boundary conditions can be represented into the following functional relationship:

$$\begin{Bmatrix} OF\left(In : U_{eIF}^{n}(I_n); Out : O^{n+1}, \delta_{n+1}^{*}(O^{n+1})\right) = 0 \\ IF\left(In : \delta_{n+1}^{*}(O^{n+1}); Out : I_{n+1}, U_{eIF}^{n+1}(I_{n+1})\right) = 0 \end{Bmatrix}$$

The outer and inner regions will be represented in the relation between the gradient of velocity and displacement thickness as follows:

$$\begin{aligned} OF \quad &: \quad \frac{d\delta^*}{dx}(O^n, I_n) = E_1 + E_2 \frac{dU_e}{dx}(I_n) \\ IF \quad &: \quad \frac{dU_e}{dx}(I_{n+1}) = F_1 + F_2 \frac{d\delta^*}{dx}(O^n, I_{n+1}) \end{aligned}$$

The graphical illustration of the Inverse Method can be seen in Fig. 2.6. for several flow conditions.

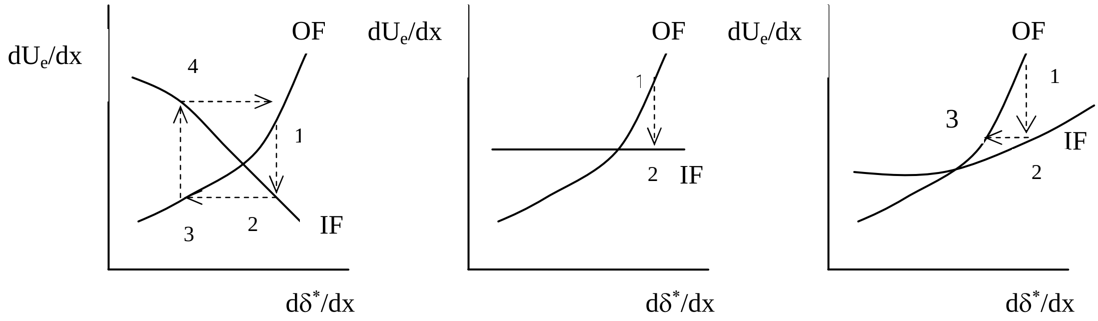

a) Attached Flow b) Separating c) Separated Flow

Figure 2.6. Graphical Illustration of the Inverse Method

In the inner region, the boundary layer equations (e.g. the integral boundary layer equations) can be transformed into the inverse form, in order to compute the output velocity. The inverse procedure of the inviscid model runs as in design process with the velocity as input and geometry as output. However it is not simple to transform the inviscid model into the inverse form. For attached flow the iteration is not convergent (Fig. 2.6.a). But this mechanism runs, if a separation point exists on the body (Fig. 2.6.b and c). The advantage of the inverse method is that separated flows can be simulated.

The disadvantages of the inverse method are:

- Attached flows cannot be simulated
- The inverse equations (of the two regions) is not simple to construct
- The solution of variables of the outer and inner region, U_{eIF}^{n} and δ_{n+1}^{*}, needs longer time than with the direct method, because the equations are not solved straightforward.

It can be observed that both of the iteration procedures (direct and inverse) diverge for at least one of the flow situations when using no relaxation. A direct or an inverse method, which assumes the dominance of one flow model over the other, fails to be applied to general flow situations. Neither a direct nor an inverse method without relaxation is able to deal with the so-call ‘*strong interaction*’ from both of the flow regions. The direct interaction method can only be used in the region upstream of the point of vanishing skin friction, at the other hand the inverse interaction method is a valid approach for the region downstream of this point.

2.3.3. Semi Inverse Method

The Semi inverse method is a synergy of the direct and inverse method. The inviscid region is solved with the direct method, but the viscous region is solved with the inverse method. In order to fit the solution between the inner region and the outer region, a relaxation procedure is additionally used. Initial value of displacement thickness (δ^*_0) is given first. Afterwards one calculates the velocity distribution (U^1_{eOF}) from the outer region (inviscid model), which is computed with the given displacement thickness (δ^*_0). At the same time one computes the velocity distribution (U^1_{eIF}) with the inverse procedure from the given displacement thickness (δ^*_0). The new displacement thickness (δ^*_1) is determined by a relaxation procedure based on the two velocity distribution solutions (U^1_{eOF}) and (U^1_{eIF}). If all parameters (δ^*_n, U^{n+1}_{eOF} und U^{n+1}_{eIF}) are convergent, these computations are terminated. The iteration scheme can be seen in Figure 2.7.

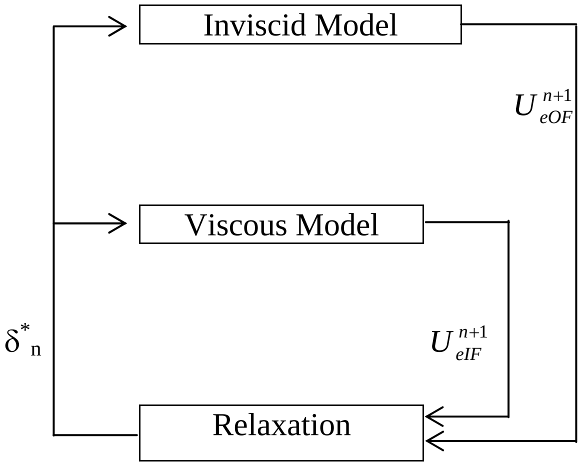

Figure 2.7. Iteration Scheme of the Semi Inverse Method

The interaction of the two models and the boundary conditions can be represented into the following functional relationship:

$$\left\{\begin{array}{l} IF\left(In:\delta^*_n(I_n);Out:I_{n+1},U^{n+1}_{eIF}(I_{n+1})\right)=0 \\ OF\left(In:\delta^*_n(I_n);Out:O^{n+1},U^{n+1}_{eOF}(O^{n+1})\right)=0 \\ RL\left(In:U^{n+1}_{eOF}(O^{n+1}),U^{n+1}_{eIF}(I_{n+1});Out:\delta^*_{n+1}(I_{n+1})\right)=0 \end{array}\right\}$$

Here *RL* designates the functional relationship of the relaxation procedure. The advantage of the semi inverse method is that simulation of separated flows is possible. The disadvantage of the semi inverse method are:

- The boundary layer is not computed straightforward. Therefore one must transform the boundary layer equations into inverse form.
- Additionally relaxation procedure is needed, therefore it takes a longer time to obtain the solution of the boundary layer.

2.3.4. Quasi-Simultaneous Method

As the semi inverse method, the quasi-simultaneous method is a synergy of the direct and the inverse method. The inviscid region is solved with the direct method, but the viscous region is approximated with the simultaneous solution of the boundary layer equations and an ‘Interaction Law’. The Interaction Law was deduced from the asymptotic theory and connects the outer and inner regions like the function of the outer deck of the boundary layer in the triple deck boundary layer theory.

With initial values of displacement thickness (δ^*_0), the velocity distribution (U^1_{eOF}) is computed by the outer region (inviscid model). Simultaneously the displacement thickness (δ^*_1) and the velocity distribution U_{eIF} are calculated from the inner region and the interaction law with input velocity distribution (U^1_{eOF}). With the displacement thickness (δ^*_1), the outer region is computed again. If the iteration is convergent this computation is terminated. The iteration scheme can be seen in Figure 2.8

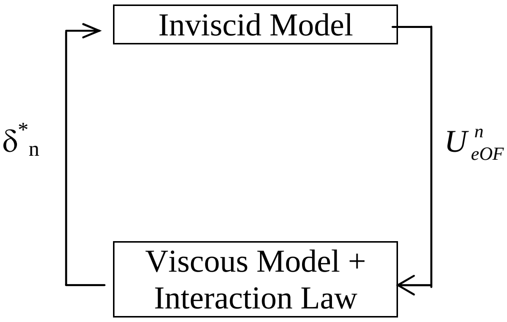

Figure 2.8. Iteration Scheme of the Quasi-Simultaneous Method

The interaction of the two models and the boundary conditions can be represented into the following functional relationship:

$$OF\left(In:\delta^*_n(I_n\ );Out:O^{n+1},U^{n+1}_{eOF}(O^{n+1})\right)=0$$

$$\begin{Bmatrix} IF\left(In:U^{n+1}_{eOF}(O^{n+1});Out:I_{n+1},U_{eIF},\delta^*_{n+1}(I_{n+1})\right)=0 \\ IL\left(U^{n+1}_{eOF}(O^{n+1},U_{eIF};\delta^*_{n+1}(I_{n+1})\right)=0 \end{Bmatrix}$$

Here *IL* is the functional relationship of the Interaction Law. The advantage of the quasi-simultaneous method is that simulation of separated flows is possible.

The disadvantage of the quasi-simultaneous method are:

- Additionally one must develop an Interaction Law between the outer and the inner region
- Simultaneous method to solve the viscous model and the Interaction Law needs more time than the direct method

2.3.5. Simultaneous Method

In this procedure all equations are solved simultaneously, which means that the boundary layer equations and the potential or Euler equations are treated as an expanded system of differential equations. The iteration runs with initial values of displacement thickness (δ^*_0) and velocity distribution (U_{e0}). Then one computes the displacement thickness and the velocity distribution at the same time by solving the expanded system of differential equations. The iteration scheme can be seen in Figure 2.9.

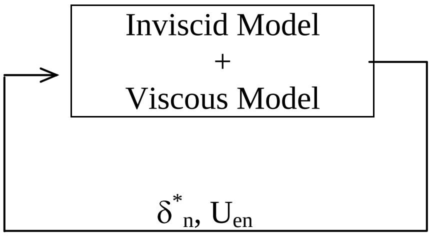

Figure 2.9. Iteration Scheme of the Simultaneous Method

The interaction of the two models and the boundary conditions can be represented by the following functional relationship:

$$\begin{Bmatrix} IF\left(I_n, \delta^*_n(I_n, O^n), U_e(O^n, I_n)\right) = 0 \\ OF\left(O^n, \delta^*_n(I_n, O^n), U_e(O^n, I_n)\right) = 0 \end{Bmatrix}$$

The advantage of the simultaneous method is that separated flows can be simulated. The disadvantages of the simultaneous method are:

- It is not simple to develop and solve the expanded system of differential equations
- Simultaneous method for solution the viscous model and the inviscid model needs more time than the direct method

In the present work a combination of the direct and semi inverse method is developed, because - regarding the programming aspects - only few changes are necessary in the inviscid model and one can develop the boundary layer calculation method separately from the inviscid model. Another reason is that one can couple the viscous model easily into many different inviscid models.

The computation of the boundary layer (the viscous aerodynamic models) in the present work is performed using the following methods:

- Integral boundary layer equation based on the procedure introduced by von Karman - Thwaites [5] for incompressible laminar flows
- Integral boundary layer equations based on the kinetics energy equation proposed by Drela and Giles [3] for compressible laminar and turbulent flows
- Integral boundary layer equations based on the Lag Entrainment method introduced by Green et. al. [11] for compressible turbulent flows
- Differential boundary layer equations based on the procedure of Hamilton et. al. [26] for compressible laminar and turbulent flows
- The incompressible flat plate boundary layer calculated using the Blasius solution [5] or the Power 1/7 Law [5] is used as the initial value for running the calculation for laminar or turbulent flows, respectively.
- The transition from laminar to turbulent flow is predicted using e^n method [3]

The viscous aerodynamic models used in the present work will be explained in the next chapter.

3. Viscous Aerodynamic Models

This chapter describes some calculation methods used to determine the boundary layer parameters. Three different calculation methods are presented, i.e. the flat plate boundary layer, the integral and the differential boundary layer equations. All of the calculation methods are limited for two dimensional problems. The application of these methods for solving of three dimensional problems is carried out via strip theory approach, which means that the local boundary layer along spanwise direction is assumed to be two dimensional.

The values of the boundary layer parameters on a flat plate (such as: boundary layer thickness δ, momentum thickness θ, displacement thickness δ^*, shape factor H and skin friction coefficient C_f) are used in the present work as the initial value for the boundary layer calculation, since the calculation process is carried out in space-marching fashion. The boundary layer on a flat plate is determined using the Blasius solution and the Power 1/7 Law for incompressible laminar and turbulent flows respectively.

Among the integral boundary layer equations, three calculation methods proposed by von Karman-Thwaites, Drela-Giles and Green et. al. are discussed. For solving the differential boundary layer equation the procedure proposed by Hamilton et. al. is used. To complete the description of the boundary layer, a laminar – turbulent transition prediction based on the e^n method is also described at the end of this chapter.

Before further description of those calculation methods, it is better to first recognize the meaning of some boundary layer parameters. Figure 3.1. shows the sketch of boundary layer on a flat plate to illustrate the physical meaning of the boundary layer thickness δ, displacement thickness δ^* and momentum thickness θ.

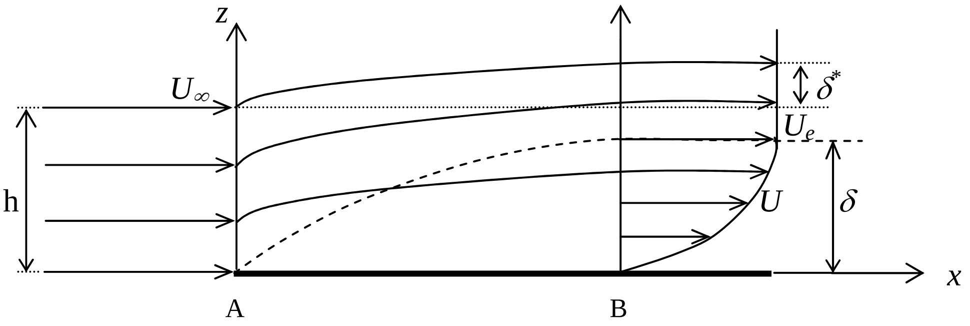

Figure 3.1. Sketch of Boundary Layer on a Flat Plate

The boundary layer thickness δ is defined as the thickness over the surface, measured in the normal direction from the surface, where the velocity is zero, up to the position of the external frictionless velocity U_e. The external streamline of the flow is displaced upward because of the presence of the boundary layer. The displacement thickness δ^* is defined as the thickness measured between the displaced and the undisturbed streamline.

The momentum thickness θ is defined from the momentum loss between stations A and B as follows (see Fig 3.1).

The momentum (per unit depth of the plate) at the station A can be described as:

Mom. A = $\rho_\infty U_\infty^2 h$

The same description for the momentum at the station B is:

Mom. B = $_0\int^h \rho U^2 dz + \rho_e \delta^* U_e^2$

The momentum loss between stations A and B is:

Mom. B – Mom. A = $\rho_e U_e^2 \theta$

From this momentum loss, the momentum thickness θ is defined as:

θ = (Mom. B – Mom. A)/$\rho_e U_e^2$ = ($_0\int^h \rho U^2 dz + \rho_e \delta^* U_e^2 - \rho_\infty U_\infty^2 h$)/$\rho_e U_e^2$

where h, ρ and U are the height of the fluid column, the density and the velocity of fluid, respectively. The subscript e denotes the condition at the edge of the boundary layer.

The relation between the momentum and the displacement thickness is given by the shape factor H defined as: $H = \delta^*/\theta$

3.1. Boundary Layer on a Flat Plate

3.1.1. The Blasius Solution: Incompressible Laminar Flow

In order to determine the boundary layer parameters on a flat plate in incompressible laminar flow, the exact solutions from Blasius are used, as follows [5]:

$$\delta = \frac{5x}{\sqrt{\mathrm{Re}_x}} \quad (3.1), \qquad \delta^* = \frac{1.73x}{\sqrt{\mathrm{Re}_x}} \quad (3.2), \qquad \theta = \frac{0.664x}{\sqrt{\mathrm{Re}_x}} \quad (3.3),$$

$$C_f = \frac{0.664}{\sqrt{\mathrm{Re}_x}} \quad (3.4), \qquad H = \frac{\delta^*}{\theta} = 2.6054 \quad (3.5)$$

with the displacement thickness:
$$\delta^* = \int_0^\infty \left(1 - \frac{\rho U}{\rho_e U_e}\right) dz \tag{3.6}$$

the momentum thickness:
$$\theta = \int_0^\infty \left(1 - \frac{U}{U_e}\right) \frac{\rho U}{\rho_e U_e} dz \tag{3.7}$$

and the skin friction coefficient:
$$C_f = \frac{2\tau_w}{\rho_e U_e^2} \tag{3.8}$$

where Re_x is the local Reynolds number and τ is the shear stress. The subscript w denotes the value at the wall.

3.1.2. The Power 1/7 Law: Incompressible Turbulent Flow

In order to calculate the boundary layer parameters on a flat plate in incompressible turbulent flow, the solutions of the Power 1/7 Law are used [5, 8]:

$$\delta = 0.37 \frac{x^{0.8}}{\mathrm{Re}_\infty^{0.2}} \quad (3.9), \qquad \delta^* = \frac{\delta}{8} \quad (3.10), \qquad \theta = \frac{7}{72}\delta \quad (3.11),$$

$$C_f = 0.0576 x^{-0.2}\, \mathrm{Re}_\infty^{-0.2} \quad (3.12), \qquad H = \frac{\delta^*}{\theta} = \frac{9}{7} \quad (3.13), \qquad C_E = 7\frac{d\delta^*}{dx} \quad (3.14)$$

where Re_∞ is the Reynolds number of the undisturbed flow and C_E is the entrainment coefficient defined as [11]:

$$C_E = \frac{1}{\rho_e U_e} \frac{d}{dx}\left[\rho_e U_e (\delta - \delta^*)\right] \tag{3.15}$$

3.2. Integral Boundary Layer Equations

3.2.1. The von Karman - Thwaites Method: Incompressible Laminar Flow

In order to compute the boundary layer parameters of an airfoil in an incompressible laminar flow, the von Karman - Thwaites method is used.

The integral of the momentum equation in the boundary layer (known as von Karman integral momentum equation) reads [5, 29]:

$$\frac{d\theta}{dx} + (H+2)\frac{\theta}{U_e}\frac{dU_e}{dx} = \frac{\tau_w}{\rho_e U_e^2} \tag{3.16}$$

In order to solve equation (3.16), the three unknown θ, H and τ_w must be linked to each other.

By introducing a new symbol *K* as:

$$K = \frac{\theta^2}{\nu}\frac{dU_e}{dx} = Z\frac{dU_e}{dx}, \qquad Z = \frac{\theta^2}{\nu} \tag{3.17}$$

the von Karman integral momentum equation (3.16) can then be written as:

$$\frac{1}{2}U_e\frac{dZ}{dx} + [f_1(K) + 2]K = f_2(K) \tag{3.18}$$

where:

$$f_1(K) = H, \qquad f_2(K) = \frac{\tau_w\theta}{\mu U_e} \tag{3.19}$$

If one introduces further a new function *F*(*K*) such as:

$$F(K) = 2f_2(K) - 4K - 2Kf_1(K) \tag{3.20}$$

then the integral momentum equation (3.18) becomes:

$$\frac{dZ}{dx} = \frac{F(K)}{U_e} \tag{3.21}$$

Waltz [5] has proposed a linear function of *K* to approximate the function *F*(*K*) as:

$$F(K) = a - bK, \qquad a = 0.45, \qquad b = 6 \tag{3.22}$$

Substitution of the equation (3.22) into (3.21) gives:

$$U_e^{\,6}Z = 0.45\int_0^x U_e^{\,5}dx \tag{3.23}$$

which can be solved for *Z* by a recursive formula:

$$U_e^{\,6}(x_n)Z(x_n) = U_e^{\,6}(x_{n-1})Z(x_{n-1}) + 0.45\int_{x_{n-1}}^{x_n} U_e^{\,5}(x)dx \tag{3.24}$$

The initial values used to solve equation (3.24) are the values of *K* and *Z* at the stagnation point [5]:

$$K_0 = 0.077, \qquad Z_0 = \frac{0.077}{(dU_e/dx)_0}$$

Thwaites suggested several simple equations to approximate the shape factor and skin friction coefficient as a function of *K* [29], as follows:

$$for\ \ 0 \le K \le 0.1: \qquad \begin{aligned} H &= 2.6052 - 3.75K + 5.24K^2 \\ f_2(K) &= 0.22 + 1.57K - 1.8K^2 \end{aligned} \tag{3.25a}$$

$$for\ \ -0.0898 \le K \le 0: \qquad \begin{aligned} H &= \frac{0.0731}{0.14 + K} + 2.088 \\ f_2(K) &= 0.22 + 1.402K + \frac{0.018K}{0.107 + K} \end{aligned} \tag{3.25b}$$

$$for\ \ K > 0.1: \qquad \begin{aligned} H &= 2.2874 \\ f_2(K) &= 0.3590 \end{aligned} \tag{3.25c}$$

The skin friction coefficient will be computed with:

$$C_f = 2f_2(K)/\mathrm{Re}_\theta \tag{3.26}$$

where the Reynolds number Re_θ is defined as:

$$\mathrm{Re}_\theta = \rho U\theta/\mu \tag{3.27}$$

As the criteria of separation flow, the following values are used:

$$K < -0.0898, \qquad H = 3.5444, \qquad f_2(K) = 0 \tag{3.28}$$

In order to extend the validity of this method for a wider range of Mach number, the values of K, H and $f_2(K)$ are corrected under consideration of the compressibility effect as follows [8]:

$$H_c = \left[1+\left(\frac{\gamma-1}{2}\right)rM_e^2\right]H \qquad (3.29a) \qquad\qquad f_{2c}(K) = \left[1+\left(\frac{\gamma-1}{2}\right)rM_e^2\right]f_2(K) \qquad (3.29b)$$

$$K_c = \left[1+\left(\frac{\gamma-1}{2}\right)rM_e^2\right]K \qquad (3.29c) \qquad\qquad r = \mathrm{Pr}^{1/3} \qquad (3.29d)$$

where γ is the ratio of the specific heat, r is the heat recovery factor, Pr is the Prandtl number and M_e is the Mach number at the edge of the boundary layer.

3.2.2. The Drela - Giles Method: Compressible Laminar and Turbulent Flow

In order to compute the boundary layer parameters of an airfoil in compressible laminar or turbulent flow, the Drela - Giles method is used. Drela and Giles formulated a coupled pair of differential equations of momentum thickness and shape factor, as follows [3, 4]:

$$\frac{d\theta}{dx} = \frac{C_f}{2} - \left(H + 2 - M_e^2\right)\frac{\theta}{U_e}\frac{dU_e}{dx} \qquad (3.30)$$

$$\frac{dH^*}{dx} = \frac{1}{\theta}\left(2C_d - \frac{1}{2}C_f\right) - \left(\frac{2H^{**}}{H^*} + 1 - H\right)\frac{H^*}{U_e}\frac{dU_e}{dx} \qquad (3.31)$$

The shape factors in equation (3.31) are defined as follows:

$$H^* = \frac{\theta^*}{\theta}, \qquad H^{**} = \frac{\delta^{**}}{\theta} \qquad (3.32)$$

with the Density Thickness: $$\delta^{**} = \int_0^\infty \left(1 - \frac{\rho}{\rho_e}\right)\frac{U}{U_e}dz \qquad (3.33)$$

and the Kinetic Energy Thickness: $$\theta^* = \int_0^\infty \left(1 - \frac{U^2}{U_e^2}\right)\frac{\rho U}{\rho_e U_e}dz \qquad (3.34)$$

The dissipation coefficient in equation (3.31) is defined as:

$$C_d = \frac{1}{\rho_e U_e^3}\int_0^\infty \tau \frac{dU}{dz}dz \qquad (3.35)$$

The derivation of the integral boundary layer equation (3.30) and (3.31) can be found in Appendix 2.

3.2.2.1. Closure Equations for Laminar Flow

In order to be able to solve the system of differential equations - Eqs. (3.30) and (3.31) -, one needs some closure equations to close the problem because the number of the equations is less than the number of the unknown variables. Some variables must be linked to each other or written as a function of the other variables.

For this purpose one introduces the kinematic shape factor H_k, as [3, 4]:

$$H_k = \frac{H - 0.29M_e}{1 + 0.113M_e} \qquad (3.36)$$

This kinematic shape factor H_k plays an important role as the closure variable, where the other variables are related to. The variables which must be written as functions of H_k are H^*, C_f, C_d and H^{**} and will be described as follows.

The relation between H^* and H_k reads [3, 4]:

$$if \quad H_k \geq 4.35: \quad H^* = 0.015\frac{(H_k - 4.35)^2}{H_k + 1} + 1.528 \tag{3.37a}$$

$$if \quad H_k < 4.35:$$

$$H^* = 0.0111\frac{(H_k - 4.35)^2}{H_k + 1} - 0.0278\frac{(H_k - 4.35)^3}{H_k + 1} + 1.528 - 0.0002\,(H_k^2 - 4.35H_k)^2 \tag{3.37b}$$

The skin friction coefficient C_f is computed as a function of H_k and the Reynolds number Re_q [3, 4]:

$$\begin{aligned} &if\ H_k < 5.5: \quad C_f = \left[0.0762\frac{(5.5 - H_k)^3}{(H_k + 1)} - 0.067\right]\frac{1}{\mathrm{Re}_q} && (a) \\ &if\ H_k \geq 5.5: \quad C_f = \left\{0.015\left[1 - \frac{1}{(H_k - 4.5)}\right]^2 - 0.07\right\}\frac{1}{\mathrm{Re}_q} && (b) \end{aligned} \tag{3.38}$$

The dissipation coefficient C_d is computed as a function of H_k, H^* and Re_q:

$$\begin{aligned} &if\ H_k < 4.0: \quad C_d = \left[0.00205(4 - H_k)^{5.5} + 0.207\right]\frac{1}{\mathrm{Re}_q}\frac{H^*}{2} && (a) \\ &if\ H_k \geq 4.0: \quad C_d = \left\{\frac{-0.0016(H_k - 4)^2}{\left[1 + 0.02(H_k - 4)^2\right]} + 0.207\right\}\frac{1}{\mathrm{Re}_q}\frac{H^*}{2} && (b) \end{aligned} \tag{3.39}$$

The value of H^{**} is related to H_k as follows [3, 4]:

$$H^{**} = M_e^{\,2}\left[\frac{0.064}{(H_k - 0.08)} + 0.251\right] \tag{3.40}$$

The steps for the computation of the boundary layer parameters of an airfoil in compressible laminar flow using the Drela-Giles method are as follows:

a. The boundary layer parameters resulted from the solution of the von Karman – Thwaites method is used as initial values applied to the leading edge region of the airfoil.
b. After 3% or 5% of the chord length from the leading edge, the system of differential equations (3.30 and 3.31) associated with the closure equations for laminar flow is solved using a 4th order Runge Kutta method (see Appendix 1.) to obtain the value of the boundary layer parameters at the next point in the downstream direction.
c. This procedure is carried out up to the transition point from laminar to turbulent flow. Beyond this transition point the computation is switched to the procedure for turbulent flow. The transition point is computed using the e^N method (see Chapter 3.2.4).

3.2.2.2. Closure Equations for Turbulent Flow

For turbulent flow, the closure equation for H^{**} remains the same as for laminar flow. The other closure equations for H^*, C_f, C_d are changed and will be described in the following.

H^* will be computed using:

$$H^* = \frac{H_k^* + 0.028M_e^2}{1 + 0.014M_e^2} \tag{3.41}$$

where:

$$if\ H_k < H_0: \quad H_k^* = \left(0.5 - \frac{4}{\mathrm{Re}_q}\right)H_r^2\,\frac{1.5}{H_k + 0.5} + 1.5 + \frac{4}{\mathrm{Re}_q} \tag{3.42a}$$

$$if\ H_k \ge H_0: \quad H_k^* = \left(H_k - H_0\right)^2 \left[\frac{0.007 \log \mathrm{Re}_\theta}{\left(H_k - H_0 + \dfrac{4}{\log \mathrm{Re}_\theta}\right)^2} + \frac{0.015}{H_k} \right] + 1.5 + \frac{4}{\mathrm{Re}_\theta} \tag{3.42b}$$

with:

$$H_r = \frac{H_0 - H_k}{H_0 - 1} \tag{3.43}$$

$$\begin{aligned} H_0 &= 3 + \frac{400}{\mathrm{Re}_\theta} \qquad if\ \ \mathrm{Re}_\theta > 400 \qquad (a) \\ H_0 &= 4 \qquad\qquad\ \ if\ \ \mathrm{Re}_\theta \le 400 \qquad (b) \end{aligned} \tag{3.44}$$

The skin friction coefficient, C_f, is computed with the following relation [3,4]:

$$if\ \ \frac{\mathrm{Re}_\theta}{\sqrt{1+0.2M_e^2}} \ge e^3:$$

$$C_f = \frac{1}{\sqrt{1+0.2M_e^2}} \left\{ 0.3e^{-1.33H_k} \left[\log_{10}\left(\frac{\mathrm{Re}_\theta}{\sqrt{1+0.2M_e^2}} \right) \right]^{-1.74-0.31H_k} + 0.00011\left[\tanh(H_{\arg}) - 1\right] \right\} \tag{3.45a}$$

$$if\ \ \frac{\mathrm{Re}_\theta}{\sqrt{1+0.2M_e^2}} < e^3:$$

$$C_f = \frac{1}{\sqrt{1+0.2M_e^2}} \left\{ 0.3e^{-1.33H_k} 3^{-1.74-0.31H_k} + 0.00011\left[\tanh(H_{\arg}) - 1\right] \right\} \tag{3.45b}$$

where:

$$\begin{aligned} H_{\arg} &= 4 - \frac{H_k}{0.875} \qquad if \quad H_k \ge -5.25 \qquad (a) \\ H_{\arg} &= 104 - \frac{H_k}{0.875} \qquad if \quad H_k < -5.25 \qquad (b) \end{aligned} \tag{3.46}$$

The dissipation coefficient C_d will be computed from:

$$C_d = \frac{C_f}{2} U_S + C_\tau (1 - U_S) \tag{3.47}$$

where the slip velocity U_S is a function of the shape factor:

$$U_S = \frac{H^*}{6} \left(\frac{4}{H_k} - 1 \right) \tag{3.48}$$

The shear stress coefficient C_τ in equation (3.47) is computed using the Lag-Entrainment method of Green et. al., which will be discussed later.

The steps for the computation of the boundary layer parameters in turbulent flow using the Drela-Giles method are described as follows:

a. The solution of the flat plate boundary layer in the incompressible turbulent flow computed from the Power 1/7 Law is used as the initial values applied to the leading edge region of an airfoil (for fully turbulent flow case) or applied to the turbulent region after the transition point (for partially turbulent flow case).

b. After 3% - 5% of the chord length from the leading edge (for fully turbulent flow case) or from transition point (for partially turbulent flow case), the system of the differential equations (3.30 and 3.31) associated with the closure equations for turbulent flow is solved using a 4th Order Runge Kutta method (see Appendix 1) to obtain the boundary layer parameters for the next point.
c. The integration of the differential equations is carried out up to the separation point, where the value of the derivative of the shape factor (dH_k/dH^*) becomes singular and C_f is less or equal to zero. In this case the Inverse Boundary Layer Method (IBLM, to be described later) is used starting from the separation point.

3.2.3. The Lag Entrainment Method from Green et. al.: Compressible Turbulent Flow

Another method to calculate the boundary layer parameters in compressible turbulent flow is the Lag Entrainment method proposed by Green et. al. [11]. They introduced an entrainment coefficient in order to take into account the ‘history’ of the flow condition. The mixture process between a turbulent region of flow and its surrounding non-turbulent irrotational flow is referred to as the entrainment of the non turbulent by the turbulent flow. This entrainment affects the growth of the boundary layer and considered to be a controlling factor in the development of the turbulent boundary layer. Green et. al. have proposed an additional equation involving the entrainment coefficient instead of momentum thickness and shape factor equations.

The system of differential equation is now as follows [11]:

$$\frac{d\theta}{dx}=\frac{C_f}{2}-\left(H+2-M_e^2\right)\frac{\theta}{U_e}\frac{dU_e}{dx} \tag{3.49}$$

$$\frac{d\overline{H}}{dx}=\frac{1}{\theta}\left(C_E-\frac{1}{2}H_1C_f\right)\frac{d\overline{H}}{dH_1}+H_1(H+1)\frac{d\overline{H}}{dH_1}\frac{1}{U_e}\frac{dU_e}{dx} \tag{3.50}$$

$$\frac{dC_E}{dx}=\frac{F}{\theta}\left\{\frac{2.8}{H+H_1}\left[\left(C_\tau\right)_{EQ0}^{1/2}-\lambda C_\tau^{1/2}\right]+\left(\frac{\theta}{U_e}\frac{dU_e}{dx}\right)_{EQ}\right\}-F\left(1+0.075M^2\frac{1+\frac{\gamma-1}{2}rM_e^2}{1+0.1M_e^2}\right)\frac{1}{U_e}\frac{dU_e}{dx} \tag{3.51}$$

The derivation of the shape factor equation (3.50) can be found in Appendix 2.

3.2.3.1. Closure Equations for Turbulent Flow

In order to solve the above equations, one needs some closure equations since the number of the equations is less than the number of the unknown variables. Some variables must be written as functions of other variables. These variables are the shape factors (H, $\overline{H}$, H_1), the derivative $d\overline{H}/dH_1$, C_f, $(\theta/Ue\ dUe/dx)_{EQ}$, C_τ and F.

Between the shape factors H, $\overline{H}$ and H_1 exists the following relations [11]:

$$H=\left(\overline{H}+1\right)\left(1+\frac{\gamma-1}{2}rM_e{}^2\right)-1 \tag{3.52}$$

$$H_1=3.15+\frac{1.72}{\overline{H}-1}-0.01(\overline{H}-1)^2 \tag{3.53}$$

$$\frac{d\overline{H}}{dH_1}=\frac{-\left(\overline{H}-1\right)^2}{1.72+0.02\left(\overline{H}-1\right)^3} \tag{3.54}$$

$\overline{H}$ is the incompressible shape factor defined as [11]:

$$\overline{H}=\frac{1}{\theta}\int_0^\infty\frac{\rho}{\rho_e}\left(1-\frac{U}{U_e}\right)dz \tag{3.55}$$

H_1 is the mass flow shape factor defined as [11]: $$H_1 = \frac{\delta - \delta^*}{\theta} \tag{3.56}$$

The equations (3.53 and 3.54) will be singular if the value of $\overline{H}$ is equal to 1. Therefore the application of this procedure is limited up to this value of $\overline{H}$.

The skin friction coefficient C_f on the profile is written as a function of shape factors, Mach number and Reynolds number as [11]:

$$C_f = C_{f_0}\left[0.9\left(\frac{\overline{H}}{H_0} - 0.4\right)^{-1} - 0.5\right] \tag{3.57}$$

H_0 is the shape factor at constant pressure and C_{f0} is the skin friction coefficient if the pressure gradient is equal to zero.

The relation of ($\overline{H}$ /H_0) and C_{f0} in the equation (3.57) is defined as [11]:

$$\frac{\overline{H}}{H_0} = \overline{H}\left\{1 - 6.55\left[\frac{C_{f_0}}{2}\left(1 + 0.04{M_e}^2\right)\right]^{1/2}\right\} \tag{3.58}$$

$$C_{f_0} = \frac{1}{F_C}\left[\frac{0.01013}{\log_{10}(F_R \operatorname{Re}_\theta) - 1.02} - 0.00075\right] \tag{3.59}$$

with the scaling factors F_C , F_R and the Reynolds number Re_θ given by [11]:

$$F_C = \left(1 + \frac{\gamma - 1}{2} r{M_e}^2\right)^{1/2} \quad (3.60), \qquad F_R = 1 + 0.056{M_e}^2 \quad (3.61),$$

$$\operatorname{Re}_\theta = \frac{\left(\frac{\rho_e}{\rho_\infty}\right)\left(\frac{U_e}{U_\infty}\right)\theta}{\left(\frac{\mu_e}{\mu_\infty}\right)} \operatorname{Re}_\infty \tag{3.62}$$

The variables at the edge of the boundary layer in the above equations (denote by the subscript e) will be given by the following relations [8]:

$$\frac{\rho_e}{\rho_\infty} = 1 - M_\infty^2 \phi_x \quad (3.63), \qquad \frac{U_e}{U_\infty} = 1 + \phi_x \quad (3.64), \qquad \frac{M_e}{M_\infty} = 1 + \left(1 + \frac{\gamma - 1}{2} M_\infty^2\right)\phi_x \quad (3.65),$$

$$\frac{\mu_e}{\mu_\infty} = \left(\frac{T_e}{T_\infty}\right)^{3/2}\left[\frac{1 + \frac{S_0}{T_\infty}}{\left(\frac{T_e}{T_\infty}\right) + \frac{S_0}{T_\infty}}\right] \quad (3.66), \qquad \left(\frac{T_e}{T_\infty}\right) = 1 - (\gamma - 1)M_\infty^2 \phi_x \quad (3.67)$$

ϕ_x is the derivative of the disturbance velocity potential in the downstream direction and S_0 is the Sutherland number, where its value is equal to 110 Kelvin for air and T represents the temperature of the fluid.

The variable $(\theta/Ue\ dUe/dx)_{\mathrm{EQ}}$ in the equation (3.51), i.e. the displacement thickness multiplied by the gradient of the velocity in equilibrium condition with constant H, is defined as a function of shape factors, skin friction and entrainment coefficient, as follows [11]:

$$\left(\frac{\theta}{U_e}\frac{dU_e}{dx}\right)_{EQ} = \frac{1}{H_1(H + 1)}\left[\frac{H_1 C_f}{2} - (C_E)_{EQ}\right] \tag{3.68}$$

where the subscript EQ represents the equilibrium condition.

The entrainment coefficient in equilibrium condition in the equation (3.68), i.e. $(C_E)_{\mathrm{EQ}}$, is defined as [11]:

$$\left(C_E\right)_{EQ} = \left(\frac{C}{1.6} + 0.0001\right)^{1/2} - 0.01 \qquad (3.69)$$

with the function *C* is:

$$C = \left(C_\tau\right)_{EQ0}\left(1 + 0.1{M_e}^2\right)^{-1}\lambda^{-2} - 0.32C_{f_0} \qquad (3.70)$$

where λ is the scaling factor of the dissipation length, its value is 1 on the airfoil and 1/2 in the wake.

The shear stress coefficient in the fluid, C_τ, is defined as a function of Mach number, entrainment coefficient and skin friction coefficient, as follows [11]:

$$C_\tau = \left(1 + 0.1{M_e}^2\right)\left(0.024C_E + 1.6C_E^2 + 0.32C_{f_0}\right) \qquad (3.71)$$

$$\left(C_\tau\right)_{EQ0} = \left(1 + 0.1{M_e}^2\right)\left[0.024\left(C_E\right)_{EQ0} + 1.6\left(C_E\right)_{EQ0}^2 + 0.32C_{f_0}\right] \qquad (3.72)$$

The subscript *EQ0* indicates the equilibrium condition without influence of the second structure of the turbulence.

The entrainment coefficient in *EQ0* is defined as [11]:

$$\left(C_E\right)_{EQ0} = H_1\left[\frac{C_f}{2} - \left(H + 1\right)\left(\frac{\theta}{U_e}\frac{dU_e}{dx}\right)_{EQ0}\right] \qquad (3.73)$$

where :

$$\left(\frac{\theta}{U_e}\frac{dU_e}{dx}\right)_{EQ0} = \frac{1.25}{H}\left[\frac{C_f}{2} - \left(\frac{\overline{H} - 1}{6.432\overline{H}}\right)^2\left(1 + 0.04{M_e}^2\right)^{-1}\right] \qquad (3.74)$$

The variable *F* in the equation (3.51) is defined as [11]:

$$F = \frac{0.02C_E + 1.334C_E^2 + 0.267C_{f_0}}{0.01 + 1.334C_E} \qquad (3.75)$$

With the above closure equations, one can solve the set of differential equations (3.49 - 3.51) for given initial values.

The steps for the computation of the boundary layer parameters in turbulent flow using the Lag Entrainment method are described as follows:

d. The solution of the flat plate boundary layer in the incompressible turbulent flow computed from the power 1/7 law is used as the initial values applied to the leading edge region of an airfoil.

e. After 3% - 5% of the chord length from the leading edge, the system of the differential equations (3.49 - 3.51) associated with the closure equations for turbulent flow is solved using a 4th Order Runge Kutta method (see Appendix 1) to obtain the boundary layer parameters for the next point.

f. The integration of the differential equations is carried out up to the separation point, where the value of the derivative of the shape factor ($d\overline{H}/dH_1$) becomes singular and C_f is less or equals to zero. In this case the Inverse Boundary Layer Method (IBLM, to be described later) is used starting from the separation point.

3.2.4. Semi Inverse Method

The semi inverse boundary layer calculation method was proposed by Melnik and Brook [15] and Howlett [20] among others. It was proposed to avoid the singularity of the value of the derivative of the shape factor ($d\overline{H}/dH_1$) in the Lag Entrainment method as the flow condition tends to separate. The extension of the Green's Lag Entrainment method to handle separated flow is carried out by choosing an appropriate velocity model applied to the separated flow region. The derivative of the shape factor ($d\overline{H}/dH_1$) will then be formulated based on this velocity model.

Mathematically, this method is derived from Green's Lag Entrainment method by modifying the differential equations (3.49 - 3.51), so that the momentum thickness θ is not directly computed from the momentum equation, but from the velocity at the edge of the boundary layer U_v. Then the displacement thickness δ^* will be computed iteratively based on the edge velocities calculated from the boundary layer equation U_v and from the inviscid equation U_e.

For modification purposes a new parameter is needed, i.e. the mass flow rate in the boundary layer defined as [20]:

$$\overline{m} = \rho_e U_e \delta^* \tag{3.76}$$

With this new variable the three differential equations from Green's Lag Entrainment (3.49-3.51) can be written as [20]:

$$\frac{dU_v}{dx} = U_v \frac{\dfrac{-1}{\overline{m}}\dfrac{d\overline{m}}{dx} + \dfrac{1}{H\theta} R_1 \dfrac{d\overline{H}}{dH_1}\left(C_E - \dfrac{C_f H_1}{2}\right) + \dfrac{C_f}{2\theta}}{(H+1)\left\{1 - \dfrac{R_1}{H}\left[\dfrac{(\gamma-1) r M_e M_\infty R_2}{R_1^2} + H_1 \dfrac{d\overline{H}}{dH_1}\right]\right\} - M_e^2 + \dfrac{(1+\phi_x) M_\infty^2}{1 - M_\infty^2 \phi_x}} \tag{3.77}$$

$$\frac{d\overline{H}}{dx} = \frac{\dfrac{d\overline{H}}{dH_1}\left\{\dfrac{1}{\theta}\left(C_E - \dfrac{C_f H_1}{2}\right)\left[1 - \dfrac{R_1(\gamma-1) r M_e M_\infty R_2}{H R_1^2}\right] - H_1\left(\dfrac{1}{\overline{m}}\dfrac{d\overline{m}}{dx} - \dfrac{C_f}{2\theta}\right)\right\}}{\left\{1 - \dfrac{R_1}{H}\left[\dfrac{(\gamma-1) r M_e M_\infty R_2}{R_1^2} + H_1 \dfrac{d\overline{H}}{dH_1}\right] - \dfrac{M_e^2}{(H+1)} + \dfrac{(1+\phi_x) M_\infty^2}{(1 - M_\infty^2 \phi_x)(H+1)}\right\}} \tag{3.78}$$

$$\frac{dC_E}{dx} = \frac{F}{\theta}\left\{\frac{R_3}{H + H_1}\left[(C_\tau)_{EQ0}^{1/2} - \lambda C_\tau^{1/2}\right] + \left(\frac{\theta}{U_e}\frac{dU_e}{dx}\right)_{EQ}\right\} - F\left(1 + 0.075 M_e^2 \frac{R_1}{1 + 0.1 M_e^2}\right)\phi_{xx} \tag{3.79}$$

New terms appeared in the equations (3.77 – 3.79) are:

$$R_1 = 1 + \frac{(\gamma-1)}{2} r M_e^2 \quad (3.80) \qquad\qquad R_2 = 1 + \frac{(\gamma-1)}{2} M_\infty^2 \quad (3.81)$$

$$\begin{aligned} R_3 &= 2.8 \qquad if \quad \overline{H} \le 2.4 && (a) \\ R_3 &= \frac{0.15}{\left(1 - \dfrac{C_2}{2}\right) 0.08 \left(1 - \eta^*\right)} \qquad if \quad \overline{H} > 2.4 && (b) \end{aligned} \tag{3.82}$$

The variables C_2 and η^* are related to the chosen velocity model in separated flow region, which will be described later in the description of the closure equations. The details of the modification procedure can be found in Appendix 3.

The semi inverse calculation method can also be written associated with the shape factor equation from Drela & Giles method as follows:

$$\frac{dU_v}{dx} = U_v \frac{\dfrac{-1}{\overline{m}}\dfrac{d\overline{m}}{dx} + \dfrac{1}{H\theta} R_1 \dfrac{d\overline{H}}{dH_1}\left(C_E - \dfrac{C_f H_1}{2}\right) + \dfrac{C_f}{2\theta}}{(H+1)\left\{1 - \dfrac{R_1}{H}\left[\dfrac{(\gamma-1) r M_e M_\infty R_2}{R_1^2} + H_1 \dfrac{d\overline{H}}{dH_1}\right]\right\} - M_e^2 + \dfrac{(1+\phi_x) M_\infty^2}{1 - M_\infty^2 \phi_x}} \tag{3.77}$$

$$\frac{dC_E}{dx} = \frac{F}{\theta}\left\{\frac{R_3}{H + H_1}\left[(C_\tau)_{EQ0}^{1/2} - \lambda C_\tau^{1/2}\right] + \left(\frac{\theta}{U_e}\frac{dU_e}{dx}\right)_{EQ}\right\} - F\left(1 + 0.075 M_e^2 \frac{R_1}{1 + 0.1 M_e^2}\right)\phi_{xx} \tag{3.79}$$

$$\frac{dH^*}{dx}=\frac{1}{\theta}\left(2C_d-\frac{1}{2}C_f\right)-\left(\frac{2H^{**}}{H^*}+1-H\right)\frac{H^*}{U_v}\frac{dU_v}{dx} \tag{3.31}$$

3.2.4.1. Closure Equations for Semi Inverse Method

Some of the closure equations of the lag entrainment method must be modified in order to be able to calculate the separated boundary layer. The modification of the closure equations involves the variables $d\overline{H}/dH_1$, $(C_E)_{EQ0}$, and C_f. Other closure equations remain the same.

The velocity profile in the separated region is assumed to be [20]:

$$\frac{U_v}{U_e}=1-C_2F_p(\eta) \tag{3.83}$$

where: $$C_2=\frac{\dot{\alpha}}{a_1(1+a_2\eta^*)},\qquad \dot{\alpha}=\frac{\delta^*}{\delta},\qquad \eta=\frac{z}{\delta},\qquad a_1=0.5,\qquad a_2=1 \tag{3.84}$$

$$\begin{aligned} &F_p(\eta)=1 && 0\le\eta\le\eta^* && (a)\\ &F_p(\eta)=F_c(\overline{\eta}) && \eta^*\le\eta\le 1 && (b)\end{aligned} \tag{3.85}$$

η^* is the height of the reversed flow region of the boundary layer in the separation region (see Fig. 3.2.). The variable F_c in equation (3.85) is known as Coles wake function defined as follows:

$$F_c(\overline{\eta})=0.5(1+\cos\pi\overline{\eta}),\qquad \overline{\eta}=\frac{\eta-\eta^*}{1-\eta^*} \tag{3.86}$$

The velocity of the reversed flow is: $$\frac{U_m}{U_e}=1-C_2 \tag{3.87}$$

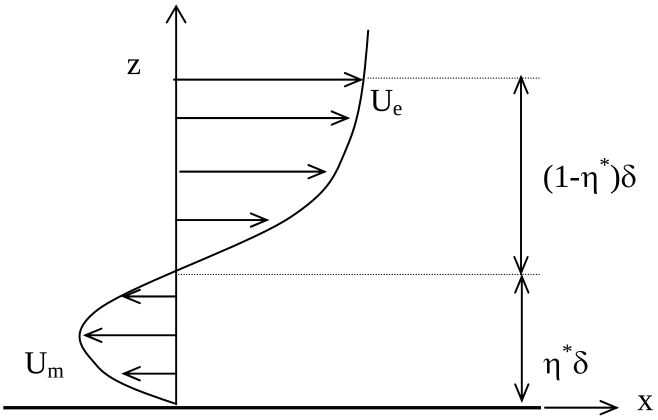

Figure 3.2. Sketch of the Reversed Flow Region in Boundary Layer

The criteria of the reversed flow region are described as follows [20]:

$$\begin{aligned} &\eta^*(\dot{\alpha})=b\dot{\alpha}+(1-b) && \text{if} && \alpha_m\le\dot{\alpha}\le 1\\ &\eta^*(\dot{\alpha})=a(\dot{\alpha}-\alpha_s)^2 && \text{if} && \alpha_s<\dot{\alpha}<\alpha_m\\ &\eta^*(\dot{\alpha})=0 && \text{if} && \dot{\alpha}\le\alpha_s\end{aligned} \tag{3.88}$$

with: $$b=\frac{d\eta^*}{d\dot{\alpha}}=2.1\quad or\quad 2.3$$

$$a = \frac{b}{4\left(1 - a_1 - \dfrac{1}{b}\right)}, \qquad \alpha_s = a_1, \qquad \alpha_m = 2\left(1 - \frac{a_1}{2}\right) - \frac{2}{b} \tag{3.89}$$

The value of b depends on how the extrapolation of the function $\overline{H}$ vs. H_1 from the original function (equation 3.53) has been carried out [15, 20].

The shape factor $\overline{H}$ is now described as a function of $\dot{\alpha}$:

$$\overline{H}(\dot{\alpha}) = \left\{1 - \left[1 + B\left(\eta^*\right)\right]\dot{\alpha}\right\}^{-1} \tag{3.90}$$

with :

$$B\left(\eta^*\right) = \frac{G_2(\eta^*)}{G_1^2(\eta^*)} - 1 \tag{3.91}$$

where:

$$G_1\left(\eta^*\right) = a_1\left(1 + a_2\eta^*\right) \tag{3.92}$$

$$G_2\left(\eta^*\right) = b_1\left(1 + b_2\eta^*\right) \tag{3.93}$$

with: $b_1 = 3/8 \quad and \quad b_2 = 5/3$

The shape factor H_1 is now also a function of $\dot{\alpha}$:

$$H_1\left(\dot{\alpha}\right) = \overline{H}\left(\dot{\alpha}\right)\left(\frac{1}{\overline{\alpha}} - 1\right) \tag{3.94}$$

The derivative ($d\overline{H} / dH_1$) will be computed as:

$$\frac{d\overline{H}}{dH_1} = \frac{1}{\left(\dfrac{dH_1}{d\overline{H}}\right)} \tag{3.95}$$

with:

$$\frac{dH_1}{d\overline{H}} = \frac{\partial H_1}{\partial \overline{H}} + \frac{\partial H_1}{\partial \dot{\alpha}} \frac{\partial \dot{\alpha}}{\partial \overline{H}} \tag{3.96}$$

Further changes in the closure equations of the Lag Entrainment method are [20]:

The entrainment coefficient in equilibrium $EQ0$ (equation 3.73) then becomes:

$$\left(C_E\right)_{EQ0} = 2K_1^2 C_2 F_p''(\eta)\Big|_{\eta=1} = 0.0064\pi^2 C_2 \tag{3.97}$$

where K_1 is the mixing length constant and its value equals to 0.08, and:

$$F_p''(\eta) = \frac{d^2 F_p(\eta)}{d\eta^2} \tag{3.98}$$

The skin friction coefficient (equation 3.57) becomes:

$$C_f = \frac{0.3e^{-1.33H}}{\left(\log_{10} \mathrm{Re}_\theta\right)^{1.74+0.31H}} + 0.00011\left[\tanh\left(4 - \frac{H}{0.875}\right) - 1\right] \quad if \quad \overline{H} < 2.4 \qquad (a)$$

$$C_f = 0 \quad if \quad \overline{H} \geq 2.4 \qquad (b) \tag{3.99}$$

The scaling factor of the dissipation length λ becomes:

On the profile:

$$\lambda = \frac{1}{1 - \eta^*} \tag{3.100a}$$

In the wake:

$$\lambda = \frac{1}{2}\frac{1}{1 - \eta^*} \tag{3.100b}$$

Finally, the displacement thickness is computed using the following iterative method [14, 20]:

$$\delta^*_{new} = \delta^*_{old} + \omega\delta^*_{old}\left(\frac{U_v}{U_e} - 1\right) \tag{3.101}$$

where :

U_v = viscous velocity (solution of the Inverse Boundary Layer Method)
U_e = inviscid velocity (solution of the TSD or the Euler equations)
ω = relaxation factor (in the present work the value of ω is chosen from 0.001 to 0.2)

The procedure to solve the semi inverse method are as follows:

a. The procedure starts if the value of $\overline{H}$ is close to 2.4. Solution of the flat plate boundary layer in incompressible turbulent flow is used as the initial value for the next point.
b. Calculate the mass flow rate with the initial value of δ^*
c. Calculate $\dot{\alpha}$ by means of the relation $\overline{H}$ - $\dot{\alpha}$. For this purpose a Newton iteration is used (see Appendix 1).
d. Afterwards H_1 and ($d\overline{H} / dH_1$) are computed.
e. U_V, $\overline{H}$ and C_E are calculated using a 4th Order Runge Kutta method.
f. The new displacement thickness (δ^*_{new}) is computed. If the value of δ^*_{new} is convergent the procedure can be proceeded for the next point otherwise the procedure must be repeated. In the present work, the convergence is reached if the relative error $[(\delta^*_{\text{new}} - \delta^*_{\text{old}})/\delta^*_{\text{old}}] \leq$ 1.0E-04 .

3.3. Differential Boundary Layer Equations: The Procedure of Hamilton et. al.

A differential method solves the differential boundary layer equations directly without modifying the equations, as carried out in the integral method. In contrast to the integral method, which produces directly the momentum thickness and shape factor, the numerical solution of the differential equation supplies the distribution of velocity within the boundary layer, which must be integrated, in order to obtain the momentum and displacement thickness. The numerical procedure used here is the finite difference method as implemented by Hamilton et. al. [26]. The boundary layer parameters in both laminar and turbulent flow can be calculated using this method. In order to solve the boundary layer equations for laminar flow, an auxiliary equation is not necessary, but a turbulence model must be added for solving the turbulent boundary layer, in order to calculate the value of the turbulent viscosity.

3.3.1. Equation Form

As the starting point is the boundary layer equations, which consist of conservative equations of mass, momentum and energy, which can be written for compressible turbulent flow in two-dimensional Cartesian coordinates, as follows [26]:

$$\frac{\partial(\rho u)}{\partial x} + \frac{\partial(\rho W)}{\partial z} = 0 \tag{3.102}$$

$$\rho u \frac{\partial u}{\partial x} + \rho W \frac{\partial u}{\partial z} = -\frac{\partial p}{\partial x} + \frac{\partial}{\partial z}\left[\left(\mu + \mu_E\right)\frac{\partial u}{\partial z}\right] \tag{3.103}$$

$$\frac{\partial p}{\partial z} = 0 \tag{3.104}$$

$$\rho u \frac{\partial h_0}{\partial x} + \rho W \frac{\partial h_0}{\partial z} = \frac{\partial}{\partial z}\left\{\frac{\mu}{\Pr}\frac{\partial h_0}{\partial z}\left(1 + \frac{\mu_E}{\mu}\frac{\Pr}{\Pr_t}\right) + \mu u \frac{\partial u}{\partial z}\left[\left(\frac{\Pr - 1}{\Pr}\right) + \frac{\mu_E}{\mu}\left(\frac{\Pr_t - 1}{\Pr_t}\right)\right]\right\} \tag{3.105}$$

The variables u and W are the velocity component in x and z direction. The symbols p and ρ stand for pressure and density. Pr and $\Pr_t$ are the laminar and turbulent Prandtl number respectively, where their values are 0.72 and 0.90. μ and μ_E are the laminar and turbulent eddy viscosity. h_0 is the total enthalpy.

In order to simulate the turbulent condition, the velocity W in the above equations is defined as:

$$W = \overline{w} + \frac{\left(\rho' w'\right)}{\rho'} \tag{3.106}$$

The symbols $\bar{\ }$ and $'$ in equation (3.106) denote the mean value and time-dependent fluctuating value.

The boundary conditions for the solution of equations (3.102) to (3.105) are as follows:

$$\begin{aligned} &if \quad z = 0 \ : \ u = 0, \quad W = 0, \quad h_0 = h_{0_w}(x) \qquad (a) \\ &if \quad z \to \infty \ : \ u \to U_e, \quad h_0 \to h_{0_e} \qquad (b) \end{aligned} \tag{3.107}$$

The subscript w and e denote the value at the wall or at the edge of the boundary layer. The number of unknown variables involved in the equations (3.102) to (3.105) is seven, i.e. u, W, p, h_0, ρ, μ and μ_E, larger than the number of the equations, which is only four. Therefore these variables must be linked to each other or some closure equations must be added, in order to close the problem. The laminar viscosity μ is computed with the Sutherland law, as follows [26]:

$$\frac{\mu}{\mu_r} = \left(\frac{T}{T_r}\right)^{3/2} \left[\frac{1 + S_0 / T_r}{T / T_r + S_0 / T_r}\right] \tag{3.108}$$

T_r, μ_r and S_0 are the reference temperature, the reference viscosity and the Sutherland number (equals to 110 Kelvin), respectively. The turbulent eddy viscosity μ_E is computed using two layer turbulence model proposed by Van Driest - Clauser, which will be explained later. The total Enthalpy h_0 is assumed to be constant. The variables u, W, p and ρ are coupled to each other by using the Levy Lee transformation of the coordinates, which will be described as follows.

3.3.2. Transformation of the Coordinate

The Cartesian coordinates (x, z) is transformed into the computational coordinates (ξ, ζ) by the Levy Lee transformation as follows [26]:

$$\xi(x) = \int_0^x \rho_e \mu_e U_e dx \tag{3.109}$$

$$\zeta(x,z) = \frac{\rho_e U_e}{\sqrt{2\xi}} \int_0^z \frac{\rho}{\rho_e} dz \tag{3.110}$$

The derivatives in the direction x and z become:

$$\frac{\partial}{\partial x} = \rho_e \mu_e U_e \frac{\partial}{\partial \xi} + \frac{\partial \zeta}{\partial x}\frac{\partial}{\partial \zeta} \tag{3.111}$$

$$\frac{\partial}{\partial z} = \frac{\rho U_e}{\sqrt{2\xi}} \frac{\partial}{\partial \zeta} \tag{3.112}$$

With these new coordinates one can defined a stream function $\psi(\xi,\zeta)$:

$$\psi(\xi,\zeta) = \sqrt{2\xi}\, f(\xi,\zeta) \tag{3.113}$$

which has properties: $\frac{\partial \psi}{\partial z} = \rho u \quad (a) \qquad \frac{\partial \psi}{\partial x} = -\rho W \quad (b)$

$$\rho W = -\rho_e \mu_e U_e \left(\sqrt{2\xi}\frac{\partial f}{\partial \xi} + \frac{f}{\sqrt{2\xi}}\right) - \frac{\partial \zeta}{\partial x}\sqrt{2\xi}\, f' \qquad \text{(c)} \tag{3.114}$$

The new variable *f* in equation (3.113) has the property: $f' = \frac{\partial f}{\partial \zeta} = \frac{u}{U_e}$ (3.115)

With new variable *f*, the momentum in the flow direction *x* (3.103) becomes:

$$l^* f''' + \left(\frac{\partial l^*}{\partial \zeta} + f \right) f'' + \beta \left[\frac{\rho_e}{\rho} - \left(f' \right)^2 \right] = 2\xi \left(f' \frac{\partial f'}{\partial \xi} - f'' \frac{\partial f}{\partial \xi} \right) \tag{3.116}$$

where:

$$l^* = \frac{\rho \mu}{\rho_e \mu_e} \left(1 + \frac{\mu_E}{\mu} \right) \quad (a), \qquad \beta = \frac{2\xi}{U_e} \frac{dU_e}{d\xi} \quad (b),$$

$$f'' = \frac{\partial^2 f}{\partial \zeta^2} \quad (c), \qquad f''' = \frac{\partial^3 f}{\partial \zeta^3} \quad (d) \tag{3.117}$$

The pressure term in equation (3.103) is eliminated by the inviscid theory (with isentropic assumption) to:

$$\frac{dp_e}{d\xi} = -\rho_e U_e \frac{dU_e}{d\xi} \tag{3.118}$$

The same procedure can be performed for the energy equation (3.105) resulting the following equation:

$$\left(\frac{l^{**}}{\Pr} \right) g'' + \left[\frac{\partial}{\partial \zeta} \left(\frac{l^{**}}{\Pr} \right) + f \right] g' + \omega' = 2\xi \left(f' \frac{\partial g}{\partial \xi} - g' \frac{\partial f}{\partial \xi} \right) \tag{3.119}$$

where:

$$g = \frac{h0}{h0_e} \quad (a), \qquad l^{**} = \frac{\rho \mu}{\rho_e \mu_e} \left(1 + \frac{\mu_E}{\mu} \frac{\Pr}{\Pr_t} \right) \quad (b),$$

$$\omega = \frac{\rho \mu}{\rho_e \mu_e} \left[\frac{\mu_E}{\mu} \left(1 - \frac{1}{\Pr_t} \right) + \left(1 - \frac{1}{\Pr} \right) \right] \left(\frac{U_e^2}{h0_e} f f'' \right) \quad (c), \tag{3.120}$$

$$g' = \frac{\partial g}{\partial \zeta} \quad (d), \qquad g'' = \frac{\partial^2 g}{\partial \zeta^2} \quad (e), \qquad \omega' = \frac{\partial \omega}{\partial \zeta} \quad (f)$$

The equations (3.116) and (3.119) can be solved for *f* and *g* under the following boundary conditions:

$$\begin{aligned} &for \quad \zeta = 0 \quad : \quad f = 0, \quad f' = 0, \quad g = g_w(\xi) \qquad (a) \\ &for \quad \zeta \to \infty \quad : \quad f' \to 1, \quad g \to 1 \qquad (b) \end{aligned} \tag{3.121}$$

3.3.3. Solution Procedure

The equations (3.116) and (3.119) can be written in general as a 2nd order differential equation:

$$\frac{\partial^2 Q}{\partial \zeta^2} + \alpha_1 \frac{\partial Q}{\partial \zeta} + \alpha_2 Q + \alpha_3 + \alpha_4 \frac{\partial Q}{\partial \xi} = 0 \tag{3.122}$$

where *Q* is a general variable.

The following are the term and coefficients of the equation (3.122) to be applied for solving the momentum equation (3.116):

$$\begin{aligned} &Q = f' \quad (a), \qquad \alpha_1 = \frac{1}{l^*}\left(\frac{\partial l^*}{\partial \zeta} + f + 2\xi\frac{\partial f}{\partial \xi}\right) \quad (b), \\ &\alpha_2 = \frac{-\beta f'}{l^*} \quad (c), \qquad \alpha_3 = \frac{\beta}{l^*}\frac{\rho_e}{\rho} \quad (d), \qquad \alpha_4 = \frac{-2\xi f'}{l^*} \quad (e) \end{aligned} \tag{3.123}$$

For solving the energy equation (3.119), the term coefficients of the equation (3.122) are:

$$\begin{aligned} &Q = g \quad (a), \qquad \alpha_1 = \frac{1}{l^{**}/\Pr}\left(\frac{\partial l^{**}/\Pr}{\partial \zeta} + f + 2\xi\frac{\partial f}{\partial \xi}\right) \quad (b), \\ &\alpha_2 = 0 \quad (c), \qquad \alpha_3 = \frac{\omega'}{l^{**}/\Pr} \quad (d), \qquad \alpha_4 = \frac{-2\xi f'}{l^{**}/\Pr} \quad (e) \end{aligned} \tag{3.124}$$

The general equation (3.122) will be solved by finite difference method on the discretized boundary layer region. The typical grids for the solution of *Q* can be seen in figure. 3.4. The index *m* and *n* refers to the index of the points in directions ξ and ζ, respectively

The derivatives of *Q* in the direction ξ and ζ at point $P_{m+1,n}$ are approximated with:

$$\left(\frac{\partial Q}{\partial \zeta}\right)_{m+1,n} = \frac{1}{D_1}\left[Q_{n+1} - K^2 Q_{n-1} - (1+K^2)Q_n\right]_{m+1} \tag{3.125}$$

$$\left(\frac{\partial^2 Q}{\partial \zeta^2}\right)_{m+1,n} = \frac{2}{D_2}\left[Q_{n+1} + K Q_{n-1} - (1+K)Q_n\right]_{m+1} \tag{3.126}$$

$$\left(\frac{\partial Q}{\partial \xi}\right)_{m+1,n} = \frac{1}{\Delta\xi}\left[Q_{m+1} - Q_m\right]_n \tag{3.127}$$

where:

$$D_1 = \left(\zeta_{n+1} - \zeta_n\right) + K^2\left(\zeta_n - \zeta_{n-1}\right) \tag{3.128a}$$

$$D_2 = \left(\zeta_{n+1} - \zeta_n\right)^2 + K\left(\zeta_n - \zeta_{n-1}\right)^2 \tag{3.128b}$$

$$K = \frac{\left(\zeta_{n+1} - \zeta_n\right)}{\left(\zeta_n - \zeta_{n-1}\right)} \tag{3.128c}$$

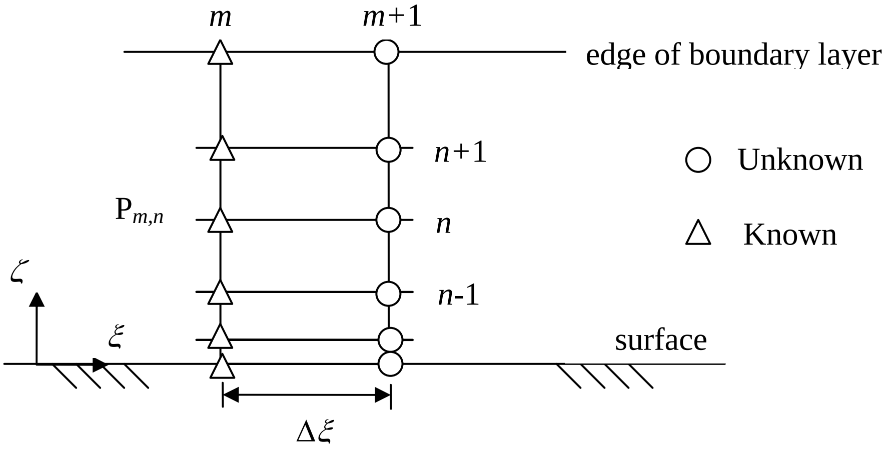

Figure 3.3. Typical Grid for the Solution of the Differential Boundary Layer Equations

Substituting equations (3.125) – (3.127) into equation (3.122), one obtains a simultaneous algebraic equation as follows:

$$A_n Q_{m+1,n+1} + B_n Q_{m+1,n} + C_n Q_{m+1,n-1} = R_n \tag{3.129}$$

where:

$$A_n = \frac{2}{D_2} + \frac{\alpha_1}{D_1} \tag{3.130a}$$

$$B_n = \frac{-2(1+K)}{D_2} - \frac{\alpha_1(1-K^2)}{D_1} + \alpha_2 + \frac{\alpha_4}{\Delta\xi} \tag{3.130b}$$

$$C_n = \frac{2K}{D_2} - \frac{K^2\alpha_1}{D_1} \tag{3.130c}$$

$$R_n = -\alpha_3 + \frac{\alpha_4 Q_{m,n}}{\Delta\xi} \tag{3.130d}$$

The system of the algebraic equation (3.129) forms a tri diagonal matrix in the direction ζ (index *n*) at a certain position in the direction ξ (index *m+1*), which can be solved efficiently using the method from Richtmyer and Morton, as follows [26]:

The solution of *Q* can be calculated by recursive procedure as follows:

$$for \quad 2 \le n \le N-1 \;\; : \;\; Q_{m+1,n} = E_n Q_{m+1,n+1} + e_n \tag{3.131}$$

with:

$$\begin{aligned} &E_2 = \frac{-A_2}{B_2} \quad (a) \qquad e_2 = \frac{R_2 - C_2 Q_{m+1,1}}{B_2} \quad (b) \\ for \quad 3 \le n \le N-1 \;\; : \;\; &E_n = \frac{-A_n}{B_n + C_n E_{n-1}} \quad (c) \qquad e_n = \frac{R_n - C_n e_{n-1}}{B_n + C_n E_{n-1}} \quad (d) \end{aligned} \tag{3.132}$$

The boundary conditions are applied at the index *n* = 1 (body surface) and *n* = N (edge of the boundary layer), which implies that the values of $Q_{m+1,1}$ and $Q_{m+1,N}$ are already available. With recursive procedure from *n* = 2 to *n* = N-1 one can obtain the solution of *Q* by means of the equation (3.131). In this procedure the solution of *Q* is computed iteratively until the convergence criterion 1.0E-03 is reached, in order to prevent redundancy of the solution, because the solution of *Q* at the station *m* in the direction ξ is assumed. As the initial value for this station, the solution of flat plate boundary layer is used. After the solution of *Q* (i.e. f' or *g* in the equation 3.123 or 3.124) is obtained, one can compute the physical values of the other variable.

The velocity distribution in the boundary layer can be computed as:

$$\frac{u}{U_e} = f' \tag{3.115}$$

The physical *z* Coordinate will be computed from:

$$z = \frac{\sqrt{2\xi}}{\rho_e U_e} \int_0^\zeta \frac{\rho_e}{\rho} d\zeta \tag{3.133}$$

The momentum thickness can be computed from:

$$\theta = \frac{\sqrt{2\xi}}{\rho_e U_e} \int_0^\infty f'(1-f')d\zeta \tag{3.134}$$

The displacement thickness will be given by:

$$\delta^* = \frac{\sqrt{2\xi}}{\rho_e U_e} \int_0^\infty (\frac{\rho_e}{\rho} - f')d\zeta \tag{3.135}$$

The shear stress at the body surface is computed from:

$$\tau_w = \mu_w \left(\frac{\partial u}{\partial z}\right)_w = \frac{l_w \rho_e \mu_e U_e^2}{\sqrt{2\xi}} f''_w \tag{3.136}$$

The local convective heat flux is computed from:

$$\overline{q}_w = \frac{l_w \rho_e \mu_e U_e h0_e}{\Pr \sqrt{2\xi}} g'_w \tag{3.137}$$

3.3.4. Turbulence Model

The turbulent eddy viscosity μ_E in the equations (3.103 and 3.105) is computed using the so-called ‘two layer’ turbulence model. In this model, the boundary layer thickness is divided into inner and outer regions. The inner region is modelled based on Van Driest analysis [26, 30] and the outer region is simulated using Clauser model [26].

The turbulent eddy viscosity in the inner region of the boundary layer is computed with the following equation:

$$\left(\frac{\mu_E}{\mu}\right)_i = \frac{\rho k^{*2} z^2}{\mu}\left[1-\exp\left(\frac{-z\sqrt{\tau\rho}}{A^*\mu}\right)\right]^2 \left|\frac{\partial u}{\partial z}\right| \tag{3.138}$$

where k^* and A^* are the von Karmans constants, which its values are 0.4 and 26, respectively.

Within the outer region of boundary layer the following equation serves for the calculation of the turbulent eddy viscosity:

$$\left(\frac{\mu_E}{\mu}\right)_o = \frac{\rho \lambda U_e}{\mu} \overline{\gamma} \delta^*_{ink} \tag{3.139}$$

where λ is constant equal to 0.0168.

$\overline{\gamma}$ is the Klebanovs intermittency factor [26] given by:

$$\begin{aligned} \overline{\gamma} &= 0.5\{1-erf\left[5(z/\delta-0.78)\right]\} \\ &\cong \frac{1}{1+5.5(z/\delta)^6} \end{aligned} \tag{3.140}$$

The boundary between the inner and the outer region is determined, if the value of the turbulent eddy viscosity in the inner region is equal to those in the outer region.

$$\left(\frac{\mu_E}{\mu}\right)_i = \left(\frac{\mu_E}{\mu}\right)_o \tag{3.141}$$

Therefore the computation of the inner turbulent eddy viscosity is carried out starting from the surface to the edge of the boundary layer. Contrary, the computation of the outer turbulent eddy viscosity is carried out starting from the edge of the boundary layer to the surface.

3.4. Laminar-Turbulent Transition: The e^n Method

The transition from laminar to turbulent flow is predicted using the e^n method. This method assumes that transition takes place, if the disturbance wave (the unstable Tollmien-Schlichting wave) growths up to e^9 ~ 8100 [3]. That means: if the value of n at a certain position x is equal to 9, then the transition takes place at this position.

For a similar flow, i.e. flow with constant shape factor H, the value of n is [3]:

$$n = \frac{dn}{d\,\mathrm{Re}_\theta}\left[\mathrm{Re}_\theta - \mathrm{Re}_{\theta 0}\right] \tag{3.142}$$

where the slope of n with respect to Re_θ and the critical Reynolds number $\mathrm{Re}_{\theta 0}$ are given by [3]:

$$\frac{dn}{d\,\mathrm{Re}_\theta} = 0.01\left\{\left[2.4H_k - 3.7 + 2.5\tanh(1.5H_k - 4.65)\right]^2 + 0.25\right\}^{0.5} \tag{3.143}$$

$$\log_{10}\mathrm{Re}_{\theta 0} = \left(\frac{1.415}{H_k - 1} - 0.489\right)\tanh\left(\frac{20}{H_k - 1} - 12.9\right) + \frac{3.295}{H_k - 1} + 0.44 \tag{3.144}$$

In the case of the constant shape factor H, the critical Reynolds number $\mathrm{Re}_{\theta 0}$ is reached at a certain place x_0. If the shape factor H is not constant along the body, one must compute the change of n along the body, as follows [3]:

$$n(x)=\int_{x_0}^{x}\frac{dn(x)}{dx}dx \tag{3.145}$$

$$\frac{dn(x)}{dx}=\frac{dn}{d\,\mathrm{Re}_\theta}\frac{(m+1)}{2}\frac{l}{\theta} \tag{3.146}$$

where:

$$l=\frac{6.54H_k-14.07}{H_k^2} \tag{3.147}$$

$$m=\left[0.058\frac{(H_k-4)^2}{H_k-1}-0.068\right]\frac{1}{l} \tag{3.148}$$

x_0 is the critical point, where the value of Re_θ is equal to $\mathrm{Re}_{\theta 0}$. In this case the critical Reynolds number $\mathrm{Re}_{\theta 0}$ depends on the value of the shape factor H along the body.

It should be noted that the integration in the equation (3.145) takes place from x_0 to the regarded point x.

4. Inviscid Aerodynamic Models

In this chapter, three different inviscid aerodynamic models, which will be coupled with the viscous aerodynamic models (i.e. the boundary layer methods described in the previous chapter), are presented. These inviscid aerodynamic models are based on the TSD equation, the Euler and the Small Disturbance Euler equations.

4.1. The Transonic Small Disturbance (TSD) Equation

4.1.1. Historical Background

The TSD equation represents a derivation of the Full Potential equation under small disturbances assumption applied for the transonic flow. It was examined in detail for the first time by Murman & Cole in 1971 applied to a thin, zero-lift airfoil [31]. A first order finite difference method is assigned to solve the equation numerically. Garabedian & Korn [32] improved the Murman's solution by using a second order scheme. Airfoil with camber and angles of attack was treated afterwards by Steger & Lomax [33] in 1972 incorporated with the Successive Over Relaxation (SOR) method applied to solve the Full Potential equation.

First publications for a wing in transonic flow go back to the works from Ballhaus & Bailey [34] as well as Bailey & Steger [35] in 1972 by solving the TSD equation. In 1974, a more efficient procedure by use of central and upwind difference schemes was introduced by Murman [36]. It can be used favourably for local subsonic and supersonic flow respectively. Furthermore it used the shock point operator to control the points, where the flow enters and leaves the supersonic zone. Murman pointed out also that the conservative formulation of the equation is suggested to be used, in order to have the correct jump conditions through the shock. With the help of shock point difference operator Murman solved also the non conservative form of the equation and shows the equivalence solution to that of the conservative one.

In 1977 Ballhaus & Goorjian [37] solved the unsteady form of the TSD equation for low frequency with the Alternatives Direct Implicit (ADI) algorithm. The code is well-known as LTRAN2 and it was used to compute an oscillating airfoil in transonic flow. The extension of this method in three-dimensional calculations has been carried out by Borland et. al. [38] in 1982 with their XTRAN3S code. They computed the unsteady solution of a swept wing in transonic flow. Between 1975 and 1981 the Approximate Factorisation (AF) algorithm has been employed by Ballhaus & Steger [39], Ballhaus et. al. [40] and Baker [41] to solve the TSD equation. The AF algorithm is the basis of the ADI algorithm and it makes possible an implicit procedure in three Cartesian coordinate directions independently in three steps of calculation process. It is substantial that the AF algorithm is faster than ADI and SOR algorithms.

Steinhoff & Jameson [42] found that several solutions ('non uniqueness' solution) can exist by solving the full potential equation as they computed a symmetrical airfoil with zero angle of attack. They received three solutions for this case. Two solutions are with lift and a solution is without lift, as it was expected. This is probably because of the isentropic assumption in the potential equation, which makes the increasing entropy through a shock can not be well simulated. Salas et. al. [43] also reported the similar situation. Therefore, researchers are interested to develop an entropy correction to be applied in the potential equation, in order to extend or to correct the isentropic assumption in the potential equation.

Between 1981 and 1985, Hafez & Lovell [44, 45] and Fuglsang & Williams [46] suggested the following form of entropy correction. The pressure distribution from the solution of the TSD or potential equation is corrected with the entropy influence, so that the pressure distribution formula consists of the isentropic and the corrected component. The formula of the correction was deduced using the Rankine - Hugoniot relationship of the local velocity before and after the shock. The irrotational assumption of the potential equation was corrected by a circulation correction, which are affected by the increasing entropy through the shock. The local velocity is formulated as sum of isentropic and non isentropic part.

In 1988 Batina [47] suggested an efficient algorithm for the solution of the unsteady TSD equation. He used the AF algorithm coupled with an internal Newton iteration. The Newton iteration was used to accelerate the time-accurate computation of the unsteady pressure distribution. He coupled also his TSD solver with an aeroelastic module. His code is well-known as CAP-TSD (Computational Aeroelastic Program - TSD) and has been applied to calculate the unsteady aerodynamics of an aircraft configuration consists of wing, tail, and fuselage and also nacelle body [48]. The CAP TSD code was continued to be developed by Batina in 1992 [49] and particularly by Mitterer et. al. [50] in 1996 with an improvement of the solution around the leading edge region. They modified the gradient of the airfoil, in order to avoid the non physical pressure within the leading edge region (the peak suction region).

Nowadays the TSD equation is still worked on by some authors. Hung et. al. [51] in 2000 worked on the finite volumes with flux upwinding for the solution of the TSD equation. Ly & Nakamichi [52] developed in 2002 a time-linearized TSD procedure. Their solution comprises of sum of the steady and unsteady parts, which are solved separately. The unsteady part is assumed to be small compared to the steady part. Recently, Greco Jr. and Sheng [53] have also presented their works on TSD equation with viscous correction to be solved in the frequency domain.

In this present work a TSD code is developed with the following characteristics:

- Three-dimensional flows
- Finite difference method
- Central and upwind difference space discretization
- Implicit Approximate Factorization (AF) algorithm
- Entropy and Vorticity correction
- Modification of the tangential boundary condition

The development of this TSD code will be explained in the following section.

4.1.2. Equation Form

As the starting point is the Full Potential equation, which can be written in velocity potential in Cartesian coordinates, as follows [54]:

$$\begin{aligned}\Phi_{tt} + 2\left(\Phi_x\Phi_{xt} + \Phi_y\Phi_{yt} + \Phi_z\Phi_{zt}\right) - \left(a^2 - \Phi_x^2\right)\Phi_{xx} - \left(a^2 - \Phi_y^2\right)\Phi_{yy} - \left(a^2 - \Phi_z^2\right)\Phi_{zz} + \\ 2\left(\Phi_x\Phi_y\Phi_{xy} + \Phi_x\Phi_z\Phi_{xz} + \Phi_y\Phi_z\Phi_{yz}\right) = 0\end{aligned} \tag{4.1}$$

Here the symbol a is the speed of sound.

The gradient of velocity potential is the velocity vector:

$$\nabla\Phi = \vec{V} \tag{4.2}$$

The velocity potential Φ satisfies the isentropic and irrotational assumptions:

$$\nabla s = 0 \text{ and } \nabla \times \nabla\Phi = 0 \tag{4.3}$$

The assumption of small disturbance is formulated as follows:

$$\Phi = \Phi_\infty + \phi = U_\infty x + \phi \tag{4.4}$$

where the velocity vector can be described as:

$$u = \Phi_x = U_\infty + \phi_x, \qquad v = \Phi_y = \phi_y, \qquad w = \Phi_z = \phi_z, \qquad \phi_x, \phi_y, \phi_z << U_\infty \tag{4.5}$$

After inserting equation (4.4) and (4.5) in the equation (4.1), the TSD equation is obtained, which can be written in the conservative form in the Cartesian coordinates, as follows [47]:

$$\frac{\partial f_0}{\partial t} + \frac{\partial f_1}{\partial x} + \frac{\partial f_2}{\partial y} + \frac{\partial f_3}{\partial z} = 0 \tag{4.6}$$

where the flux terms are given by:

$$f_0 = -\left(Af_t + Bf_x\right), \qquad f_1 = Ef_x + Ff_x^2 + Gf_y^2,$$
$$f_2 = f_y + Hf_xf_y, \qquad f_3 = f_z \tag{4.7}$$

where the disturbance velocity f_x, f_y and f_z are normalised with the uniform undisturbed velocity $U_{¥}$. In the equation (4.6) the nonlinear terms are retained in the forms of f_xf_{xx}, f_yf_{xy} and f_xf_{yy} in order still to be able to simulate a discontinuity in the flow field.

The coefficients of the flux terms in eq. (4.7) can be written, as follows [48]:

$$A = M_\infty^2, \qquad B = 2M_\infty^2, \qquad E = 1 - M_\infty^2,$$
$$F = -\frac{1}{2}(g+1)M_\infty^2, \qquad G = \frac{1}{2}(g-3)M_\infty^2, \qquad H = -(g-1)M_\infty^2, \tag{4.8}$$

For two dimensional cases, the term f_2 in the equation (4.6), G and H in the equation (4.7) become to zero.

4.1.3. Solution Procedure

To solve the TSD equation numerically, the following steps must be applied [47]:

- The domains of the problem (space and time domain) are distributed in discrete points under finite difference theory. The space and time derivatives in the TSD equation are approximated by finite difference. After these discretization and approximation, the finite difference equation of TSD equation (4.6) can be obtained.
- This finite difference equation is solved under certain boundary conditions. Two solution procedures must be applied to obtain the real time (unsteady) solutions of this finite difference equation, i.e. Time Linearized Step (TLS) and Time Accurate Step (TAS). The TLS is applied to generate an intermediate solution in the next time level, as base for the final solution under the use of the TAS. For steady cases only the TLS is used because there is no change of the boundary condition. In both procedures the Approximate Factorization (AF) algorithm is used to accelerate the computation process. The AF algorithm makes the implementation of the solution procedure in three independent Cartesian directions possible.

These steps are explained in detail in the following section.

4.1.3.1. Time Accurate Step (TAS)

In order to describe the solution procedures, the TSD equation (4.6) is symbolically written as:

$$R(f) = 0 \tag{4.9}$$

The velocity potential at the time level (n+1), f^{n+1}, is defined as sum of the assumed velocity potential, f^*, and the deviation between them, as follows:

$$f^{n+1} = f^* + \Delta f \tag{4.10}$$

With this definition, the TSD equation (4.9) can be written after applying 1st order Taylor series as:

$$\left(\frac{\partial R}{\partial f}\right)_{f=f^*} \Delta f = -R\left(f^*\right) \tag{4.11}$$

This equation is solved subject to a specified boundary condition to obtain the value of deviation of velocity potential Δf. This value of Δf will update the value of f^{n+1} through equation (4.10). An internal iteration is applied to obtain the convergence solution, which means that $f^{n+1} \sim f^*$ and $\Delta f \sim 0$.

In the TAS, the boundary conditions change from the previous time step due to the movement of the body, but there is no change of boundary condition in the internal iteration process.

4.1.3.2 Time Linearized Step (TLS)

The velocity potential at the time level (*), ϕ^*, in equation (4.10) is defined as sum of velocity potential at the time level (n), ϕ^n, and the deviation between them, as follows:

$$\phi^* = \phi^n + \Delta\phi \tag{4.12}$$

With this definition, the TSD equation (4.9) can be written after applying 1st order Taylor series as:

$$\left(\frac{\partial R}{\partial \phi}\right)_{\phi=\phi^n} \Delta\phi = -R\left(\phi^n\right) \tag{4.13}$$

As before, this equation is solved subject to a specified boundary condition to obtain the value of deviation of velocity potential $\Delta\phi$. This value of $\Delta\phi$ will update the value of ϕ^* through equation (4.12). In the TLS there is no change of the boundary conditions.

The solution procedure is sketched in figure 4.1.

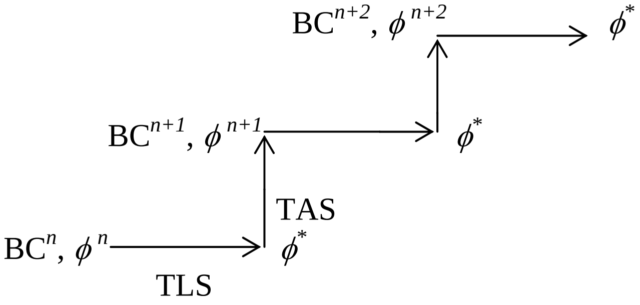

BC^n, ϕ^n = the boundary condition and velocity potential at time level n
TLS = Time Linearized Step (horizontal)
TAS = Time Accurate Step (vertical)

Figure 4.1. Solution Procedure of the TSD Equation

4.1.4. Discretization of the TSD Equation

Discretization of the time and space derivation, which are involved in the TSD equation, are carried out using Finite Difference Method.

4.1.4.1. Discretization of the Time Derivative

In order to include the history of the flow development, a 2nd order backwards difference is used to discretize the time derivative at the time level (*).

The 1st derivative of time has the following form:

$$\phi_t = \frac{3\phi^* - 4\phi^n + \phi^{n-1}}{2\Delta t} \tag{4.14}$$

The 2nd derivative of time has the following form:

$$\phi_{tt} = \frac{2\phi^* - 5\phi^n + 4\phi^{n-1} + \phi^{n-2}}{(\Delta t)^2} \tag{4.15}$$

where the time step is taken uniform.

4.1.4.2. Discretization of the Space Derivative

The discretization of the space derivative is based on the direction of the propagation of the disturbance. For a disturbance in subsonic flows the discretization with central differences is selected, because the disturbance spreads in all directions (up- and downstream). In supersonic flows, the disturbance spreads only in one direction (downstream); therefore the discretization with backward difference is suitable.

The 1st derivative in subsonic or supersonic flows will be approximated using the 1st order backward differences, as follows:

$$\phi_x = \frac{\phi_{i,j,k} - \phi_{i-1,j,k}}{\Delta x} \tag{4.16}$$

For the 2nd derivative in supersonic flows the 1st or 2nd order backward differences is used, as follows:

$$\phi_{xx} = \frac{\phi_{i,j,k} - 2\phi_{i-1,j,k} + \phi_{i-2,j,k}}{(\Delta x)^2} \tag{4.17.a}$$

$$\phi_{xx} = \frac{2\phi_{i,j,k} - 5\phi_{i-1,j,k} + 4\phi_{i-2,j,k} - \phi_{i-3,j,k}}{(\Delta x)^2} \tag{4.17.b}$$

For the second derivative in subsonic flows the 2nd order central difference is used, as follows:

$$\phi_{xx} = \frac{\phi_{i-1,j,k} - 2\phi_{i,j,k} + \phi_{i+1,j,k}}{(\Delta x)^2} \tag{4.18}$$

Here as example only the derivative in the x flow direction is presented. The index *i*, *j* and *k* denote the *x*, *y* and *z* direction.

With the above discretization and by defining the velocity potential as:

$$\phi = \phi^* + \Delta\phi \tag{4.19}$$

then the fluxes in equation (4.7) can be written as:

$$f_0 = -A\phi_t - B\phi_x = -A\left(\phi_t^* + \Delta\phi_t\right) - B\left(\phi_x^* + \Delta\phi_x\right) \tag{4.20.a}$$

$$\frac{\partial f_0}{\partial t} = -\frac{A}{(\Delta t)^2}\left(2\phi^* - 5\phi^n + 4\phi^{n-1} - \phi^{n-2}\right) - \frac{2A}{(\Delta t)^2}\Delta\phi - \frac{B}{2\Delta t}\left(3\phi_x^* - 4\phi_x^n + \phi_x^{n-1}\right) - \frac{3B}{2\Delta t} \tag{4.20.b}$$

$$\begin{aligned} f_1 &= E\phi_x + F\phi_x^2 + G\phi_y^2 \\ &= E\left(\phi_x^* + \Delta\phi_x\right) + F\left((\phi_x^*)^2 + 2\phi_x^*\Delta\phi_x + (\Delta\phi_x)^2\right) + G\left((\phi_y^*)^2 + 2\phi_y^*\Delta\phi_y + (\Delta\phi_y)^2\right) \\ &\cong E\left(\phi_x^* + \Delta\phi_x\right) + F\left((\phi_x^*)^2 + 2\phi_x^*\Delta\phi_x\right) + G\left((\phi_y^*)^2 + 2\phi_y^*\Delta\phi_y\right) \end{aligned} \tag{4.21.a}$$

$$\frac{\partial f_1}{\partial x} = \frac{\partial}{\partial x}\left(E\phi_x^* + F(\phi_x^*)^2\right) + \frac{\partial}{\partial x}\left(G(\phi_y^*)^2\right) + \frac{\partial}{\partial x}\left(E + 2F\phi_x^*\right)\Delta\phi_x + \frac{\partial}{\partial x}\left(2G\phi_y^*\right)\Delta\phi_y \tag{4.21.b}$$

$$\begin{aligned} f_2 &= \phi_y + H\phi_x\phi_y \\ &= \left(\phi_y^* + \Delta\phi_y\right) + H\left(\phi_x^* + \Delta\phi_x\right)\left(\phi_y^* + \Delta\phi_y\right) \\ &= \left(\phi_y^* + \Delta\phi_y\right) + H\left(\phi_x^*\phi_y^* + \phi_y^*\Delta\phi_x + \phi_x^*\Delta\phi_y + \Delta\phi_x\Delta\phi_y\right) \\ &\cong \left(\phi_x^* + H\phi_x^*\phi_y^*\right) + \left(\Delta\phi_y + H\phi_y^*\Delta\phi_x + H\phi_x^*\Delta\phi_y\right) \end{aligned} \tag{4.22.a}$$

$$\frac{\partial f_2}{\partial y} = \frac{\partial}{\partial y}\left(\phi_x^* + H\phi_x^*\phi_y^*\right) + \frac{\partial}{\partial y}\left(\Delta\phi_y + H\phi_y^*\Delta\phi_x + H\phi_x^*\Delta\phi_y\right) \tag{4.22.b}$$

$$f_3 = \phi_z = \phi_z^* + \Delta\phi_z \tag{4.23.a}$$

$$\frac{\partial f_3}{\partial z} = \frac{\partial}{\partial z}\left(\phi_z^*\right) + \frac{\partial}{\partial z}\left(\Delta\phi_z\right) \tag{4.23.b}$$

Here, the square of the deviation of the velocity potentials $(\Delta\_\_)^2$ in the fluxes have been neglected.

Using of the above equations (4.21 – 4.23), the TSD equation (4.6) can be written as a finite difference equation, as follows:

$$\begin{aligned}&\Delta\phi + \frac{3B}{4A}\Delta t\Delta\phi_x - \frac{(\Delta t)^2}{2A}\frac{\partial}{\partial x}\left(E\Delta\phi_x + 2F\phi_x^*\Delta\phi_x + 2G\phi_y^*\Delta\phi_y\right) - \\ &\quad \frac{(\Delta t)^2}{2A}\frac{\partial}{\partial y}\left(\Delta\phi_y + H\phi_x^*\Delta\phi_y + H\phi_y^*\Delta\phi_x\right) - \frac{(\Delta t)^2}{2A}\frac{\partial}{\partial z}\Delta\phi_z = R\left(\phi^*,\phi^n,\phi^{n-1},\phi^{n-2}\right)\end{aligned} \tag{4.24}$$

where $R(\phi^*, \phi^n, \phi^{n-1}, \phi^{n-2})$ is:

$$\begin{aligned}R\left(\phi^*,\phi^n,\phi^{n-1},\phi^{n-2}\right) = &-\frac{1}{2}\left(2\phi^* - 5\phi^n + 4\phi^{n-1} - \phi^{n-2}\right) - \frac{B}{4A}\Delta t\left(3\phi_x^* - 4\phi_x^n + \phi_x^{n-1}\right) + \\ &\frac{(\Delta t)^2}{2A}\frac{\partial}{\partial x}\left(E\phi_x^* + F(\phi_x^*)^2 + G(\phi_y^*)^2\right) + \\ &\frac{(\Delta t)^2}{2A}\frac{\partial}{\partial y}\left(\phi_y^* + H\phi_x^*\phi_y^*\right) + \frac{(\Delta t)^2}{2A}\frac{\partial}{\partial z}\phi_z^*\end{aligned} \tag{4.25}$$

4.1.4.3. Coordinates Transformation

To solve the TSD equation one needs only a Cartesian grid with H type, which is symmetrical with the surface $z = 0$. The upper and lower surface of the wing lay directly as the first plane without thickness above and below the symmetry plane $z = 0$. This is because the tangential boundary condition, which must be imposed, contains the slope of the surface (not the surface coordinate). This boundary condition will be discussed later in section 4.1.6.

In order to obtain a non dimensional form of the TSD equation, the Cartesian coordinates (x, y, z) are transformed into computational coordinates (ξ, η, ζ), which are defined as simple normalised coordinates, as follows:

$$\xi = \xi(x,y) = \frac{x - x_{le}(y)}{x_{te}(y) - x_{le}(y)}, \qquad \eta = y/b, \qquad \zeta = z/c \tag{4.26}$$

The subscript *le* and *te* denote leading and trailing edge respectively. The notations b and c denote the span and chord respectively.

Figure 4.2 shows an example of the physical and computational coordinates which are needed to solve the two-dimensional TSD equation.

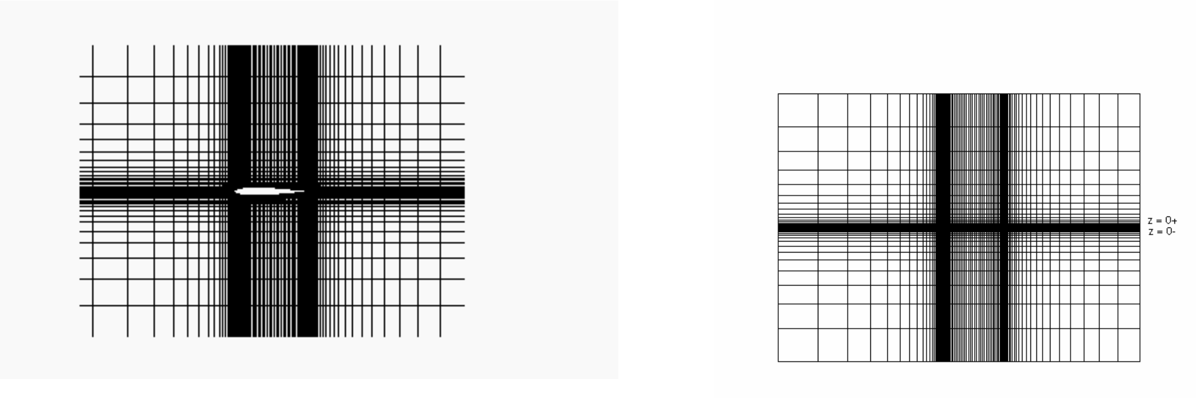

a. Physical Coordinates b. Computational Coordinates

Figure 4.2. Transformation of Coordinates

The derivatives in the Cartesian coordinates are transformed to normalised coordinates using chain rule, as follows:

$$\frac{\partial}{\partial x} = \frac{\partial}{\partial \xi}\xi_x, \qquad \frac{\partial}{\partial y} = \frac{\partial}{\partial \xi}\xi_y + \frac{1}{b}\frac{\partial}{\partial \eta}, \qquad \frac{\partial}{\partial z} = \frac{1}{c}\frac{\partial}{\partial \zeta} \tag{4.27}$$

The TSD equation (4.24) can then be written in the computational coordinate (ξ, η, ζ) as follows:

$$\begin{aligned}\{\ 1+\frac{3B}{4A}\Delta t\xi_x\frac{\partial}{\partial\xi}-\frac{\Delta t^2}{2A}\xi_x\frac{\partial}{\partial\xi}\frac{\partial}{\partial\xi}\left[E\xi_x+2F\xi_x{}^2\phi_\xi^*+(2G+H)\xi_y\left(\xi_y\phi_\xi^*+\phi_\eta^*\right)+\frac{\xi_y^2}{\xi_x}+H\xi_y^2\phi_\xi^*\right]-\\ \frac{\Delta t^2}{2A}\xi_x\frac{\partial}{\partial\xi}\frac{\partial}{\partial\eta}\left[(2G+H)\left(\xi_y\phi_\xi^*+\phi_\eta^*\right)+2\left(\frac{\xi_y}{\xi_x}+H\phi_\xi^*\xi_y\right)\right]-\frac{\Delta t^2}{2A}\frac{\partial}{\partial\eta}\frac{\partial}{\partial\eta}\left(1+H\phi_\xi^*\xi_x\right)-\\ \frac{\Delta t^2}{2A}\frac{\partial}{\partial\zeta}\frac{\partial}{\partial\zeta}\ \}\Delta\phi=R\left(\phi^*,\phi^n,\phi^{n-1},\phi^{n-2}\right)\end{aligned} \tag{4.28}$$

where now the term $R(\phi^*,\phi^n,\phi^{n-1},\phi^{n-2})$ changes to:

$$\begin{aligned}R\left(\phi^*,\phi^n,\phi^{n-1},\phi^{n-2}\right)=-\frac{1}{2}\left(2\phi^*-5\phi^n+4\phi^{n-1}-\phi^{n-2}\right)-\frac{B}{4A}\Delta t\xi_x\left(3\phi_x^*-4\phi_x^n+\phi_x^{n-1}\right)+\\ \frac{(\Delta t)^2}{2A}\xi_x\frac{\partial}{\partial\xi}\left(E\xi_x\phi_\xi^*+F\xi_x{}^2(\phi_\xi^*)^2+G(\xi_y\phi_\xi^*+\phi_\eta^*)^2+\frac{\xi_y}{\xi_x}\left(\xi_y\phi_\xi^*+\phi_\eta^*\right)\left(1+H\xi_x\phi_\xi^*\right)\right)+\\ \frac{(\Delta t)^2}{2A}\frac{\partial}{\partial\eta}\left[\left(\xi_y\phi_\xi^*+\phi_\eta^*\right)\left(1+H\xi_x\phi_\xi^*\right)\right]+\frac{(\Delta t)^2}{2A}\frac{\partial}{\partial\zeta}\phi_\zeta^*\end{aligned} \tag{4.29}$$

The equations (4.28) and (4.29) are actually the finite difference form of the TSD equation for the TAS solution procedure. However, those equations remain valid for the TLS procedure by changing the velocity potential ϕ^* with ϕ^n.

4.1.5. The Approximate Factorization (AF) Algorithm

In order to obtain Time TLS and TAS solutions of the TSD equation, the Approximate Factorization (AF) algorithm is used. The idea of the AF algorithm is to distribute the solution procedure in three independent computational coordinates successively, by which the calculation time can be reduced.

The left hand side (LHS) of the TSD equation (4.28) is approximated as multiplication (or factorization) of three independent differential operators, as follows:

$$LHS \cong L_\xi L_\eta L_\zeta\ \Delta\phi \tag{4.30}$$

where L_ξ, L_η, and L_ζ: are as follows:

$$\begin{aligned}L_\xi=1+\frac{3B}{4A}\Delta t\xi_x\frac{\partial}{\partial\xi}-\frac{\Delta t^2}{2A}\xi_x\frac{\partial}{\partial\xi}\frac{\partial}{\partial\xi}\\ \left[E\xi_x+2F\xi_x{}^2\phi_\xi^*+(2G+H)\xi_y\left(\xi_y\phi_\xi^*+\phi_\eta^*\right)+\frac{\xi_y^2}{\xi_x}+H\xi_y^2\phi_\xi^*\right]\end{aligned} \tag{4.31.a}$$

$$L_\eta=1-\frac{\Delta t^2}{2A}\frac{\partial}{\partial\eta}\frac{\partial}{\partial\eta}\left(1+H\phi_\xi^*\xi_x\right) \tag{4.31.b}$$

$$L_\zeta=1-\frac{\Delta t^2}{2A}\frac{\partial}{\partial\zeta}\frac{\partial}{\partial\zeta} \tag{4.31.c}$$

It is shown in Ref. [55] that the error of approximation is proportional with $(\Delta t)^2(\Delta\xi)^{-1}$ $(\Delta\eta)^{-1}\Delta\phi$, which implies that it will be zero if the residue $\Delta\phi$ is equal to zero.

The TSD equation (4.28) can then be approximated as:

$$L_\xi L_\eta L_\zeta\ \Delta\phi = R(\phi^*,\phi^n,\phi^{n-1},\phi^{n-2}) \tag{4.32}$$

With this factorizing, the TSD equation can be solved to obtain $\Delta\phi$ through sweeping procedures in three directions successively.

The 1st sweeping is carried out in the flow direction ξ, by modifying equation (4.32) as follows:

$$L_\xi \Delta\phi^\xi = R\left(\phi^*, \phi^n, \phi^{n-1}, \phi^{n-2}\right) \tag{4.33}$$

where:

$$\Delta\phi^\xi = L_\eta L_\zeta \; \Delta\phi \tag{4.34}$$

and $R(\phi^*,\phi^n,\phi^{n-1},\phi^{n-2})$ contains the given boundary conditions. This equation is solved for $\Delta\phi^\xi$

The 2nd sweeping is carried out in the spanwise direction η, by modifying equation (4.34) as follows:

$$L_\eta \, \Delta\phi^\eta = \Delta\phi^\xi \tag{4.35}$$

where:

$$\Delta\phi^\eta = L_\zeta \; \Delta\phi \tag{4.36}$$

and $\Delta\phi^\xi$ is the result from the previous ξ sweeping.

The last sweeping is carried out in the vertical direction ζ to solve eq. (4.36):

$$L_\zeta \; \Delta\phi = \Delta\phi^\eta \tag{4.36}$$

where $\Delta\phi^\eta$ is the result from the previous η sweeping. This equation is solved for $\Delta\phi$

The detail of the sweeping procedures can be read in Ref. [55].

4.1.6. Boundary Conditions

The following boundary conditions must be imposed, in order to solve the TSD equation:

a. Far field boundary conditions

Far fore the body : $\phi = 0$ (4.37a)

Far aft the body : $\phi_x + \phi_t = 0$ (4.37b)

Far above/below the body : $\phi_z = 0$ (4.37c)

Far away from span tip : $\phi_y = 0$ (4.37d)

The subscript means the associated derivative.

b. The tangential boundary condition on the body surface:

$$\phi_z^\pm = f_x^\pm + f_t + \delta_x^{*\pm} \tag{4.38}$$

where f is die function of the body surface and δ^* is the displacement thickness along the body surface. The superscript +/- denotes the upper/lower surface. The subscript means the associated derivative.

In this procedure the tangential boundary condition (4.38) is modified by incorporating the velocity in flow direction $(1+\phi_x)$, in order to give a correction in the ϕ_z particularly on the leading edge region where the slope of the surface f_x is large, as follows:

$$\phi_z^\pm = \left(f_x^\pm + \delta_x^{*\pm}\right)\left(1 + \phi_x\right) + f_t \tag{4.39}$$

This is because the gradient of the surface f_x is proportional with tan α (local angle of attack), which is equal to $\phi_z/(1+\phi_x)$ (see Fig. 4.3.)

Only if the airfoil is thin and the disturbance velocity ϕ_x is small, it is sufficient to use the equation (4.38).

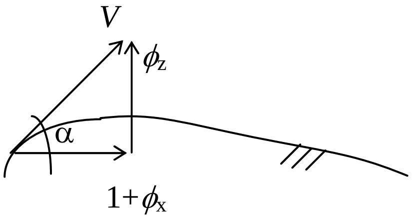

Figure 4.3. Tangential Boundary Condition

Mitterer et. al. [50] has also modified the slope of the surface using the Riegel's rule, in order to reduce the peak suction in the leading edge, as follows:

$$\left(f_x^{\pm}\right)_{new} = \frac{f_x^{\pm}}{\sqrt{1+\left(f_x^{\pm}\right)^2}} \tag{4.40}$$

This modification makes the large slope of the surface at the leading edge near one and remains the small slope near its original value.

c. Symmetry boundary condition
   In the symmetry plane governs the following boundary condition:

$$\phi_y = 0 \tag{4.41}$$

d. In the wake the following boundary condition must be imposed :

$$\left[\phi_z\right] = \delta_x^{*+} - \delta_x^{*-} \tag{4.42a}$$

$$[\phi_x + \phi_t] = 0 \tag{4.42b}$$

The symbol [] denotes the difference (jump) of the quantity in the bracket across the wake.

4.1.7. Entropy Correction

If a strong shock presents at the body, then the entropy across the shock is not constant anymore due to the discontinuity of the increasing pressure across the shock. In order that the TSD equation still to be able to be used to analyse the flow with shock wave, a correction must be introduced into the TSD equation due to the increasing entropy across the shock. This is because the TSD equation (and also the Full Potential equation) is derived by assuming the isentropic condition overall in the flow domain.

Following Fuglsang et. al. [46], the increasing entropy across a shock can be calculated as:

$$\frac{\Delta s}{c_v} = \ln\left[r^{\upsilon}\left(\frac{\upsilon - r}{\upsilon r - 1}\right)\right] \tag{4.43}$$

where:

$$\upsilon = \frac{\gamma+1}{\gamma-1} \qquad r = \frac{\bar{u}_2}{\bar{u}_1} = \frac{R^2}{\bar{u}_1^2} \qquad \bar{u} = 1+\phi_x - u_s \qquad R = \sqrt{1+\frac{2(1-M_\infty^2)}{(\gamma+1)M_\infty^2}} \tag{4.44}$$

u_s = the speed of the shock motion
c_v = heat capacity at constant volume
$\bar{u}$ = effective flow speed

The subscripts 1 and 2 denote the conditions before and after the shock. In this procedure the exponent of *r* in equation (4.43) (i.e. υ) is modified with γ, in order to reduce the value of Δs. By using the original value (υ) the stability of the calculation is disturbed and the convergence of the calculation can not be achieved.

This entropy correction will be taken into account in the formulation of the pressure coefficient, which now comprises as sum of isentropic and non isentropic parts, as follows [46]:

$$C_p = C_{pi} + C_{p_s} \tag{4.45}$$

where the isentropic part is:

$$C_{pi} = \frac{2}{\gamma M_\infty^2}\left\{\left[1+\frac{\gamma-1}{2}M_\infty^2\left(1-\nabla\phi\circ\nabla\phi+2\frac{\partial\phi}{\partial t}\right)\right]^{\frac{\gamma}{\gamma-1}}-1\right\} \tag{4.46}$$

and the non isentropic part is:

$$C_{p_s} = \frac{2(s-s_\infty)/c_v}{\gamma(\gamma-1)M_\infty^2} \tag{4.47}$$

The streamwise disturbance speed after shock must be modified due to the entropy jump, which can be written as [56]:

$$u = \phi_x - \frac{(s-s_\infty)/c_v}{\gamma(\gamma-1)M_\infty^2} \tag{4.48}$$

4.2. The Euler Equations

The Euler equations describe the inviscid, non isentropic, compressible and rotational flow. The equations are derived from the Navier-Stokes equations by neglecting its viscous terms. The Euler equations are a set of the differential equations, which consist of one continuity equation, three momentum equations in the Cartesian coordinate directions and one energy equation.

4.2.1. Equation Form

The Euler equations can be written in dimensionless conservative form in three dimensional Cartesian coordinates (x, y, z), as follows [30, 57]:

$$\frac{\partial\{q\}}{\partial t}+\frac{\partial\{f\}}{\partial x}+\frac{\partial\{g\}}{\partial y}+\frac{\partial\{h\}}{\partial z}=0 \tag{4.49}$$

where the vector $\{q\}$ and the fluxes $\{f\}$, $\{g\}$ and $\{h\}$ are:

$$\{q\}=\begin{Bmatrix}\rho\\ \rho u\\ \rho v\\ \rho w\\ e\end{Bmatrix}\quad \{f\}=\begin{Bmatrix}\rho u\\ \rho uu+p\\ \rho uv\\ \rho uw\\ (e+p)u\end{Bmatrix}\quad \{g\}=\begin{Bmatrix}\rho v\\ \rho vu\\ \rho vv+p\\ \rho vw\\ (e+p)v\end{Bmatrix}\quad \{h\}=\begin{Bmatrix}\rho w\\ \rho wu\\ \rho wv\\ \rho ww+p\\ (e+p)w\end{Bmatrix} \tag{4.50}$$

where the dimensionless variables are as follows: ρ is the density, u, v and w are the component of velocity in the Cartesian coordinates x, y and z direction. The notations t, e and p represent the time, the specific total energy and the pressure.

The set of the equations (4.49) consists of 5 (five) equation (i.e. eq. 4.50) with 6 (six) variables, i.e. ρ, u, v, w, e and p. Therefore one closure equation must be added in order be able to solve this set of equations. The pressure relation derived from the state and energy equations is chosen as the closure equation as follows [30, 57]:

$$p=(\gamma-1)\left[e-\frac{\rho}{2}\left(u^2+v^2+w^2\right)\right] \tag{4.51}$$

where $\gamma = c_p/c_v$ is the isentropic constant.

Physically the Euler equations describe that the temporal change of the vector $\{q\}$ is balanced by the local change of the fluxes $\{f\}$, $\{g\}$ and $\{h\}$.

The dimensionless variables are derived by normalising the dimension variables (with symbol $^{-}$) with respect to a reference values, as follows:

$$\begin{aligned}&x=\frac{\bar{x}}{L^*} && y=\frac{\bar{y}}{L^*} && z=\frac{\bar{z}}{L^*} && \rho=\frac{\bar{\rho}}{\rho^*}\\ &u=\frac{\bar{u}}{u^*} && v=\frac{\bar{v}}{u^*} && w=\frac{\bar{w}}{u^*} &&\\ &p=\frac{\bar{p}}{\rho^* {u^*}^2} && e=\frac{\bar{e}}{\rho^* {u^*}^2} && t=\frac{\bar{t}u^*}{L^*} &&\end{aligned} \tag{4.52}$$

where the reference values are the reference length L^*, velocity u^*, pressure p^* and density ρ^*, which are related to the undisturbed condition (∞) and the characteristic length of the body (c), as follows:

$$u^* = \sqrt{\frac{\overline{p}_\infty}{\overline{\rho}_\infty}} \qquad \rho^* = \overline{\rho}_\infty \qquad p^* = \rho^* {u^*}^2 = \overline{p}_\infty \qquad L^* = c \tag{4.53}$$

4.2.1.1. Coordinates Transformation

In order to compute the flow around an arbitrary body, it is an advantage to transform the Euler equations from the Cartesian coordinates (x, y, z) into the body-fitted coordinates (ξ,η,ζ). This transformation avoids interpolation or extrapolation of the values of the state vector $\{Q\}$ especially on the body surface.

The transformation of the coordinates is as follows [30, 57]:

$$\xi = \xi(x,y,z,t), \quad \eta = \eta(x,y,z,t), \quad \zeta = \zeta(x,y,z,t), \quad \tau = t \tag{4.54}$$

The derivatives in the equation (4.49) are written by the chain rule as follows:

$$\begin{aligned}
&\frac{\partial}{\partial x} = \xi_x \frac{\partial}{\partial \xi} + \eta_x \frac{\partial}{\partial \eta} + \varsigma_x \frac{\partial}{\partial \varsigma}, \quad \frac{\partial}{\partial y} = \xi_y \frac{\partial}{\partial \xi} + \eta_y \frac{\partial}{\partial \eta} + \varsigma_y \frac{\partial}{\partial \varsigma} \\
&\frac{\partial}{\partial z} = \xi_z \frac{\partial}{\partial \xi} + \eta_z \frac{\partial}{\partial \eta} + \varsigma_z \frac{\partial}{\partial \varsigma}, \quad \frac{\partial}{\partial t} = \frac{\partial}{\partial \tau} + \xi_t \frac{\partial}{\partial \xi} + \eta_t \frac{\partial}{\partial \eta} + \varsigma_t \frac{\partial}{\partial \varsigma}
\end{aligned} \tag{4.55}$$

where the transformation metrics are given by:

$$\begin{aligned}
\xi_x &= J^{-1}\left(y_\eta z_\varsigma - z_\eta y_\varsigma\right), & \xi_y &= J^{-1}\left(z_\eta x_\varsigma - x_\eta z_\varsigma\right) \\
\xi_z &= J^{-1}\left(x_\eta y_\varsigma - y_\eta x_\varsigma\right), & \xi_t &= -x_\tau \xi_x - y_\tau \xi_y - z_\tau \xi_z \\
\eta_x &= J^{-1}\left(z_\xi y_\varsigma - y_\xi z_\varsigma\right), & \eta_y &= J^{-1}\left(x_\xi z_\varsigma - z_\xi x_\varsigma\right) \\
\eta_z &= J^{-1}\left(x_\varsigma y_\xi - y_\varsigma x_\xi\right), & \eta_t &= -x_\tau \eta_x - y_\tau \eta_y - z_\tau \eta_z \\
\varsigma_x &= J^{-1}\left(y_\xi z_\eta - z_\xi y_\eta\right), & \varsigma_y &= J^{-1}\left(z_\xi x_\eta - x_\xi z_\eta\right) \\
\varsigma_z &= J^{-1}\left(x_\xi y_\eta - y_\xi x_\eta\right), & \varsigma_t &= -x_\tau \varsigma_x - y_\tau \varsigma_y - z_\tau \varsigma_z
\end{aligned} \tag{4.56}$$

with the Determinant of Jacobi matrix:

$$\begin{aligned}
J &= \frac{\partial(x,y,z,t)}{\partial(\xi,\eta,\varsigma,\tau)} \\
&= x_\xi J\xi_x + y_\xi J\xi_y + z_\xi J\xi_z \\
&= x_\xi\left(y_\eta z_\varsigma - z_\eta y_\varsigma\right) - y_\xi\left(x_\eta z_\varsigma - z_\eta x_\varsigma\right) + z_\xi\left(x_\eta y_\varsigma - y_\eta x_\varsigma\right)
\end{aligned} \tag{4.57}$$

Figure 4.4 represents an example of the physical and computational coordinates applied to solve the two-dimensional Euler equations.

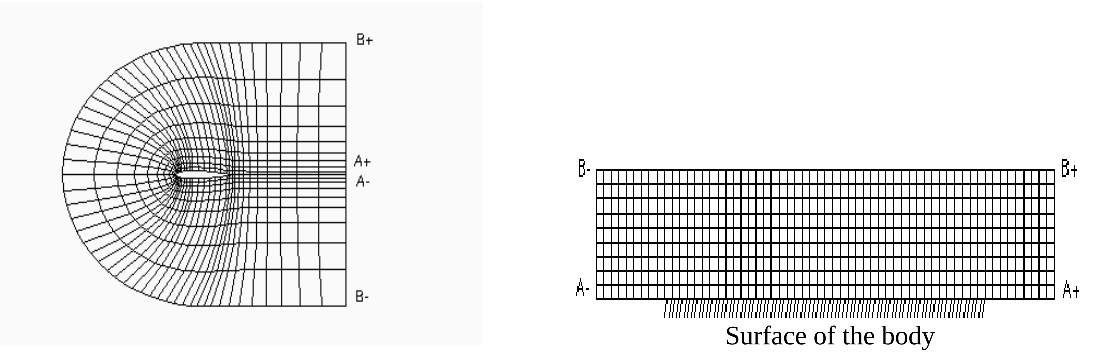

a. Physical coordinate b. Computational coordinate

Figure 4.4. Coordinates Transformation

With the above relations the Euler equations (4.49) become to:

$$\frac{\partial\{Q\}}{\partial\tau}+\frac{\partial\{F\}}{\partial\xi}+\frac{\partial\{G\}}{\partial\eta}+\frac{\partial\{H\}}{\partial\varsigma}=0 \tag{4.58}$$

with the new conservative state vector $\{Q\}$ and the fluxes $\{F\}$, $\{G\}$ and $\{H\}$ as:

$$\begin{aligned}
&\{Q\}=J\{q\}\\
&\{F\}=J\xi_t\{q\}+J\xi_x\{f\}+J\xi_y\{g\}+J\xi_z\{h\}\\
&\{G\}=J\eta_t\{q\}+J\eta_x\{f\}+J\eta_y\{g\}+J\eta_z\{h\}\\
&\{H\}=J\varsigma_t\{q\}+J\varsigma_x\{f\}+J\varsigma_y\{g\}+J\varsigma_z\{h\}
\end{aligned} \tag{4.59}$$

or in the extended formulation:

$$\{Q\}=J\begin{Bmatrix}\rho\\ \rho u\\ \rho v\\ \rho w\\ e\end{Bmatrix}\quad \{F\}=J\begin{Bmatrix}\rho U\\ \rho Uu+\xi_x p\\ \rho Uv+\xi_y p\\ \rho Uw+\xi_z p\\ (e+p)U-\xi_t p\end{Bmatrix}\quad \{G\}=J\begin{Bmatrix}\rho V\\ \rho Vu+\eta_x p\\ \rho Vv+\eta_y p\\ \rho Vw+\eta_z p\\ (e+p)V-\eta_t p\end{Bmatrix}\quad \{H\}=J\begin{Bmatrix}\rho W\\ \rho Wu+\varsigma_x p\\ \rho Wv+\varsigma_y p\\ \rho Ww+\varsigma_z p\\ (e+p)W-\varsigma_t p\end{Bmatrix} \tag{4.60}$$

where U, V and W are the contravariant velocities in the normal direction of the surface with constant ξ, η and ζ , respectively:

$$\begin{aligned}
U&=\xi_x u+\xi_y v+\xi_z w+\xi_t\\
V&=\eta_x u+\eta_y v+\eta_z w+\eta_t\\
W&=\varsigma_x u+\varsigma_y v+\varsigma_z w+\varsigma_t
\end{aligned} \tag{4.61}$$

4.2.2. Numerical Solution of the Euler Equations

The Euler equations are solved numerically using finite volume method. The physical space is distributed in small hexahedral control volume with the state vector $\{Q\}$ is assumed to be constant and assigned in the cell centre. The cell centre is marked by the indices (k, l, m), which correspond with the curvilinear coordinates (ξ, η, ζ) in the numerical space. The fluxes F, G and H are evaluated on each face of the cell, which are marked by the indices (k+1/2, l+1/2, m+1/2). This situation is represented in figure 4.5.

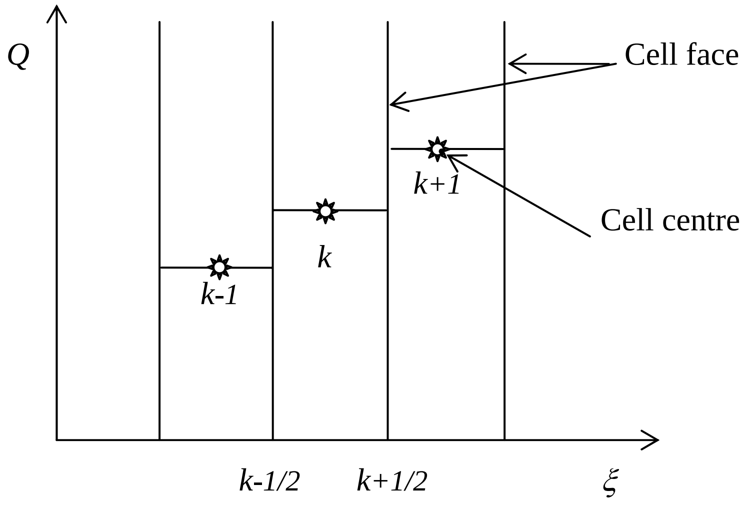

Fig. 4.5. Schematic Representation of the State Vector *Q*

The space discretization of the Euler equations (4.58) is as follows:

$$\frac{\partial\{Q\}_{k,l,m}}{\partial\tau}+\frac{\{F\}_{k+1/2,l,m}-\{F\}_{k-1/2,l,m}}{\Delta\xi}+\frac{\{G\}_{k,l+1/2,m}-\{G\}_{k,l-1/2,m}}{\Delta\eta}+\frac{\{H\}_{k,l,m+1/2}-\{H\}_{k,l,m-1/2}}{\Delta\varsigma}=0 \tag{4.62}$$

Because the length of the side of control volume in numerical space (i.e. $\Delta\xi$ or $\Delta\eta$ or $\Delta\zeta$) equals to one, then the Euler equations can be written in semi discrete form as:

$$\frac{\partial\{Q\}_{k,l,m}}{\partial\tau}=-R_{k,l,m} \tag{4.63}$$

with:

$$R_{k,l,m}=\left[\{F\}_{k+1/2,l,m}-\{F\}_{k-1/2,l,m}\right]+\left[\{G\}_{k,l+1/2,m}-\{G\}_{k,l-1/2,m}\right]+\left[\{H\}_{k,l,m+1/2}-\{H\}_{k,l,m-1/2}\right] \tag{4.64}$$

4.2.2.1. Evaluation of the Fluxes

The Flux Difference Splitting (FDS) method proposed by Roe [58] is used to compute the fluxes at the cell face. The semi discrete form of the Euler equations is decoupled in three directional quasi linear forms which are independent of each other. This step is called as 'Dimension Splitting'.

The decoupled quasi linear form of the Euler equations can be written as:

$$\begin{aligned}
\left.\frac{\partial\{Q\}}{\partial\tau}\right|_{\xi}+\frac{\partial\{F\}}{\partial\xi}&=\left.\frac{\partial\{Q\}}{\partial\tau}\right|_{\xi}+A\frac{\partial\{Q\}}{\partial\xi}=0\\
\left.\frac{\partial\{Q\}}{\partial\tau}\right|_{\eta}+\frac{\partial\{G\}}{\partial\eta}&=\left.\frac{\partial\{Q\}}{\partial\tau}\right|_{\eta}+B\frac{\partial\{Q\}}{\partial\eta}=0\\
\left.\frac{\partial\{Q\}}{\partial\tau}\right|_{\varsigma}+\frac{\partial\{H\}}{\partial\varsigma}&=\left.\frac{\partial\{Q\}}{\partial\tau}\right|_{\varsigma}+C\frac{\partial\{Q\}}{\partial\varsigma}=0
\end{aligned} \tag{4.65}$$

Each differential equation describes a Riemann problem on a cell surface with ξ , η or ζ constant, which do not affect each other. The final solution of the state vector *Q* is the sum of the solution of the individual quasi linear form:

$$\frac{\partial\{Q\}}{\partial\tau}=\left.\frac{\partial\{Q\}}{\partial\tau}\right|_{\xi}+\left.\frac{\partial\{Q\}}{\partial\tau}\right|_{\eta}+\left.\frac{\partial\{Q\}}{\partial\tau}\right|_{\varsigma} \tag{4.66}$$

Here only the evaluation of the flux *F* is presented as example. The evaluation of the fluxes *G* and *H* is carried out similarly.

Consider the cell (*k*, *l*, *m*). For this cell, the equation (4.65) in the ξ direction with constant η and ζ can be written as:

$$\left.\frac{\partial\{Q\}}{\partial\tau}\right|_{\xi}+\frac{\partial\{F\}}{\partial\xi}=0$$
$$\left.\frac{\partial\{Q\}}{\partial\tau}\right|_{\xi}+\frac{F_{k+1/2}-F_{k-1/2}}{\Delta\xi}=0 \tag{4.67}$$

where the indices *l* and *m* are neglected, in order to write it briefly. The flux $F_{k+1/2}$ in eq.(4.67) is represented as averaged fluxes of left and right cells plus the flux differences.

$$F_{k+1/2}=\frac{1}{2}\left[F\left(Q^{L}_{k+1/2}\right)+F\left(Q^{R}_{k+1/2}\right)-\left|\overline{A}_{k+1/2}\right|\left(Q^{R}_{k+1/2}-Q^{L}_{k+1/2}\right)\right] \tag{4.68}$$

where: $Q^{L}_{k+1/2}=Q_k$, $\quad Q^{R}_{k+1/2}=Q_{k+1}$

The term $\frac{1}{2}\left|\overline{A}_{k+1/2}\right|\left(Q^{R}_{k+1/2}-Q^{L}_{k+1/2}\right)$ can be regarded as Dissipation term in the Central Difference Scheme.

The Jacobi Matrix $\overline{A}$ will be calculated via Roe's mean values as [58]:

$$\overline{A}=\overline{R}\ \left|\overline{\Lambda}\right|\ \overline{L} \tag{4.69}$$

with $\overline{R}$ and $\overline{L}$ are matrix of the right and left eigenvectors respectively, which are satisfying the relation $\overline{L}=\overline{R}^{-1}$

Finally the flux $F_{k+1/2}$ can be written as:

$$F_{k+1/2}=\frac{1}{2}\left[F\left(Q^{L}_{k+1/2}\right)+F\left(Q^{R}_{k+1/2}\right)-\overline{R}_{k+1/2}\left|\overline{\Lambda}_{k+1/2}\right|\alpha_{k+1/2}\right] \tag{4.70}$$

with the wave's strength:

$$\alpha_{k+1/2}=\overline{L}_{k+1/2}\left(Q^{R}_{k+1/2}-Q^{L}_{k+1/2}\right) \tag{4.71}$$

In order to obtain a solution with higher order, the **MUSCL** (**M**onotonic **U**pstream **S**cheme for **C**onservation **L**aws) extrapolation is used [57].

The extrapolation can be applied to the conservative, primitive or the characteristic variables. The state vector *Q* will be regarded not constant anymore, but it will be extrapolated from the state vector of the two-neighbouring cells as shown in fig. 4.6.

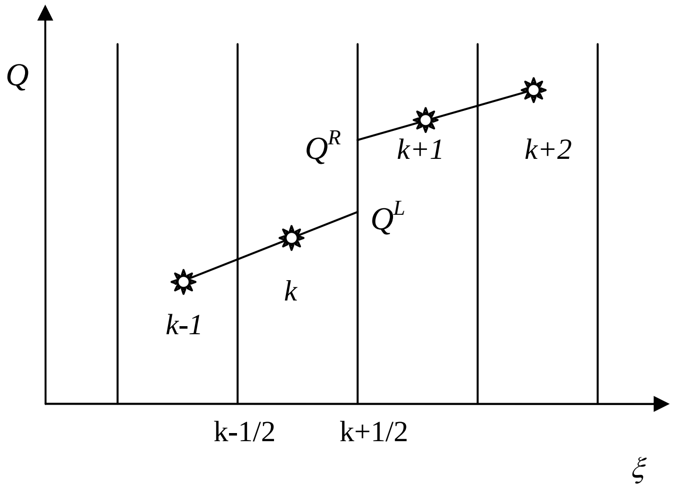

Fig. 4.6. Extrapolation of the State Vector *Q*

At the cell face *k+1/2* the state vector *Q* will be calculated as:

$$Q^L = Q_k + \frac{1}{2}\psi^L_{k+1/2}(Q_k - Q_{k-1}), \quad Q^R = Q_{k+1} + \frac{1}{2}\psi^R_{k+1/2}(Q_{k+2} - Q_{k+1}) \tag{4.72}$$

where the extrapolation function ψ is defined as:

$$\begin{aligned} \psi^L_{k+1/2} &= \psi(r^L_{k+1/2}), \quad r^L_{k+1/2} = \frac{Q_{k+1} - Q_k}{Q_k - Q_{k-1}} \\ \psi^R_{k+1/2} &= \psi(r^R_{k+1/2}), \quad r^R_{k+1/2} = \frac{Q_{k+1} - Q_k}{Q_{k+2} - Q_{k+1}} \end{aligned} \tag{4.73}$$

For the preservation of the TVD (Total Variation Diminishing) characteristic, the order of calculation at its extreme value must be reduced to one. This means, the value of ψ must be limited to one. This was ensured by such a Limiter. Examples of the Limiter are the Minmod and Van Albada Limiter as follows:

- Minmod Limiter : $\psi = \text{minmod}(1,r)$ (4.74a)
- Van Albada Limiter 1 : $\psi = \dfrac{2r}{r^2+1}$ (4.74b)
- Van Albada Limiter 2 : $\psi = \dfrac{r^2+r}{r^2+1}$ (4.74c)

4.2.2.2. Time Integration

After the spatial discretisation has been analyzed, now the time integration of the Euler equations is presented. Both explicit and also implicit time integrations are presented. The semi discrete Euler equations (4.63) are the starting point for this analysis:

$$\frac{\partial\{Q\}_{k,l,m}}{\partial\tau} = -R_{k,l,m} \tag{4.63}$$

with:

$$R_{k,l,m} = \left[\{F\}_{k+1/2,l,m} - \{F\}_{k-1/2,l,m}\right] + \left[\{G\}_{k,l+1/2,m} - \{G\}_{k,l-1/2,m}\right] + \left[\{H\}_{k,l,m+1/2} - \{H\}_{k,l,m-1/2}\right] \tag{4.64}$$

4.2.2.2.1. Explicit Time Integration

The Predictor Corrector Scheme applied for the integration of the state vector in time. The equation (4.63) can be discretized as follows:

$$Q^{n+1} - Q^n = -R^{n+1}\Delta\tau \tag{4.75}$$

where the spatial indices (k, l, m) are neglected. The index n designates the time level.
The Predictor step to be applied to solve eq.(4.75) is:

$$\overline{Q}^{n+1} = Q^n - R^n\Delta\tau \tag{4.76}$$

where the state vector Q and R term are already exist in time level n (Q^n and R^n). Then the estimated R term in time level $n+1$ ($\overline{R}^{n+1}$) is computed from eq. (4.75) with the estimated value $\overline{Q}^{n+1}$.
The Corrector step is carried out as follows:

$$Q^{n+1} = \frac{1}{2}\left(Q^n + \overline{Q}^{n+1} - \overline{R}^{n+1}\Delta\tau\right) \tag{4.77}$$

In order to ensure the stability of the computation, the maximum time step ($\Delta\tau$) is limited by the **CFL** (**C**ourant **F**riedrich **L**evy) number, which describes the relationship between the cell length and the disturbance length. In order to maintain the stability of the computation, the CFL number is limited on maximal one [57]. To accelerate the computation of steady cases, one can use the '*local time stepping*' technique, where the time step for each cell is chosen as maximal as possible. But the local time stepping technique makes the computation process runs not in time accurate fashion, which must be performed for calculation of unsteady cases.

Therefore, for calculation of unsteady cases the global minimum time step must be used on all cells. This is called as *‘global time stepping’* technique.

4.2.2.2.2. Implicit Time Integration

Equation (4.63) can be written in discrete form as:

$$Q^{n+1} - Q^{n} = -R^{n+1}\Delta\tau \tag{4.75}$$

The term R^{n+1} will be linearised using 1st order Taylor series:

$$R^{n+1} = R^{n} + \left.\frac{\partial R}{\partial Q}\right|_{n} \Delta Q \tag{4.78}$$

with: $\Delta Q = Q^{n+1} - Q^{n}$

Substitution eq. (4.78) in eq. (4.75) gives:

$$\left(I + \Delta\tau \left.\frac{\partial R}{\partial Q}\right|_{n} \right)\Delta Q = -\Delta\tau R^{n} \tag{4.79}$$

The RHS (rights hand side) of eq. (4.79) determines the accuracy of the solution and the LHS (left hand side) of eq. (4.79) determines the convergence characteristic and the damping of the computation. Numerical solution of the eq. (4.79) is carried out using the **LU-SSOR** technique (**L**ower **U**pper - **S**ymmetric **S**uccessive **O**ver **R**elaxation) proposed by Yoo and Jameson [59, 60].

The LHS is written as follows [57]:

$$\begin{pmatrix} \frac{I}{\Delta\tau} + \left.\left(A^{+} - A^{-} + B^{+} - B^{-} + C^{+} - C^{-}\right)\right|_{k,l,m} \\ + \left(A^{-}_{k+1,l,m} + B^{-}_{k,l+1,m} + C^{-}_{k,l,m+1}\right) \\ - \left(A^{+}_{k-1,l,m} + B^{+}_{k,l-1,m} + C^{+}_{k,l,m-1}\right) \end{pmatrix} \Delta Q = -R^{n}_{k,l,m} \tag{4.80}$$

with the Jacobi matrix [57]:

$$A^{\pm} = \frac{1}{2}\left(A \pm r_A I\right), \quad B^{\pm} = \frac{1}{2}\left(B \pm r_B I\right), \quad C^{\pm} = \frac{1}{2}\left(C \pm r_C I\right) \tag{4.81}$$

with: $r_A = \omega_D \left|\Lambda_{A,\max}\right|, \quad r_B = \omega_D \left|\Lambda_{B,\max}\right|, \quad r_C = \omega_D \left|\Lambda_{C,\max}\right|$

$\Lambda_{A,\max}$, $\Lambda_{B,\max}$ and $\Lambda_{C,\max}$ are the largest eigenvalues of the Jacobi matrix *A*, *B* and *C* in the eq. (4.65), respectively. ω_D is the Dissipation factor; its value affects the damping of the computation. Here the value of ω_D is chosen between 1 and 1.3, where higher value means stronger damping.

The set of equations (4.80) can be written symbolically, as follows [57]:

$$\left[D + U + L\right]\Delta Q = -R^{n}_{k,l,m} \tag{4.82}$$

with:

$$\begin{aligned} D &= \frac{I}{\Delta\tau} + \left.\left(A^{+} - A^{-} + B^{+} - B^{-} + C^{+} - C^{-}\right)\right|_{k,l,m} \\ &= \frac{I}{\Delta\tau} + \left(r_A + r_B + r_C\right)I \end{aligned} \tag{4.83a}$$

= Entries on the diagonal matrix

$$U = \left(A^{-}_{k+1,l,m} + B^{-}_{k,l+1,m} + C^{-}_{k,l,m+1}\right) \tag{4.83b}$$

= Entries on the upper triangular matrix

$$L = -\left(A^{+}_{k-1,l,m} + B^{+}_{k,l-1,m} + C^{+}_{k,l,m-1}\right) \tag{4.83c}$$

= Entries on the lower triangular matrix

Factorization of the LHS of eq. (4.82) leads to:

$$[D+L]\ \left[D^{-1}(D+U)\right]\Delta Q = -R^n_{k,l,m} \tag{4.84}$$

This equation will be solved with two sweeping steps, as follows:
The 1st sweeping solved ΔQ^* from:

$$[D+L]\Delta Q^* = -R^n_{k,l,m} \tag{4.85a}$$

with given data D, L and R
The 2nd sweeping solved ΔQ from:

$$\begin{gathered}\left[D^{-1}(D+U)\right]\Delta Q = \Delta Q^* \\ [D+U]\Delta Q = D\Delta Q^*\end{gathered} \tag{4.85b}$$

with given data D, U and ΔQ^*
Finally the state vector Q in time level $n+1$ can be computed from:

$$Q^{n+1} = Q^n + \Delta Q \tag{4.86}$$

In order to compute unsteady cases, the *'dual time stepping'* technique is used [59]. The temporal change of the state vector is replaced by a finite approximation with arbitrary order and the RHS is assigned, which must be relaxed to zero. That means, one needs an internal relaxation by the pseudo time τ^*. The formulation of the solution of the unsteady Euler equations with the dual time step technique is as follows:

$$\frac{\partial Q}{\partial \tau^*} = -\left[\frac{\partial Q}{\partial \tau} + R\right] = -R^* \tag{4.87}$$

where τ^* the pseudo time is.
Discretisation of the LHS of eq. (4.87) leads to:

$$\Delta Q^v = -\Delta\tau^*\left[R^*\Big|^v + \frac{\partial R^*}{\partial Q}\Big|^v \Delta Q^v\right] \tag{4.88}$$

$$\left[I + \Delta\tau^* \frac{\partial R^*}{\partial Q}\Big|^v\right]\Delta Q^v = -\Delta\tau^* R^*\Big|^v \tag{4.89}$$

where the symbol v represents the index of the internal iteration.
Because eq. (4.89) has a similar form as eq. (4.79), then the LU-SSOR procedure can also be used to solve this equation, as follows:

$$[D^*+L]\ \left[D^{*-1}(D^*+U)\right]\Delta Q^v = -R^{*v}_{k,l,m} \tag{4.90}$$

The Diagonal Matrix D^* will be given by:

$$D^* = \frac{I}{\Delta\tau^*} + \left(\frac{r_t}{\Delta\tau} + r_A + r_B + r_C\right)I \tag{4.91}$$

where the symbol r_t associated with the order of the finite approximation of $\frac{\partial Q}{\partial \tau}$.

The finite approximation of $\frac{\partial Q}{\partial \tau}$ in eq. (4.87) will be determined as follows:

for 1st order of approximation: $$\frac{\partial Q}{\partial \tau} = \frac{Q^v - Q^n}{\Delta\tau} \tag{4.92a}$$

for 2nd order of approximation: $$\frac{\partial Q}{\partial \tau} = \frac{3Q^v - 4Q^n + Q^{n-1}}{2\Delta\tau} \tag{4.92b}$$

The value of r_t in eq. (4.91) is [57]: r_t = 1 for 1st order and r_t = 1.5 for 2nd order of approximation.
It can be seen that the eq. (4.90) has a similar form with the eq. (4.84); therefore the solution of eq. (4.90) can be obtained using the previous two sweeping steps, i.e. eq. (4.85a) and (4.85b). If the solution ΔQ^v *is* convergent, then the time accurate solution Q^{n+1} is obtained.

4.2.3. Boundary Conditions

The boundary conditions to be applied for solving the Euler equations can be derived from the eigenvalues, eigenvector and characteristic variable of the Euler equations. Here only two dimensional boundary conditions are presented as example.

4.2.3.1. Far-Field Boundary Conditions

From the analysis of the characteristic variable W , the far-field boundary conditions can be classified into four types, as in the following.

a. Subsonic Inflow

If the inflow velocity at far-field boundary is subsonic, three characteristic variables W (associate with three positive eigenvalues) must be given and one characteristic variable W (associates with one negative eigenvalue) must be extrapolated.
The density ρ at far-field boundary can be computed as follows [30, 55, 57]:

$$\rho_b = \rho_a + \frac{(p_b - p_a)}{c^2} \tag{4.93}$$

where c is the speed of sound.
The pressure p at far-field boundary can be computed from [30, 55, 57]:

$$p_b = \frac{1}{2}\left\{(p_a + p_i) \pm \rho c\left[\tilde{k}_x(u_a - u_i) + \tilde{k}_y(v_a - v_i)\right]\right\} \tag{4.94}$$

where: $\tilde{k}_x = \dfrac{\xi_x}{\sqrt{\xi_x^2 + \xi_y^2}}, \quad \tilde{k}_y = \dfrac{\xi_y}{\sqrt{\xi_x^2 + \xi_y^2}}$

and the + and – signs denote the positive and negative k direction, respectively (see fig. 4.7).
The velocity components u and v at far-field boundary can be computed using [30, 55, 57]:

$$u_b = u_a \pm \tilde{k}_x \frac{(p_a - p_b)}{\rho c} \qquad v_b = v_a \pm \tilde{k}_y \frac{(p_a - p_b)}{\rho c}$$

where the + and – signs denote the positive and negative k direction, respectively.
The subscript b is the value at the boundary, a is the value outside the boundary (mirror cell) and i is the value in the interior of the computational space (see fig. 4.7)

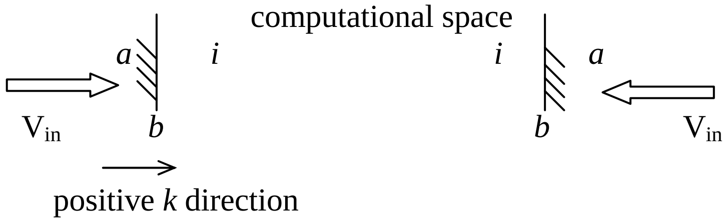

Fig. 4.7. Schematic of Far-Field Boundary Condition (Inflow)

b. Subsonic Outflow

If the outflow velocity at far-field boundary subsonic is, three characteristic variables W (associate with three positive eigenvalues) must be extrapolated and one characteristic variable W (associates with negative eigenvalue) must be given.

The density ρ at far-field boundary can be determined as [30, 55, 57]:

$$\rho_b = \rho_i + \frac{(p_b - p_i)}{c^2} \tag{4.95}$$

The pressure p at far-field boundary will be as [30, 55, 57]:

$$p_b = \frac{1}{2}\left\{(p_a + p_i) \pm \rho c\left[\tilde{k}_x(u_i - u_a) + \tilde{k}_y(v_i - v_a)\right]\right\} \tag{4.96}$$

The velocity component u and v will be [30, 55, 57]:

$$u_b = u_i \pm \tilde{k}_x \frac{(p_i - p_b)}{\rho c} \qquad v_b = v_i \pm \tilde{k}_y \frac{(p_i - p_b)}{\rho c}$$

where the + and – signs denote the positive and negative k direction, respectively (see fig. 4.8)

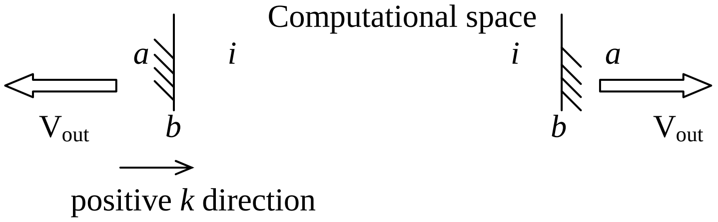

Fig. 4.8. Schematic of Far-Field Boundary Condition (Outflow)

c. Supersonic Inflow

If the inflow velocity at far-field boundary supersonic is, all characteristic variables W (associate with four positive eigenvalues) must be given.

For this condition these eigenvalues are: $a_k^1, a_k^2, a_k^3, a_k^4 > 0$

The characteristic variables are: $W_{1b} = W_{1a}$, $W_{2b} = W_{2a}$, $W_{3b} = W_{3a}$, $W_{4b} = W_{4a}$

The subscript b is the value at the boundary and a is the value outside the boundary (mirror cell).

d. Supersonic Outflow

If the outflow velocity at far-field boundary supersonic is, all characteristic variables W (four positive eigenvalues) must be extrapolated.

For this condition these eigenvalues are: $a_k^1, a_k^2, a_k^3, a_k^4 > 0$

The characteristic variables are: $W_{1b} = W_{1i}$, $W_{2b} = W_{2i}$, $W_{3b} = W_{3i}$, $W_{4b} = W_{4i}$

The subscript b is the value at the boundary and i is the value in the interior of the computational space

4.2.3.2. Solid Body Boundary Conditions

The boundary conditions at solid body surface must satisfy the kinematics boundary condition, where the flow must be attached (tangential) at the solid body boundary. In order to satisfy the kinematics boundary condition, the velocity components in normal direction of solid body surface must be zero.

The characteristic variables are as follows [57]:

For positive k direction: $W_{1b} = W_{1i}$, $W_{2b} = W_{2i}$, $\theta_b = 0$, $W_{4b} = W_{4i}$

For negative k direction: $W_{1b} = W_{1i}$, $W_{2b} = W_{2i}$, $\theta_b = 0$, $W_{3b} = W_{3i}$

where θ_b is the contravariant velocity at solid body boundary:

$$\theta_b = \left(\tilde{k}_x u_b + \tilde{k}_y v_b + \tilde{k}_t\Big|_b\right) = 0 \tag{4.97}$$

with $\tilde{k}_t\Big|_b$ is the velocity of the body motion.

The primitive variables can be derived analogous with far-field boundary condition, as follows:

$$\rho_b = \rho_i + \frac{(p_b - p_i)}{c^2} \tag{4.98}$$

$$u_b = u_i - \tilde{k}_x \left(\tilde{k}_x u_i + \tilde{k}_y v_i + \tilde{k}_t \Big|_b \right) \tag{4.99}$$

$$v_b = v_i - \tilde{k}_y \left(\tilde{k}_x u_i + \tilde{k}_y v_i + \tilde{k}_t \Big|_b \right) \tag{4.100}$$

$$\frac{p_b}{\rho_b c} = \frac{p_i}{\rho_i c} \mp \left(\tilde{k}_x u_i + \tilde{k}_y v_i + \tilde{k}_t \Big|_b \right) \tag{4.101}$$

where the sign – and + show the positive k and negative k direction, respectively.

If the existence of the boundary layer will be considered, then the normal velocity component due to boundary layer must also be computed, as follows:

$$v_n = \frac{d}{dx}(U_e \delta^*) \tag{4.102}$$

where subscript n is normal direction, e is edge of the boundary layer and δ^* is the displacement thickness. In this formulation the derivative of the displacement thickness is assumed to be taken in the x (streamwise) direction only.

Then the tangential velocity components must be actualized with the normal velocity component eq. (4.102), as follows:

$$u'_b = u_b - \frac{dn}{dx} v_n, \quad v'_b = v_b - \frac{dn}{dy} v_n \tag{4.103}$$

where the subscript b stands for boundary and symbol n is the unit normal vector.

The solid body boundary condition can also be derived through the ‚Zero Flux' concepts. This concept states, that the flux normal to body is equal to the pressure term. This is because the value of the contravariant velocity at the solid body boundary is equal to zero. Formulation of the solid body boundary condition through the zero flux concepts for two dimensional flows with and without influence of boundary layer will be presented as follows: Consider two dimensional Euler equations:

$$\frac{\partial\{Q\}}{\partial \tau} + \frac{\partial\{F\}}{\partial \xi} + \frac{\partial\{G\}}{\partial \eta} = 0 \tag{4.104}$$

with:

$$\{Q\} = J \begin{Bmatrix} \rho \\ \rho u \\ \rho v \\ e \end{Bmatrix} \quad \{F\} = J \begin{Bmatrix} \rho U \\ \rho U u + \xi_x p \\ \rho U v + \xi_y p \\ (e+p)U - \xi_t p \end{Bmatrix} \quad \{G\} = J \begin{Bmatrix} \rho V \\ \rho V u + \eta_x p \\ \rho V v + \eta_y p \\ (e+p)V - \eta_t p \end{Bmatrix} \tag{4.105}$$

a. Without Boundary Layer

At the solid body boundary the contravariant velocity V must be zero: $V = 0$ then the state vector and fluxes at solid body boundary are:

$$Q_b = J \begin{Bmatrix} \rho \\ \rho u \\ \rho v \\ e \end{Bmatrix} \qquad F_b = J \begin{Bmatrix} \rho U \\ \rho u U + \xi_x p \\ \rho v U + \xi_z p \\ U(e+p) - \xi_t p \end{Bmatrix} \qquad G_b = J \begin{Bmatrix} 0 \\ \eta_x p \\ \eta_y p \\ \eta_t p \end{Bmatrix} \tag{4.106}$$

Note that the flux G_b consists only the pressure terms without convective terms.

b. With Boundary Layer

The normal velocity component due to boundary layer displacement thickness is represented by eq. (4.102).

The tangential velocity components will be corrected as written in eq. (4.103):

$$u' = u - \frac{dn}{dx} v_n \qquad v' = v - \frac{dn}{dy} v_n \tag{4.103}$$

The contravariant velocity will be corrected with eq. (4.103), as follows:

$$U = u' \frac{d\xi}{dx} + v' \frac{d\xi}{dy} \qquad V = u' \frac{d\eta}{dx} + v' \frac{d\eta}{dy} \tag{4.107}$$

Finally the state vector and the fluxes can be written as:

$$Q_b = J \begin{Bmatrix} \rho \\ \rho u' \\ \rho v' \\ e \end{Bmatrix} \qquad F_b = J \begin{Bmatrix} \rho U \\ \rho u' U + \xi_x p \\ \rho v' U + \xi_z p \\ U(e+p) - \xi_t p \end{Bmatrix} \qquad G_b = J \begin{Bmatrix} \rho V \\ \rho u' V + \eta_x p \\ \rho v' V + \eta_z p \\ V(e+p) - \eta_t p \end{Bmatrix} \tag{4.108}$$

4.3. The Time-Linearized Euler Equations

The starting point is the Euler equations in computational coordinates (ξ,η,ζ):

$$\frac{\partial\{Q\}}{\partial\tau}+\frac{\partial\{F\}}{\partial\xi}+\frac{\partial\{G\}}{\partial\eta}+\frac{\partial\{H\}}{\partial\varsigma}=0 \tag{4.58}$$

with the conservative state vector Q and the fluxes F, G and H are given by:

$$\begin{aligned}
\{Q\} &= J\{q\}\\
\{F\} &= J\xi_t\{q\}+J\xi_x\{f\}+J\xi_y\{g\}+J\xi_z\{h\}\\
\{G\} &= J\eta_t\{q\}+J\eta_x\{f\}+J\eta_y\{g\}+J\eta_z\{h\}\\
\{H\} &= J\varsigma_t\{q\}+J\varsigma_x\{f\}+J\varsigma_y\{g\}+J\varsigma_z\{h\}
\end{aligned} \tag{4.59}$$

The Euler equations above will be linearized under the assumption of small perturbation, i.e. the unsteady perturbation is assumed to be small compared to the steady part.

A variable Z can be decomposed into a steady and an unsteady part, as follows:

$$Z = Z_0 + Z_1 \tag{4.109}$$

where Z_0 and Z_1 are the steady and unsteady component of the variable Z, respectively. It is assumed that: $Z_1 << Z_0$

Under this assumption and by neglecting the 2nd order terms, the state vector Q and the fluxes F, G and H become [57, 61]:

$$\begin{aligned}
Q &= Jq\\
&= (J_0+J_1)(q_0+q_1)\\
&\cong J_0q_0 + J_0q_1 + J_1q_0
\end{aligned} \tag{4.110a}$$

$$\begin{aligned}
F &= J\xi_tq + J\xi_xf + J\xi_yg + J\xi_zh\\
&= [(J\xi_t)_0 + (J\xi_t)_1]\,(q_0+q_1) + [(J\xi_x)_0 + (J\xi_x)_1]\,(f_0+f_1) + [(J\xi_y)_0 + (J\xi_y)_1]\,(g_0+g_1) +\\
&\quad [(J\xi_z)_0 + (J\xi_z)_1]\,(h_0+h_1)\\
&\cong [(J\xi_t)_0\,q_0 + (J\xi_x)_0\,f_0 + (J\xi_y)_0\,g_0 + (J\xi_z)_0\,h_0] +\\
&\quad [(J\xi_t)_0\,q_1 + (J\xi_x)_0\,f_1 + (J\xi_y)_0\,g_1 + (J\xi_z)_0\,h_1] +\\
&\qquad [(J\xi_t)_1\,q_0 + (J\xi_x)_1\,f_0 + (J\xi_y)_1\,g_0 + (J\xi_z)_1\,h_0]
\end{aligned} \tag{4.110b}$$

$$\begin{aligned}
G &= J\eta_tq + J\eta_xf + J\eta_yg + J\eta_zh\\
&= [(J\eta_t)_0 + (J\eta_t)_1]\,(q_0+q_1) + [(J\eta_x)_0 + (J\eta_x)_1]\,(f_0+f_1) + [(J\eta_y)_0 + (J\eta_y)_1]\,(g_0+g_1) +\\
&\quad [(J\eta_z)_0 + (J\eta_z)_1]\,(h_0+h_1)\\
&\cong [(J\eta_t)_0\,q_0 + (J\eta_x)_0\,f_0 + (J\eta_y)_0\,g_0 + (J\eta_z)_0\,h_0] +\\
&\quad [(J\eta_t)_0\,q_1 + (J\eta_x)_0\,f_1 + (J\eta_y)_0\,g_1 + (J\eta_z)_0\,h_1] +\\
&\quad [(J\eta_t)_1\,q_0 + (J\eta_x)_1\,f_0 + (J\eta_y)_1\,g_0 + (J\eta_z)_1\,h_0]
\end{aligned} \tag{4.110c}$$

$$\begin{aligned}
H &= J\zeta_tq + J\zeta_xf + J\zeta_yg + J\zeta_zh\\
&= [(J\zeta_t)_0 + (J\zeta_t)_1]\,(q_0+q_1) + [(J\zeta_x)_0 + (J\zeta_x)_1]\,(f_0+f_1) + [(J\zeta_y)_0 + (J\zeta_y)_1]\,(g_0+g_1) +\\
&\quad [(J\zeta_z)_0 + (J\zeta_z)_1]\,(h_0+h_1)\\
&\cong [(J\zeta_t)_0\,q_0 + (J\zeta_x)_0\,f_0 + (J\zeta_y)_0\,g_0 + (J\zeta_z)_0\,h_0] +\\
&\quad [(J\zeta_t)_0\,q_1 + (J\zeta_x)_0\,f_1 + (J\zeta_y)_0\,g_1 + (J\zeta_z)_0\,h_1] +\\
&\qquad [(J\zeta_t)_1\,q_0 + (J\zeta_x)_1\,f_0 + (J\zeta_y)_1\,g_0 + (J\zeta_z)_1\,h_0]
\end{aligned} \tag{4.110d}$$

by splitting the steady part from the unsteady one, as follows:

$$\begin{aligned}
Q &= Q_0 + Q_1\\
F &= F_0 + F_1\\
G &= G_0 + G_1\\
H &= H_0 + H_1
\end{aligned} \tag{4.111}$$

Two sets of differential equation system can be obtained [57, 61]:

steady :

$$\frac{\partial\{Q_0\}}{\partial\tau}+\frac{\partial\{F_0\}}{\partial\xi}+\frac{\partial\{G_0\}}{\partial\eta}+\frac{\partial\{H_0\}}{\partial\varsigma}=0 \tag{4.112}$$

unsteady (time-linearized):

$$\frac{\partial\{Q_1\}}{\partial\tau}+\frac{\partial\{F_1\}}{\partial\xi}+\frac{\partial\{G_1\}}{\partial\eta}+\frac{\partial\{H_1\}}{\partial\varsigma}=0 \tag{4.113}$$

where:

$$\begin{aligned}
Q_0 &= J_0 q_0\\
F_0 &= (J\xi_x)_0 f_0 + (J\xi_y)_0\, g_0 + (J\xi_z)_0\, h_0\\
G_0 &= (J\eta_x)_0 f_0 + (J\eta_y)_0\, g_0 + (J\eta_z)_0\, h_0\\
H_0 &= (J\zeta_x)_0 f_0 + (J\zeta_y)_0\, g_0 + (J\zeta_z)_0\, h_0
\end{aligned} \tag{4.114}$$

$$\begin{aligned}
Q_1 &= Q_{11} + Q_{12}\\
&= J_0 q_1 + J_1 q_0\\
F_1 &= F_{11} + F_{12}\\
&= [(J\xi_x)_0 f_1 + (J\xi_y)_0\, g_1 + (J\xi_z)_0\, h_1] + [(J\xi_x)_1 f_0 + (J\xi_y)_1\, g_0 + (J\xi_z)_1\, h_0]\\
G_1 &= G_{11} + G_{12}\\
&= [(J\eta_x)_0 f_1 + (J\eta_y)_0\, g_1 + (J\eta_z)_0\, h_1] + [(J\eta_x)_1 f_0 + (J\eta_y)_1\, g_0 + (J\eta_z)_1\, h_0]\\
H_1 &= H_{11} + H_{12}\\
&= [(J\zeta_x)_0 f_1 + (J\zeta_y)_0\, g_1 + (J\zeta_z)_0\, h_1] + [(J\zeta_x)_1 f_0 + (J\zeta_y)_1\, g_0 + (J\zeta_z)_1\, h_0]
\end{aligned} \tag{4.115}$$

The subscripts 1 and 2 describe the component associated with the disturbed state vector (and fluxes) and with the disturbed metrics, respectively.

The unsteady metrics $(J\xi_t)_0$, $(J\eta_t)_0$, $(J\zeta_t)_0$ are negligible, because the metrics of reference-state is steady; as follows:

$$(Jk_t)_0 = -\, x_{\tau 0}\,(Jk_x)_0 - y_{\tau 0}\,(Jk_y)_0 - z_{\tau 0}\,(Jk_z)_0 \qquad \text{with: } k = \xi,\ \eta,\ \zeta \tag{4.116a}$$

Reference state: $x_{\tau 0} = y_{\tau 0} = z_{\tau 0} = 0$

Unsteady metrics become: $(Jk_t)_0 = 0$ (4.116b)

The resulted steady equation (the first set of the differential equations 4.112) is actually the steady form of the Euler equation. It represents the Euler equations under a steady condition. The second set of the differential equations (4.113) is the time-linearized Euler equation, which can be described in the following form:

$$\frac{\partial\{Q_{11}\}}{\partial\tau}+\frac{\partial\{F_{11}\}}{\partial\xi}+\frac{\partial\{G_{11}\}}{\partial\eta}+\frac{\partial\{H_{11}\}}{\partial\varsigma}=-\left[\frac{\partial\{Q_{12}\}}{\partial\tau}+\frac{\partial\{F_{12}\}}{\partial\xi}+\frac{\partial\{G_{12}\}}{\partial\eta}+\frac{\partial\{H_{12}\}}{\partial\varsigma}\right] \tag{4.117}$$

4.3.1. Linearization with Harmonic Term

If the unsteady part Z_1 in the eq. (4.109) is assumed to be harmonic:

$$Z_1 = \tilde{Z}e^{ik\tau} \tag{4.118}$$

then the state Q_1 and Fluxes F, G und H are transformed to [57, 61]:

$$\begin{aligned}
Q_{11} &= \tilde{Q}_1 e^{ik\tau} = J_0\tilde{q}e^{ik\tau}\\
Q_{12} &= \tilde{Q}_2 e^{ik\tau} = \tilde{J}q_0 e^{ik\tau}
\end{aligned} \tag{4.119a}$$

$$\begin{aligned} F_{11} &= \tilde{F}_1 e^{ik\tau} = [(J\xi_x)_0 \tilde{f} + (J\xi_y)_0 \tilde{g} + (J\xi_z)_0 \tilde{h}] e^{ik\tau} \\ F_{12} &= \tilde{F}_2 e^{ik\tau} = [(\tilde{J}\tilde{\xi}_\tau) q_0 + (\tilde{J}\tilde{\xi}_x) f_0 + (\tilde{J}\tilde{\xi}_y) g_0 + (\tilde{J}\tilde{\xi}_z) h_0] e^{ik\tau} \end{aligned} \tag{4.119b}$$

$$\begin{aligned} G_{11} &= \tilde{G}_1 e^{ik\tau} = [(J\eta_x)_0 \tilde{f} + (J\eta_y)_0 \tilde{g} + (J\eta_z)_0 \tilde{h}] e^{ik\tau} \\ G_{12} &= \tilde{G}_2 e^{ik\tau} = [(\tilde{J}\tilde{\eta}_\tau) q_0 + (\tilde{J}\tilde{\eta}_x) f_0 + (\tilde{J}\tilde{\eta}_y) g_0 + (\tilde{J}\tilde{\eta}_z) h_0] e^{ik\tau} \end{aligned} \tag{4.119c}$$

$$\begin{aligned} H_{11} &= \tilde{H}_1 e^{ik\tau} = [(J\varsigma_x)_0 \tilde{f} + (J\varsigma_y)_0 \tilde{g} + (J\varsigma_z)_0 \tilde{h}] e^{ik\tau} \\ H_{12} &= \tilde{H}_2 e^{ik\tau} = [(\tilde{J}\tilde{\varsigma}_\tau) q_0 + (\tilde{J}\tilde{\varsigma}_x) f_0 + (\tilde{J}\tilde{\varsigma}_y) g_0 + (\tilde{J}\tilde{\varsigma}_z) h_0] e^{ik\tau} \end{aligned} \tag{4.119d}$$

Inserting the above relations in the time-linearized Euler equation (4.117):

$$\begin{aligned} \frac{\partial\{Q_{11}\}}{\partial\tau} &= \frac{\partial\{\tilde{Q}_1 e^{ik\tau}\}}{\partial\tau} = e^{ik\tau}\frac{\partial\{\tilde{Q}_1\}}{\partial\tau} + ik\tilde{Q}_1 e^{ik\tau} \\ \frac{\partial\{Q_{12}\}}{\partial\tau} &= \frac{\partial\{\tilde{Q}_2 e^{ik\tau}\}}{\partial\tau} = ik\tilde{Q}_2 e^{ik\tau} \end{aligned} \tag{4.120}$$

produces the following result:

$$\frac{\partial\{\tilde{Q}_1\}}{\partial\tau} + \frac{\partial\{\tilde{F}_1\}}{\partial\xi} + \frac{\partial\{\tilde{G}_1\}}{\partial\eta} + \frac{\partial\{\tilde{H}_1\}}{\partial\varsigma} = \tilde{S}_1 + \tilde{S}_2 \tag{4.121}$$

with: $$\tilde{S}_1 = -ik\tilde{Q}_1, \qquad \tilde{S}_2 = \left[ik\tilde{Q}_2 + \frac{\partial\{\tilde{F}_2\}}{\partial\xi} + \frac{\partial\{\tilde{G}_2\}}{\partial\eta} + \frac{\partial\{\tilde{H}_2\}}{\partial\varsigma} \right] \tag{4.122}$$

The term $\tilde{S}_2$ is related with the deformation of the nets (grids) and the steady condition (of the state vector and fluxes). Because the deformation of the nets and the steady state condition are known; the term $\tilde{S}_2$ can be viewed as a constant component of source term. The term $\tilde{S}_1$ represents the variable component of source term.

The time-linearized state vector and fluxes in Eq. (4.121) and (4.122) can be written as follows [57, 61]:

$$\tilde{Q}_1 = J_0\tilde{q} \tag{4.123a}$$

$$\tilde{F}_1 = [(J\xi_x)_0 \tilde{f} + (J\xi_y)_0 \tilde{g} + (J\xi_z)_0 \tilde{h}] \tag{4.123b}$$

$$\tilde{G}_1 = [(J\eta_x)_0 \tilde{f} + (J\eta_y)_0 \tilde{g} + (J\eta_z)_0 \tilde{h}] \tag{4.123c}$$

$$\tilde{H}_1 = [(J\varsigma_x)_0 \tilde{f} + (J\varsigma_y)_0 \tilde{g} + (J\varsigma_z)_0 \tilde{h}] \tag{4.123d}$$

$$\tilde{Q}_2 = \begin{Bmatrix} \rho \\ \rho u \\ \rho v \\ \rho w \\ e \end{Bmatrix}_0 \tilde{J} \tag{4.123e}$$

$$\tilde{F}_2 = \begin{Bmatrix} \rho_0 U_2 \\ (\rho u)_0 U_2 + \tilde{J}\tilde{\xi}_x p_0 \\ (\rho v)_0 U_2 + \tilde{J}\tilde{\xi}_y p_0 \\ (\rho w)_0 U_2 + \tilde{J}\tilde{\xi}_z p_0 \\ (e_0 + p_0) U_2 - \tilde{J}\tilde{\xi}_t p_0 \end{Bmatrix} \tag{4.123f}$$

$$\tilde{G}_2 = \begin{Bmatrix} \rho_0 V_2 \\ (\rho u)_0 V_2 + \tilde{J}\tilde{\eta}_x p_0 \\ (\rho v)_0 V_2 + \tilde{J}\tilde{\eta}_y p_0 \\ (\rho w)_0 V_2 + \tilde{J}\tilde{\eta}_z p_0 \\ (e_0 + p_0) V_2 - \tilde{J}\tilde{\eta}_t p_0 \end{Bmatrix} \quad (4.123g) \qquad \tilde{H}_2 = \begin{Bmatrix} \rho_0 W_2 \\ (\rho u)_0 W_2 + \tilde{J}\tilde{\zeta}_x p_0 \\ (\rho v)_0 W_2 + \tilde{J}\tilde{\zeta}_y p_0 \\ (\rho w)_0 W_2 + \tilde{J}\tilde{\zeta}_z p_0 \\ (e_0 + p_0) W_2 - \tilde{J}\tilde{\zeta}_t p_0 \end{Bmatrix} \quad (4.123h)$$

The time linearized Euler equations (4.121) can be written in semi-discrete form, as follows:

$$\frac{\partial \{\tilde{Q}_1\}_{k,l,m}}{\partial \tau} = -\tilde{R}_{k,l,m} \tag{4.124}$$

where:

$$\begin{aligned} \tilde{R}_{k,l,m} &= \{\tilde{F}_1\}_{k+1/2,l,m} - \{\tilde{F}_1\}_{k-1/2,l,m} + \{\tilde{G}_1\}_{k,l+1/2,m} - \{\tilde{G}_1\}_{k,l-1/2,m} + \\ &\quad \{\tilde{H}_1\}_{k,l,m+1/2} - \{\tilde{H}_1\}_{k,l,m-1/2} - \{\tilde{S}_1\}_{k,l,m} - \{\tilde{S}_2\}_{k,l,m} \end{aligned} \tag{4.125a}$$

$$\{\tilde{Q}_1\}_{k,l,m} = \overline{V}_{k,l,m} \{\tilde{q}\}_{k,l,m} \tag{4.125b}$$

$$\{\tilde{S}_1\}_{k,l,m} = -ik\{\tilde{Q}_1\}_{k,l,m} \tag{4.125c}$$

$$\{\tilde{S}_2\}_{k,l,m} = -\begin{bmatrix} ik\{\tilde{Q}_2\}_{k,l,m} + \{\tilde{F}_2\}_{k+1/2,l,m} - \{\tilde{F}_2\}_{k-1/2,l,m} + \{\tilde{G}_2\}_{k,l+1/2,m} - \{\tilde{G}_2\}_{k,l-1/2,m} + \\ \{\tilde{H}_2\}_{k,l,m+1/2} - \{\tilde{H}_2\}_{k,l,m-1/2} \end{bmatrix} \tag{4.125d}$$

The indices *k, l* and *m* are the indices of cells in ξ, η and ζ direction.
The solution of eq.(4.124) is solved by using the explicit integration, as already presented in section 4.2.2.

4.3.2. Boundary Conditions

4.3.2.1. Far-Field Boundary Conditions

a. Subsonic Inflow

The linearized density ρ at far-field-boundary can be determined, as follows [57]:

$$\tilde{\rho}_b = \tilde{\rho}_a + \frac{(\tilde{p}_b - \tilde{p}_a)}{\overline{c}^2} \tag{4.126}$$

The linearized pressure p at the far-field-boundary can be determined, as follows [57]:

$$\tilde{p}_b = \frac{1}{2}\left\{(\tilde{p}_a + \tilde{p}_i) \pm \overline{\rho c}\left[\tilde{k}_x(\tilde{u}_a - \tilde{u}_i) + \tilde{k}_y(\tilde{v}_a - \tilde{v}_i)\right]\right\} \tag{4.127}$$

where the sign (+) is for positive *k* direction and sign (–) for negative *k* direction.
The linearized velocity *u* and *v* at far-field-boundary can be determined, as [57]:

$$\tilde{u}_b = \tilde{u}_a \pm \tilde{k}_x \frac{(\tilde{p}_a - \tilde{p}_b)}{\overline{\rho c}} \tag{4.128}$$

$$\tilde{v}_b = \tilde{v}_a \pm \tilde{k}_y \frac{(\tilde{p}_a - \tilde{p}_b)}{\overline{\rho c}} \tag{4.129}$$

where the sign (+) is for positive *k* direction and sign (–) is for negative *k* direction.

b. Subsonic Outflow

The linearized density ρ at far-field-boundary can be determined, as follows [57]:

$$\tilde{\rho}_b = \tilde{\rho}_i + \frac{(\tilde{p}_b - \tilde{p}_i)}{\overline{c}^2} \tag{4.130}$$

The linearized pressure *p* at far-field-boundary becomes:

$$\tilde{p}_b = \frac{1}{2}\left\{\left(\tilde{p}_a + \tilde{p}_i\right) \pm \overline{\rho c}\left[\tilde{k}_x\left(\tilde{u}_i - \tilde{u}_a\right) + \tilde{k}_y\left(\tilde{v}_i - \tilde{v}_a\right)\right]\right\} \tag{4.131}$$

The linearized velocity *u* and *v* become:

$$\tilde{u}_b = \tilde{u}_i \pm \tilde{k}_x \frac{\left(\tilde{p}_i - \tilde{p}_b\right)}{\overline{\rho c}} \tag{4.132}$$

$$\tilde{v}_b = \tilde{v}_i \pm \tilde{k}_y \frac{\left(\tilde{p}_i - \tilde{p}_b\right)}{\overline{\rho c}} \tag{4.133}$$

where the sign (+) is for positive *k* direction and sign (–) is for negative *k* direction.

For supersonic inflow and outflow, the linearized boundary condition is still the same with the given or extrapolated value, as written in section 4.2.3.1

4.3.2.2. Solid Body Boundary Condition

The linearized body boundary condition can be written, as follows [57]:

$$\tilde{\rho}_b = \tilde{\rho}_i + \frac{\left(\tilde{p}_b - \tilde{p}_i\right)}{\bar{c}^{2}} \tag{4.134}$$

$$\tilde{u}_b = \tilde{u}_i - \tilde{k}_x\left(\tilde{k}_x\tilde{u}_i + \tilde{k}_y\tilde{v}_i + \tilde{k}_t\Big|_b\right) \tag{4..135}$$

$$\tilde{v}_b = \tilde{v}_i - \tilde{k}_y\left(\tilde{k}_x\tilde{u}_i + \tilde{k}_y\tilde{v}_i + \tilde{k}_t\Big|_b\right) \tag{4.136}$$

$$\frac{\tilde{p}_b}{\tilde{\rho}_b\bar{c}} = \frac{\tilde{p}_i}{\tilde{\rho}_i\bar{c}} \mp \left(\tilde{k}_x\tilde{u}_i + \tilde{k}_y\tilde{v}_i + \tilde{k}_t\Big|_b\right) \tag{4.137}$$

where the sign (+) is for negative *k* direction and sign (–) is for positive *k* direction.

More information about the time-linearized Euler equations, its boundary conditions and its application for wing can be found in Refs. [62, 63].

5. Flutter Analysis

In this chapter the flutter analysis in the time domain is presented. The aeroelastic equation is written in term of physical displacement and then will be transformed by means of the concept generalized displacement. Finally the aeroelastic equation in generalized displacement is transformed into State Space equation, which can be integrated exactly and approximately, in order to compute the response of the structure in time domain. The flutter speed is determined, if the response of the structure shows neutral response as function of the time.

5.1. Aeroelastic Equation in the Physical Displacement

The aeroelastic equation is derived by energy analysis as in the following. The structure is regarded as a dynamic system of mass (*m*), damping (*c*) and stiffness (*k*). As the starting point is the Lagranges equation, which can be written as [64]:

$$\frac{d}{dt}\left(\frac{\partial E_k}{\partial \dot{z}}\right)-\left(\frac{\partial E_k}{\partial z}\right)+\left(\frac{\partial E_p}{\partial z}\right)+\left(\frac{\partial F_d}{\partial \dot{z}}\right)=F_o \tag{5.1}$$

where E_k, E_p, F_d and F_0 are kinetic energy, strain energy, damping force and external aerodynamic force, respectively. z is the physical displacement of the dynamic system as function of space (x,y) and time (t), $z = f(x,y,t)$. $\dot{z}$ is the time derivative of the physical displacement.

The kinetic energy is defined as: $$E_k = \frac{1}{2}m\left(\dot{z}\right)^2 \tag{5.2}$$

The strain/potential energy is given by: $$E_p = \frac{1}{2}kz^2 \tag{5.3}$$

The damping force from the Rayleigh's dissipation function is: $$F_d = \frac{1}{2}c\left(\dot{z}\right)^2 \tag{5.4}$$

Inserting E_k, E_p and F_d into Lagrange's equation, one can obtain the aeroelastic equation in physical displacement as follows:

$$m\ddot{z}+c\dot{z}+kz=F_o \tag{5.5}$$

The aeroelastic equation (5.5) for multi Degree of Freedom (DOF) can be written in matrix as:

$$[m]\left\{\ddot{z}\right\}+[c]\left\{\dot{z}\right\}+[k]\{z\}=\{F_o\} \tag{5.6}$$

It could be happened that the matrices [*m*], [*c*] or [*k*] are coupled. It depends on the characteristic of the structure. A system with coupled mass or stiffness matrix is known as dynamically or statically coupled system.

5.2. Aeroelastic Equation in the Generalized Displacement

The physical displacement is assumed as sum of the undefinitely free mode of motion (mode shapes) multiplied by the generalized displacement. With the separation variable technique of time (*t*) and space function (*x*,*y*), the physical displacement can be described as: [65]

$$z(x,y,t)=\sum_{i=1}^{\infty}\Phi_i(x,y)q_i(t) \tag{5.7}$$

where : Φ_i = the mode of motion (mode shape) of the structure for the mode *i*
q_i = the generalized displacement for the mode *i*

In matrix notation, equation (5.7) becomes to:

$$\{z\} = [\Phi]\{q\} \tag{5.8}$$

The generalized displacement represents the contribution of the individual free oscillation form in the physical displacement. The mode of motion (vibration mode shape) can be obtained by performing the modal analysis of the dynamic structure.

The aeroelastic equation (5.6) is transformed in term of the generalized displacement by substituting equation (5.8) into equation (5.6):

$$[m][\Phi]\left\{\ddot{q}\right\} + [c][\Phi]\left\{\dot{q}\right\} + [k][\Phi]\{q\} = \{F_o\} \tag{5.9}$$

Multiplying equation (5.9) with the transpose of mode shape matrix $[\Phi]^T$, one obtains:

$$[M]\left\{\ddot{q}\right\} + [C]\left\{\dot{q}\right\} + [K]\{q\} = \{Q\} \tag{5.10}$$

where:

$[M] = [\Phi]^T[m][\Phi]$ = the generalised mass matrix

$[C] = [\Phi]^T[c][\Phi]$ = the generalised damping matrix

$[K] = [\Phi]^T[k][\Phi]$ = the generalised stiffness matrix

$\{Q\} = [\Phi]^T\{F_0\}$ = the generalised aerodynamic forces

The forms of the generalized matrices [*M*], [*C*] and [*K*] are diagonal because of the Orthogonality of the vibration mode shapes matrix. The relationship between the generalized mass, damping and stiffness are [65, 66]:

$$[K] = \left[\omega_n^2 M\right] \qquad \left[\omega_n^2\right] = [M]^{-1}[K] \qquad [C] = [2\varsigma][K]^{1/2}[M]^{1/2} \tag{5.11}$$

where :

ω_n = natural frequency of the vibration mode

ζ = damping coefficient of the vibration mode

The generalized aerodynamic forces can be written as follows [65, 66]:

$$Q_i = \frac{1}{2}\rho_\infty U_\infty^2 \int \Delta Cp(x,y,t)\Phi_i(x,y)dS \tag{5.12}$$

Finally the equation (5.10) can be written as follows:

$$\left\{\ddot{q}\right\} = -[M]^{-1}[K]\{q\} - [M]^{-1}[C]\left\{\dot{q}\right\} + [M]^{-1}\{Q\} \tag{5.13}$$

5.3. Aeroelastic Equation in the State Space Form

The equation (5.13) is transformed into State Space form, as follows [66]:

$$\begin{Bmatrix} \dot{q} \\ \ddot{q} \end{Bmatrix} = \begin{bmatrix} 0 & [I] \\ -[M]^{-1}[K] & -[M]^{-1}[C] \end{bmatrix} \begin{Bmatrix} q \\ \dot{q} \end{Bmatrix} + \begin{bmatrix} 0 & 0 \\ 0 & [M]^{-1} \end{bmatrix} \begin{Bmatrix} 0 \\ Q \end{Bmatrix} \tag{5.14}$$

The equation (5.13) lies in the second row of the equation (5.14). The first row of the equation (5.14) works as a dummy equation.

The equation (5.14) can be written briefly as:

$$\left\{\dot{X}\right\} = [A]\{X\} + [B]\{u\} \tag{5.15}$$

with the State Vectors {*X*} and {*u*} and the State Transition matrices [*A*] and [*B*] as the following:

$$\left\{X\right\}=\begin{Bmatrix} q \\ \dot{q} \end{Bmatrix},\quad \left\{\dot{X}\right\}=\begin{Bmatrix} \dot{q} \\ \ddot{q} \end{Bmatrix},\quad \{u\}=\begin{Bmatrix} 0 \\ Q \end{Bmatrix},\quad [B]=\begin{bmatrix} 0 & 0 \\ 0 & [M]^{-1} \end{bmatrix}$$

$$[A]=\begin{bmatrix} 0 & [I] \\ -[M]^{-1}[K] & -[M]^{-1}[C] \end{bmatrix}=\begin{bmatrix} 0 & [I] \\ -\left[\omega_n^2\right] & -\left[2\varsigma\omega_n\right] \end{bmatrix} \tag{5.16}$$

5.4. Solution of the Aeroelastic Equation

The aeroelastic equation in State Space form is solved in time domain. The equation (5.15) is integrated in time domain, in order to compute the response of the system, as follows [66]:

$$\{X(t)\}=\exp[At]\{X_0\}+\int_0^t \exp[A(t-\tau)][B]\{u(\tau)\}d\tau \tag{5.17}$$

where: $\{X(t)\}$ = response of the system at time t

$\{X_0\}$ = the initial values of $\{X\}$

The first and the second term of the equation (5.17) is the Homogeneous and the Non Homogeneous solution of the equation (5.15) respectively.

In discrete form, the solution is carried out recursively from time step n to (n+1), as follows:

$$\{X(n+1)\Delta t\}=\exp[A\Delta t]\{X(n\Delta t)\}+\int_{n\Delta t}^{(n+1)\Delta t}\exp[A((n+1)\Delta t-\tau)][B]\{u(\tau)\}d\tau \tag{5.18}$$

where Δt the time step is.

The Homogeneous solution is solved exactly, as follows [67]:

$$\begin{aligned} L_h &= \exp[A\Delta t]\{X(n\Delta t)\} \\ &= [\psi]\left\{X^n\right\}=\begin{bmatrix} \psi_{11} & \psi_{12} \\ \psi_{21} & \psi_{22} \end{bmatrix}\left\{X^n\right\} \end{aligned} \tag{5.19}$$

with ψ_{11}, ψ_{12}, ψ_{21} and ψ_{22} as follows [67]:

$$\begin{aligned} \psi_{11} &= e^{-[\varsigma\omega_n]\Delta t}\left\{\cos\left[\omega_n(1-\varsigma^2)^{1/2}\Delta t\right]+\varsigma(1-\varsigma^2)^{-1/2}\sin\left[\omega_n(1-\varsigma^2)^{1/2}\Delta t\right]\right\} \\ \psi_{12} &= e^{-[\varsigma\omega_n]\Delta t}\omega_n^{-1}(1-\varsigma^2)^{-1/2}\sin\left[\omega_n(1-\varsigma^2)^{1/2}\Delta t\right] \\ \psi_{21} &= -e^{-[\varsigma\omega_n]\Delta t}\omega_n(1-\varsigma^2)^{-1/2}\sin\left[\omega_n(1-\varsigma^2)^{1/2}\Delta t\right] \\ \psi_{22} &= e^{-[\varsigma\omega_n]\Delta t}\left\{\cos\left[\omega_n(1-\varsigma^2)^{1/2}\Delta t\right]-\varsigma(1-\varsigma^2)^{-1/2}\sin\left[\omega_n(1-\varsigma^2)^{1/2}\Delta t\right]\right\} \end{aligned} \tag{5.20}$$

The Non Homogeneous solution is approximated, because the value of $\{u\}$ are not known in the time interval from nt to (n+1)t. It is assumed that the value of $\{u\}$ are linear in these time interval [66].

$$\begin{aligned} L_{nh} &= \int_{n\Delta t}^{(n+1)\Delta t}\exp[A((n+1)\Delta t-\tau)][B]\{u(\tau)\}d\tau \\ &= [\theta][B]\left(\left\{u^{n+1}\right\}+\left\{u^n\right\}\right)/2 \end{aligned} \tag{5.21}$$

where:

$$\begin{aligned} [\theta] &= \int_{n\Delta t}^{(n+1)\Delta t}\exp[A((n+1)\Delta t-\tau)]d\tau=[A]^{-1}\exp[A\tau]_0^{\Delta t} \\ &= \begin{bmatrix} -2\varsigma/\omega_n & -\omega_n^{-2} \\ 1 & 0 \end{bmatrix}[\psi]_0^{\Delta t}=\begin{bmatrix} \theta_{11} & \theta_{12} \\ \theta_{21} & \theta_{22} \end{bmatrix} \end{aligned} \tag{5.22}$$

with θ_{11}, θ_{12}, θ_{21} and θ_{22} are as follows [55]:

$$\theta_{11} = e^{-[\varsigma\omega_n]\Delta t}\left\{\frac{-2\varsigma}{\omega_n}\cos\left[\omega_n(1-\varsigma^2)^{1/2}\Delta t\right] + \left(\frac{1-2\varsigma^2}{\omega_n\left(1-\varsigma^2\right)^{1/2}}\right)\sin\left[\omega_n(1-\varsigma^2)^{1/2}\Delta t\right]\right\} + \frac{2\varsigma}{\omega_n}$$

$$\theta_{12} = -e^{-[\varsigma\omega_n]\Delta t}\left\{\frac{\varsigma}{\omega_n^2(1-\varsigma^2)^{1/2}}\sin\left[\omega_n(1-\varsigma^2)^{1/2}\Delta t\right] + \frac{1}{\omega_n^2}\cos\left[\omega_n(1-\varsigma^2)^{1/2}\Delta t\right]\right\} + \frac{1}{\omega_n} \qquad (5.23)$$

$$\theta_{21} = -e^{-[\varsigma\omega_n]\Delta t}\left\{\frac{\varsigma}{(1-\varsigma^2)^{1/2}}\sin\left[\omega_n(1-\varsigma^2)^{1/2}\Delta t\right] + \cos\left[\omega_n(1-\varsigma^2)^{1/2}\Delta t\right]\right\} - 1 = \psi_{11} - 1$$

$$\theta_{22} = e^{-[\varsigma\omega_n]\Delta t}\omega_n^{-1}(1-\varsigma^2)^{-1/2}\sin\left[\omega_n(1-\varsigma^2)^{1/2}\Delta t\right] = \psi_{12}$$

Since the value of $\{u^{n+1}\}$ are not yet known, it will be approximated from the previous time step, as follows [66]:

$$\left\{u^{n+1}\right\} \cong \left\{u^{n}\right\} + \left[\left\{u^{n}\right\} - \left\{u^{n-1}\right\}\right] \qquad (5.24)$$

With these approximation, the Non Homogeneous solution becomes to (by inserting eq. 5.24 into eq. 5.21):

$$L_{nh} = [\theta][B]\left(\left\{3u^{n}\right\} - \left\{u^{n-1}\right\}\right)/2 \qquad (5.25)$$

The complete solution can now be written as the following:

$$\left\{X^{n+1}\right\} = [\psi]\left\{X^{n}\right\} + [\theta][B]\left(\left\{3u^{n}\right\} - \left\{u^{n-1}\right\}\right)/2 \qquad (5.26)$$

The above procedure is known as Transition Matrix Method for aeroelastic calculation.

5.5. Boundary Condition for Aeroelastic Coupling

The tangential boundary condition of the aerodynamic calculation must be modified for aeroelastic analysis. The boundary condition contains both steady and unsteady part involving the elastic or the flexible vibration mode shapes.

For the TSD equation, the tangential boundary condition for aeroelastic analysis is formulated as follows [65]:

$$\phi_z^{\pm} = f_{x\ R}^{\pm}\,|_{St} + \left[f_x^{\pm} + f_t^{\pm}\right]_R |_{Ust} + \left[f_x^{\pm} + f_t^{\pm}\right]_F |_{Ust} \qquad (5.27)$$

where:

$\phi_z^{\pm}$ = down wash disturbance (component of speed in vertical *z* direction) or derivative of disturbance potential in z direction of the upper (+) and lower (-) surface of the wing.

$f_{x\ R}^{\pm}\,|_{St}$ = Slope of the upper (+) and lower (-) surface (*f*) in steady (*St*) Rigid Body Motion (*R*).

$\left[f_x^{\pm} + f_t^{\pm}\right]_R |_{Ust}$ = Slope of the upper (+) and lower (-) surface (*f*) in unsteady (*Ust*) Rigid Body Motion (*R*).

$\left[f_x^{\pm} + f_t^{\pm}\right]_F |_{Ust}$ = Slope of the upper (+) and lower (-) surface (*f*) in unsteady (*Ust*) Flexible/Elastic Motion (*F*).

The steady part associates with the rigid geometry of the wing and angle of attack. The unsteady rigid body motion part associates with the pitching and heaving oscillation of the wing.

The unsteady flexible motion part represents the vibration mode shapes of the wing, as follows [65]:

$$\left[f_x^{\pm} + f_t^{\pm}\right]_F |_{Ust} = [\Phi_x]\{q\} + \frac{1}{U_\infty}[\Phi]\left\{\dot{q}\right\} \qquad (5.28)$$

where: $[\Phi_x]$ = slope of the vibration mode shapes

$\{q\}$ = the generalized displacement

$\left\{\dot{q}\right\}$ = the time derivative of the generalized displacement

It should be noted that the tangential boundary condition is always corrected with the presence of the boundary layer and slope modification as already discussed in the previous chapter.

The steps for the flutter analysis can be written as follows:

1. Determination of the structural data.
   In order to form the mass, damping and stiffness matrices ($[m]$, $[c]$ and $[k]$) of the structure.
2. Modal analysis of the dynamic system.
   In order to obtain the vibration mode shapes $[\Phi]$ and the natural frequencies $[\omega_n]$.
3. Computation of the generalized mass -, damping and stiffness matrices ($[M]$, $[C]$ and $[K]$)
4. Building of the State Space matrices:
   The State Transition matrix $[A]$, $[B]$ and the initial values $\{X^n\}$
5. Computation of the steady aerodynamic forces $\{Q\}_{St}$ for a certain Mach number and angle of attack and other steady parameter with steady boundary condition
6. Computation of the response of the system $\{X^{n+1}\}$ by means of solution of the State Space equation for a certain given Mach number, speed (U_∞) and dynamic pressure ($0.5\rho_\infty U_\infty^2$), with the following step:
   - computation of the tangential boundary condition, i.e. equation (5.27) with input data: $\{X^n\}$, $[\alpha]$ and other parameter.
   - computation of the aerodynamic forces ($\{Q\}_{Ust}$ as time-dependent function) with input data: speed, dynamic pressure and the tangential boundary condition.
   - solving the State Space equation by means of the equation (5.26) to obtain the response at the next time step: $\{X^{n+1}\}$
   - repeating these steps until 3 or 4 cycles of the oscillation
   - analysis of the response system whether the process of the response is under damped, neutral or divergent.

The flutter speed is defined, if the behaviour of the response in the time domain is neutral. If the response is under damped, the speed and the dynamic pressure must be increased and the response system must be calculated again. Fig. 5.1. shows the flow chart of the flutter analysis in time domain by means of State Space equation

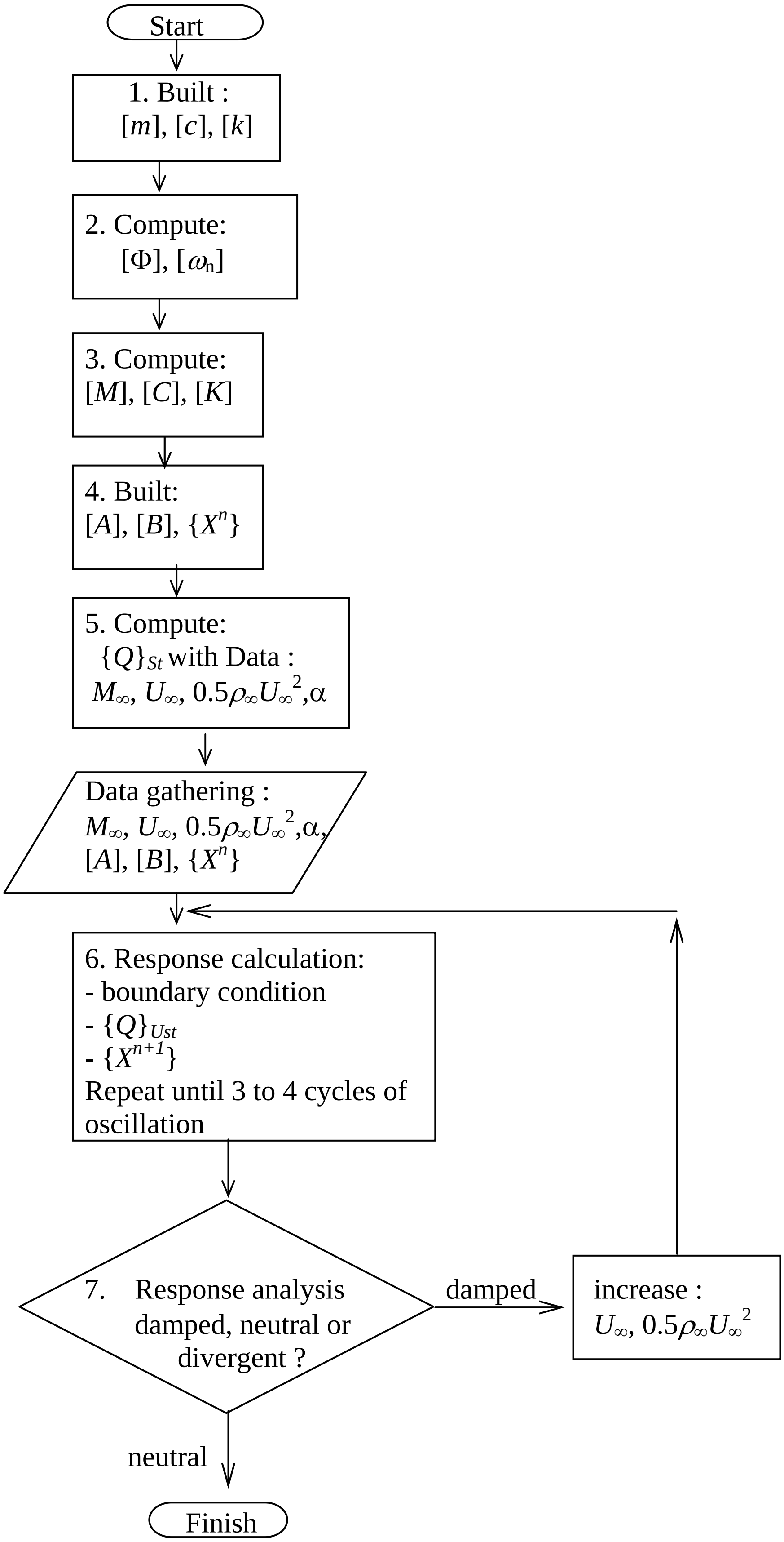

Fig. 5.1. Flow Chart of Flutter Analysis in the Time Domain

6. Steady and Unsteady Aerodynamic Results

In this chapter some steady and unsteady aerodynamic results calculated with and without the developed viscous - inviscid interaction method are presented. In order to have a systematic representation, this chapter is divided into three sub chapter.
The first part of this chapter serves for validating of the inviscid model, the viscous model and the transition model as individual model. The validation work is carried out by comparing the computational results either with other numerical results or experimental data. In the second part of this chapter, the developed viscous - inviscid interaction method is used to compute some steady cases. Results for attached as well as separated flow around airfoils and axis-symmetric body are presented. The last part of this chapter presents some results of unsteady cases of airfoils and wings, which oscillate harmonically in an uniform flow.

6.1. Validation

6.1.1. Validation of the Inviscid Aerodynamic Model

The problem concerned with the aerodynamic simulation in transonic flow is the appearance of the shock, which must be simulated both its position and its strength correctly. Therefore an aerodynamic Code must absolutely have the ability for the computation of the shock. Here the results of the developed inviscid aerodynamic model (TSD) are presented for AGARD two dimensional (2D) test case CT1 [68] with the following data:

Airfoil : NACA 0012
Mach number : $M = 0.8$
Angle of attack : $\alpha = 1.25$ Grad

This case is one of eight AGARD 2D test cases for validating the inviscid model. This case is selected because of the appearance of a strong shock on the upper surface and a weak one on the lower surface. The objective of this test case is to test the sensitivity of an aerodynamic Code against the appearance of a strong as well as a weak shock.

The computed pressure and Mach distribution for this case are shown in Figs. 6.1. and 6.2. As reference data are the result of the Euler Code of Institute of Fluid Mechanics Technische Universität München (called FLMEu Code) and the result of the Euler Code from Jameson [68]. For the simulation of this case the computational space is discretised in (160x30) points for TSD Code and (180x30) cells for FLMEu Code. The cells on the airfoil surface (upper and lower) consist of 120 cells. The edge of far field is chosen to be 10 times of chord of airfoil. The Off-Body distance is 10^{-4} times of chord of airfoil.

The improvement of the TSD Code from the original one can be seen clearly in Fig. 6.1. The original TSD Code (TSD orig) can not compute the shock position and shock strength correctly. On the upper surface the position of the shock is too far aft compared with the other results. On the lower surface the TSD original Code gives no shock. The shock was absorbed too much. At the leading edge appears also a peak suction, which has no physical meaning. By the developed TSD (TSD present) the pressure distribution on both surfaces agrees well with the reference data. The shock on lower surface calculated using the developed TSD method is a little bit weaker compared with the results from Jameson and FLMEu. The shock position and also the Mach contour can be seen in fig. 6.2. The position of both shocks from the developed TSD is in good agreement with the FLMEu results. Differences between both Mach contour results are in the leading and trailing edge region.

The lift, drag and moment coefficients for this case can be seen in Table 6.1. The deviation of the lift, drag and moment coefficients between the TSD results (present and original) and the mean values of the Euler results can be seen in table 6.2.
Other validation results can be found in Ref. [55].

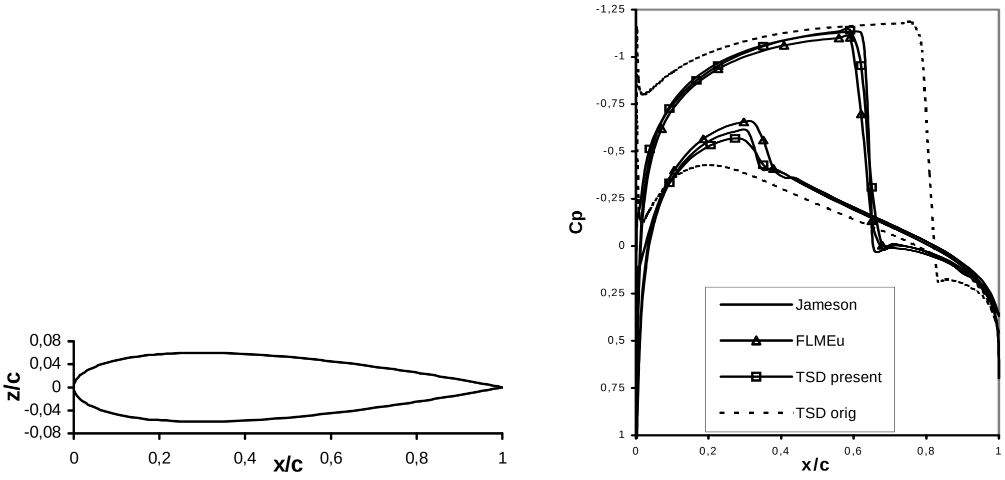

(a) Geometry of NACA 0012 airfoil (b) Pressure distribution

Fig. 6.1. Geometry and Pressure Distribution of NACA 0012 at M = 0.8, α = 1.25 deg

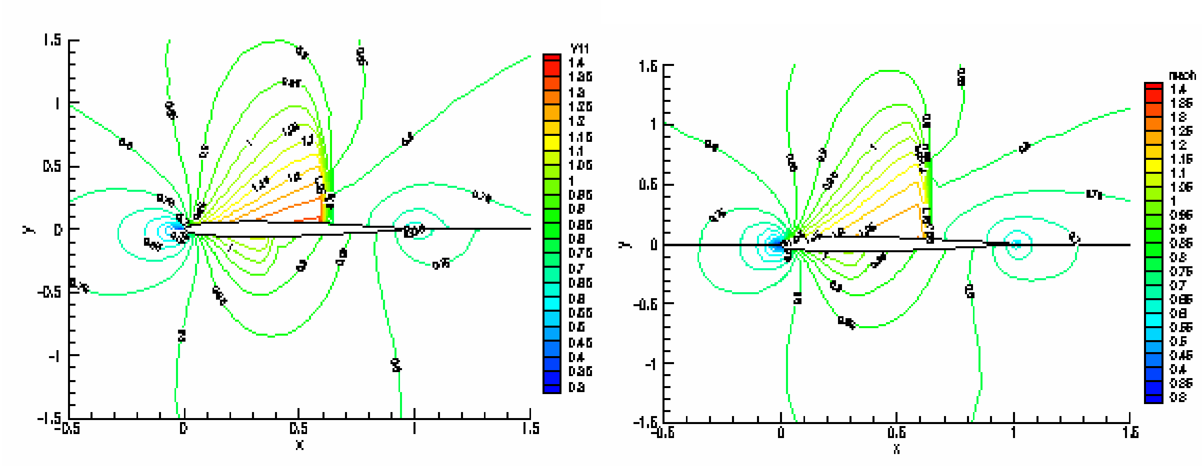

(a) FLMEu (b) TSD

Fig. 6.2. Mach Contour of NACA 0012 at M = 0.8, α = 1.25 deg

Table 6.1. Lift, Drag and Moment Coefficients of NACA 0012 at M = 0.8, α = 1.25 deg

	Cl	Cd (drag count)	Cm	Mesh	Grid Type
Jameson (Euler)	0.3632	230	-0.0397	320 x 64	O
FLMEu (Euler)	0.3486	221	-0.0358	180 x 30	C
TSD-Present	0.3593	229	-0.0389	160 x 30	H (Cartesian)
TSD-orig	0.6586	476	-0.1334	160 x 30	H (Cartesian)
Mean value of the Euler results	0.3559	225.5	-0.03775		

1 drag count = 0.0001

Table 6.2. Deviation of Lift, Drag and Moment Coefficients from the Mean Values of Euler NACA 0012 at M = 0.8, α = 1.25 deg

	$\Delta Cl/Cl_{mean}$	$\Delta Cd/Cd_{mean}$	$\Delta Cm/Cm_{mean}$
TSD-Present	0.96%	1.55%	3.05%
TSD-orig	85.05%	111.05%	253.38%

6.1.2. Validation of the Viscous Models

Validation of the boundary layer calculation methods developed here are presented in this sub chapter. Incompressible laminar and turbulent flow on a flat plate are selected as test cases.

6.1.2.1. Flat Plate in Incompressible Laminar Flow

The flow parameters are as follows:

Mach number : M = 0.
Angle of attack : $\alpha = 0.$ deg
Reynolds number : Re = 1.0 E+05 (based on the plate length)

Three different boundary layer methods, i.e. Karman-Thwaites, Drela-Giles and Differential Methods, are validated with the exact solution of Blasius [5] as reference. In order to implement the Drela-Giles Method, the Karman-Thwaites procedure must be used as initial values. After 3%-5% of the plate length from the leading edge, the Drela-Giles method can then be implemented. The distribution of the displacement thickness and skin friction are depicted in figure 6.3. All the three methods show good agreement for this case.
A small modification in the skin friction closure equation of Drela-Giles Method is carried out as follows:

from :
$$for\ H_k < 5.5 \quad C_f = \left[0.0762\frac{(5.5-H_k)^3}{(H_k+1)} - 0.067\right]\frac{1}{\mathrm{Re}_q} \tag{3.38a.}$$

change into :
$$for\ H_k < 5.5 \quad C_f = \left[0.0727\frac{(5.5-H_k)^3}{(H_k+1)} - 0.07\right]\frac{1}{\mathrm{Re}_q} \tag{6.1}$$

The reason of this modification is to increase the growth of the shape factor and the momentum thickness (see equations 3.30 and 3.31). With the original equation (3.38a.) the value of the shape factor H became smaller than those of Blasius and Karman-Thwaites results. A small value of shape factor causes a small value of displacement thickness.

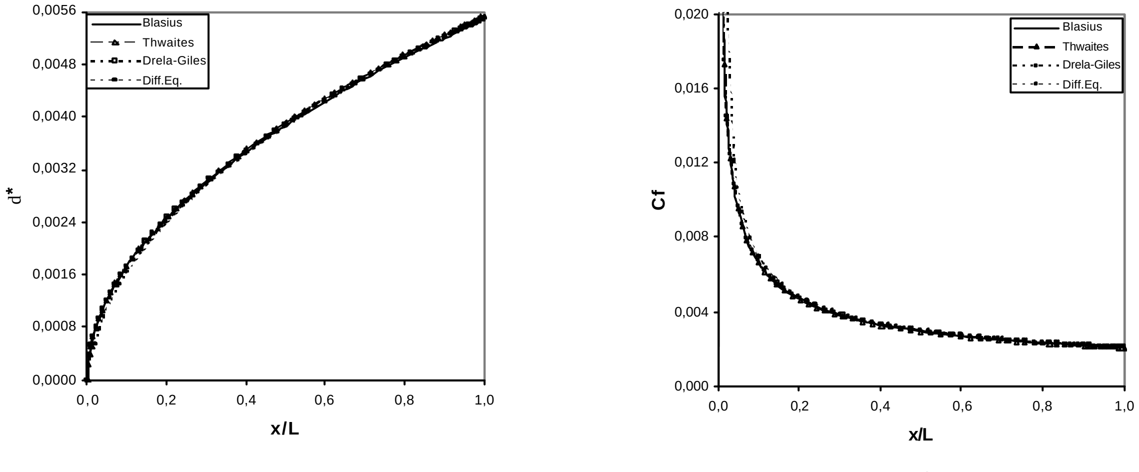

(a) Displacement thickness (b) Skin friction

Fig. 6.3. Displacement Thickness and Skin Friction of a Flat Plate at M = 0., $\alpha = 0.$, Re = 1.0E+05

6.1.2.2. Flat Plate in Incompressible Turbulent Flow

The flow parameters are as follows:

Mach number : M = 0.
Angle of attack : $\alpha = 0.$ deg
Reynolds number : Re = 1.0 E+07 (based on the plate length)

Three different boundary layer methods, i.e. Differential equation, Drela-Giles and Greens Lag Entrainment Methods, will be compared with the solution of Power 1/7 Law as reference. The solution of the Power 1/7 Law will be used as initial values to start calculation with the Drela-Giles and the Greens methods. After 3%-5% of the plate length from the leading edge the Drela-Giles and Green methods can then be started.

The displacement thickness and skin friction distribution can be seen in figure 6.4. In general all methods are in good agreement. The Drela-Giles method supplies a little bit larger skin friction and displacement thickness compared with the results from Green method and Power 1/7 Law. The differential method supplies larger skin friction than those from other methods at the leading and trailing edge region.

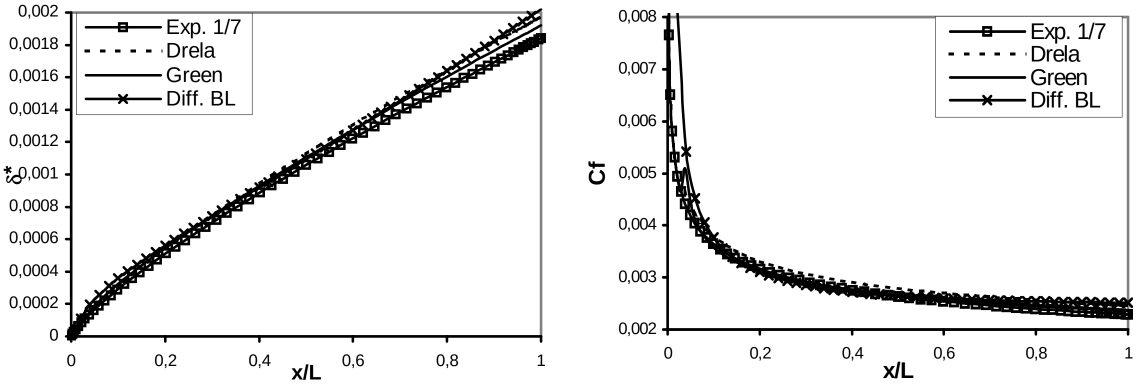

(a) Displacement thickness (b) Skin friction

Fig. 6.4. Displacement Thickness and Skin friction of a Flat Plate
at M = 0., α = 0., Re = 1.0E+07

6.1.3. Validation of the Transition Prediction Method

This sub chapter serves for validating of the e^n transition prediction method with experimental data and other numerical methods. Two cases are selected, i.e. transition flow on a flat plate and around NACA 0012 airfoil.

6.1.3.1. Flat Plate with Laminar-Turbulent Transition

The flow parameters are as follows:

Mach number : M = 0.
Angle of attack : α = 0. deg
Reynolds number : Re = 1.7E+06 /m

As reference data is the experimental data from Schubauer and Klebanoff [5, 69]. The experiment from Schubauer and Klebanoff discovers a transition region approximately between 1.75 m to 2.5 m from leading edge of the plate. This transition region corresponds with the Reynolds number between 3.0E+06 to 4.2Ë+06. Figure 6.5. represents the shape factor and skin friction. In this simulation two different boundary layer methods are used, i.e. Drela-Giles and Thwaites-Green methods. In the Thwaites-Green method the laminar and the turbulent region was simulated with the Karman-Thwaites and Greens Lag Entrainment method respectively, because the Karman-Thwaites method has no turbulent closure equations and the Greens method has no closure equations for laminar flow. The Drela-Giles method has closure equations for both laminar and turbulent flows.

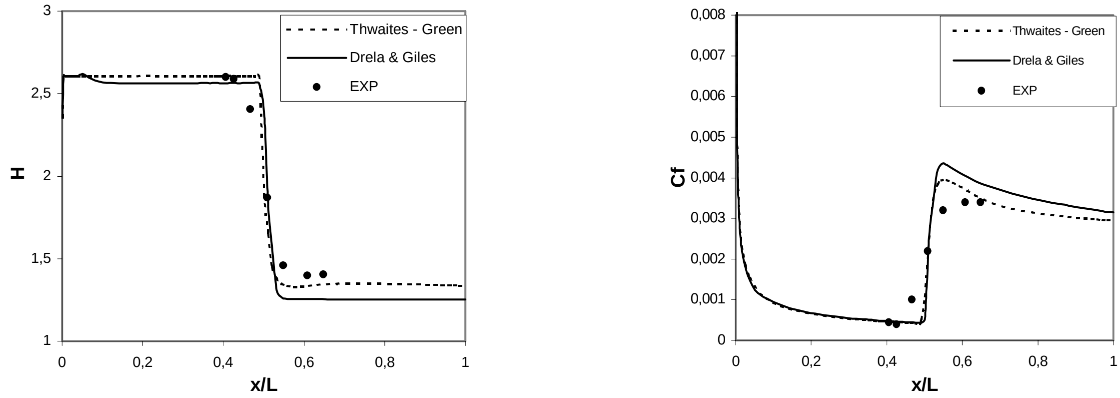

(a) Shape factor (b) Skin Friction

Fig. 6.5. Shape Factor and Skin Friction of a Flat Plate at M = 0., α = 0., Re = 1.7E+06/m

In this simulation the length of the plate is 3.75 m, which correspond to the Reynolds number 6.37Ë+06. From fig. 6.7 it can be seen that the e^n method could compute the transition region very well. The computation result shows sharper and narrower transition region compared with the experimental data. In fig. 6.5a. the computed shape factor of the Drela-Giles method is smaller than experiment data. The shape coefficient of the Thwaites-Green method agrees with the experiment data in the laminar region, but it is smaller than the experiment data in the turbulent region. The value of the laminar and turbulent shape factor from the experiment is 2.6 and 1.4 respectively. In fig. 6.5b. the numeric and experimental values of the skin friction show good agreement in the laminar region, but the computed skin friction are larger than the experiment data in the turbulent region.

6.1.3.2. NACA 0012 Airfoil with Laminar-Turbulent Transition

The flow parameters are as follows:

Mach number	: M = 0.5
Angle of attack	: α = 0. deg
Reynolds number	: Re = 2.89E+06 (based on chord length)

The experimental data of Thibert, Grandjacques and Bateman [70] will be used as reference for the pressure distribution. The numerical data from Wolles [4] serves as reference for the displacement thickness and skin friction distribution. Wolles has performed his calculation using simultaneously viscous - inviscid interaction. The Full Potential equation is used as inviscid model and the Drela-Giles method with the e^n transition method as viscous model. The goal of this simulation is to examine the influence of one boundary layer method (here is the Drela-Giles method) into different inviscid models (here are the TSD and Euler equations) and also the influence of different boundary layer methods (here are the Thwaites-Green and Drela-Giles methods) into one inviscid model (here is the TSD equation).

The results of the pressure, displacement thickness and skin friction distribution calculated using coupled TSD and FLMEu with the Drela-Giles boundary layer method are presented in fig. 6.6.

From experiment it is found that the transition region is laid from 40% to 50% chord from the leading edge. The experimental pressure distribution shows irregular values in this transition region as shown also by the numerical solutions. Between the TSD+BL and the FLMEu+BL results there is a small deviation in the pressure distribution from leading edge up to 40% chord (see fig. 6.6a.). The transition region can be recognised also from the skin friction distribution. The skin friction solutions of TSD+BL and FLMEu+BL show also the transition region from 40% to 50% chord (see fig.6.6c.).

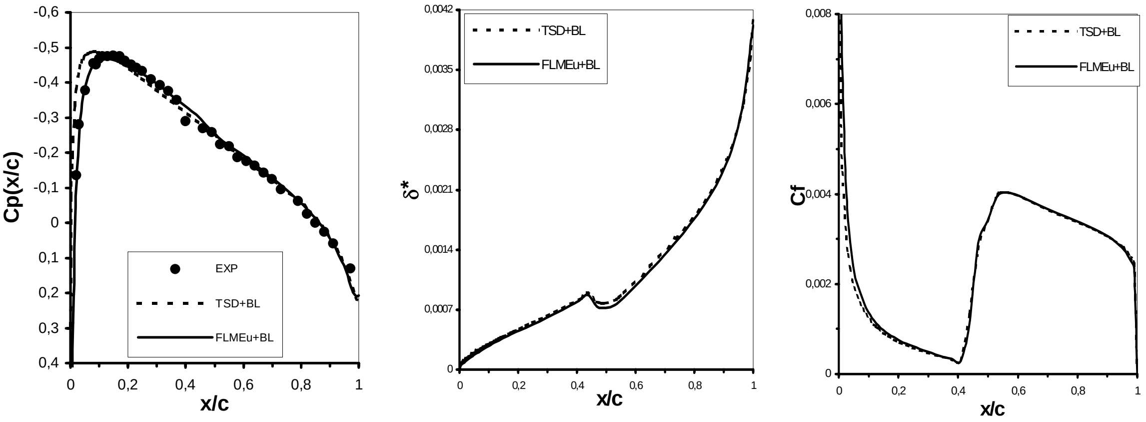

(a) Pressure (b) Displacement thickness (c) Skin friction

Fig. 6.6. Pressure, Displacement Thickness and Skin Friction of NACA 0012 at M = 0.5, α = 0., Re = 2.89E+05 (Comparison between TSD+Boundary Layer and Euler+Boundary Layer)

The displacement thickness and skin friction distribution, which are computed using coupled TSD + Thwaites-Green and TSD + Drela-Giles methods, can be seen in fig. 6.7. The TSD + Thwaites-Green method gives an earlier transition region compared with the result from TSD + Drela-Giles method. The transition region predicted by both of methods show good agreement with the experimental results (laid between 40%-50% chord from leading edge). Compared to the Wolles result, both of methods (TSD + Thwaites-Green and TSD + Drela-Giles) supply an earlier transition region. The skin friction calculated with TSD + Drela-Giles is larger than those from TSD + Thwaites-Green in the turbulent region.

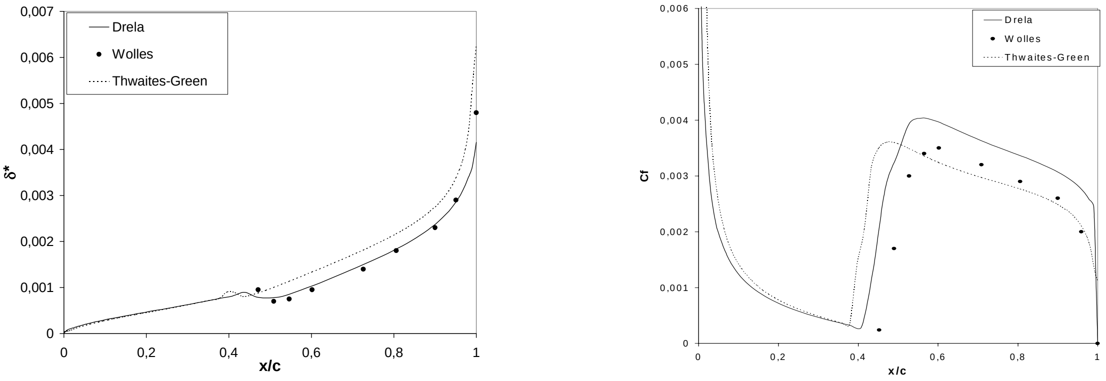

(a) Displacement Thickness (b) Skin Friction

Fig. 6.7. Displacement Thickness and Skin Friction Distribution of NACA 0012 at M = 0.5, α = 0., Re = 2.89E+05 (Comparison between TSD+Thwaites-Green and TSD+Drela-Giles Methods)

The above validating results have been partly published in ‘*Indo-German Conference 2001*’ and in ‘*Jurnal Sains dan Teknologi Aeronotika*‘ (the Journal of the Indonesian Association of the Aerodynamics Specialists) [71].

6.2. Steady Aerodynamic Results

After the validation of the individual model (i.e. viscous, inviscid and transition models) has been performed, the developed viscous - inviscid interaction method will be used to investigate some steady cases. The selected cases must represent some physical flow conditions such as attached flow, flow with separation bubble and shock-induced separated flow. The method is also used to investigate the flow around an axis-symmetrical body.

6.2.1. Transonic Attached Flow

The flow around airfoil RAE 2822 with the following flow parameters is examined:

Mach number	: M = 0.725
Reynolds number	: Re = 6.5E+06 (based on chord)
Angle of attack	: α = 2.42 deg

This case is known as CT6 case in AGARD [72] and was selected as one of five test cases for codes validation in '**V**iscous **T**ransonic **A**irfoil (**VTA**) Workshop 1987' [73]. The numerical results obtained from the present VII method are compared with the experimental data from Cook, McDonald, and Firmin [72]. The angle of attack in the experiment is 2.92 degrees (uncorrected) with lift coefficient C_l equals to 0.743. In order to obtain the same lift coefficient as those in experiment, the angle of attack in this simulation must be reduced to 2.42 degrees. The TSD and FLMEu equations coupled with boundary layer calculation method from Drela-Giles are used to calculate this case. The simulation is carried out using (180x30) cells and (160x30) points for FLMEu and TSD Codes respectively. The flow condition is assumed to be fully turbulent. Figures 6.8 and 6.9. show the geometry, pressure, displacement thickness and skin friction distribution.

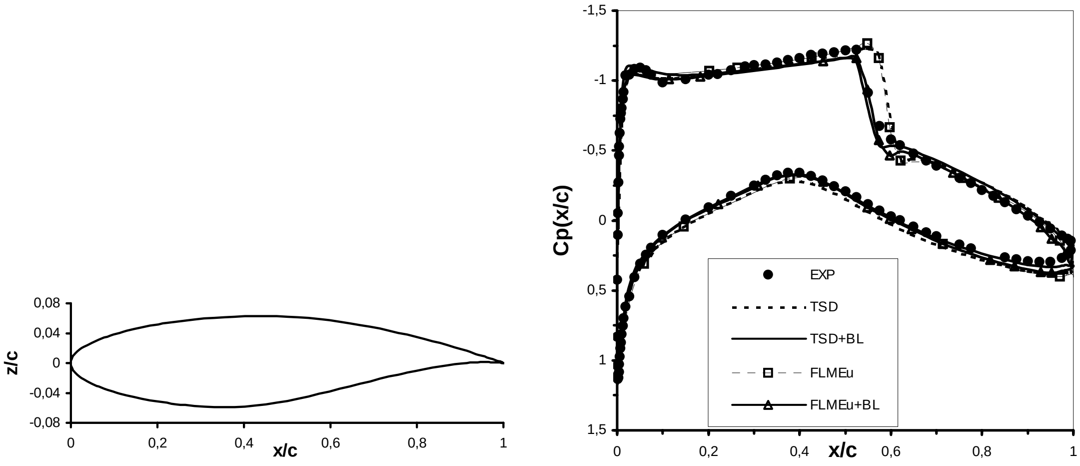

(a) Geometry (b) Pressure Distribution

Fig. 6.8. Geometry and Pressure Distribution of RAE 2822 Airfoil at M = 0.725, Re = 6.5E+06, α = 2.42 deg

One can see from fig. 6.8 that the pressure distribution calculated using VII method agrees well with the experimental data. Small deviation can be seen in the shock region on the upper surface and trailing edge on the lower surface. The displacement thickness increases sharply in the shock region as can be seen in fig. 6.9a. Conversely the skin friction decreases sharply in the shock region as depicted in fig. 6.9b. The displacement thickness calculated using FLMEu+Boundary layer (FLMEu+BL) is closer to the experimental results compared with those from TSD+Boundary layer. Conversely the skin friction calculated using TSD+Boundary layer (TSD+BL) seems to be closer to the experiment results.

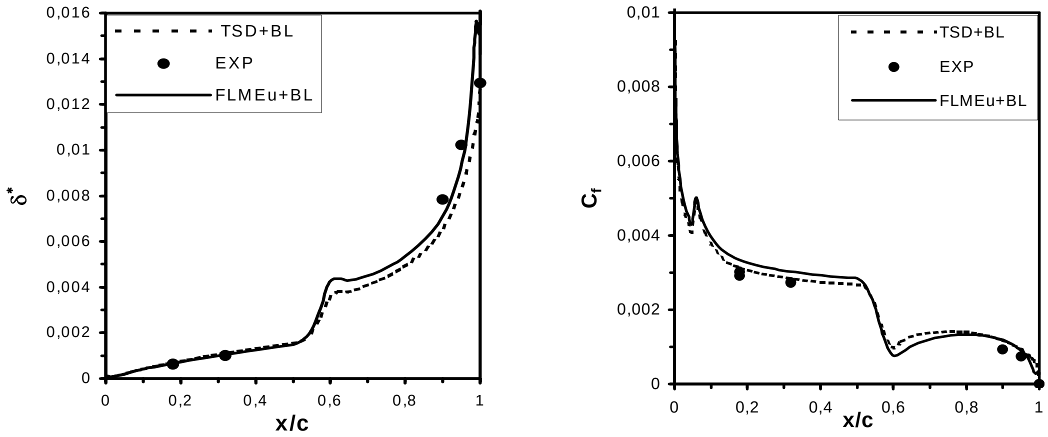

(a). Displacement thickness (b) Skin friction

Fig. 6.9. Displacement Thickness and Skin Friction on the Upper Surface of RAE 2822 at M = 0.725, Re = 6.5E+06, α = 2.42 deg

The lift and drag coefficients for this case are depicted in Table 6.3. together with the results obtained from the VTA Workshop 1987.

Table 6.3. Lift and Drag Coefficients of RAE 2822 Airfoil at M = 0.725, Re = 6.5E+06, α_{exp} = 2.92 deg (uncorrected)

	C_l	C_d (drag count)	Error (%)		α (deg)	Remark
			C_l	C_d		
Experiment	0.743	127	-	-	2.92	Cook et.al
TSD	**0.821**	**150**	**10.49**	**18.11**	**2.42**	**Present**
FLMEu	**0.820**	**148**	**10.36**	**16.53**	**2.42**	**Present**
TSD+BL	**0.746**	**134**	**0.42**	**5.51**	**2.42**	**Present**
FLMEu+BL	**0.742**	**131**	**-0.13**	**3.15**	**2.42**	**Present**
Full Potential+BL	0.740	131	-0.40	3.15	2.56	Dargel & Thiede $^{1)}$
Full Potential+BL	0.822	132	10.63	3.94	2.47	Haase & Echtle $^{1)}$
Euler+BL	0.723	113	-2.69	-11.02	2.44	Drela & Giles $^{1)}$
Euler+BL	0.756	180	1.75	41.73	2.60	Chen et.al. $^{1)}$
Navier Stokes (Baldwin-Lomax)	0.747	123	0.54	-3.14	2.30	Maksymiuk & Pulliam $^{1)}$
Navier Stokes (Johnson-King)	0.717	113	-3.49	-11.02	2.40	Coakley $^{1)}$
Range value in VTA Workshop	0.717 up to 0.822	113 up to 180	-3.49 up to 10.63	-3.14 up to 41.73	2.30 up to 2.80	

1 drag count = 0.0001, $^{1)}$ in VTA Workshop 1987 [73]

Twenty three (23) scientists have been participated in the VTA Workshop 1987. They represented their results for some test cases, which were computed using the Navier Stokes, Euler equations plus Boundary layer and Full potential equation plus Boundary layer. Compared with the results of this Workshop, the aerodynamic coefficients calculated using the present TSD+BL and FLMEu+BL are in the range of the Workshop's results. The developed methods show a better result than some Workshop's results, and lay in the same level with the results from Dargel & Thiede (using Full Potential+BL) and from Maksymiuk & Pulliam (using Navier Stokes + Baldwin Lomax turbulence model). Compared with the experimental results, the deviation of the lift and drag coefficients calculated with TSD+BL are 0.42% and 5.51% respectively and calculated with FLMEu+BL is –0.13% and 3.15% respectively. Compared with the results from inviscid model (TSD and FLMEu), the present VII method improves the lift and drag coefficients around 10% and 13% respectively.

6.2.2. Transonic Flow with Separation Bubble

The flow around airfoil RAE 2822 with the following flow parameters is examined:

Mach number	: M = 0.75
Reynolds number	: Re = 6.2E+06 (based on chord)
Angle of attack	: α = 2.93 deg

This case is known as CT 10 case in AGARD [72] and was selected as one of five test cases VTA Workshop 1987 [73]. The numerical results are compared with experimental data by Cook, McDonald, and Firmin [72]. The angle of attack in the experiment is 3.19 deg (uncorrected) associated with lift coefficient C_l = 0.743. In order to obtained same lift coefficient, the angle of attack by present simulation is reduced to 2.93 degrees. In this simulation, the TSD method is coupled with the boundary layer method from Drela-Giles and Greens Lag Entrainment, in order to examine the influence of different boundary layer methods. The simulation is conducted using Cartesian grid with (160x30) points around flow field. The flow condition is assumed to be fully turbulent flow. Figures 6.10 and 6.11. represent the pressure, displacement thickness and skin friction distribution.

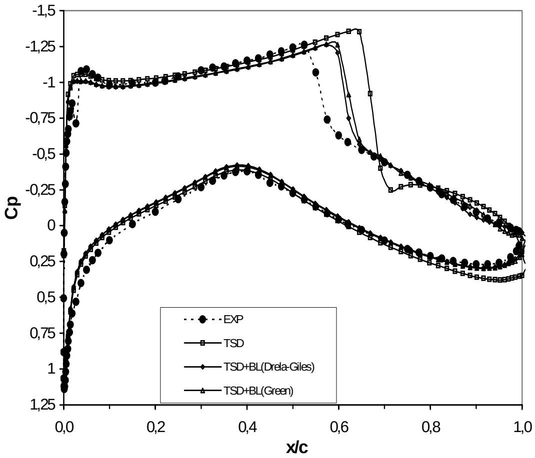

Fig. 6.10. Pressure Distribution of RAE 2822 Airfoil
at M = 0.75, Re = 6.2E+06, α = 2.93 deg

Without addition of the displacement thickness, the lift coefficient C_l from the inviscid model (TSD) is 0.8370 and the pitching moment coefficient C_m is -0.1523. The pressure distribution on the upper surface agrees well with the experimental result until 52% chord from the leading edge. But the position of the shock lays at 68% chord from leading edge. This position is far behind the shock position from the experiment, which is located in 58% (see fig. 6.10). After the boundary layer was added on the airfoil, the lift coefficient decreases to 0.7465 and the pitching moment coefficient is –0.1228 calculated using Greens Lag Entrainment boundary layer method. By using the boundary layer method of Drela-Giles the lift coefficient is 0.7287 and the pitching moment coefficient is -0.1168. The pressure distributions obtained from VII using both boundary layer methods are little bit larger than the experiment results from leading edge to 52% chord. The influence of the Drela-Giles boundary layer method seems to be a little bit larger than those of Greens Lag Entrainment boundary layer method. By using the Drela-Giles method, the shock position is found at around 62% chord from leading edge, at the other hand by using the Greens Lag Entrainment method lays the shock position at around 63% chord from leading edge. A small separation bubble is found just after shock position as shown by zero skin friction region in fig. 6.11b.

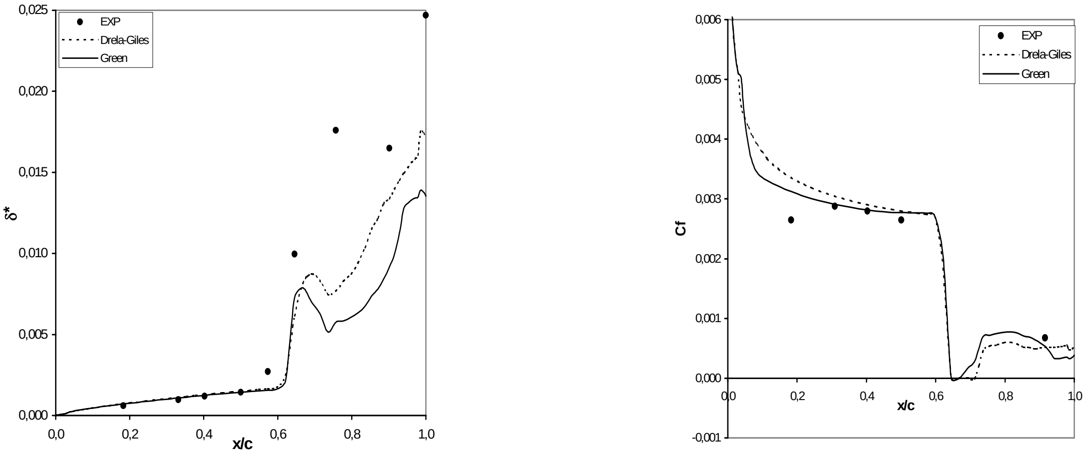

(a) Displacement thickness (b) Skin friction

Fig. 6.11. Displacement Thickness and Skin Friction on the Upper Surface of RAE 2822 at M = 0.75, Re = 6.2E+06, α = 2.93 deg

The lift and drag coefficients for this case are depicted in Table 6.4. together with the results obtained from the VTA Workshop 1987.

Table 6.4. Lift and Drag Coefficients of RAE 2822 Airfoil at M = 0.75, Re = 6.2E+06, α_{exp} = 3.19 deg (uncorrected)

	C_l	C_d (drag count)	Error (%)		α (deg)	Remark
			C_l	C_d		
Experiment	0.743	242	-	-	3.19	Cook et.al
TSD	**0.837**	**289**	**12.65**	**19.42**	**2.93**	**Present**
TSD+BL(Drela)	**0.729**	**226**	**-1.88**	**-6.61**	**2.93**	**Present**
TSD+BL(Green)	**0.747**	**256**	**0.54**	**5.78**	**2.93**	**Present**
Full Potential+BL	0.740	230	-0.40	-4.96	2.96	Dargel & Thiede $^{1)}$
Euler+BL	0.733	224	-1.34	-7.44	2.70	Drela & Giles $^{1)}$
Navier Stokes (Baldwin-Lomax)	0.838	289	12.78	19.42	2.72	Maksymiuk & Pulliam $^{1)}$
Navier Stokes (Baldwin-Lomax)	0.859	298	15.61	23.14	2.80	Coakley $^{1)}$
Navier Stokes (Johnson-King)	0.745	243	0.27	0.41	2.80	Coakley $^{1)}$
Range value in VTA Workshop	0.740 up to 0.859	224 up to 298	-0.40 up to 15.61	-7.44 up to 23.14	2.50 up to 2.96	

1 drag count = 0.0001, $^{1)}$ in VTA Workshop 1987 [73]

Compared with the results from VTA Workshop, the developed TSD+BL (Green) supplies the aerodynamic coefficients in the range of the Workshop's results but the lift coefficient obtained using TSD+BL (Drela) lies a little bit lower. The developed VII method shows better results than some Workshop participants results. The present results lie in the same level with the results from Dargel & Thiede (Full Potential+BL) and from Drela & Giles

(Euler+BL). Compared with the experiment, the deviation of lift and drag coefficients is -1.88% and -6.61% respectively (using TSD+BL Drela) and 0.54% and 5.78% respectively (using TSD+BL Green). In comparison with the results of the inviscid model (TSD), the developed VII method improves the lift and drag coefficient around 10% and 13% respectively. The best agreement with experiment for this case is the Coakley's result, which is computed using Navier-Stokes Code with Johnson-King turbulence model. This method supplies result for $C_l = 0.745$ and for $C_d = 243$ drag counts with angle of attack 2.80 degrees. The Navier-Stokes Code with Baldwin-Lomax turbulence model (from Coakley and Maksymiuk & Pulliam) supplies over predicted values for the two aerodynamic coefficients.

6.2.3. Transonic Flow with Shock-Induced Separation

The flow around airfoil NACA 0012 with the following flow parameters is examined:

Mach number : M = 0.799
Reynolds number : Re = 9.0E+06 (based on chord)
Angle of attack : $\alpha = 2.26$ deg (corrected)

This case is also selected as one of five test cases in VTA Workshop 1987 [73]. The present results will be compared with the experimental data from Harris [74] and numerical results from Cvrlje [75] and Prananta [76]. Cvrlje calculated this case using Navier-Stokes Code plus Baldwin-Lomax turbulence model (NS-BL). Prananta calculated this case using Navier-Stokes Code with Spalart-Almaras turbulence model (NS-SA). The present TSD and FLMEu Codes are coupled with boundary layer method from Drela-Giles to simulate this case. The simulation is carried out with (180x30) cells and (160x30) points for FLMEu and TSD Code respectively. The flow condition is assumed to be fully turbulent flow. Fig. 6.12 and 6.13. show the pressure, displacement thickness and skin friction distribution. Only pressure distribution result computed using NS-BL is available. At the other hand from NS-SA calculations only pressure distribution and skin friction results are available. From the experiment there are no skin friction and displacement thickness data.

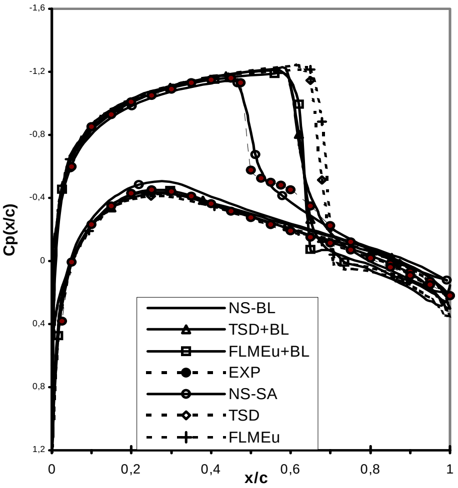

Fig. 6.12. Pressure Distribution of NACA 0012 Airfoil
at M = 0.799, Re = 9.0E+06, $\alpha = 2.26$ deg

From fig. 6.12. it can be seen that the shock location computed by TSD+BL and FLMEu+BL agrees well with those of NS-BL (Navier-Stokes with Baldwin-Lomax turbulence model). The shock is located at 64% chord from the leading edge. The shock location lies still behind the experimental situation, which is located at 50% chord from leading edge. The shock location from NS-SA (Spalart Almaras turbulence model) is near to the experiment at about 51% chord from leading edge. Without influence of the boundary layer, the TSD and FLMEu procedure supply the shock location at around 70% chord. It can be seen from the skin friction distribution that a shock-induced separation is occurred, which is designated by the zero or negative values of skin friction (see fig. 6.13b). From the TSD+BL and FLMEu+BL results, the separation started from 65% chord. On the other hand, the separation calculated with the NS-SA occurred after 51% chord result followed by reattachment of the flow at around 97% chord.

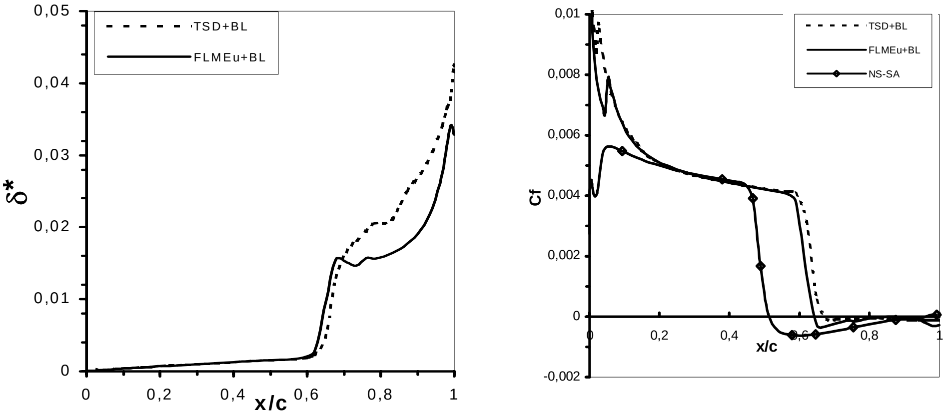

(a) Displacement thickness (b) Skin friction

Fig. 6.13. Displacement Thickness and Skin Friction on the Upper Surface of NACA 0012 at M = 0.799, Re = 9.0E+06, α = 2.26 deg

The lift and drag coefficients for this case are depicted in Table 6.5. together with the results obtained from the VTA Workshop 1987.

Table 6.5. Lift and Drag Coefficients of NACA 0012 Airfoil at M = 0.799, Re = 9.0E+06, α = 2.26 deg

	Cl	Cd (drag count)	Error (%)		Remark
			Cl	Cd	
Experiment	0.390	331	-	-	Haris
TSD	**0.558**	**497**	**43.08**	**50.15**	**Present**
FLMEu	**0.541**	**486**	**38.72**	**46.83**	**Present**
TSD+BL	**0.464**	**431**	**18.97**	**30.21**	**Present**
FLMEu+BL	**0.454**	**416**	**16.41**	**25.68**	**Present**
Euler+BL	0.312	337	-20.0	1.81	Drela & Giles 1)
Navier Stokes – BL (Baldwin-Lomax)	0.472	445	21.02	34.44	Maksymiuk & Pulliam 1)
Navier Stokes – BL	0.476	446	22.05	34.74	Coakley 1)
Navier Stokes – BL	0.433	409	11.03	23.56	Cvrlje [75]
Navier Stokes – JK (Johnson-King)	0.300	345	-23.08	4.23	Coakley 1)
Range value in VTA Workshop	0.300 up to 0.476	337 up to 446	-23.08 up to 22.05	1.81 up to 34.74	

1 drag count = 0.0001, 1) in VTA Workshop 1987

The non viscous models (TSD and FLMEu) supply the aerodynamic coefficients outside of the range of the VTA Workshop. That means: for this case the use of the non viscous model is not appropriate. Compared with the Workshop‘s results, the developed TSD+BL and FLMEu+BL supply the aerodynamic coefficients inside of the range value in the Workshop. Compared with the experiment the deviation of lift and drag coefficient is 18.97% and 30.21% (calculated using TSD+BL) and 16.41% and 25.68% (calculated using FLMEu+BL) respectively. Most methods used in the Workshop supply larger lift and drag coefficients compared to the experiment except those from Drela & Giles (Euler + Boundary Layer) and from Coakley (Navier Stokes + Johnson King turbulence model), which supply smaller lift coefficient. The best agreement of the shock location with experiment is the Navier Stokes Code with Johnson King turbulence model from Coakley. For this test case, there are no results from potential equation was presented in VTA Workshop 1987.

6.2.4. Investigation of the Flow around Axis-symmetrical Bodies

In this sub chapter the application of the developed viscous – inviscid interaction method for the computation of flow around an axis-symmetrical body is presented. For this purpose the TSD equation is transformed into [55]:

$$\frac{\partial f_0}{\partial t}+\frac{\partial f_1}{\partial x}+\frac{\partial f_2}{\partial r}+\frac{f_2}{r}=0 \tag{6.2}$$

where the fluxes are:

$$f_0=-(A\phi_t+B\phi_x) \qquad f_1=E\phi_x+F\phi_x^2 \qquad f_2=\phi_r \tag{6.3}$$

r is the component of the coordinates in radial direction of the body.
The coefficients A, B, E, and F are remain unchanged.

$$A=M_\infty^2, \qquad B=2M_\infty^2, \qquad E=1-M_\infty^2, \qquad F=-\frac{1}{2}(\gamma+1)M_\infty^2$$

In the computational coordinate, the TSD equation (6.2) becomes to:

$$-\frac{\partial}{\partial t}\left(A\frac{\phi_t}{\xi_x}+B\phi_\xi\right)+\frac{\partial}{\partial\xi}\left[E\phi_\xi\xi_x+F(\phi_\xi\xi_x)^2\right]+\frac{\partial}{\partial\zeta}\left(\frac{\phi_\zeta}{\xi_x}\right)+\frac{1}{\zeta}\left(\frac{\phi_\zeta}{\xi_x}\right)=0 \tag{6.4}$$

with:

$$\xi(x)=\frac{x}{L} \qquad \zeta=\frac{r}{L} \tag{6.5}$$

where L is the length of the body.
The solution of the equation (6.4) is carried out using the Approximate Factorization (AF) algorithm, which is already discussed in chapter 4.1.
The AF form of the equation (6.4) is:

$$L_\xi L_\zeta\Delta\phi=-R\left(\phi^*,\phi^n,\phi^{n-1},\phi^{n-2}\right) \tag{6.6}$$

with:

$$L_\xi=1+\left(\frac{3B}{4A}\xi_x\Delta t\right)\frac{\partial}{\partial\xi}-\left(\frac{\xi_x\Delta t^2}{2A}\right)\frac{\partial}{\partial\xi}F_1\frac{\partial}{\partial\xi} \tag{6.7}$$

$$L_\zeta=1-\left(\frac{\xi_x\Delta t^2}{2A}\right)\frac{\partial}{\partial\zeta}\frac{1}{\xi_x}\frac{\partial}{\partial\zeta}-\left(\frac{\Delta t^2}{2A}\right)\frac{1}{\varsigma}\frac{\partial}{\partial\zeta} \tag{6.8}$$

$$F_1=E\xi_x+2F\phi_\xi^*\xi_x^2 \tag{6.9}$$

$$\begin{aligned}R\left(\phi^*,\phi^n,\phi^{n-1},\phi^{n-2}\right)=-\frac{1}{2}\left(2\phi^*-5\phi^n+4\phi^{n-1}-\phi^{n-2}\right)-&\\ \frac{B}{4A}\Delta t\xi_x\left(3\phi_x^*-4\phi_x^n+\phi_x^{n-1}\right)+&\\ \frac{(\Delta t)^2}{2A}\xi_x\frac{\partial}{\partial\xi}\left(E\xi_x\phi_\xi^*+F\xi_x{}^2\phi_\xi^{*2}\right)+\frac{(\Delta t)^2}{2A}\left(\frac{\partial}{\partial\zeta}+\frac{1}{\varsigma}\right)\phi_\zeta^*&\end{aligned} \tag{6.10}$$

The 1st sweeping of the equation (6.6) will be carried out in the ξ direction for all constant value of ς:

$$L_\xi\Delta\phi^*=-R\left(\phi^*,\phi^n,\phi^{n-1},\phi^{n-2}\right) \tag{6.11}$$

The 2nd sweeping will be done in die ς direction for all constant value of ξ, after the temporary solution $\Delta\phi^*$ has been found from the 1st sweeping :

$$L_\zeta\Delta\phi=\Delta\phi^* \tag{6.12}$$

The solution $\phi^{n+1}=\phi^n+\Delta\phi$ will be convergence if $\Delta\phi\sim 0$. The computation of the pressure distribution is carried out as discussed in chapter 4.1.

This TSD equation will be coupled with the boundary layer calculation method from Drela-Giles to calculate the flow around an axis-symmetrical body.

A set of Body of Revolution (BoR) of **M**esserschmidt **B**olkow **B**lohm (**MBB**) called as BoR 1, 3 and 5 are examined [77]. Its fore and aft body are represented with 3. order polynomial as follows:

Fore body :

$$r(x) = a_3\, x^3 + a_2\, x^2 + a_1\, x \tag{6.13}$$

with :

$a_1 = 3\, r_{max}/x_1$, $a_2 = -3\, r_{max}/x_1^2$, $a_3 = r_{max}/x_1^3$, $x_1 = 0.5\, L$

Aft body :

$$r(x) = b_3\, x^3 + b_2\, x^2 + b_1\, x + b_0 \tag{6.14}$$

with :

$b_0 = (L\, r_{max}/(x_2-L)^3)(3x_2L-L^2-3x_2^2)$, $b_1 = 3x_2^2\, r_{max}/(x_2-L)^3$,

$b_2 = -3x_2\, r_{max}/(x_2-L)^3$, $b_3 = r_{max}/(x_2-L)^3$

The value of x_2 is different for each BoR as follows:

for BoR 1 : $x_2 = 0.5\, L$

for BoR 3 : $x_2 = 0.6875\, L$

for BoR 5 : $x_2 = 0.8125\, L$

The value of L and r_{max} are 800 mm und 60 mm respectively.

Fig. 6.14. shows the geometry of MBBs BoR 1, 3 and 5.

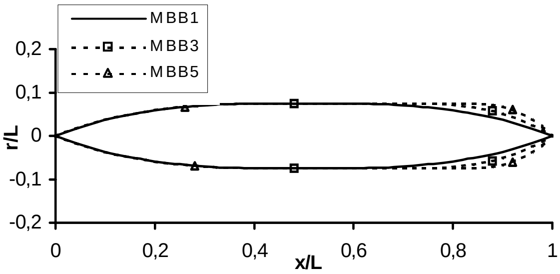

Fig. 6.14. Geometry of MBBs Body of Revolution 1, 3 and 5

The flow parameter, which has to be simulated are as follows:

Mach number,	M = 0.8
Reynolds number,	Re = 1.0E+07 (based on length L)
Angle of attack,	$\alpha = 0$ deg

The flow condition is assumed to be fully turbulent. The pressure, skin friction and displacement thickness distribution of the MBBs BoR 1, 3 and 5 are presented in fig. 6.15. It looks that the more steeply geometry the more steeply the pressure distribution and the more largely skin friction. This increasing skin friction will not automatically increase the entire drag, because the pressure drag within the region of the trailing edge becomes smaller because of the change of geometry within this region. For BoR 5 there is a small separated region around the trailing edge (Cf < 0), as can be seen in fig. 6.15b.

Comparison of the present results with the experiment of Lorenz Meyer and Aulehla [77] and Navier Stokes calculation (with Baldwin Lomax turbulence model) using software RAMPANT [78] for BoR 3 is depicted in fig. 6.16. A large deviation in the pressure distribution between the present TSD+BL and the experiment and the Navier Stokes results occurs in the flat region of the body (approximately from 40% to 70% of the body length), where the flow became slower after a leading edge expansion.

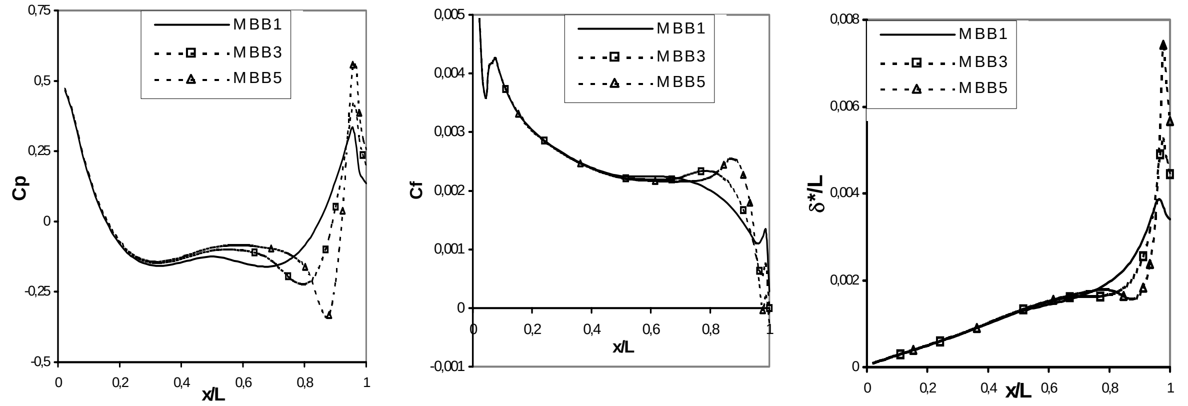

(a) Pressure (b) Skin Friction (c) Displacement Thickness

Fig. 6.15. Pressure, Skin Friction and Displacement Thickness of MBBs BoR 1, 3 and 5 at M = 0.8, Re = 1.0E+07, α = 0 deg

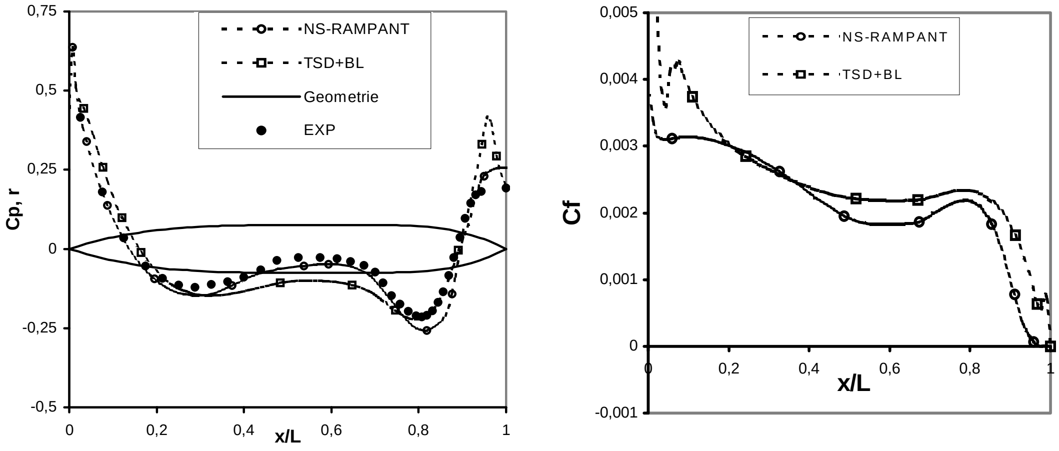

(a) Pressure (b) Skin Friction

Fig. 6.16. Pressure and Skin friction of MBBs BoR 3 at M = 0.8, Re = 1.0E+07, α = 0 deg

Comparison of the pressure distribution between the present result and the experiment for MBBs BoR 1 and 5 can be seen in fig 6.17. Again the deviation of the pressure distribution between the TSD+BL and the experiment occurred in flat region of the bodies. The above results have been partially published in Ref. [79].

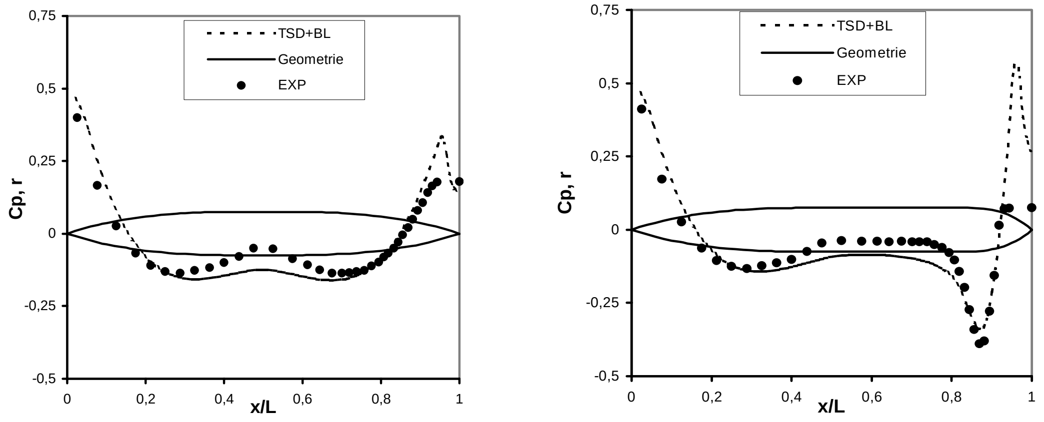

(a) BoR 1 (b) BoR 5

Fig. 6.17. Pressure Distribution of MBBs BoR 1 and 5 at M = 0.8, Re = 1.0E+07, α = 0 deg

6.3. Unsteady Aerodynamic Results

In this chapter the developed viscous - inviscid interaction method is used to compute some unsteady test cases. The unsteady condition is produced by a harmonically pitching motion of a body in a uniform flow. The oscillation of the body is sinusoidal, as follows:

$$\alpha(\tau) = \alpha_0 + \alpha_1 \sin(k\tau) \tag{6.15}$$

where :

α_0 is mean angle of attack
α_1 is amplitude of angle of attack
k is reduced frequency ($k = \omega c/U$)
τ is the non dimensional time

In order to test the ability of the developed method, the selected unsteady cases must cover or consider the following variation:

- variation of Mach number and Reynolds number
- variation of mean angle of attack
- variation of amplitude of angle of attack
- variation of reduced frequency of the oscillation
- variation of geometry
- two and three-dimensional flow
- symmetrical and unsymmetrical flow

With the above consideration the following unsteady cases are selected:

1. AGARD CT5 test case for NACA 0012 airfoil [80]
2. AGARD CT5 test case for LANN wing [81]
3. NASA E24 test case for Delta wing [82]

The simulation parameters of the above unsteady test cases are presented in table 6.6.

Table 6.6.The Selected Unsteady Test Cases

No.	Case	M	Re ($x10^6$)	α_0	α_1	k	x_p	AR	Flow	
									sym	unsym
1.	CT5 NACA 0012	0.755	5.5	0.016	2.51	0.1628	0.25 c	∞	x	
2.	CT5 LANN Wing	0.82	7.3	0.6	0.25	0.204	0.621 cr	7.92		x
3.	E24 Delta Wing	0.88	9.0	0.0	0.5	0.340	0.652 cr	1.24	x	

Notes:

M = Mach number
Re = Reynolds number
α_0 = mean angle of attack
α_1 = amplitude of angle of attack
k = reduced frequency ($k = \omega c/U$)
x_p = pitching axis

AR = Aspect Ratio
sym = symmetrical flow
unsym = unsymmetrical flow
c = chord
cr = root chord

Another unsteady aerodynamic results calculated using the developed VII method can be found in Ref. [55]. A part of the results has been published in Ref. [83, 84].

6.3.1. AGARD Test Case CT5 for NACA 0012

The simulation parameter for this case is tabulated in Table 6.7.

Table 6.7. Simulation Parameter of AGARD CT5 Test Case for NACA 0012

Simulation Parameter			Remark
Mach number	M	0.755	
Reynolds number	Re	5.5E+06	based on chord
Mean angle of attack	α_0	0.016 ^{o}	
Amplitude angle of attack	α_1	2.51 ^{o}	
Reduced Frequency	*k*	0.1628	based on chord
Pitching axis	x_p/c	0.25	from leading edge
Moment ref. axis	x_m/c	0.25	from leading edge

The developed TSD plus boundary layer method from Drela-Giles will be used to simulate this case with following grid parameter:

Table 6.8. Grid Parameter

Grid Parameter	
Points on surface	120
Grid dimension (x-z plane)	160 x 30
Grid type (Cartesian)	H
Total points	4800
Off Body distance	10^{-3} c
Far field distance	10 c

Before the unsteady calculation can be carried out, the steady calculation with mean angle of attack data must be first accomplished. The steady pressure, displacement thickness and skin friction are depicted in figures 6.18. and 6.19. As comparison data is the pressure distribution result from Cvrlje [75]. The steady experimental data is unfortunately not available.

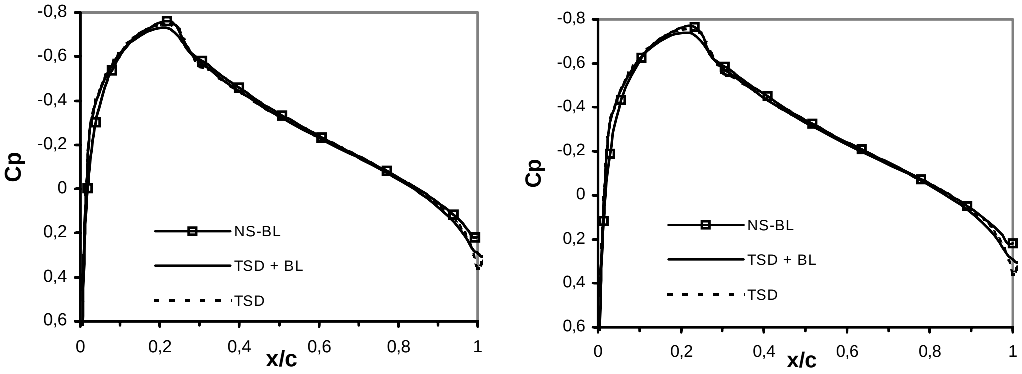

(a) Lower Surface

(b) Upper Surface

Fig. 6.18. Steady Pressure Distribution of NACA 0012
CT5 Case, M = 0.755, Re = 5.5E+06, α_0 = 0.016 ^{o}

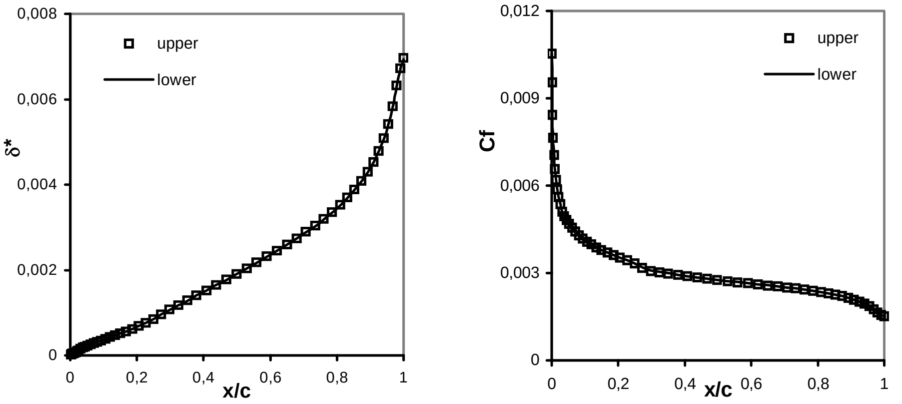

(a) Displacement Thickness (b) Skin Friction

Fig. 6.19. Steady Displacement Thickness and Skin Friction of NACA 0012
CT5 Case, M = 0.755, Re = 5.5E+06, $\alpha_0 = 0.016^{o}$

The pressure distribution between the TSD+BL and the NS-BL agrees well for this case. From the pressure distribution, displacement thickness and skin friction one can see that the flow condition is almost symmetrical with respect to x-y plane.

After the steady calculation was accomplished, the unsteady calculation can be performed using the initial condition from steady results. The simulation is carried out for three cycles of the oscillation, in order to obtain convergent results. For this simulation one cycle of the oscillation is divided into 720 time steps uniformly. The unsteady result of lift and moment coefficient for the last cycle the oscillation are presented in figure 6.20. together with experimental results from Landon [80] and numerical results from Cvrlje [75].

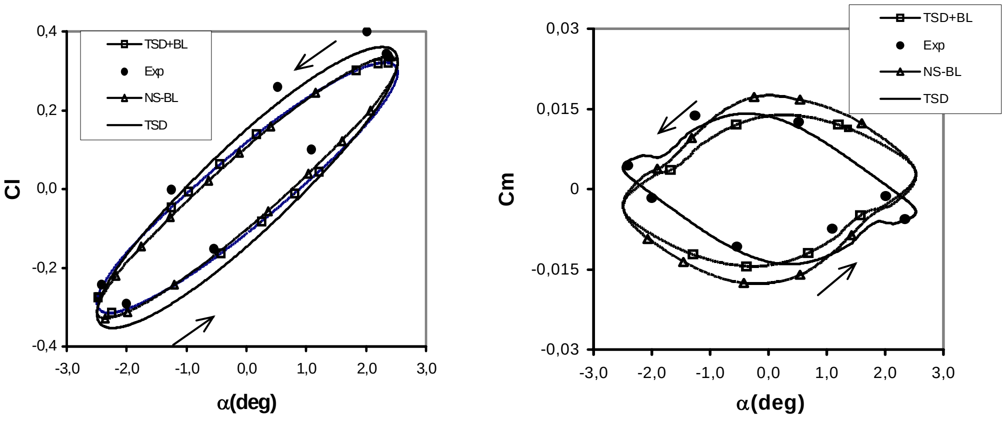

(a) Lift (b) Moment

Fig. 6.20. Unsteady Lift and Moment of NACA 0012
CT5 Case, M = 0.755, Re = 5.5E+06, $\alpha_0 = 0.016^{o}$, $\alpha 1 = 2.51^{o}$, $x_p = 0.25c$, k = 0.1628

As expected, the lift coefficient (peak-to-peak value) calculated from TSD is the largest one compared with the other numerical results. The influence of the boundary layer into the TSD tends to reduce the lift coefficient close to the Navier Stokes solution. The lift coefficient from TSD+BL and from Navier Stokes (NS-BL) solution agree well each other. Compared to the experimental results the developed method TSD+BL supplies a good agreement of the lift coefficient particularly in the range of the negative angle of attack. For the positive angle of attack the two numerical results (TSD+BL and NS-BL) supply smaller lift coefficient. The results of the TSD lie in the proximity of the experiment particularly as the airfoil moved downward from its highest position (see fig. 6.20a.). That does not meant that the TSD solution is the best solution (closer to the experiment), but probably the experiment was not so correctly performed. The symmetrical condition from the measured unsteady lift coefficient can not be seen clearly. It seems also, that the experiment was probably performed using smaller reduced frequency. If the Navier Stokes solution can be accepted as numerical reference solution (because the Navier Stokes equations describe the fluid flows most completely), then the quality of the solution of the TSD can be increased because of the addition of the boundary layer.

The moment coefficient is turned counter clockwise because of the addition of the boundary layer in to the TSD method. The magnitude of the moment coefficient of Navier Stokes is larger than the result of TSD plus boundary layer.

The unsteady pressure distribution is presented in figure 6.22 for eight different angles of attack of the airfoil, where the pressure measurements were performed. The measured angle of attack of the airfoil is presented in fig. 6.21. (point a. to h.).

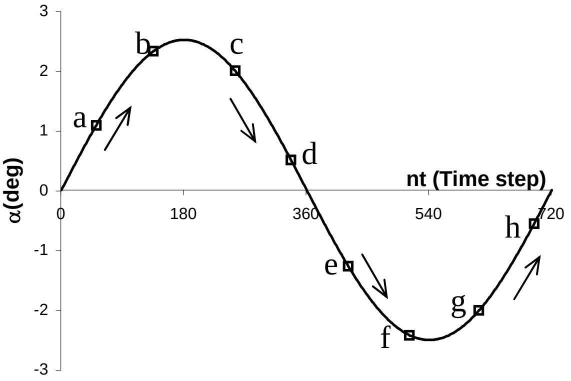

Fig. 6.21. The Measured Angle of Attack, AGARD CT5 NACA 0012

The deviation of the pressure distribution from numerical and experimental data occurs mainly in the region of the shock (see fig. 6.22. b to d, f to h). The shock position from experiment mostly lies behind the shock positions from numerical results. In the comparison with the Navier Stokes solution (NS-BL), the developed TSD+BL method supplies the earlier shock position (in front of the shock position of the NS-BL). The shock position calculated by the TSD still lies behind the shock from NS-BL. The earlier shock position causes smaller magnitude of the moment coefficient as already presented in fig. 6.20.

Referring fig. 6.22a. and e, the TSD+BL method still shows a small shock, which is shown very soft by the Navier Stokes solution. For this case it seems that the influence of the boundary layer into the TSD equation is larger than the influence of the viscous terms in the Navier Stokes equations. From the experiment it is unclear whether an shock arises or not for this angle of attack. Unfortunately the experimental data on the lower surface of the airfoil are too few inadequate to show the shock position more precisely, if the shock arises on the lower surface (see fig. 6.22.a, 6.22.f h).

It is interesting to analyze the figure 6.22.a and e. From numerical data the shock on the lower surface of the airfoil arises at the position a., although the instantaneous angle of attack is positive ($\alpha = 1.09\,^{o}$). Contrary, the shock arises on the upper surface of the airfoil at the position e., although the angle of attack is already negative ($\alpha = -1.25\,^{o}$). For steady case the situation is inversely, the shock occurs on the upper surface of the airfoil at positive value of angle of attack and on the lower surface at negative value of angle of attack.

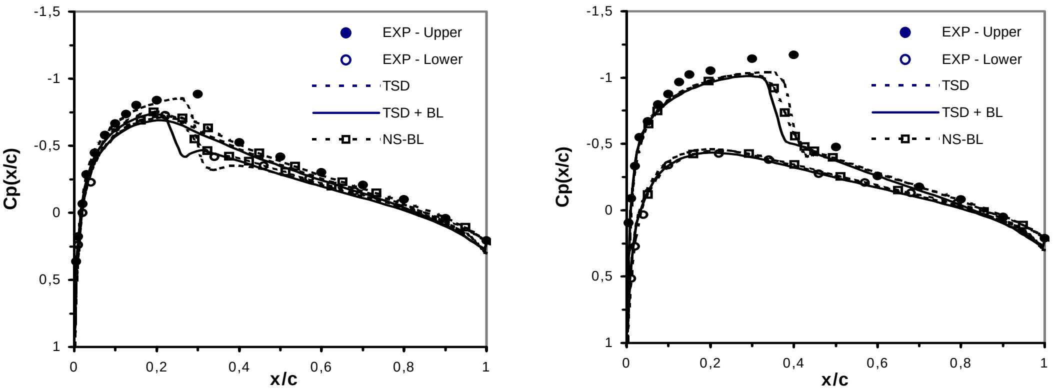

(a) α = 1.09° (upward) (b) α = 2.34 ° (upward)

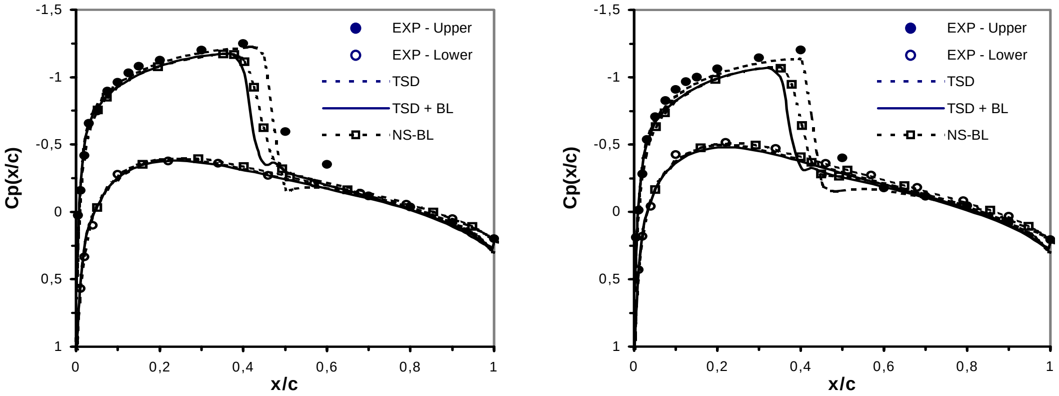

(c) α = 2.01 ° (downward) (d) α = 0.52 ° (downward)

Fig. 6.22. Unsteady Pressure Distribution of NACA 0012
CT5 Case, M = 0.755, Re = 5.5E+06, α_0 = 0.016°, α1 = 2.51°, x_p = 0.25c, k = 0.1628

If one compares fig. 6.22.b. with c, it can be seen that the shock at the position b. (α = 2.34 °) is smaller than those at the position c (α = 2.01 °), although the angle of attack at position b. is larger than those at the position c. The same phenomenon happens also between position f. (α = -2.41 °) and g. (α = -2.0 °). The oscillation of airfoil retards the reaction of the flow (responds lift and moment). This delay develops because the movement of the airfoil changes the effective angle of attack. The mechanism of the changed angle of attack is presented in fig 6.23.

In fig. 6.23., αa and α are the flow angle of attack (effectively) and instantaneous measured angles of attack (geometric) respectively, Ui is the induced velocity due to the airfoil oscillation, Ua is the actually flow velocity, U∞ is the undisturbed flow velocity. The flow angle of attack becomes larger (or more positive), if the airfoil moves downward (fig. 6.23.b. and d). Contrary, the flow angle of attack becomes smaller (or more negative), if the airfoil moves upward (fig. 6.23.a. and c). The induced velocity depends on the reduced frequency *k* and on the location of the pitch axis *xp*. (Ui/U∞ = *k xp*/*c*).

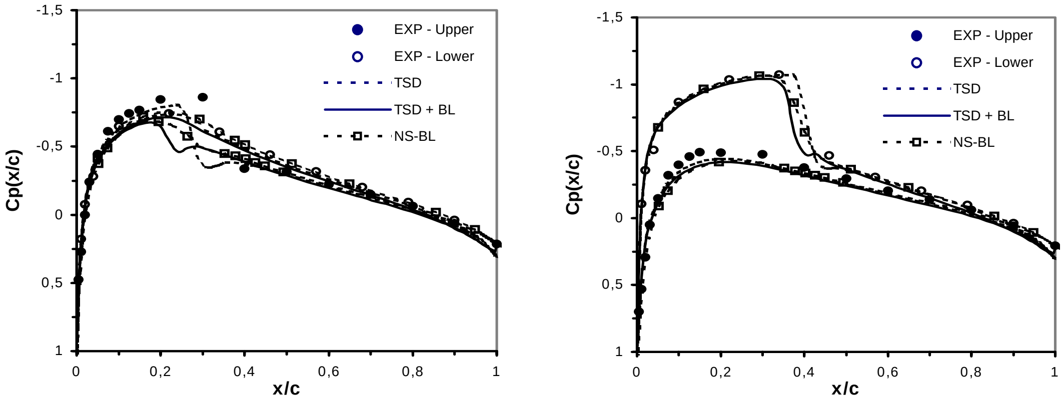

(e) α = -1.25 ° (downward)　　　　(f) α = -2.41 ° (downward)

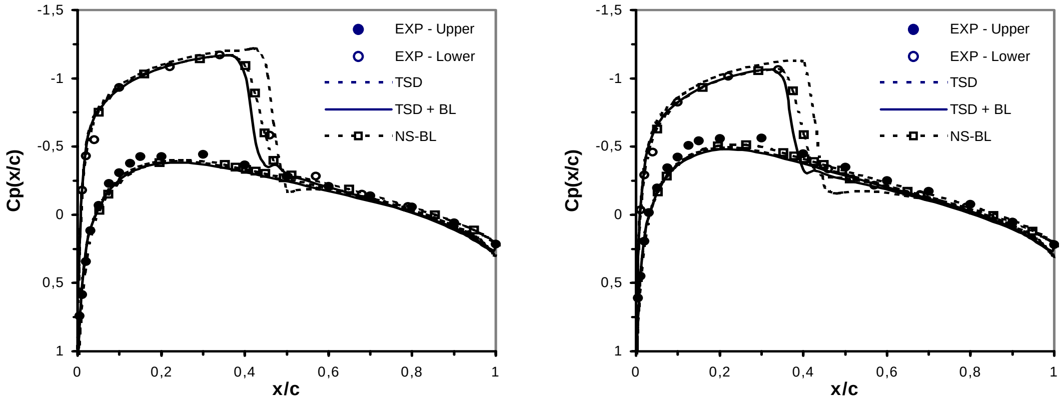

(g) α = -2.0 ° (upward)　　　　(h) α = -0.54 ° (upward)

Fig. 6.22. Unsteady Pressure Distribution of NACA 0012 (continued)
CT5 Case, M = 0.755, Re = 5.5E+06, α_0 = 0.016°, α1 = 2.51°, x_p = 0.25c, k = 0.1628

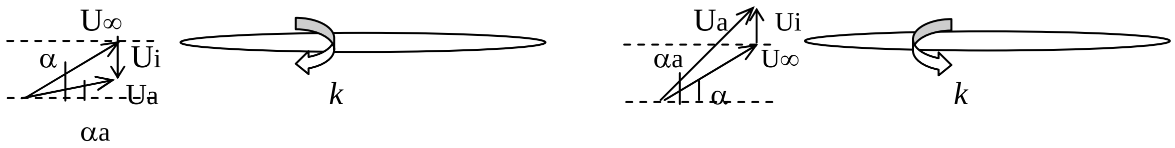

|αa| < |α|, αa < α　　　　|αa| > |α|, αa > α

(a) upward motion, α > 0　　　　(b) downward motion, α > 0

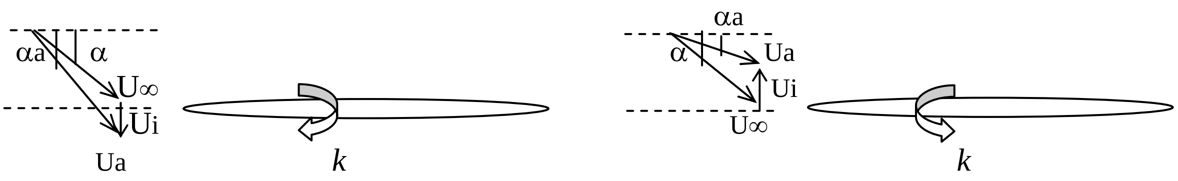

|αa| > |α|, αa < α　　　　|αa| < |α|, αa > α

(c) upward motion, α < 0　　　　(d) downward motion, α < 0

Fig. 6.23. The Actual Angle of Attack due to Pitching Motion

By fig. 6.22. b.(α = 2.34°), the flow angle of attack is actually smaller than 2.34 because of the upward movement of the airfoil and by fig. 6.22. c (α = 2.01 °) the actual angle of attack is larger than 2.01 because of the downward movement of the airfoil. Therefore the shock intensity at position b. is smaller than at position c.

In figure 6.24 can be seen the unsteady displacement thickness for the eight measured angles of attack. On the upper surface the displacement thickness from position g. to h and from a. to b becomes larger as the airfoil moved upward. The displacement thickness decreases sharply from position c to f. as the airfoil moved downward. On the lower surface of the airfoil the situation is reciprocally. The displacement thickness becomes smaller from position g. to h. and from a. to b as the airfoil moved upward. From position c to f. the displacement thickness increases as the airfoil moved downward. The shock position can also be recognized from the displacement thickness value, that is the position where the displacement thickness increases sharply (e.g. for strong shock see fig. 6.24 b.-d.).

Figure 6.25 shows the unsteady skin friction for the eight measured angles of attack. On the upper surface, the skin friction becomes smaller within the shock range from position a. to b as the airfoil moved upward and increases sharply from the position c to f as the airfoil moved downward. By the position g. and h. it can be seen, that there is almost no change of skin friction. On the lower surface, the skin friction from the position g. to h. and a. to b. increases, when the airfoil moved upward. By the position c and d there is nearly no change of skin friction can be seen. From the position e. to f., the skin friction becomes smaller. Unfortunately there are no comparison data from experiment available.

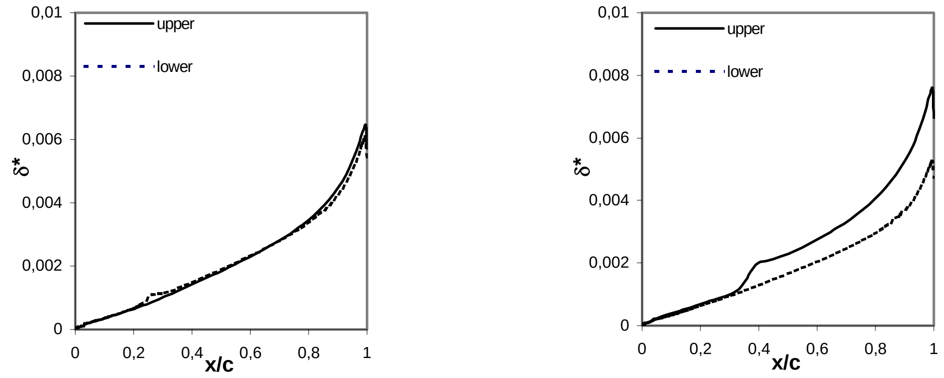

(a) $\alpha = 1.09^{o}$ (upward)

(b) $\alpha = 2.34^{o}$ (upward)

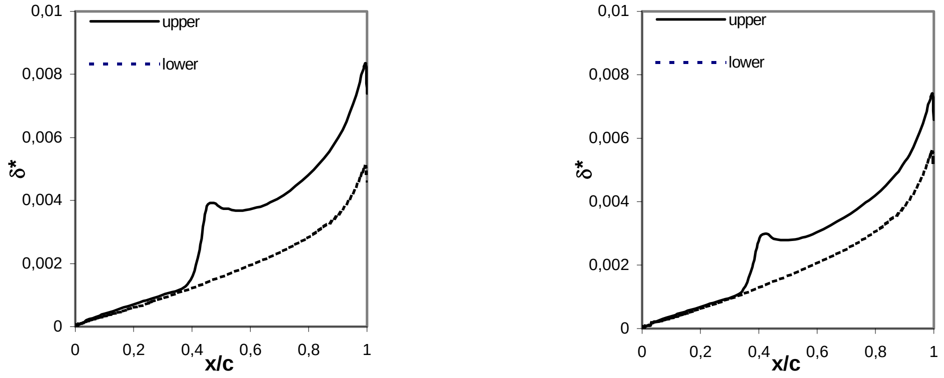

(c) $\alpha = 2.01^{o}$ (downward)

(d) $\alpha = 0.52^{o}$ (downward)

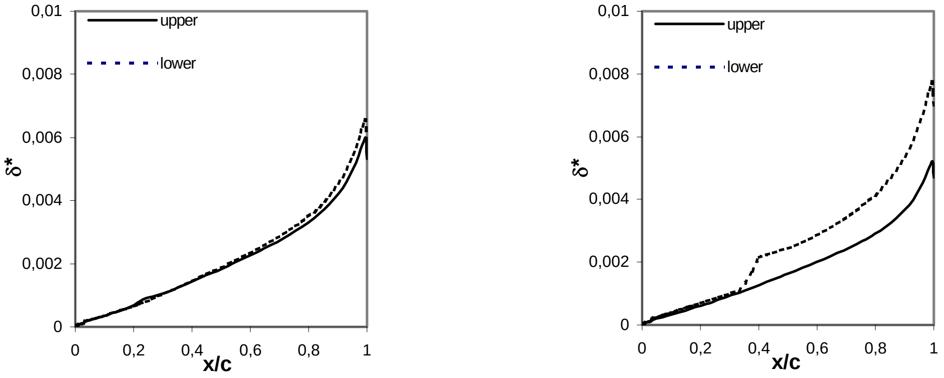

(e) $\alpha = -1.25^{o}$ (downward)

(f) $\alpha = -2.41^{o}$ (downward)

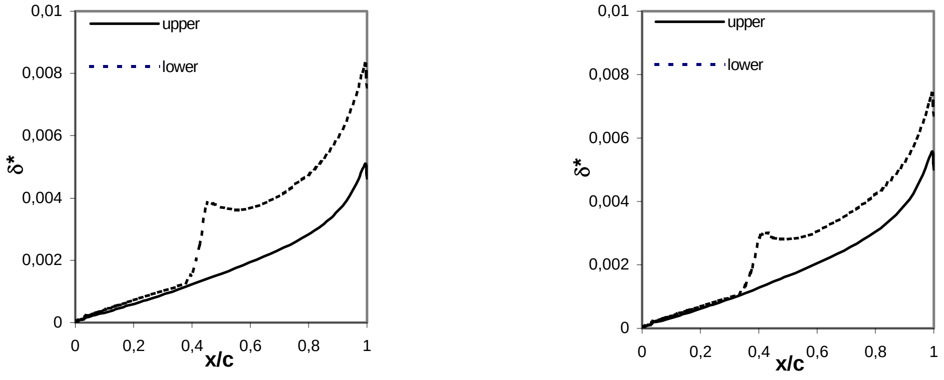

(g) $\alpha = -2.0^{o}$ (upward)

(h) $\alpha = -0.54^{o}$ (upward)

Fig. 6.24. Unsteady Displacement Thickness of NACA 0012

CT5 Case, M = 0.755, Re = 5.5E+06, $\alpha_0 = 0.016^{o}$, $\alpha 1 = 2.51^{o}$, $x_p = 0.25c$, k = 0.1628

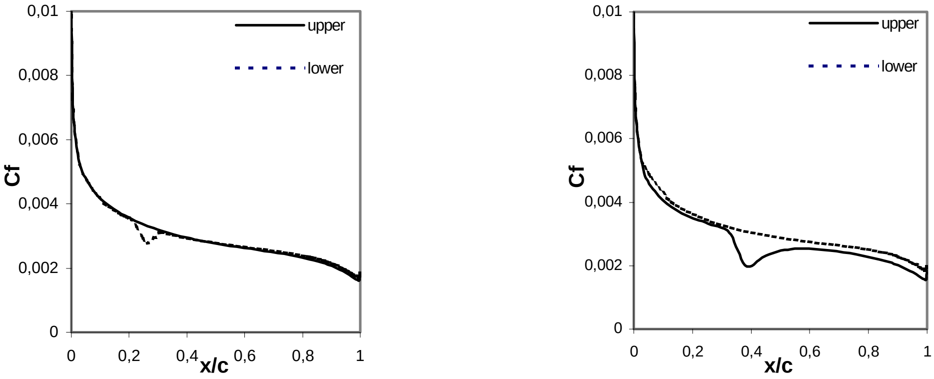

(a) $\alpha = 1.09^o$ (upward)

(b) $\alpha = 2.34^o$ (upward)

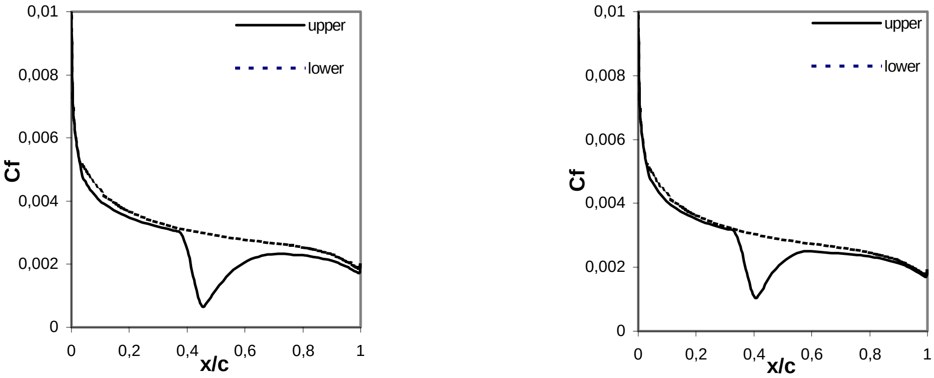

(c) $\alpha = 2.01^o$ (downward)

(d) $\alpha = 0.52^o$ (downward)

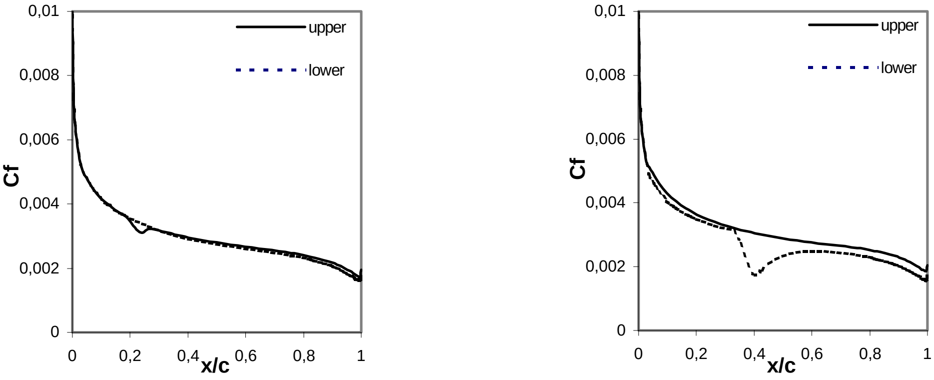

(e) $\alpha = -1.25^o$ (downward)

(f) $\alpha = -2.41^o$ (downward)

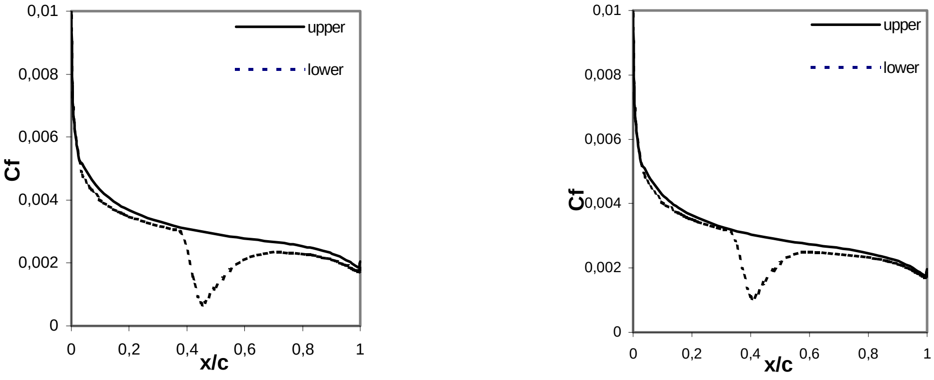

(g) $\alpha = -2.0^o$ (upward)

(h) $\alpha = -0.54^o$ (upward)

Fig. 6.25. Unsteady Skin Friction of NACA 0012

CT5 Case, M = 0.755, Re = 5.5E+06, $\alpha_0 = 0.016^o$, $\alpha 1 = 2.51^o$, $x_p = 0.25c$, k = 0.1628

6.3.2. AGARD Test Case CT5 for LANN Wing

The LANN wing was designed together in the 1980s by **L**ockheed, **A**FSOR, **N**ASA and **N**LR. The wing represents a typical wing of a transonic transport aircraft with large sweep angle, large aspect ratio and supercritical airfoil. The geometry of the wing is presented in Fig. 6.26. The parameters of geometry are presented in Table 6.9. The aerodynamic characteristics of the wing have been intensively measured in wind tunnel.

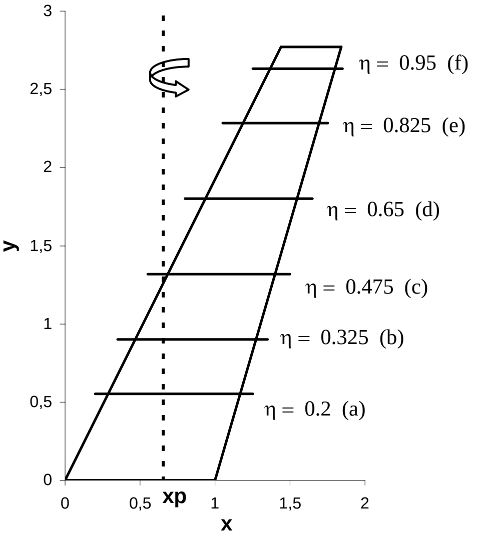

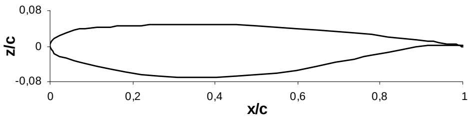

(b) Root Chord

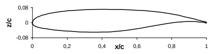

(c) Tip Chord

(a) Planform

Fig. 6.26. Geometry of the LANN Wing

Table 6.9. Geometry Parameter of the LANN Wing

Parameter		
Span	s	2.77
Root Chord	cr	1.0
Taper Ratio	ct/cr	0.4
Aspect Ratio	AR	7.92
Sweep Angle: Leading edge	φ_{LE}	27.49^{o}
Trailing edge	φ_{TE}	16.91^{o}
Thickness	t/c	12%
Twist	θ	-4.8^{o}

The AGARD CT5 test case is one of 10 selected test cases for code validation within the ECARP 1996 (**E**uropean **C**omputational **A**erodynamic **R**esearch **P**roject) [23], where 30 organizations (industry, university and research organizations) within European countries have been involved and participated.

The simulation parameter of the CT5 case are shown in table 6.10. The simulation is carried out using the TSD, the non linear Euler (FLMEu) and the linearized Euler (FLMSDEu) codes both with and without boundary layer coupling. As boundary layer calculation method is the two-dimensional integral method of Drela and Giles, which is used in strip theory approach along the wingspan. The grid parameters for the FLMEu and the FLMSDEu codes are the same grid parameters used in ECARP 1996 and are presented in table 6.11. The used grid for FLMEu/FLMSDEu codes in near field of the wing is depicted in Fig. 6.27.

Table 6.10. Simulation Parameter of AGARD CT5 Test Case for LANN Wing

Simulation parameter			Remark
Mach number	M	0.82	
Reynolds number	Re	7.3E+06	based on the root chord
Mean angle of attack	α_0	0.6^o	
Amplitude angle of attack	α_1	0.25^o	
Reduced Frequency	*k*	0.204	based on the root chord
Pitching axis	x_p/cr	0.621	from leading edge of the root chord
Moment Ref. axis	x_m/cr	0.25	from leading edge of the root chord

Table 6.11. Grid Parameter for Simulation of AGARD CT5 Test Case for LANN Wing

Grid parameter	TSD	FLMEu/FLMSDEu
Grid type (xz – yz planes)	H-H	C-H
Surface Cells (x and y directions)	2400 (120 x 20)	3360 (120 x 28)
Total Cells (x, y and z directions)	144000 (160 x 30 x 30)	204800 (160 x 40 x 32)
Offbody Distance	10^{-3} cr	$5x10^{-3}$ cr
Far field distance:		
front, above, below	10 cr	10 cr
rear	10 cr	8 cr
span	2 s	2 s

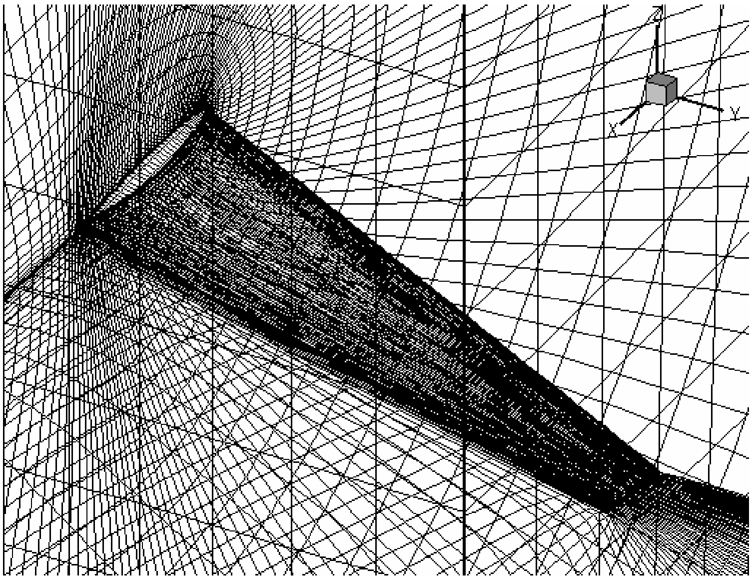

Fig. 6.27. The Grid for FLMEu/FLMSDEu Code in Near-Field of the Wing

The simulation of the case was performed with the following steps:

1. Simulation of the steady case (calculated with mean angle of attack without pitching motion) using the inviscid models (i.e. TSD and FLMEu codes).
2. Simulation of the unsteady case (with steady results as initial values) using the inviscid models (i.e. TSD, FLMEu and FLMSDEu codes).
3. Simulation of the steady case using the viscous – inviscid interaction (VII) models, i.e. TSD+BL and FLMEu+BL codes.
4. Simulation of the unsteady case using the viscous – inviscid interaction (VII) models, i.e. TSD+BL, FLMEu+BL and FLMSDEu+BL codes.

The resulted pressure distribution at 6 cuts (stations) along the wing span are presented and compared with the experimental results from Zwaan [81]. The positions of the spanwise stations are η = 0.2, 0.325, 0.475, 0.65, 0.825 and 0.95 (see Fig. 6.26).

6.3.2.1. Results of the Inviscid Models

Figure 6.28 shows the steady pressure distribution results from the inviscid models TSD, FLMEu and FLMSDEu (the 0th harmonic pressure distribution). It can be seen that the pressure distribution calculated using all codes are in good agreement. A small difference between the TSD and the FLMEu results lies in the leading edge region, whereby the pressure distribution on the upper surface from TSD is smaller (more negative/suction) than those from FLMEu (see fig. 6.28a. and b).

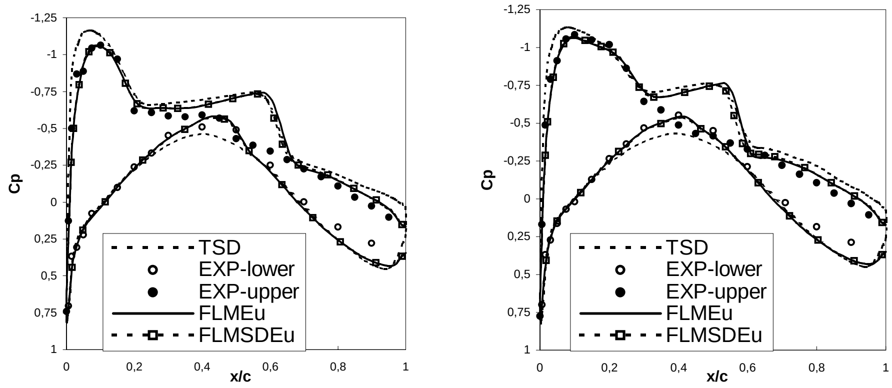

(a) η = 0.2 (b) η = 0.325

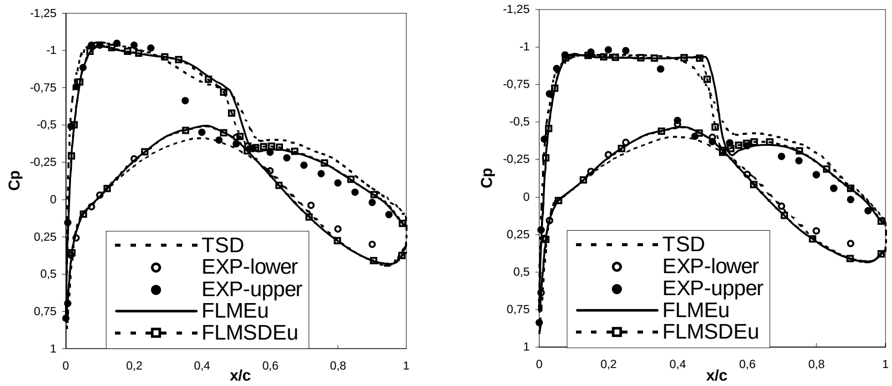

(c) η = 0.475 (d) η = 0.65

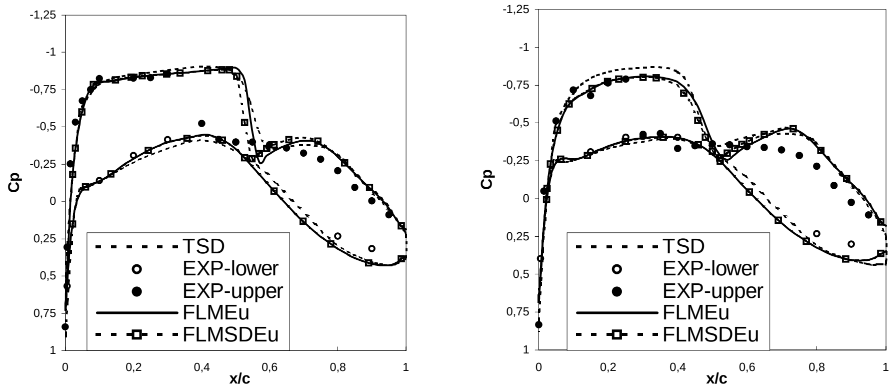

(e) η = 0.825 (f) η = 0.95

Fig. 6.28. Steady Pressure Distribution of the LANN Wing
CT5, M=0.82, $\alpha 0=0.6$
(Comparison between the TSD, FLMEu and FLMSDEu results)

The shock intensity from TSD results is small compared to those from FLMEu results. A small shift of the shock location can be observed between the FLMEu and the FLMSDEu results. The shock location from the FLMSDEu result is a little bit in front of that from the FLMEu result. Compared to the experiment, the ‘supersonic – supersonic’ shock (in the leading edge region) can be well simulated by all methods (see Fig.6.28a. and b.), but the ‘supersonic – subsonic’ shock lies far behind the experiment values for all stations.

The unsteady pressure distribution calculated by the inviscid models TSD, FLMEu and FLMSDEu are presented in Fig. 6.29 and Fig. 6.30 for real and imaginary part respectively. In order to obtain the convergent results, the simulation of the pitching oscillation was carried out using 3 cycles of the oscillation, where each oscillation is divided into 60 uniformly time steps.

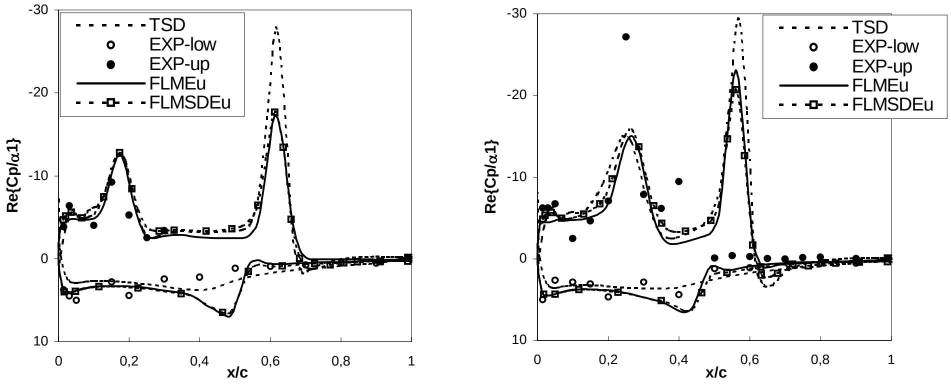

(a) η = 0.2 (b) η = 0.325

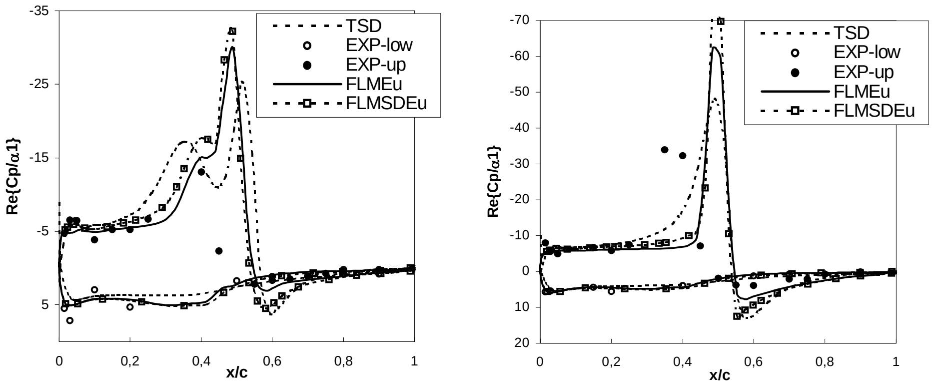

(c) η = 0.475 (d) η = 0.65

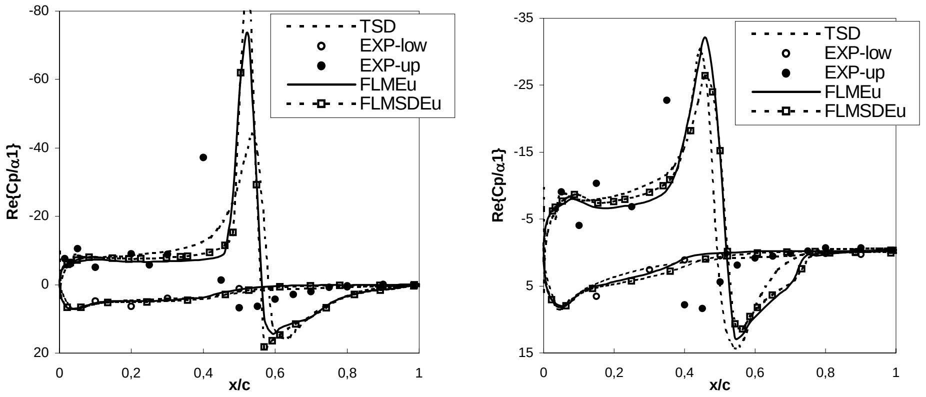

(e) η = 0.825 (f) η = 0.95

Fig. 6.29. Real Part of the Unsteady Pressure Distribution of the LANN Wing, CT5, M=0.82, α0=0.6, α1=0.25, k=0.204, xp=0.621cr (Comparison between the TSD, FLMEu and FLMSDEu results)

It can be seen that the numerical results from all inviscid methods have a good agreement in general. The shock intensity of TSD result is smaller than those from FLMEu and FLMSDEu results except at the station a (η=0.2) and b (η=0.325) for real part of the pressure distribution, where the shock intensity of TSD is larger (see fig. 6.29a and b.). The FLMSDEu supplies larger shock intensity for real part and smaller for imaginary part than from FLMEu.

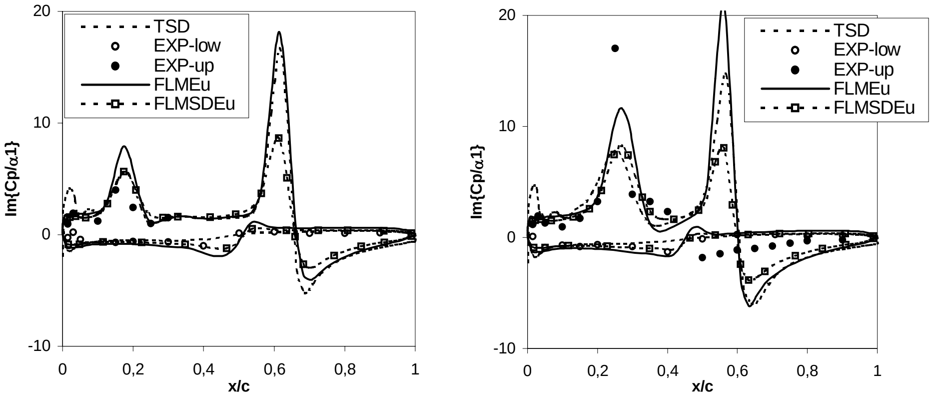

(a) η = 0.2 (b) η = 0.325

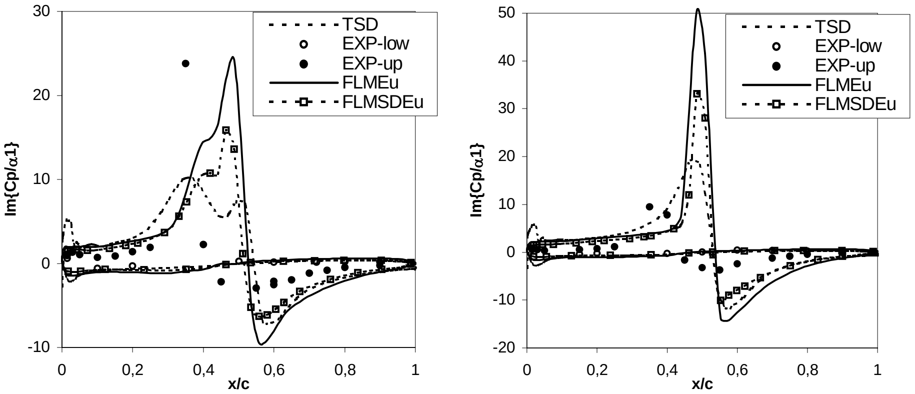

(c) η = 0.475 (d) η = 0.65

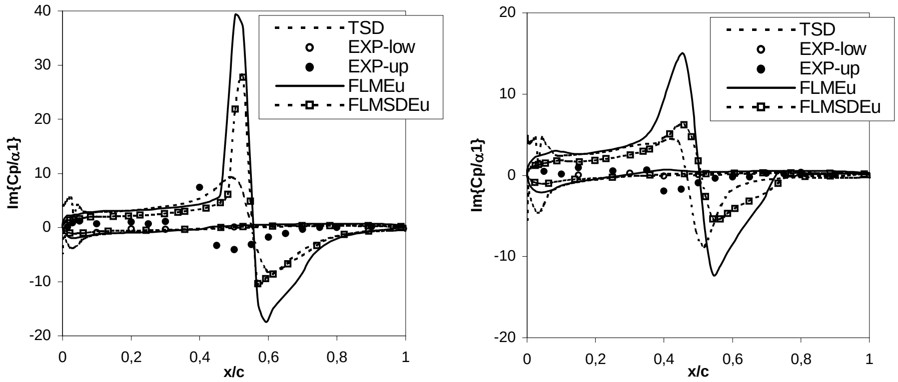

(e) η = 0.825 (f) η = 0.95

Fig. 6.30. Imaginary Part of the Unsteady Pressure Distribution of the LANN Wing,
CT5, M=0.82, α0=0.6, α1=0.25, k=0.204, xp=0.621cr
(Comparison between the TSD, FLMEu und FLMSDEu results)

All of the numerical results are not comparable with the experimental result for both the shock intensity and the shock location. The shock intensity from numerical results is larger than those from the experiment and the shock location is far behind those from the experiment.

6.3.2.2. Results of the Viscous - Inviscid Interaction (VII) Models

In fig. 6.31 the steady pressure distribution calculated by VII models (i.e. TSD+BL, FLMEu+BL and FLMSDEu+BL) are presented. The pressure distribution from all methods agree with the experimental result in general. From the leading edge to 25% of the chord all methods supply larger/more positive pressure coefficients than the experiment on the upper surface of the wing. The differences between the TSD+BL and the FLMEu+BL can be seen in the leading edge region (fig. 6.31a. and b) and in the shock region of the outboard stations (fig. 6.31c to f).

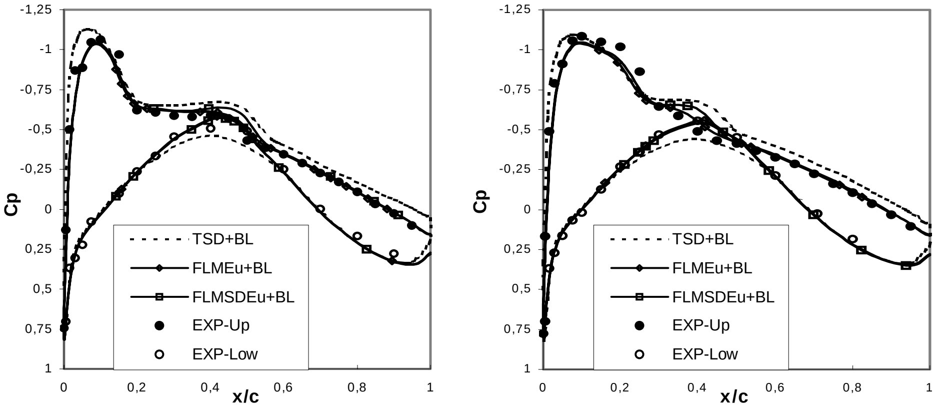

(a) η = 0.2

(b) η = 0.325

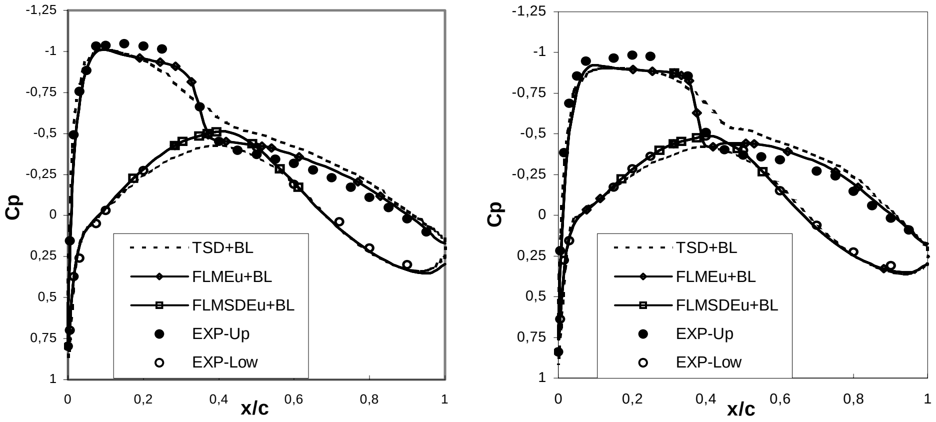

(c) η = 0.475

(d) η = 0.65

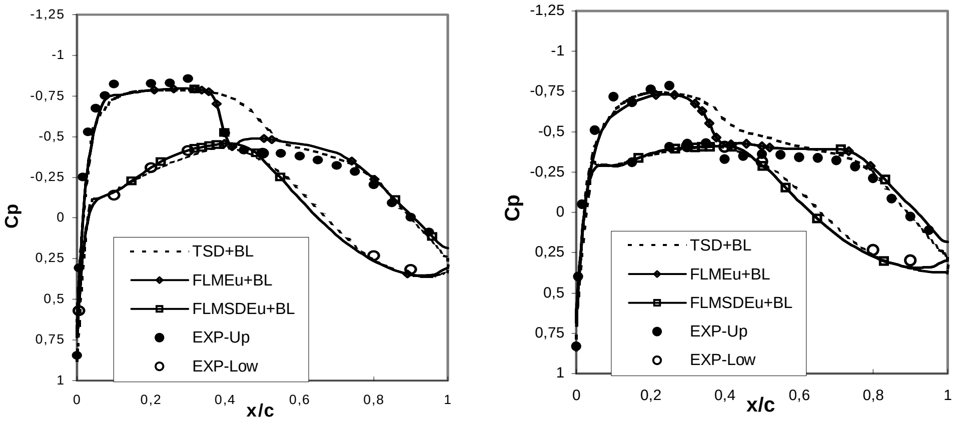

(e) η = 0.825

(f) η = 0.95

Fig. 6.31. Steady Pressure Distribution of the LANN Wing
CT5, M=0.82, Re=7.3E+06, α0=0.6
(Comparison between the TSD+BL, FLMEu+BL and FLMSDEu+BL results)

Between the FLMEu+BL and FLMSDEu+BL a small difference can be observed in the shock region at the spanwise stations a. (η=0.2) and b. (η=0.325). The shock intensity and shock location of the FLMSDEu+BL are a little bit larger than and behind those from FLMEu+BL for these stations, respectively. For other stations a difference between the FLMEu+BL and FLMSDEu+BL results is hardly recognizable. Comparison with the experimental results shows that the FLMEu+BL code supplies the best agreement of the pressure distribution for all spanwise stations.

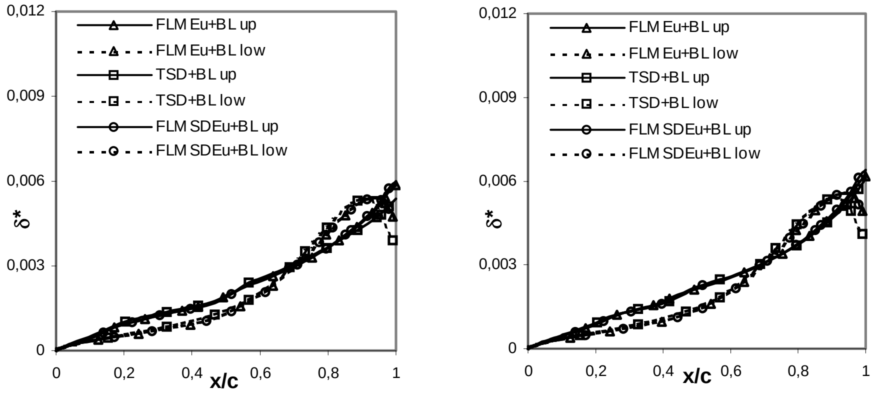

(a) η = 0.2

(b) η = 0.325

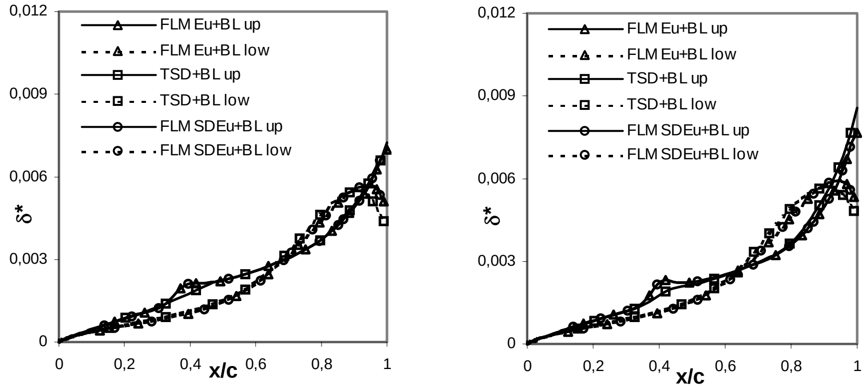

(c) η= 0.475

(d) η = 0.65

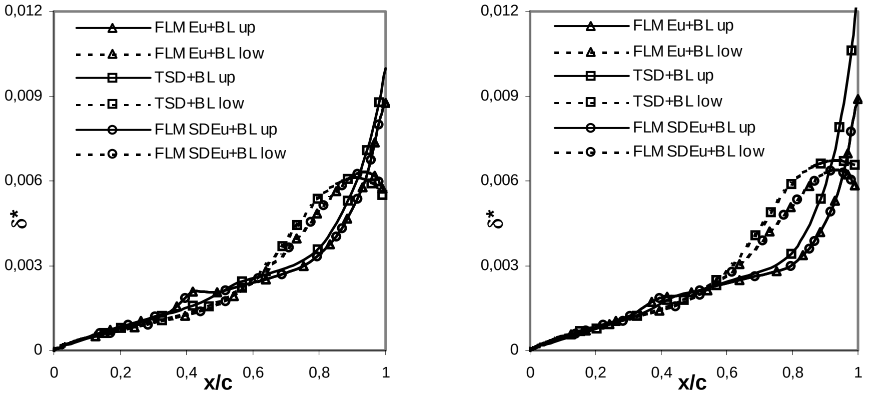

(e) η = 0.825

(f) η = 0.95

Fig. 6.32. Displacement Thickness of the LANN Wing
CT5, M=0.82, Re=7.3E+06, $\alpha0=0.6$
(Comparison between the TSD+BL, FLMEu+BL and FLMSDEu+BL results)

Figure 6.32. shows the steady displacement thickness, which was calculated by TSD+BL, FLMEu+BL and FLMSDEu+BL codes. All results of the displacement thickness in general

agree each other. Differences between result from the TSD+BL and the FLMEu+BL can be seen in the shock region at the outboard station. In the shock region on the upper surface, the displacement thickness from TSD+BL is smaller than those from FLMEu+BL (see fig. 6.32c. to f.). At the outboard station the displacement thickness after the shock from TSD+BL is larger than those from FLMEu+BL (see fig. 6.32e. and f.). For all stations a difference between the FLMEu+BL and FLMSDEu+BL results is hardly recognizable. The value of the displacement thickness per chord tends to increase from inboard to outboard station (see Fig.6.32a. to f.). This corresponds with the increasing pressure from inboard to outboard station (see also fig. 6.31a. to f.). On the lower surface of the wing, there is no change of the displacement thickness can be seen.

The steady skin friction calculated using the TSD+BL, FLMEu+BL and FLMSDEu+BL codes is presented in fig. 6.33. All results seems to show a good agreement to each other. Differences between the TSD+BL and the FLMEu+BL can be seen in the shock region. The skin friction on the upper surface calculated using TSD+BL is larger than those from FLMEu+BL (see fig. 6.33c. to f.). A difference between the FLMEu+BL and FLMSDEu+BL results almost can not be recognized. On the lower surface of the wing nearly there is no change of skin friction to be seen. Unfortunately the displacement thickness and skin friction from the experimental results are not available.

The unsteady pressure distributions calculated using the viscous – inviscid interaction (VII) models, i.e. TSD+BL, FLMEu+BL and FLMSDEu+BL, are presented in fig.6.34 and fig. 6.35 for real and imaginary part, respectively. In order to obtain the convergent results, the simulation was carried out for 3 cycles of the oscillation, each of them is divided into 60 uniformly time steps. It can be seen that all numerical results in general show a good agreement to each other. The shock intensity of TSD+BL result is smaller than that of FLMEu+BL result. At the outboard station the TSD+BL code supplies very soft shock (see fig. 6.34f. and 6.35f.), whereby the shock calculated using FLMEu+BL code is still strong. The shock location produced by TSD+BL code is behind those produced by FLMEu+BL code particularly at the inboard stations of the wing (see fig.6.34a-b and 6.35a-b).

Differences between FLMEu+BL and FLMSDEu+BL results appear mostly in the shock region for the real part of the unsteady pressure distribution. The shock intensity of the FLMSDEu+BL result is larger than those from FLMEu+BL result. The shock location of FLMSDEu+BL result is behind those of FLMEu+BL result, but in front of those of TSD+BL result particularly at inboard station of the wing (see fig.6.34a-b and 6.35a-b). For the imaginary part the unsteady pressure distribution, the results from FLMEu+BL and FLMSDEu+BL are in good agreement.

The shock intensity and location calculated from all numerical codes are in general showing good agreement with the experimental result. The best agreement with the experimental result is supplied by the FLMEu+BL code. The pressure distribution of FLMEu+BL and experiment agrees well and the shock location of the experiment can be well simulated with the FLMEu+BL code. Nevertheless the shock intensity showed by the experiment can not be completely simulated.

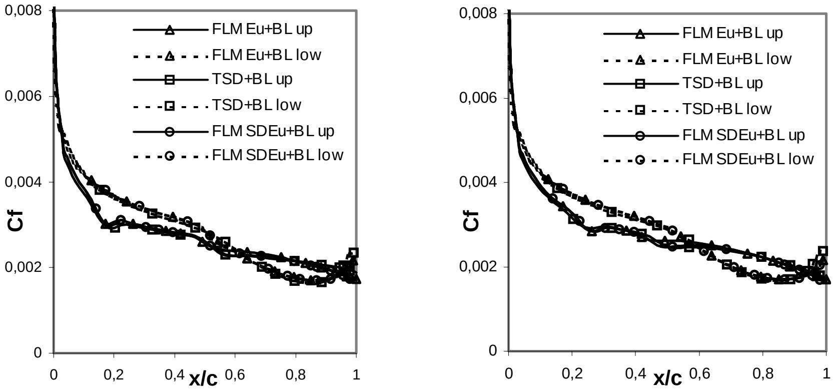

(a) η = 0.2 (b) η = 0.325

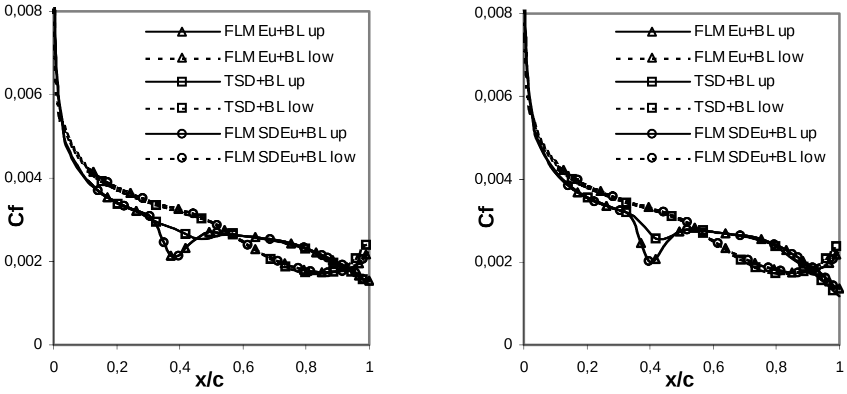

(c) η = 0.475 (d) η = 0.65

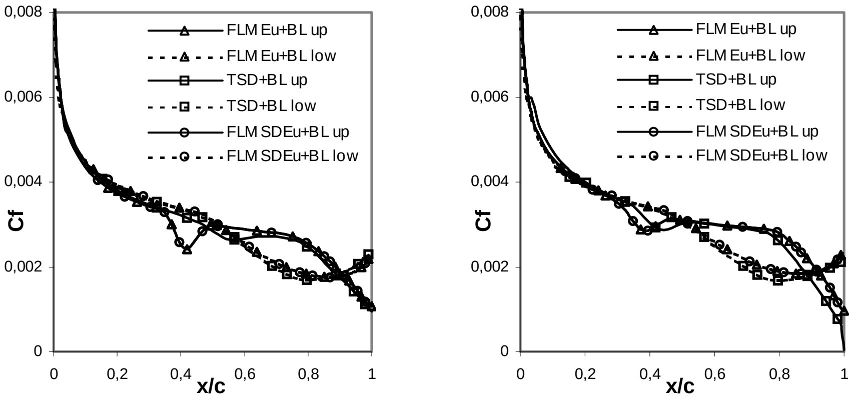

(e) η = 0.825 (f) η = 0.95

Fig. 6.33. Skin Friction of the LANN Wing
CT5, M=0.82, Re=7.3E+06, α0=0.6,
(Comparison between the TSD+BL, FLMEu+BL and FLMSDEu+BL results)

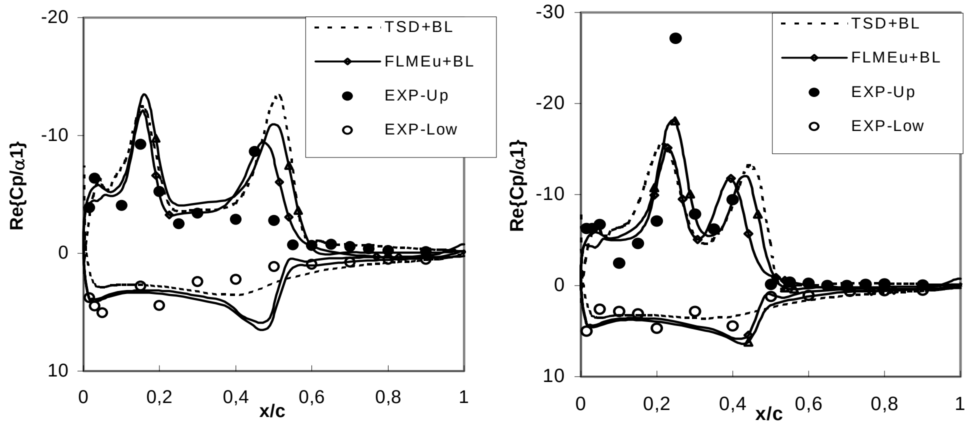

(a) η = 0.2

(b) η = 0.325

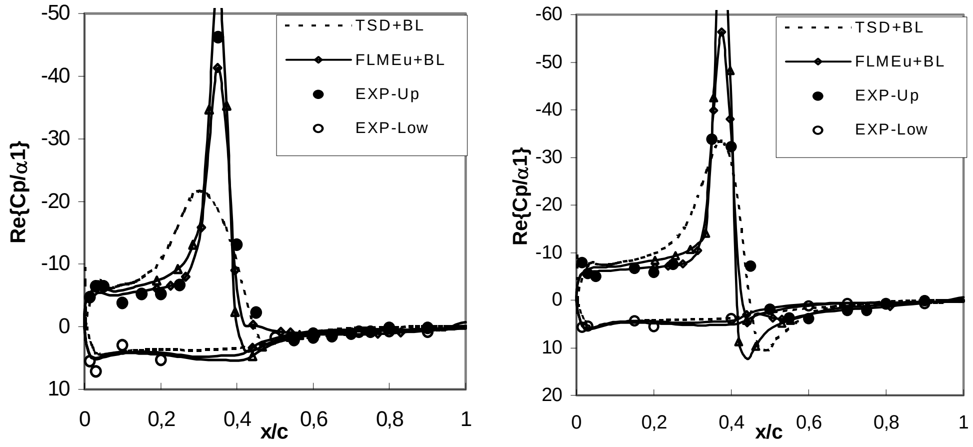

(c) η = 0.475

(d) η = 0.65

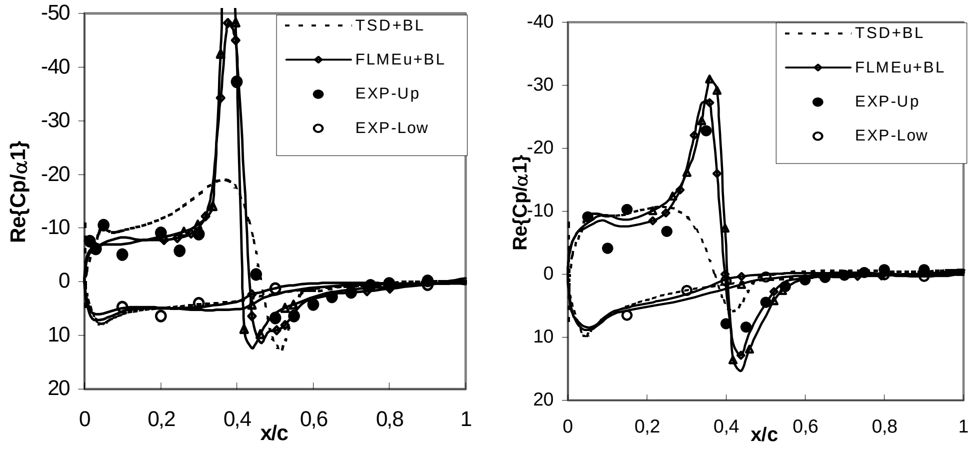

(e) η = 0.825

(f) η = 0.95

Fig. 6.34. Real Part of the Unsteady Pressure Distribution of the LANN Wing, CT5, M=0.82, Re=7.3E+06, α0=0.6, α1=0.25, k=0.204, xp=0.621cr (Comparison between the TSD+BL, FLMEu+BL and FLMSDEu+BL results)

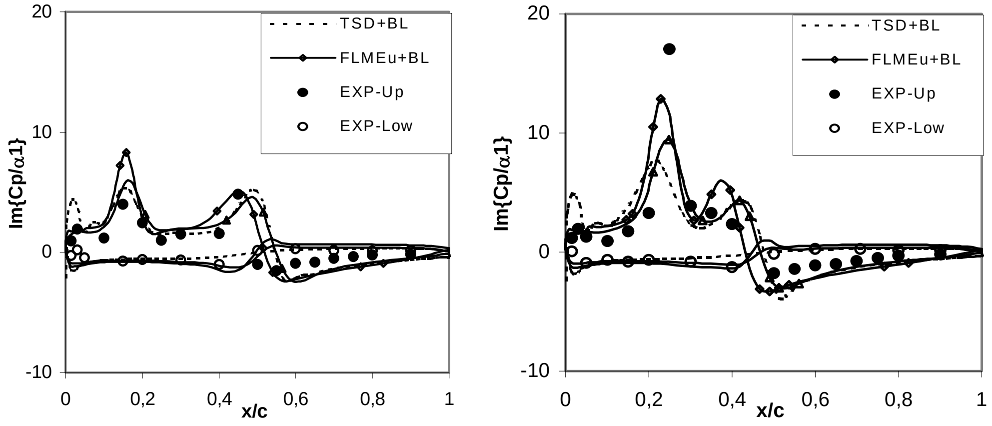

(a) η = 0.2 (b) η = 0.325

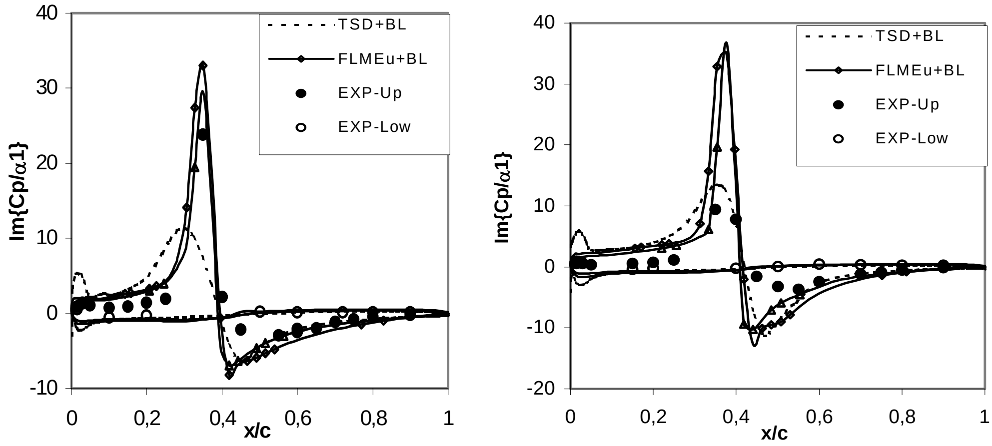

(c) η = 0.475 (d) η = 0.65

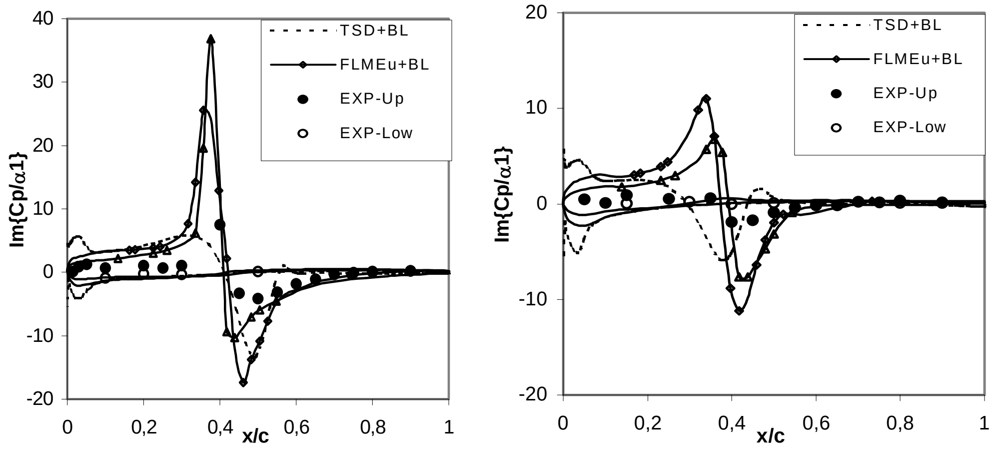

(e) η = 0.825 (f) η = 0.95

Fig. 6.35. Imaginary Part of the Unsteady Pressure Distribution of the LANN Wing, CT5, M=0.82, Re=7.3E+06, α0=0.6, α1=0.25, k=0.204, xp=0.621cr (Comparison between the TSD+BL, FLMEu+BL and FLMSDEu+BL results)

6.3.2.3. Comparison between Inviscid, VII and Navier Stokes results

In this sub chapter the results of CT5 test case calculated using inviscid model (FLMEu), VII model (FLMEu+BL) and Navier Stokes codes are compared each other, in order to examine the influence of boundary layer. The Navie Stokes results are obtained using the Navier Stokes codes from the Institute for Aerodynamics (formerly Institute for Fluid Mechanics -FLM-) of the Technical University Munich (TUM) and from the Aerospace Department of Technical University Delft (TUD). The code from FLM TUM is developed by Dipl. -Ing. Alexander Pechloff with the Spalart Almaras turbulence model (abbreviation: NS-SA) [85] and the code from TUD is developed by Dr. ir. Bima Prananta with the Baldwin Lomax turbulence model (abbreviation: NS-BL) [76]. The compared results are the Mach distribution, steady and unsteady pressure distribution and also lift-, drag-, and moment coefficients.

Figure 6.36. shows the Mach number distribution on the upper surface of the wing, which are calculated using FLMEu, FLMEu+BL and Navier Stokes codes, in steady condition.

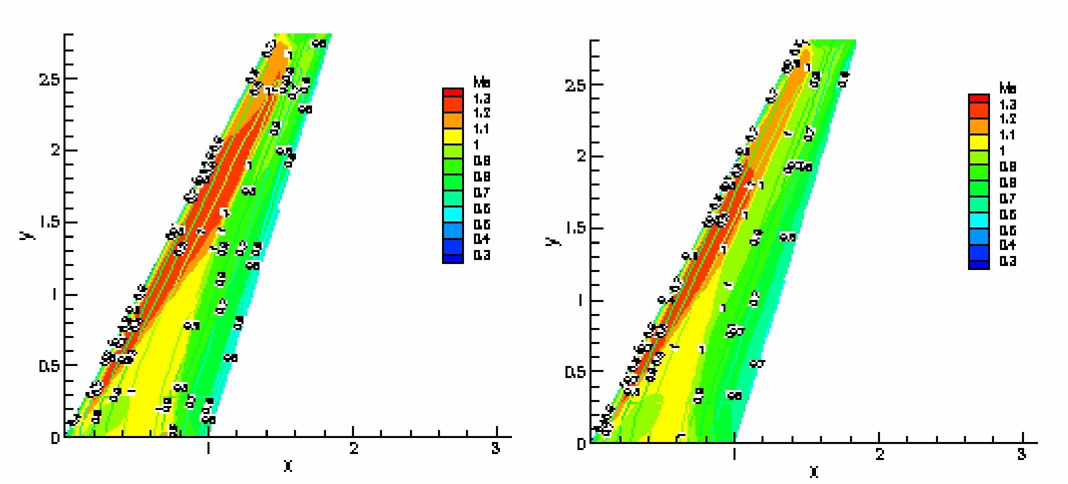

(a) Euler (FLMEu) (b) Euler + boundary layer (FLMEu+BL)

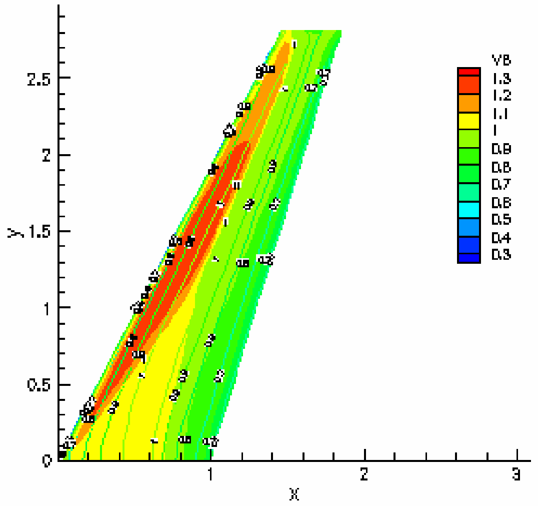

(c) Navier Stokes Spalart Almaras (NS-SA)

Fig 6.36. Mach Number Distribution on the Upper Surface of the LANN Wing
CT5 test case, M=0.82, Re=7.3E+06, α0=0.6

It can be seen that the supersonic region at the leading edge of the wing becomes smaller because of the influence of the boundary layer. The shock location is shifted forwards because of the presence of the boundary layer (see the Mach 1 line in fig. 6.36a and b.). The results from the FLMEu+BL and Navier Stokes are in good agreement (see fig. 6.36b. and c).

The steady pressure distributions calculated from FLMEu, FLMEu+BL and Navier Stokes (NS-SA and NS-BL) codes are presented in fig. 6.37. The pressure distribution on the upper surface of the wing is strongly different with the presence of the boundary layer (see FLMEu and the FLMEu+BL results). The shock from FLMEu+BL lies in front of that from FLMEu with weaker intensity. The shock location resulted from FLMEu+BL is mostly in front of the shock of NS-SA and NS-BL results (see fig. 6.37a, c, d and e). Between the NS-SA and the NS-BL results there is almost no differences to be seen. The shock of NS-SA seems to be sharper than that from NS-BL. On the lower surface of the wing the deviation between inviscid and VII results is in the trailing edge region, where the FLMEu+BL gives more negative pressure compared to the FLMEu results and shows good agreement with Navier Stokes results.

Table 6.12. shows the aerodynamic coefficients (lift, drag and moments) for steady condition of CT5 case, which was computed using TSD, FLMEu, FLMSDEu (with and without boundary layer) and Navier Stokes codes. The influence of the boundary layer can be seen from the changing of the aerodynamic coefficients. The lift and drag coefficient become smaller and the moment coefficient becomes larger (more positive) because of the presence of the boundary layer.

It can be seen from this table that the lift coefficient from all numerical results are larger than that from the experimental result. The best agreement with the experimental result was given by the FLMEu+BL code, which has 5.31% error compared to the experimental value. On the other side the Navier Stokes code NS-SA produced approximately 12 % error and the TSD+BL code gives approximately 10% error from the experiment for lift coefficient. It seems that the influence of the boundary layer on the Euler equations is larger than its influence on the TSD the equation and the Euler + boundary layer code gives underestimated value compared to the Navier Stokes.

A different sign between experimental and numerical results can be seen for the moment coefficient. The moment coefficient from the experiment is positive (leading edge upwards) but all calculations results show negative moment coefficient (leading edge downwards).

Table 6.12. Steady Aerodynamic Coefficients of CT5 Case of LANN Wing

	C_L	Error C_L (%)	C_D	C_M
EXP	0.320		-	0.037
NS-SA	0.359	12.34	0.0203	-0.0597
FLMEu	0.447	39.69	0.0225	-0.0794
FLMEu+BL	0.337	5.31	0.0186	-0.0557
FLMSDEu	0.442	38.12	0.0222	-0.0787
FLMSDEu+BL	0.349	9.06	0.0189	-0.0586
TSD	0.453	41.56	0.0234	-0.0810
TSD+BL	0.353	10.31	0.0205	-0.0606

In figures 6.38 and 6.39, the real and imaginary parts of the unsteady pressure distribution calculated using FLMEu, FLMEu+BL and Navier Stokes codes are presented. The Navier Stokes results was computed using the Navier Stokes code from the Technical University Delft with Baldwin Lomax turbulence model (NS-BL). The unsteady results from Navier Stokes with turbulence model Spalart Almaras (NS-SA) are unfortunately unavailable. The unsteady pressure distribution on the upper surface of the wing is strongly changed because of the presence of the boundary layer. From the comparison between the FLMEu and the FLMEu+BL the following can be written: the shock location shifts forward and the shock intensity becomes smaller because of the boundary layer.

Comparison with NS-BL result shows that the shocks of FLMEu+BL lie in front of those of NS-BL result with stronger intensity (see fig. 6.38 and 6.39).

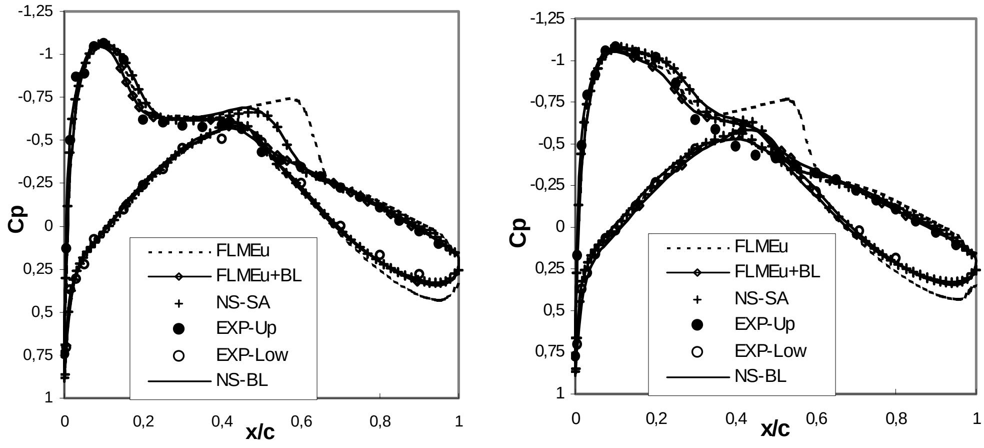

(a) η = 0.2 (b) η = 0.325

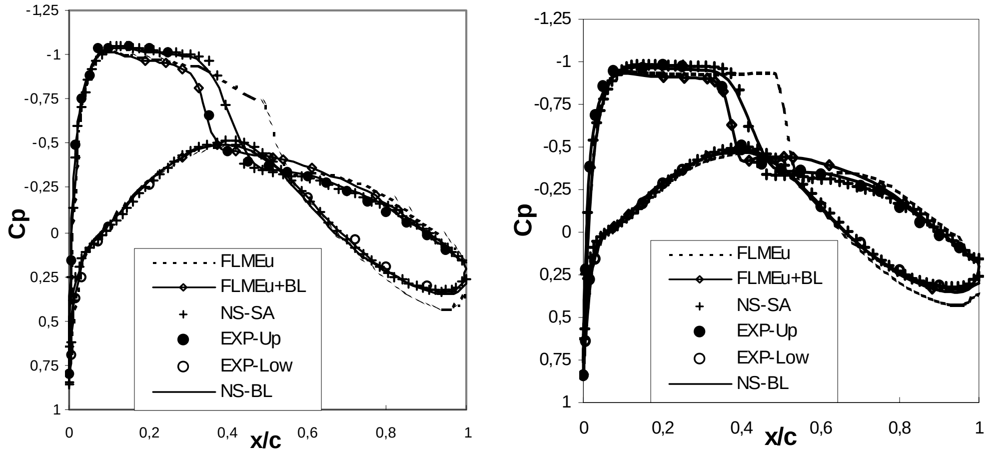

(c) η = 0.475 (d) η = 0.65

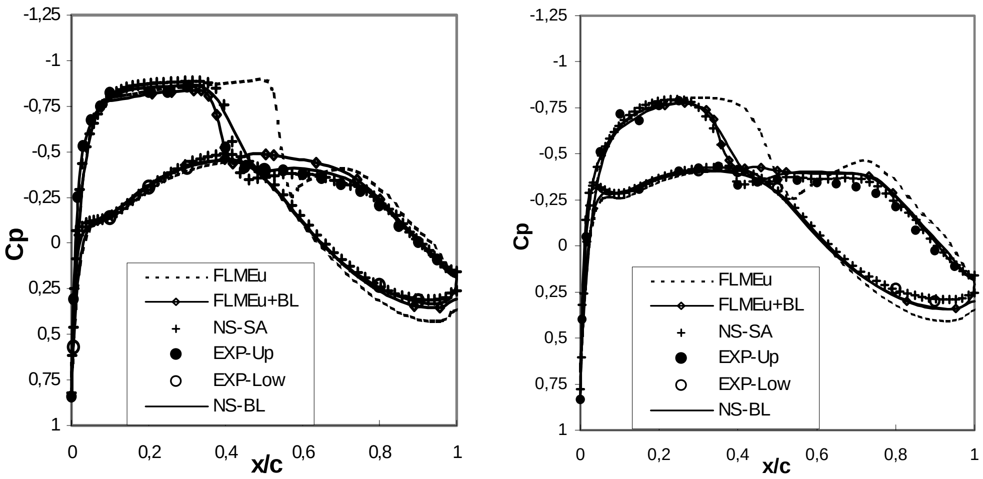

(e) η = 0.825 (f) η = 0.95

Fig. 6.37. Steady Pressure Distribution of LANN Wing,
CT5, M=0.82, Re=7.3E+06, α0=0.6, α1=0.25, k=0.204, xp=0.621cr
(Comparison between Euler, Euler+BL and Navier-Stokes Results)

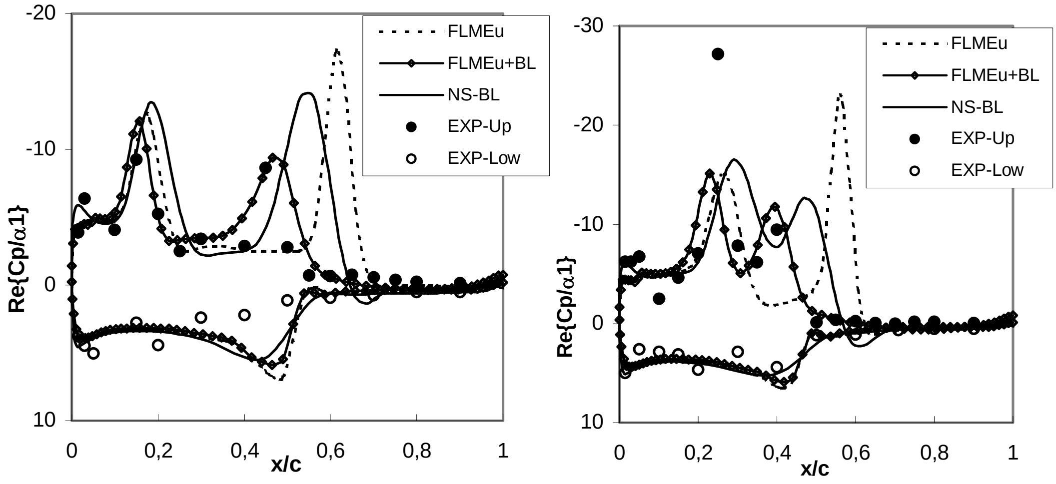

(a) η = 0.2

(b) η = 0.325

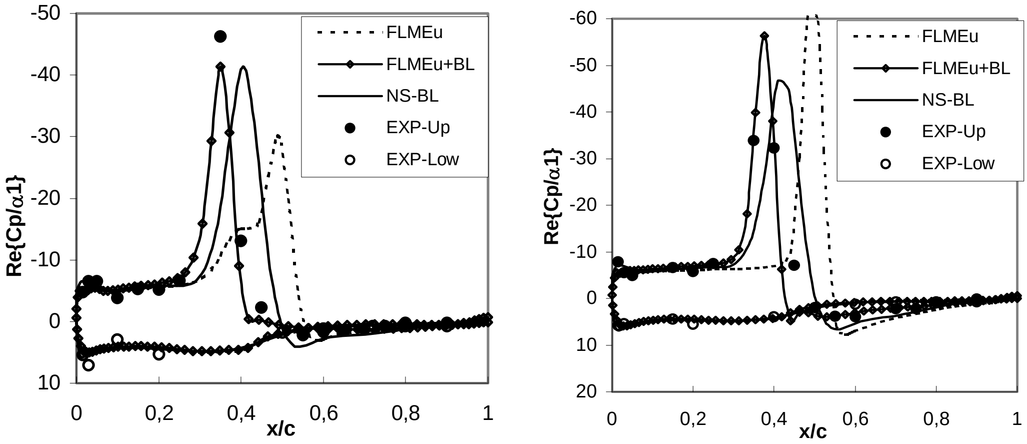

(c) η = 0.475

(d) η = 0.65

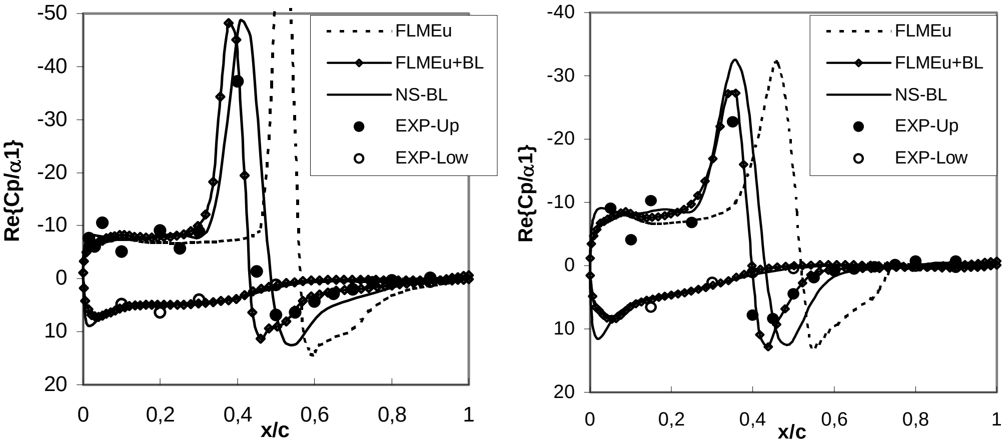

(e) η = 0.825

(f) η = 0.95

Fig. 6.38. Real Part of Unsteady Pressure Distribution of LANN Wing, CT5, M=0.82, Re=7.3E+06, α0=0.6, α1=0.25, k=0.204, xp=0.621cr (Comparison between Euler, Euler+BL and Navier-Stokes Results)

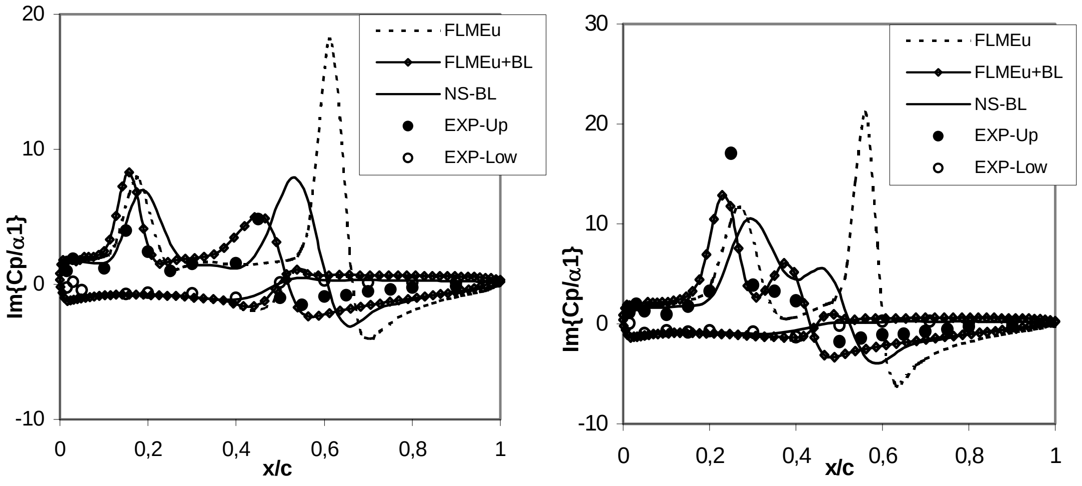

(a) η = 0.2

(b) η = 0.325

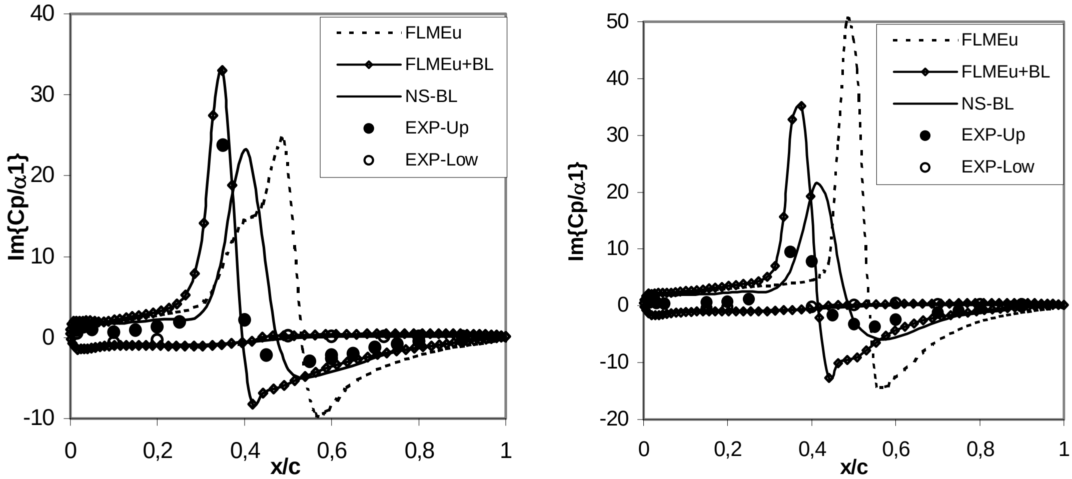

(c) η = 0.475

(d) η = 0.65

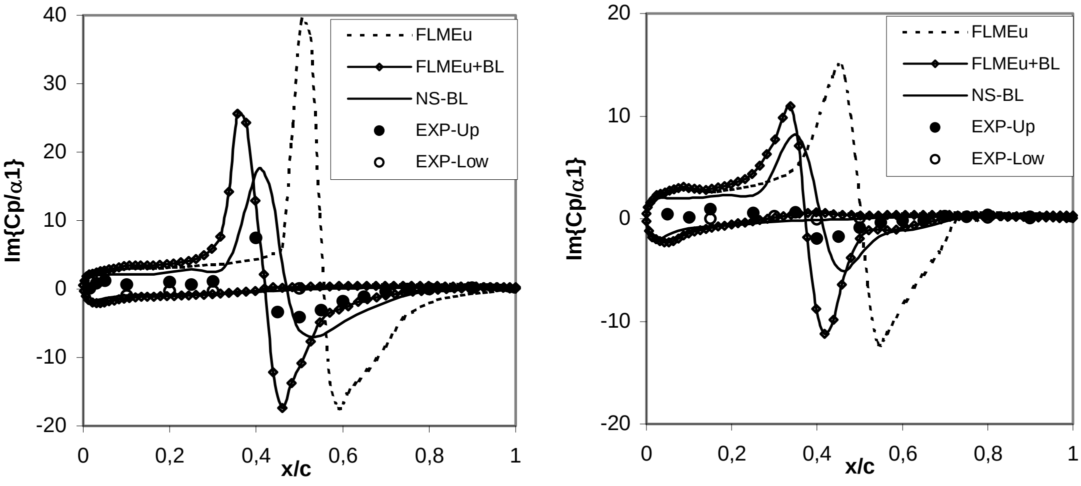

(e) η = 0.825

(f) η = 0.95

Fig. 6.39. Imaginary Part of Unsteady Pressure Distribution of LANN Wing, CT5, M=0.82, Re=7.3E+06, α0=0.6, α1=0.25, k=0.204, xp=0.621cr (Comparison between Euler, Euler+BL and Navier-Stokes Results)

Table 6.13 and fig. 6.40. represent the aerodynamic coefficients (lift and moment) for unsteady CT5 case, which was computed using TSD, FLMEu and FLMSDEu (with and without boundary layer) codes. The C_L^* and C_M^* mean: C_L and C_M divided with $\pi\alpha_1$ ($C_L^* = C_L/\pi\alpha_1$, $C_M^* = C_M/\pi\alpha_1$). The influence of the boundary layer can be measured by the changing of the aerodynamic coefficient. The amplitude of the unsteady lift and moments become smaller and the phase angles of the lift and moments become larger (more positive) because of the presence of the boundary layer. The unsteady lift and moment coefficient as function of angle of attack are presented in fig. 6.41. It can be seen clearly that the unsteady lift and moment are strongly changed due to boundary layer.

Table 6.13. Unsteady Aerodynamic Coefficients of CT5 Case of LANN Wing

	Re{C_L^*}	Im{C_L^*}	$\lvert C_L^*\rvert$	Phase C_L^*(deg)	Re{C_M^*}	Im{C_M^*}	$\lvert C_M^*\rvert$	Phase C_M^*(deg)
EXP	1.889	-0.296	1.912	-8.91	0.453	0.156	0.479	19
FLMEu	2.108	-0.658	2.208	-17.30	-1.350	0.312	1.385	166.99
FLMEu+BL	1.919	-0.349	1.950	-10.31	-1.159	0.149	1.168	172.67
FLMSDEu	2.261	-0.659	2.355	-16.25	-1.482	0.296	1.511	168.70
FLMSDEu+BL	2.191	-0.369	2.221	-9.56	-1.342	0.141	1.349	174
TSD	2.212	-0.591	2.289	-14.96	-1.490	0.271	1.514	169.69
TSD+BL	2.126	-0.292	2.146	-7.82	-1.361	0.113	1.366	175.25

$C_L^* = C_L/\pi\alpha_1$, $C_M^* = C_M/\pi\alpha_1$

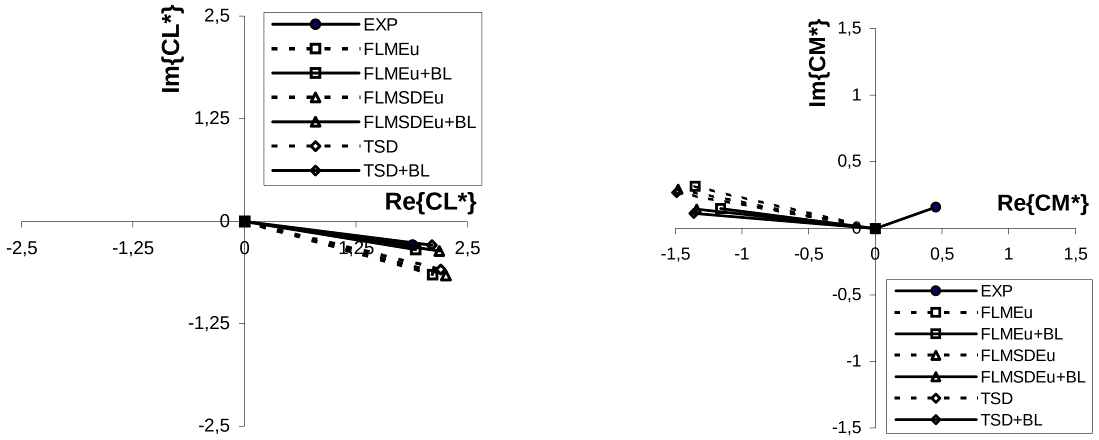

Fig. 6.40. Unsteady Aerodynamic Coefficients of CT5 Case of LANN Wing

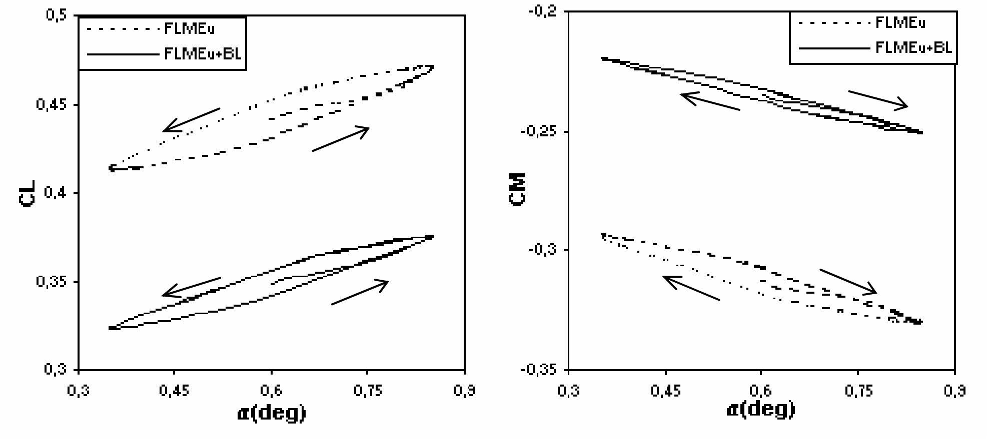

(a) Lift (b) Moment

Fig. 6.41. Unsteady Lift and Moment Coefficients of LANN Wing, CT5, M=0.82, Re=7.3E+06, α0=0.6, α1=0.25, k=0.204, xp=0.621cr (Comparison between Euler and Euler+BL Results)

6.3.3. Test Case E24 for Delta Wing of NASA

This sub chapter presents the results of the developed VII method used to simulate the test case E24 of the delta wing of NASA Langley. The geometry of the wing is presented in Fig. 6.42 and Table 6.14. The wing has a parabolic airfoil with 6% thickness along the wing span.

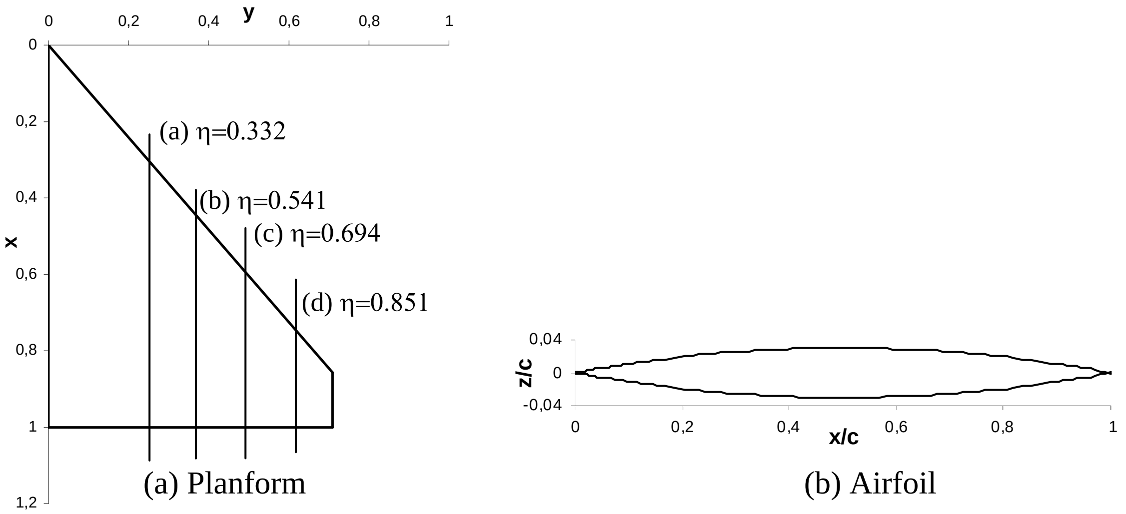

(a) Planform

(b) Airfoil

Fig. 6.42. Geometry of Delta Wing of NASA Langley

Table 6.14. Geometric Parameter of Delta Wing of NASA Langley

Parameter		
Span	s	0.7094
Root Chord	cr	1.0
Taper Ratio	ct/cr	0.1423
Aspect Ratio	AR	1.242
Sweep : Leading Edge	φ_{LE}	50.4^{o}
Trailing Edge	φ_{TE}	0.0^{o}
Thickness	t/c	6%
Twist	θ	0.0^{o}

For the simulation of this case the TSD and the non linear FLMEu codes are used both with and without boundary layer coupling. As the boundary layer calculation method is again the method of Drela and Giles. The simulation parameters of the test case E24 is shown in Table 6.15. The grid parameters for this simulation is presented in Table 6.16. The grid used for FLMEu code is depicted in Fig. 6.43.

Table 6.15. Parameter of Simulation of Test Case E24 for Delta Wing of NASA

Parameter of simulation			Remark
Mach number	M	0.885	
Reynolds number	Re	1.0E+07	based on the root chord
Mean angle of attack	α_0	$0.0\ ^{o}$	
Amplitude angle of attack	α_1	$0.5\ ^{o}$	
Reduced Frequency	*k*	0.346	based on the root chord
Pitching axis	x_p/cr	0.652	from LE of the root chord
Moment ref. axis	x_m/cr	0.25	from LE of the root chord

Table 6.16. Grid parameter for Simulation of Test Case E24 for Delta Wing of NASA

Grid parameter	TSD	FLMEu
Grid type (xz – yz plane)	H-H	C-H
Surface cells (x and y direction)	2400 (120 x 20)	2640 (120 x 22)
Total cells (x, y and z direction)	144000 (160 x 30 x 30)	153600 (160 x 32 x 30)
Offbody distance	10^{-3} cr	10^{-3} cr
Far field distance:		
above, below	10 cr	10 cr
fore, aft	10 cr	10 cr
spanwise	2 s	2 s

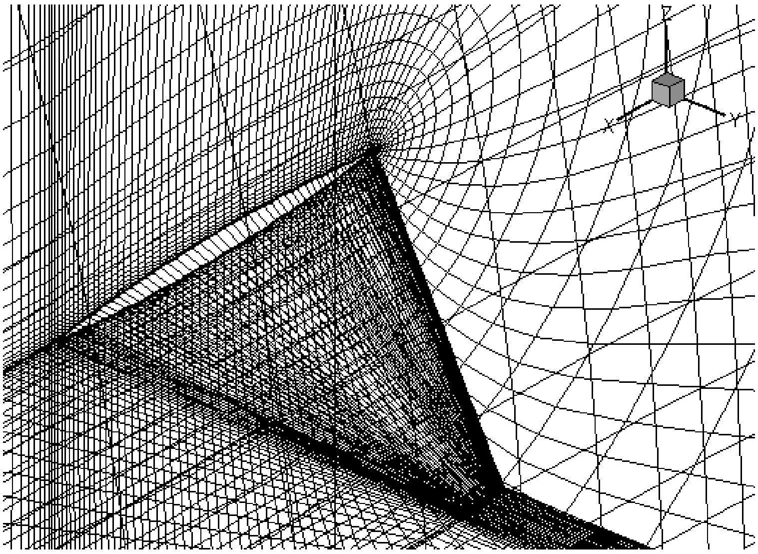

Fig. 6.43. Grid in the Near-Field for FLMEu Code

The simulation was accomplished with the following order:

1. Simulation of steady condition of test case E24 (calculated with mean angle of attack without pitching motion) using TSD and FLMEu codes.
2. Simulation of unsteady of test case E24 (with the steady initial values from step 1) using TSD and FLMEu codes.
3. Simulation of steady condition of the case by TSD plus boundary layer and FLMEu plus boundary layer codes.
4. Simulation of unsteady of test case E24 by TSD plus boundary layer and FLMEu plus boundary layer codes.

The pressure distribution from numerical result at four spanwise stations are presented and compared with the experimental result from Bennet and Walker [82]. The positions of the spanwise stations are η = 0.332, 0.541, 0.694, and 0.851 (see Fig. 6.42).

In fig. 6.44 the steady pressure distribution resulted from inviscid models (TSD and FLMEu) and from viscous - inviscid models (TSD+BL and FLMEu+BL) are presented. It can be seen that the pressure distribution between the TSD and the FLMEu agrees well each other. A small difference between the TSD and the FLMEu codes lies in the leading edge region, whereby the pressure distribution on the upper surface from TSD result is smaller (more negative) than those from FLMEu (see Fig. 6.44). The shock position and the shock intensity between the TSD and FLMEu are a little bit different. The shock location from TSD result lies behind that from FLMEu with larger shock intensity. The inclusion of boundary layer in the calculations makes the shock intensity smaller and shifts the shock location a little bit forward (see Fig.6.44). The influence of the boundary layer in this case is small or not so meaningful. Comparing with the experimental result, all numerical results are in good agreement at inboard stations, but at outboard stations are more positive than the experimental result.

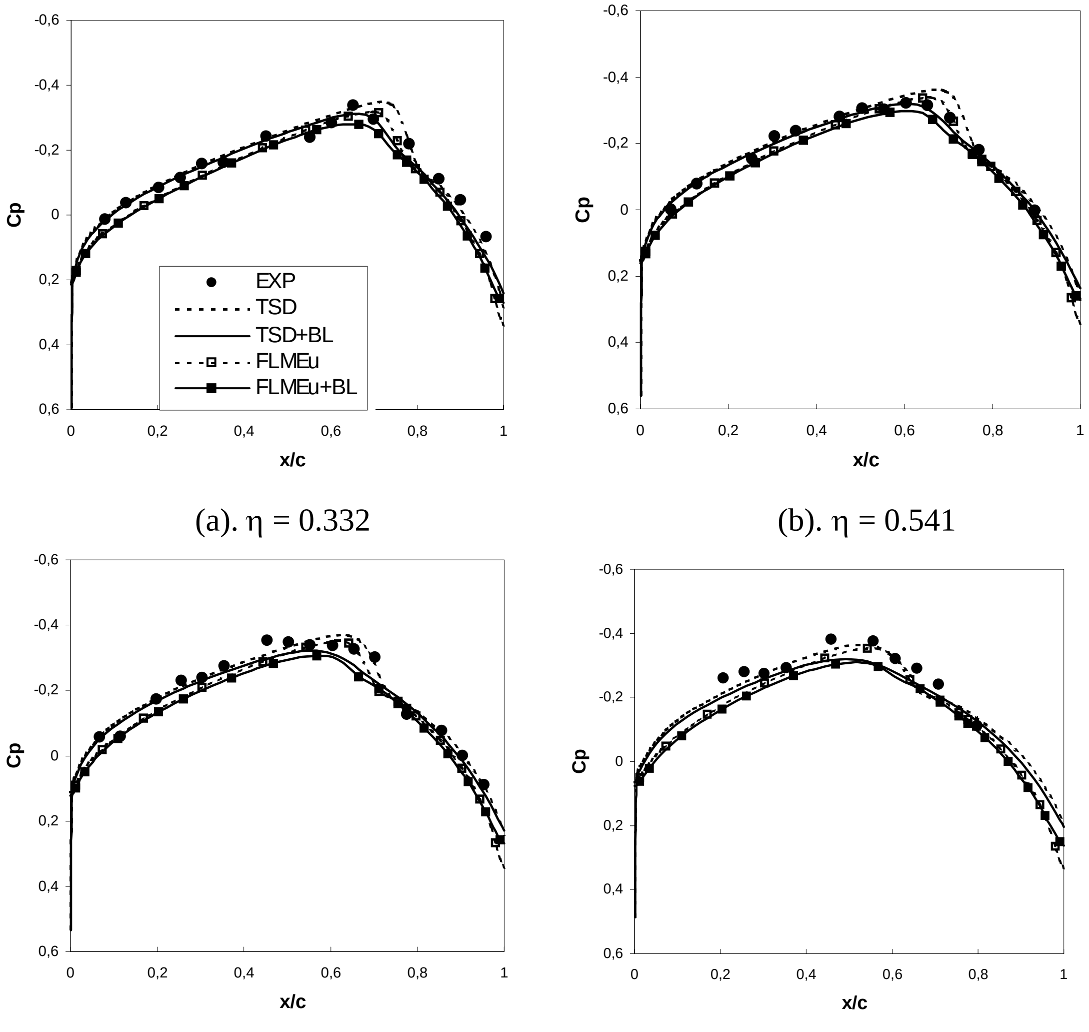

(a). η = 0.332

(b). η = 0.541

(c). η = 0.694

(d). η = 0.851

Fig. 6.44. Steady Pressure Distribution of Delta Wing from NASA
Test Case E24, M = 0.885, α0 = 0, Re=1.0E+07

The displacement thickness and skin friction for this test case are presented in Fig. 6.45. Between the TSD+BL and the FLMEu+BL result can be seen a small difference within the trailing edge region. The skin friction from FLMEu+BL in this region is lower than those from TSD+BL. Inversely, the displacement thickness from FLMEu+BL is larger than those from TSD+BL within this region. The displacement thickness of the two results (TSD+BL and FLMEu+BL) at the outboard stations look larger than those at the inboard stations.

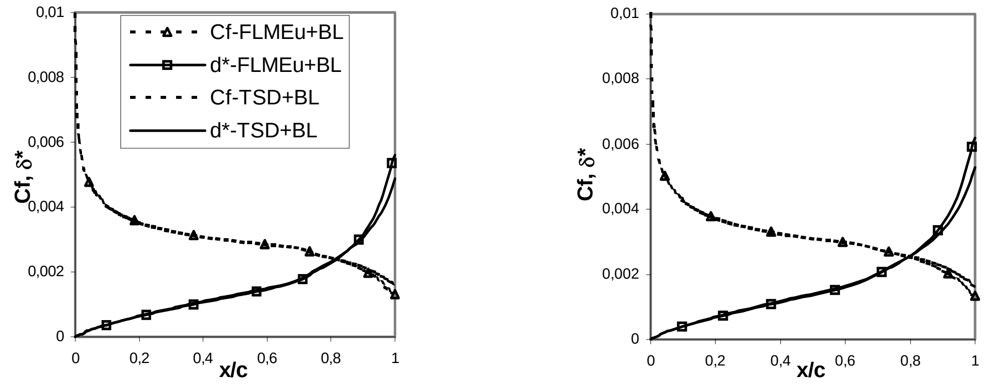

(a). η = 0.332 (b). η = 0.541

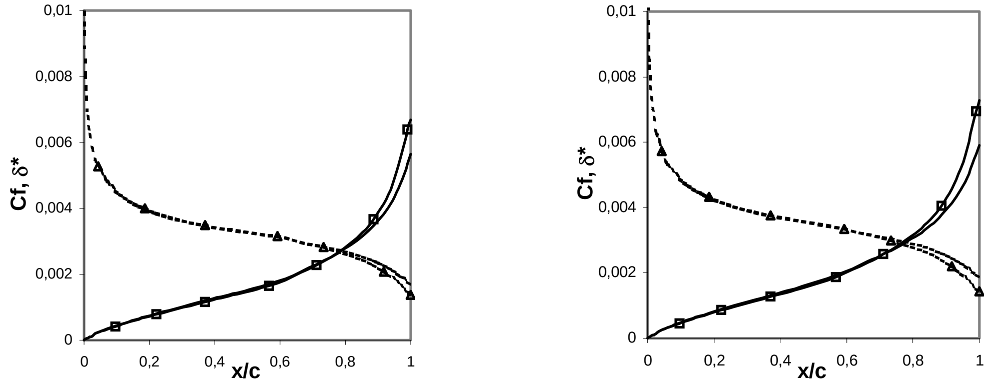

(c). η = 0.694 (d). η = 0.851

Fig. 6.45. Displacement Thickness and Skin Friction of the Upper Surface of Delta Wing from NASA, Test Case E24, M = 0.885, α0 = 0, Re=1.0E+07

Figures 6.46 and 6.47 represent the real part and the imaginary part of the unsteady pressure distribution of the test case E24. It can be seen that the influence of the boundary layer must be considered. The shock location and shock intensity were affected strongly by the boundary layer. The best agreement with the experimental result is supplied by the FLMEu+BL code rather than by the TSD+BL code. For all stations the real part of the unsteady pressure distribution of the test case E24 can be well simulated (see Fig.6.46), but unfortunately the imaginary part of the unsteady pressure distribution of the experiment cannot be well simulated by these calculations. The numerical results are more positive than those of the experiment (see Fig. 6.47)

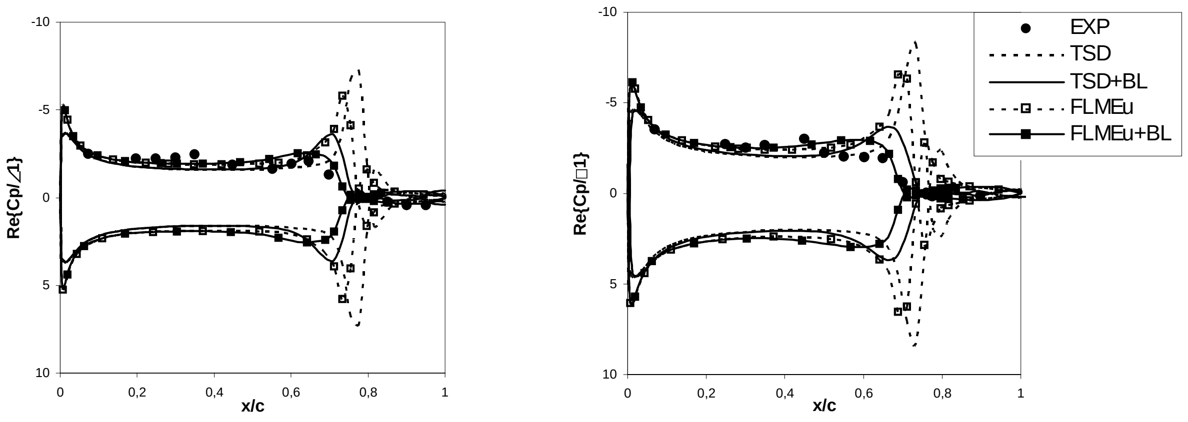

(a). η = 0.332 (b). η = 0.541

Fig. 6.46. Real Part of Unsteady Pressure Distribution of Delta Wing from NASA Test Case E24, M = 0.885, Re=1.0E+07, α0 = 0, α1 = 0.5, k = 0.346, xp = 0.652cr

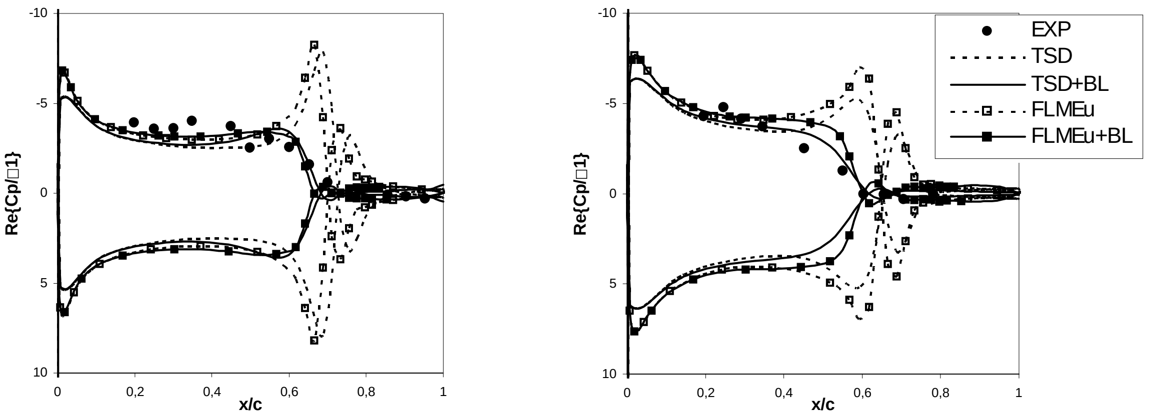

(c). η = 0.694 (d). η = 0.851

Fig. 6.46. Real Part of Unsteady Pressure Distribution of Delta Wing from NASA Test Case E24, M = 0.885, Re=1.0E+07, α0 = 0, α1 = 0.5, k = 0.346, xp = 0.652cr

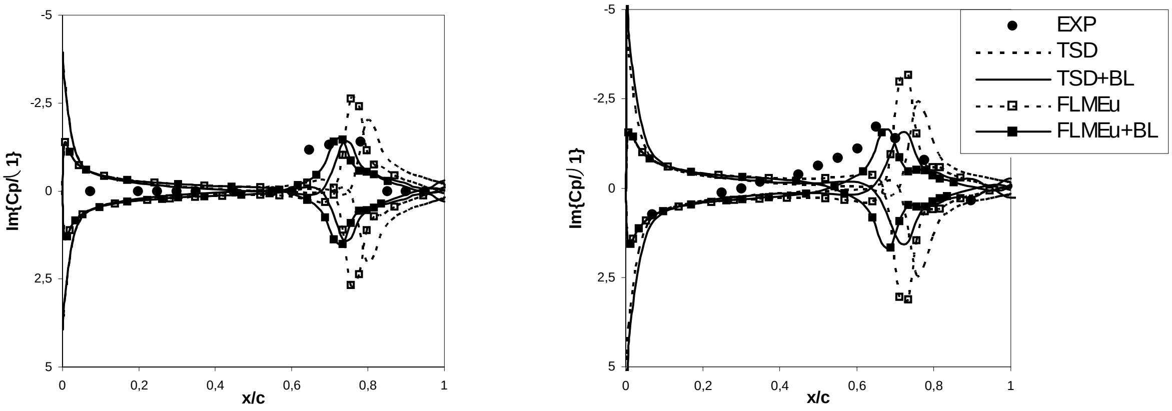

(a). η = 0.332 (b). η = 0.541

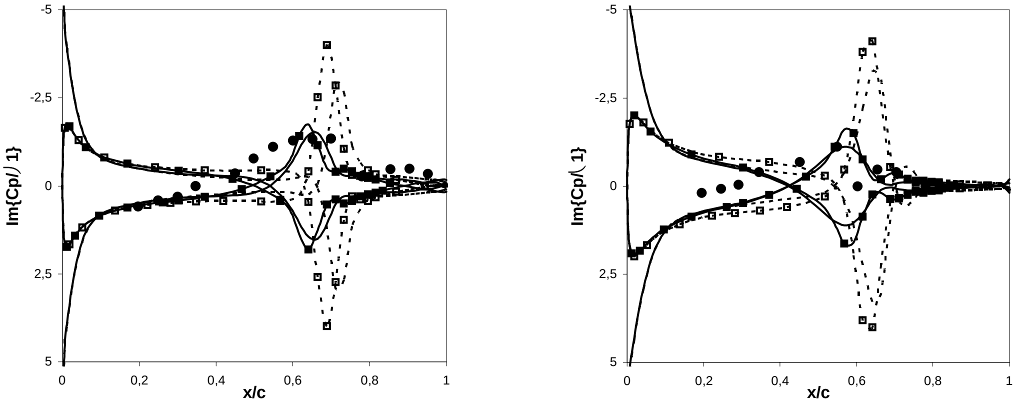

(c). η = 0.694 (d). η = 0.851

Fig. 6.47. Imaginary Part of Unsteady Pressure Distribution of Delta Wing from NASA Test Case E24, M = 0.885, Re=1.0E+07, α0 = 0, α1 = 0.5, k = 0.346, xp = 0.652cr

7. Flutter Results

In this chapter the flutter results for two airfoils and a wing are presented. The selected airfoils are NACA 64A010 and NLR 7301 with the structural data proposed by Isogai [86] and DLR [87], respectively. The selected wing is the AGARD wing 445.6 with structural data from NASA [88]. The computation of the unsteady aerodynamic forces, which is necessary for the flutter analysis, is carried out using the TSD and TSD plus boundary layer (TSD+BL) codes, in order to examine the influence of the boundary layer on the flutter results. The boundary layer calculation method of Drela-Giles is used to compute the boundary layer parameters. The modal and flutter analysis are performed with the State Transition Matrix method, as already discussed in Chapter 5. The flutter results are compared with experimental data and other numerical calculations.

7.1. Transonic Dip of the Isogais Model

The flutter characteristic of the Isogais model is computed for various Mach numbers, in order to examine the 'Transonic Dip', that is the lowest flutter speed in transonic regime.

7.1.1. The Isogais Model

The aeroelastic equation for a 2 Degree of Freedom (DoF) system can be derived from force analysis, i.e. equilibrium of the forces, as follows (see Fig. 7.1):

$$\begin{aligned} &m_1\left(\ddot{h}+x_\alpha b\ddot{\alpha}\right)+k_h h+L=0 \\ &m_1 x_\alpha b\ddot{h}+I_\alpha\ddot{\alpha}+k_\alpha\alpha-M_{ea}=0 \end{aligned} \tag{7.1}$$

where:

h, α = physical displacement (i.e. heaving and pitching DoF)
m_1 = mass of system
k_h = stiffness of system in heaving motion = $m_1\ \omega_h^2$
k_α = stiffness of system in pitching motion = $I_\alpha\ \omega_\alpha^2$
I_α = moment of inertia of system = $m_1 r_\alpha^2 b^2$
r_α = radius of gyration = $(I_\alpha / m_1 b^2)^{1/2}$
x_α = static unbalance (normalised with semi chord b)
b = semi chord
ω_h = uncoupled natural frequency in heaving motion
ω_α = uncoupled natural frequency in pitching motion
L = aerodynamic force (positive up)
M_{ea} = aerodynamic moment w.r.t. elastic axis (positive 'nose up')

Equation (7.1) will be normalised with mass (m_1) and semi chord (b) as follows:

$$\begin{aligned} &\frac{\ddot{h}}{b}+x_\alpha\ddot{\alpha}+\omega_h^2\frac{h}{b}=\frac{-L}{m_1 b} \\ &x_\alpha\frac{\ddot{h}}{b}+r_\alpha^2\ddot{\alpha}+r_\alpha^2\omega_\alpha^2\alpha=\frac{M_{ea}}{m_1 b^2} \end{aligned} \tag{7.2}$$

which can be written in matrix notation as:

$$\begin{bmatrix} 1 & x_\alpha \\ x_\alpha & r_\alpha^2 \end{bmatrix}\begin{Bmatrix} \dfrac{\ddot{h}}{b} \\ \ddot{\alpha} \end{Bmatrix}+\begin{bmatrix} \omega_h^2 & 0 \\ 0 & r_\alpha^2\omega_\alpha^2 \end{bmatrix}\begin{Bmatrix} \dfrac{h}{b} \\ \alpha \end{Bmatrix}=\begin{Bmatrix} \dfrac{-L}{m_1 b} \\ \dfrac{M_{ea}}{m_1 b^2} \end{Bmatrix} \tag{7.3}$$

Here the physical displacements (h/b) and α are still a function of time t , as:

$$(h/b) = f(t),\ \alpha = f(t)$$

The time variable t will be transformed into non dimensional time τ as follows:

$$t = \frac{\tau}{\omega_\alpha} \tag{7.4}$$

With this non dimensional time variable, the derivative of the physical displacement will be transformed to:

$$\begin{aligned} \frac{d^2(h/b)}{dt^2} &= \omega_\alpha^2 \frac{d^2(h/b)}{d\tau^2} \\ \frac{d^2\alpha}{dt^2} &= \omega_\alpha^2 \frac{d^2\alpha}{d\tau^2} \end{aligned} \tag{7.5}$$

Equation (7.3) will be transformed into non dimensional form as follows:

$$\begin{bmatrix} 1 & x_\alpha \\ x_\alpha & r_\alpha^2 \end{bmatrix} \begin{Bmatrix} \ddot{\dfrac{h}{b}} \\ \ddot{\alpha} \end{Bmatrix} + \begin{bmatrix} \left(\dfrac{\omega_h}{\omega_\alpha}\right)^2 & 0 \\ 0 & r_\alpha^2 \end{bmatrix} \begin{Bmatrix} \dfrac{h}{b} \\ \alpha \end{Bmatrix} = \begin{Bmatrix} \dfrac{-L}{m_1 b \omega_\alpha^2} \\ \dfrac{M_{ea}}{m_1 b^2 \omega_\alpha^2} \end{Bmatrix} \tag{7.6}$$

which can be written in general form as:

$$[m]\{\ddot{z}\} + [k]\{z\} = \{F_o\} \tag{7.7}$$

where :

$$[m] = \begin{bmatrix} 1 & x_\alpha \\ x_\alpha & r_\alpha^2 \end{bmatrix},\quad [k] = \begin{bmatrix} \left(\dfrac{\omega_h}{\omega_\alpha}\right)^2 & 0 \\ 0 & r_\alpha^2 \end{bmatrix},\quad \{z\} = \begin{Bmatrix} \dfrac{h}{b} \\ \alpha \end{Bmatrix},\quad \{F_o\} = \begin{Bmatrix} \dfrac{-L}{m_1 b \omega_\alpha^2} \\ \dfrac{M_{ea}}{m_1 b^2 \omega_\alpha^2} \end{Bmatrix} \tag{7.8}$$

Compared to the equation (5.6), this system does not have damping term ([C] = 0). The mass matrix of the system is coupled (i.e. the system can be said as dynamically coupled). Equation (7.8) will be solved subject to a set of structural data, which was proposed by Isogais. The structural data of the Isogais model [86] is presented in Table 7.1.

In order to obtain the dynamic characteristic (the coupled natural frequencies and mode shapes) of the structure, an analysis of modal of the system must be carried out prior to the flutter calculation.

Table 7.1. Structural Data of the Isogais Model

Parameter		
Airfoil		NACA 64A010
Steady angle of attack	$\alpha 0$	0^{o}
Radius of gyration	r_α	1.865
Static unbalance (normalised with semi chord b)	x_α	1.8
Position of elastic axis (normalised with semi chord b)	a	- 2 (from semi chord)
Uncoupled natural frequency in heaving motion	ω_h	100 Hz
Uncoupled natural frequency in pitching motion	ω_α	100 Hz
Ratio of structural to fluid mass, $m_1/(\pi\rho_\infty b^2)$	μ	60

7.1.2. Modal Analysis of the Isogais Model

The modal equation can be derived from equation (7.7) by neglecting the external force vector $\{F_o\}$ as follows:

$$[m]\left\{\ddot{z}\right\}+[k]\{z\}=0 \tag{7.9}$$

or in extended form:

$$\begin{bmatrix}1 & x_\alpha \\ x_\alpha & r_\alpha^2\end{bmatrix}\begin{Bmatrix}\ddot{\dfrac{h}{b}} \\ \ddot{\alpha}\end{Bmatrix}+\begin{bmatrix}\left(\dfrac{\omega_h}{\omega_\alpha}\right)^2 & 0 \\ 0 & r_\alpha^2\end{bmatrix}\begin{Bmatrix}\dfrac{h}{b} \\ \alpha\end{Bmatrix}=0 \tag{7.10}$$

The physical coordinate will be assumed as a harmonic function:

$$\begin{Bmatrix}\dfrac{h}{b} \\ \alpha\end{Bmatrix}=\begin{Bmatrix}\dfrac{\bar{h}}{b} \\ \bar{\alpha}\end{Bmatrix}e^{i\omega t}=\begin{Bmatrix}\dfrac{\bar{h}}{b} \\ \bar{\alpha}\end{Bmatrix}e^{i(\omega/\omega_\alpha)\tau}, \qquad \begin{Bmatrix}\ddot{\dfrac{h}{b}} \\ \ddot{\alpha}\end{Bmatrix}=-\left(\dfrac{\omega}{\omega_\alpha}\right)^2\begin{Bmatrix}\dfrac{h}{b} \\ \alpha\end{Bmatrix} \tag{7.11}$$

Substitution of eq. (7.11) into eq. (7.10) gives:

$$\begin{bmatrix}\left(\dfrac{\omega_h}{\omega_\alpha}\right)^2-\left(\dfrac{\omega}{\omega_\alpha}\right)^2 & -\left(\dfrac{\omega}{\omega_\alpha}\right)^2 x_\alpha \\ -\left(\dfrac{\omega}{\omega_\alpha}\right)^2 x_\alpha & r_\alpha^2\left[1--\left(\dfrac{\omega}{\omega_\alpha}\right)^2\right]\end{bmatrix}\begin{Bmatrix}\dfrac{h}{b} \\ \alpha\end{Bmatrix}=0 \tag{7.12}$$

The coupled natural frequencies can be calculated by putting the determinant of the matrix equals to zero:

$$Det\left\|\begin{bmatrix}\left(\dfrac{\omega_h}{\omega_\alpha}\right)^2-\left(\dfrac{\omega}{\omega_\alpha}\right)^2 & -\left(\dfrac{\omega}{\omega_\alpha}\right)^2 x_\alpha \\ -\left(\dfrac{\omega}{\omega_\alpha}\right)^2 x_\alpha & r_\alpha^2\left[1--\left(\dfrac{\omega}{\omega_\alpha}\right)^2\right]\end{bmatrix}\right\|.=0 \tag{7.13}$$

The determinant of matrix leads to characteristic equation:

$$\left(\frac{\omega}{\omega_\alpha}\right)^4\left(r_\alpha^2-x_\alpha^2\right)-\left(\frac{\omega}{\omega_\alpha}\right)^2 r_\alpha^2\left[1+\left(\frac{\omega_h}{\omega_\alpha}\right)^2\right]+r_\alpha^2\left(\frac{\omega_h}{\omega_\alpha}\right)^2=0 \tag{7.14}$$

Solutions of the characteristic equation (7.14) is:

$$\left(\frac{\omega}{\omega_\alpha}\right)_{1,2}=\sqrt{\frac{r_\alpha^2\left[1+\left(\dfrac{\omega_h}{\omega_\alpha}\right)^2\right]\pm\sqrt{\left\{-r_\alpha^2\left[1+\left(\dfrac{\omega_h}{\omega_\alpha}\right)^2\right]\right\}^2-4\left(r_\alpha^2-x_\alpha^2\right)r_\alpha^2\left(\dfrac{\omega_h}{\omega_\alpha}\right)^2}}{2\left(r_\alpha^2-x_\alpha^2\right)}} \tag{7.15}$$

By inserting the structural data (Table 7.1):

$$\left(\frac{\omega_h}{\omega_\alpha}\right)=1, \quad r_\alpha^2=3.48, \quad x_\alpha=1.8$$

into equation (7.15), one obtains the coupled natural frequency :

$$\left(\frac{\omega}{\omega_\alpha}\right)_1=0.7134, \quad \left(\frac{\omega}{\omega_\alpha}\right)_2=5.3377, \quad \omega_1=71.34 \quad Hz, \quad \omega_2=533.77 \quad Hz \tag{7.16}$$

The vibration mode shapes can be calculated from eq. (7.12) as follows:

$$\frac{(h/b)}{\alpha} = \frac{(\omega/\omega_\alpha)^2 x_\alpha}{(\omega_h^2 - \omega^2)/\omega_\alpha^2} \tag{7.17}$$

By inserting the value of the frequencies and structural data in the equation (7.17), one obtains:

$$\left(\frac{h/b}{\alpha}\right)_1 = 1.8655, \quad \left(\frac{h/b}{\alpha}\right)_2 = -1.8655 \tag{7.18}$$

The mode shapes are:

$$[\Phi] = \begin{bmatrix} \begin{Bmatrix} h/b \\ \alpha \end{Bmatrix}_1 & \begin{Bmatrix} h/b \\ \alpha \end{Bmatrix}_2 \end{bmatrix} = \begin{bmatrix} 1.8655\alpha_1 & -1.8655\alpha_2 \\ \alpha_1 & \alpha_2 \end{bmatrix} = \begin{bmatrix} 1.8655 & -1.8655 \\ 1 & 1 \end{bmatrix} \tag{7.19}$$

where $\alpha_1 = \alpha_2 = 1$ has been assumed.

With these value of the mode shape, one can calculate the generalised mass and stiffness matrices as follows:

$$[M] = [\Phi]^T [m][\Phi] =$$

$$[M] = \begin{bmatrix} 1.8655 & 1 \\ -1.8655 & 1 \end{bmatrix} \begin{bmatrix} 1 & 1.8 \\ 1.8 & 3.48 \end{bmatrix} \begin{bmatrix} 1.8655 & -1.8655 \\ 1 & 1 \end{bmatrix} = \begin{bmatrix} 13.6757 & 0 \\ 0 & 0.2443 \end{bmatrix} \tag{7.20}$$

$$[K] = [\Phi]^T [k][\Phi] =$$

$$[K] = \begin{bmatrix} 1.8655 & 1 \\ -1.8655 & 1 \end{bmatrix} \begin{bmatrix} 1 & 0 \\ 0 & (3.48) \end{bmatrix} \begin{bmatrix} 1.8655 & -1.8655 \\ 1 & 1 \end{bmatrix} = \begin{bmatrix} 6.96 & 0 \\ 0 & 6.96 \end{bmatrix} \tag{7.21}$$

The location of the pivot point of the vibration mode can be calculate through the following geometrical relation (See Fig. 7.2) :

$$\tan\alpha \cong \alpha = \frac{(h/b)}{a - \frac{x_{pv}}{b}}, \qquad \frac{x_{pv}}{b} = a - \left(\frac{h/b}{\alpha}\right) \tag{7.22}$$

Inserting equation (7.18) and the elastic axis a into equation (7.22), one obtains the pivot point of the vibration modes from semi chord, as follows:

$$\begin{aligned} \frac{x_{pv1}}{b} &= a - \left(\frac{h/b}{\alpha}\right)_1 = -2 - 1.8655 = -3.8655 \\ \frac{x_{pv2}}{b} &= a - \left(\frac{h/b}{\alpha}\right)_2 = -2 + 1.8655 = -0.1345 \end{aligned} \tag{7.23}$$

The pivot points of the first and the second vibration mode lay at 1.433 chord fore and 0.433 chord aft of the leading edge. The vibration mode shapes of this system is shown in fig. 7.3.

7.1.3. Flutter Analysis of the Isogais Model

Flutter analysis of the Isogais Model will be carried out using State Space equation (5.15):

$$\left\{\dot{X}\right\} = [A]\{X\} + [B]\{u\} \tag{5.15}$$

with the State Vectors $\{X\}$ and $\{u\}$ and the State Transition Matrices $[A]$ and $[B]$ as follows:

$$\left\{X\right\} = \begin{Bmatrix} q \\ \dot{q} \end{Bmatrix},\quad \left\{\dot{X}\right\} = \begin{Bmatrix} \dot{q} \\ \ddot{q} \end{Bmatrix},\quad \{u\} = \begin{Bmatrix} 0 \\ Q \end{Bmatrix},\quad [B] = \begin{bmatrix} 0 & 0 \\ 0 & [M]^{-1} \end{bmatrix},\quad [A] = \begin{bmatrix} 0 & [I] \\ -\left[\omega_n^2\right] & 0 \end{bmatrix} \tag{7.24}$$

Inserting [M] from eq. (7.20) and [ω_n] from eq. (7.16), the State Transition Matrices [A] and [B] will be:

$$[A] = \begin{bmatrix} 0 & 1 & 0 & 0 \\ -\left(\dfrac{\omega}{\omega_\alpha}\right)_1^2 & 0 & 0 & 0 \\ 0 & 0 & 0 & 1 \\ 0 & 0 & -\left(\dfrac{\omega}{\omega_\alpha}\right)_2^2 & 0 \end{bmatrix} = \begin{bmatrix} 0 & 1 & 0 & 0 \\ -(0.7134)^2 & 0 & 0 & 0 \\ 0 & 0 & 0 & 1 \\ 0 & 0 & -(5.3377)^2 & 0 \end{bmatrix} \tag{7.25}$$

$$[B] = \begin{bmatrix} 0 & 0 & 0 & 0 \\ 0 & M_1^{-1} & 0 & 0 \\ 0 & 0 & 0 & 0 \\ 0 & 0 & 0 & M_2^{-1} \end{bmatrix} = \begin{bmatrix} 0 & 0 & 0 & 0 \\ 0 & (13.6757)^{-1} & 0 & 0 \\ 0 & 0 & 0 & 0 \\ 0 & 0 & 0 & (0.2443)^{-1} \end{bmatrix} \tag{7.26}$$

The initial value of the state vector {X} are:

$$\left\{X^n\right\}\Big|_{n=0} = \left[q_1,\ \overset{*}{q_1},\ q_2,\ \overset{*}{q_2}\right]^T_{n=0} = \left[0.,\ 0.01,\ 0.,\ 0.01\right]^T \tag{7.27}$$

which means the system is disturbed with an initial velocity of the generalised displacement.

In order to check the value of the coupled natural frequencies, the characteristic of the system is computed with zero dynamic pressure for some cycles of oscillation. The response of the system is shown in Fig. 7.4. In this computation the value of the time step $\Delta\tau = 0.09786$ is used, which corresponds to the time step $\Delta t = 0.0009786$ sec. The natural frequencies can be computed from the response of the system, as follows:

$$\left(\frac{\omega}{\omega_\alpha}\right) = \frac{2\pi}{N\Delta\tau} \tag{7.28}$$

where : N = number of time step in one periods of the response oscillation.

$\Delta\tau$ = dimensionless time step increment

The number of the time step N for the first and the second mode is approximately 90 and 12 time steps, respectively. From equation (7.29) the natural frequencies can be computed as:

$$\left(\frac{\omega}{\omega_\alpha}\right)_1 = \frac{2\pi}{(90)(0.09786)} = 0.7134, \quad \left(\frac{\omega}{\omega_\alpha}\right)_2 = \frac{2\pi}{(12)(0.09786)} = 5.3505$$

The deviation of the natural frequencies of the second mode from exact calculation (eq. 7.16) is 0.24%. Fig. 7.4a and 7.4b show the response of both mode shapes in term of generalized displacement (with corresponding frequency ω_1/ω_α and ω_2/ω_α) and fig. 7.4c shows the physical response (h/b and α). From fig. 7.4c can be seen that the value of the uncoupled frequency (ω_h and ω_α) are the same.

Before the flutter calculation is performed, it is important to analyze or to validate the quality of the aerodynamic forces. For this purpose, the steady and unsteady pressure distribution of the test case AGARD CT8 for the NACA 64A010 airfoil with the following data:

Mach number	M = 0.796
Reynolds number	Re =1.2E+07 (based on chord)
Mean angle of attack	$\alpha0 = 0$
Amplitude angle of attack	$\alpha1 =1.02$
Pitching axis	xp = 0.25c
Reduced frequency	k = 0.202 (based on chord)

are evaluated and presented in Fig. 7.5. Comparison between the experimental of Davis [89] and numerical results shows a good agreement. The influence of the boundary layer for this case is small because the Reynolds number is high.

In order to simulate the Transonic Dip phenomenon, the response of the system will be computed in the range Mach number from M = 0.7 to M = 0.9. Therefore the steady aerodynamic forces for those Mach number must be first computed prior to the flutter analysis. The steady pressure distribution of this airfoil for these different Mach numbers is shown in Fig. 7.6. Since the airfoil is symmetric and the angle of attack is zero, the airfoil produces no lift.

Flutter analysis is then carried out for each Mach number. The response of the system is computed until a neutral response is found for each Mach number. This is carried out by starting the given speed (U_∞) and dynamic pressure ($0.5\rho_\infty U_\infty^2$) with low values and then increasing it step by step. Fig. 7.7 shows the diagram of flutter speed index (V^*), flutter frequency (ω_f/ω_α), ratio of the amplitude of the Responses $(h/b)/\alpha$ and phase lag between (h/b) and α versus Mach number.

The flutter speed index (V *) is defined as:

$$V^* = \frac{V_f}{b\omega_\alpha\sqrt{\mu}} \tag{7.29}$$

where:

V_f = flutter speed
b = semi chord
ω_α = uncoupled frequency in pitching motion
μ = ratio of structural to fluid mass

The value of flutter speed index will be compared with the results from Alonso and Jameson (using Euler equation) [90], Isogai (using TSD equation) [86] and the linear method (Doublet Lattice Method -DLM) [2, 86]. It can be seen in fig. 7.7a that the flutter speed index (V*) of the TSD Present method has the same form with the result from Alonso & Jameson. The Transonic Dip for this system calculated with the TSD Present is occurred at M = 0.85 with $V^* = 0.53$ equivalent with the Alonso and Jamesons result. The Isogais result supplies the Transonic Dip at M = to 0.8375 with $V^* = 0.48$. The linear method (DLM) can not show the Transonic Dip phenomenon. From Mach number 0.7 up to the Dip location the flutter speed index becomes smaller. By the TSD Present method the decreasing process is slowly similar with the Alonso & Jamesons results. At the other side this decreasing process by Isogais result is steeper than those of the present method, although the two results are based on the TSD equation.

The deviation is supposed because of the following:

- the TSD equation of Isogai does not have entropy and vorticity correction, which is used in the Present method.

- the flutter analysis used by Isogai is the U-g method, where the aeroelastic equation is solved in frequency domain. In the Present method the aeroelastic equation is solved in time domain, which was also used by Alonso & Jameson. The flutter analysis in time domain ensures that the coupling between fluid and structure is carried out in time-accurate procedures. The generalized aerodynamics forces calculation remain pure in time domain without any extrapolation or interpolation as is usually found by the frequency-domain flutter analysis.

After the Dip location, the flutter speed index calculated with non linear aerodynamic methods increases discontinue. This happens due to the changing of the flutter mode. Flutter is occurred in the first mode before the Dip location and then changed into the second mode after the Dip. This changing can be seen clearly in the flutter frequency diagram fig. 7.7b. Flutter occurs with the frequency near by the first mode (ω_1/ω_α = 0.7134) before the Dip and then the flutter frequency increases near by the second mode (ω_2/ω_α = 5.3377) after the Dip. The changing of the flutter mode can not be seen by the result of the linear aerodynamic method (DLM). By the Present method lies the changing of the flutter mode at M = 0.86875 prior to the Alonso & Jamesons result (at M = 0.875) and Isogais result (at M = 0.9). By the Isogais results, flutter of the system can not be found at the range of Mach number between 0.85 and 0.9.

The neutral response of the system at the Mach number 0.7 can be seen in Fig. 7.8 with the V^* = 1.26. One can see that the ratio of (h/b) to α is approximately one (see also Fig. 7.7c) with the phase lag is approximately 30 degrees at this condition.

The response of the system at the Dip (M = 0.85) for various V^* can be seen in Fig. 7.9. An under damped response of the system is shown in the fig. 7.9a with V^* = 0.26. The neutral response (flutter) at this Mach number is shown in fig. 7.9b with V^* = 0.53. A divergent response of the system is shown in fig. 7.9c with V^* = 0.77.

From the neutral response (Fig 7.9b) one can see that the Ratio of (h/b) to α is approximately 1.86 (see also Fig.7.7c). This value is same with the Ratio of (h/b) to α in the first mode shape (see equation 7.18). That means: the dominant flutter mode is the first mode. There is almost no phase lag between (h/b) and α at this neutral response (see fig. 7.7d).
Compared with Fig. 7.8 (the neutral response at Mach 0.7), the Ratio of (h/b) to α becomes larger and on the other hand the phase lag between (h/b) and α becomes smaller with the increasing Mach number (see fig. 7.7c. and d).

The neutral Response at M = 0.86875 can be seen in Fig. 7.10 with V^* = 2.4. One can see that now the α displacement is larger than (h/b) (see also Fig. 7.7c). That means: the dominant flutter mode is the second mode.
The above flutter results have been partially published in Ref. [91].

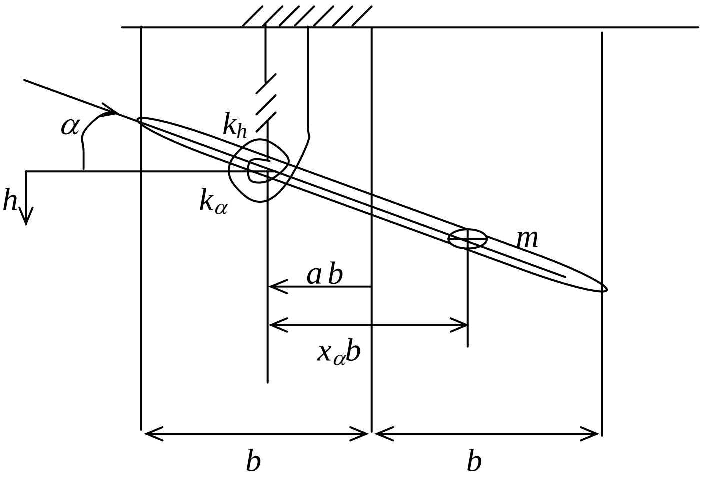

Fig. 7.1. Two Degree of Freedom (D.o.F) System

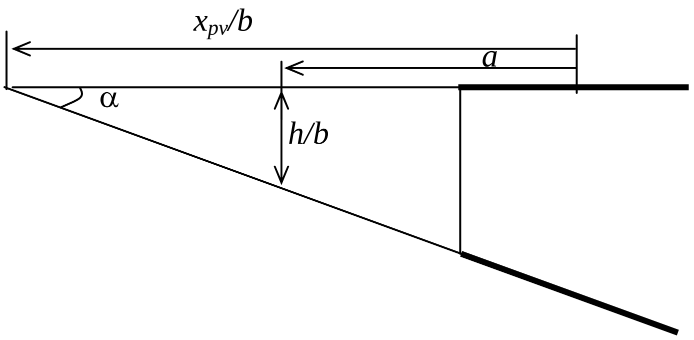

Fig. 7.2. Geometric Relation to Determine the Pivot Point of Vibration Mode

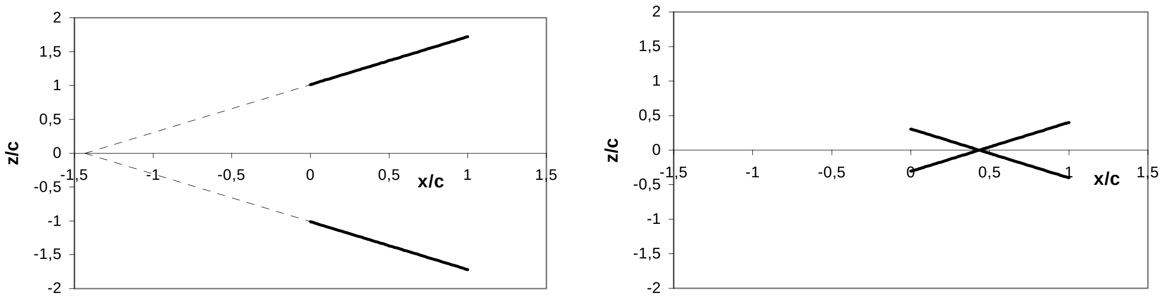

(a). 1. Mode

(b). 2. Mode

Fig. 7.3. The Vibration Mode Shapes of Isogais Model

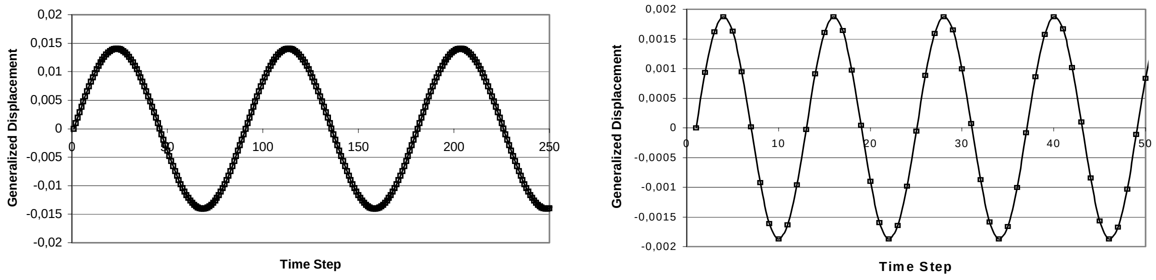

(a). Generalised Displacement of 1st Mode (b). Generalised Displacement of 2nd Mode

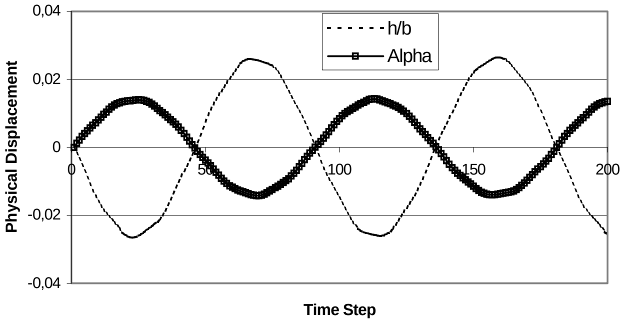

(c). Response in Physical Displacement

Fig. 7.4. Response of Isogais Model at Zero Dynamic Pressure

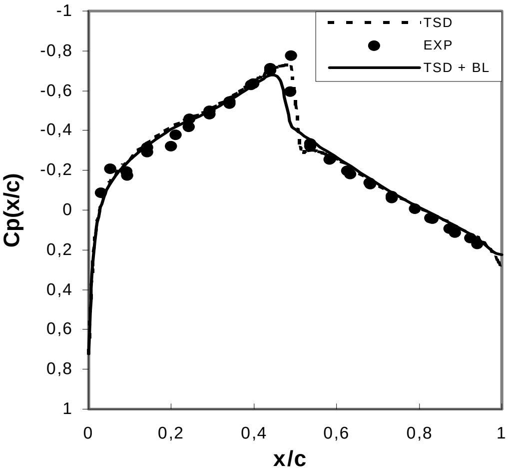

Fig. 7.5.(a). Steady Pressure Distribution of NACA 64A010 Airfoil at M=0.796, Re=1.2E+07, $\alpha 0=0$

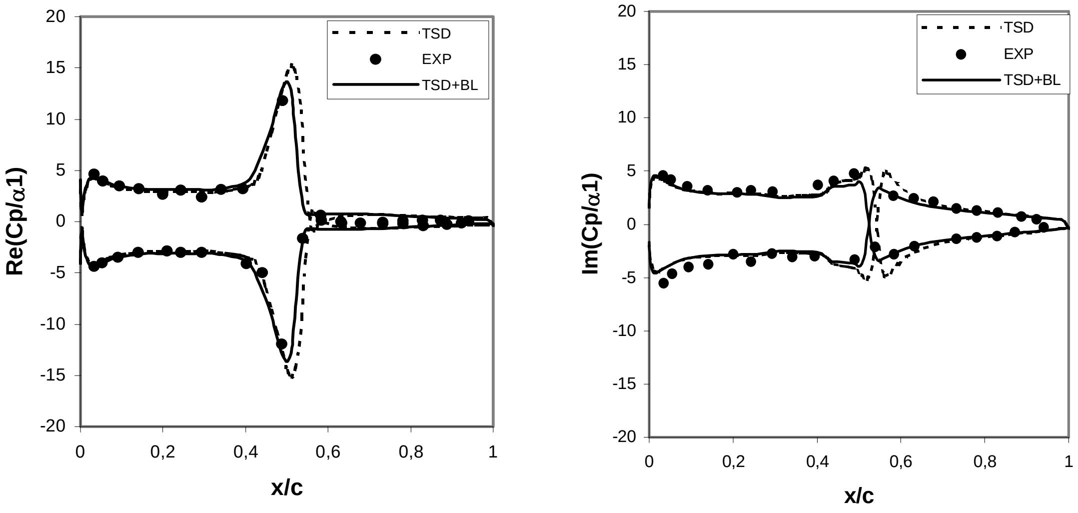

(b). Real Part

(c) Imaginary Part

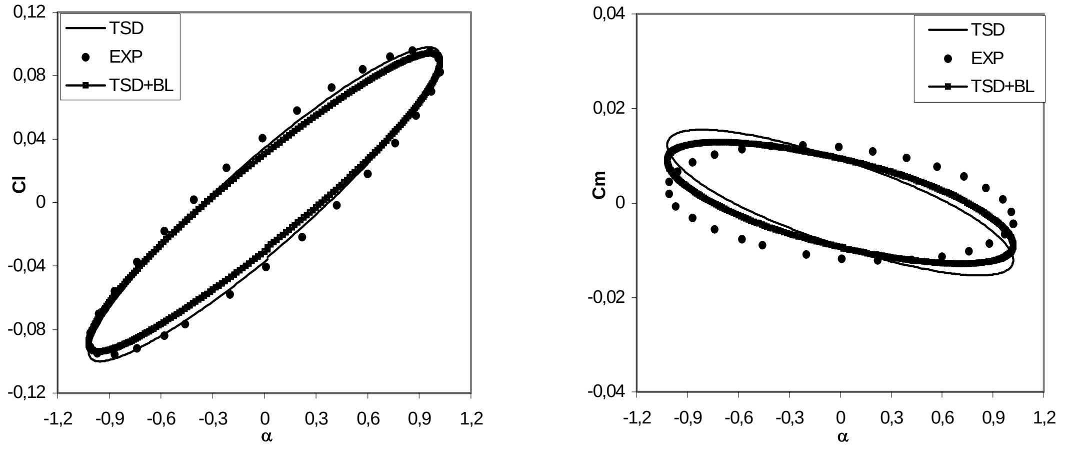

(d). Unsteady Lift Coefficient

(e). Unsteady Moment Coefficient

Fig. 7.5. Steady and Unsteady Pressure Distribution and
Unsteady Lift and Moment Coefficients of NACA 64A010 Airfoil
M=0.796, Re=1.2E+07, α0=0, α1=1.02, k=0.202, xp=0.25

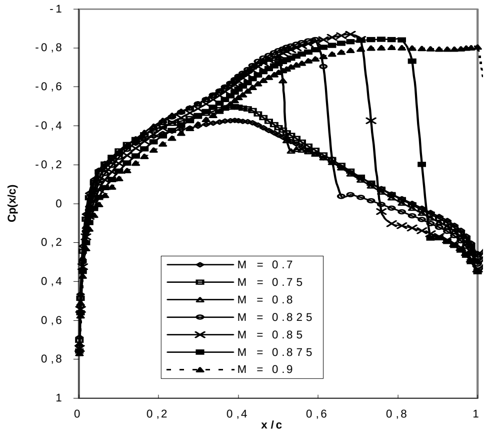

Fig. 7.6. Steady Pressure Distribution of NACA 64A010 Airfoil
for Various Mach Number and α0 = 0

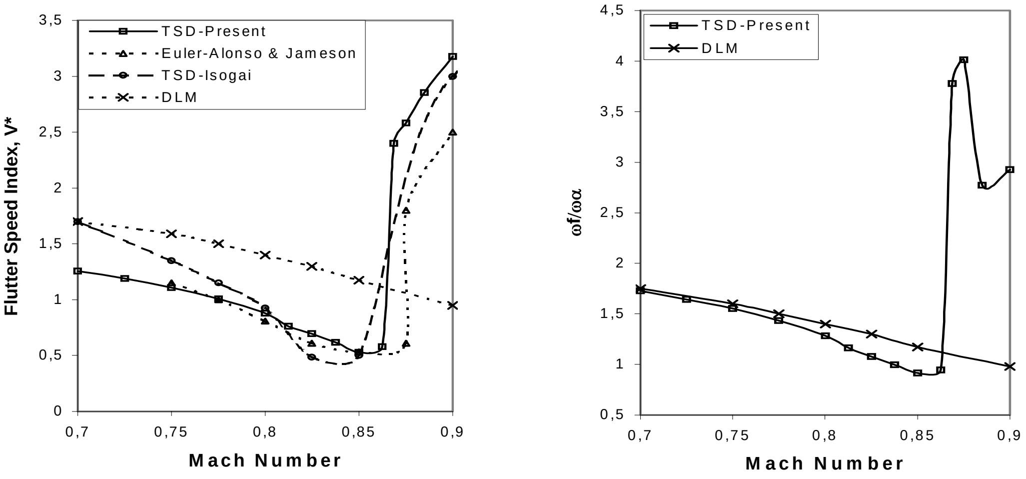

7.7.(a). Flutter Speed Index

7.7.(b). Flutter Frequency

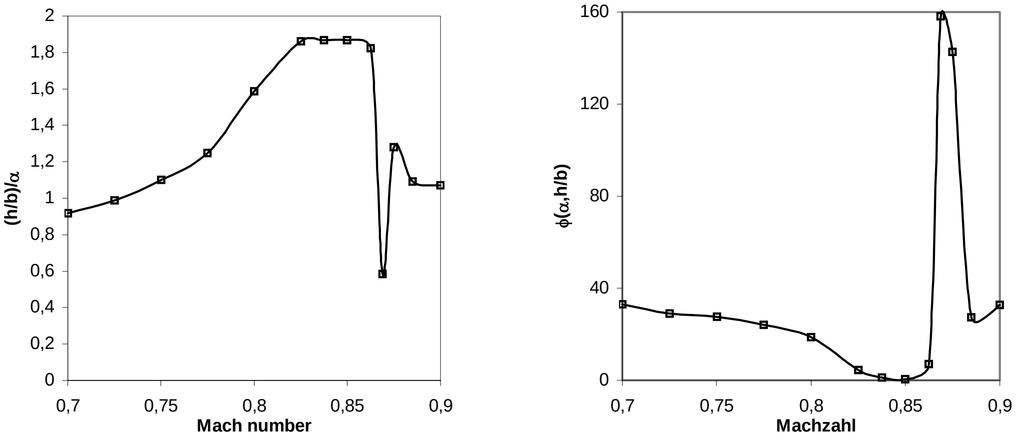

7.7.(c). Ratio of Amplitude

7.7.(d). Phase Lag

Fig. 7.7. Diagram of Flutter Speed Index, Flutter Frequency,
Ratio of Amplitude and Phase Lag versus Mach number of the Isogais Model

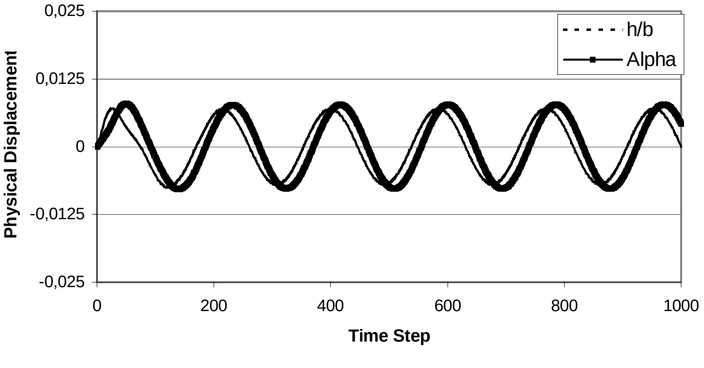

Fig. 7.8. Neutral Response of System at M = 0.7, $V^* = 1.26$

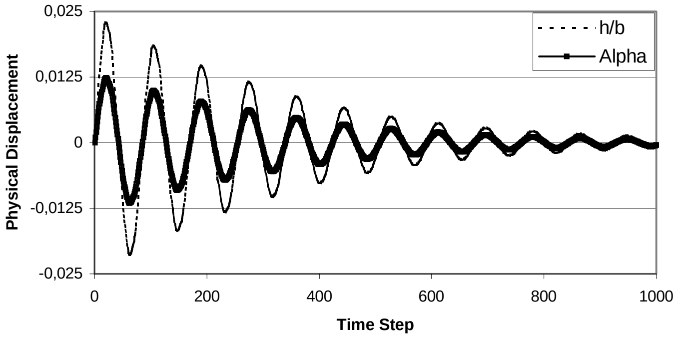

(a). Damped Response at M = 0.85, V^* = 0.26

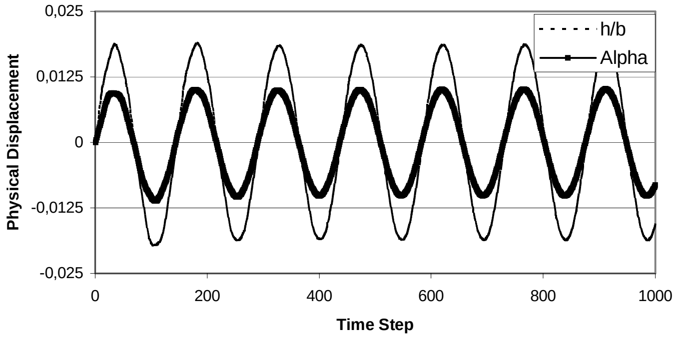

(b). Neutral Response at M = 0.85, V^* = 0.53

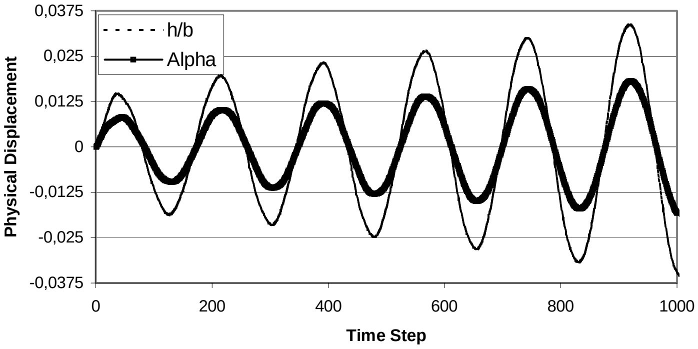

(c). Divergent Response at M = 0.85, V^* = 0.77

Fig. 7.9. Response at the Dip (M = 0.85) for various V^*

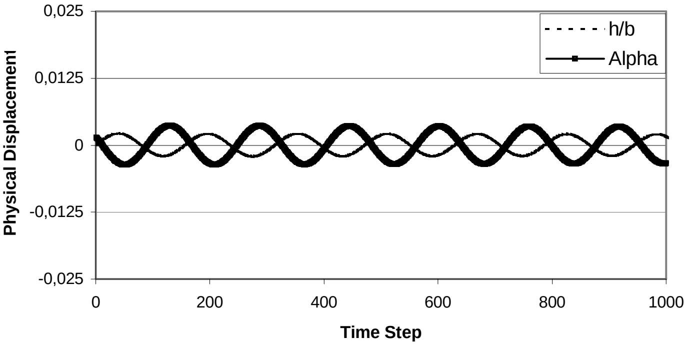

Fig. 7.10. Neutral Response at M = 0.86875, V^* = 2.4

7.2. Transonic Dip of the DLR Model

This sub chapter presents the flutter characteristic of the DLR model (i.e. 2D aeroelastic model with airfoil NLR7301) for various Mach numbers, in order to examine the Transonic Dip phenomenon of this model. The influence of the boundary layer into flutter characteristic is also examined.

7.2.1. The DLR Model

The aeroelastic equation of the DLR Model is formulated as follows:

$$\begin{bmatrix} 1 & x_\alpha \\ x_\alpha & r_\alpha^2 \end{bmatrix} \begin{Bmatrix} \frac{\ddot{h}}{c} \\ \ddot{\alpha} \end{Bmatrix} + \begin{bmatrix} \left(\frac{\omega_h}{\omega_\alpha}\right) & 0 \\ 0 & r_\alpha^2 \end{bmatrix} \begin{Bmatrix} \frac{h}{c} \\ \alpha \end{Bmatrix} = \begin{Bmatrix} \frac{-L}{m_1 c \omega_\alpha^2} \\ \frac{M_{ea}}{m_1 c^2 \omega_\alpha^2} \end{Bmatrix} \qquad (7.30)$$

Equation (7.30) is normalised with chord c instead of semi chord b as by equation (7.6). The damping matrix of the system is assumed to be zero. Table 7.2 shows the structural data of the DLR model (taken from the 2nd Campaign in Ref. [87]).

Table 7.2. Structural Data of the DLR Model

Parameter		
Airfoil		NLR 7301
Steady angle of attack from experiment	$\alpha 0$	1.25^o
Radius of gyration	r_α	0.197
Static unbalance (normalised with chord *c*)	x_α	0.0484
Position of the elastic axis (normalised with chord *c*)	a	0.25(from leading edge)
Uncoupled natural frequency in heaving motion	ω_h	206.6 Hz
Uncoupled natural frequency in pitching motion	ω_α	271.9Hz
Ratio of structure to fluid density, ρ_m/ρ_∞	μ	299.5

In order to reduce the complexity of the flutter analysis, the Reynolds number and the ratio of structure to fluid density are assumed to be constant for all Mach number. The Reynolds number for this simulation is 1.7E+06 based on chord.

7.2.2. Modal Analysis of the DLR Model

With the structural data from Table 7.2:

$$\left(\frac{\omega_h}{\omega_\alpha}\right) = 0.76, \quad r_\alpha^2 = 0.0388, \quad x_\alpha = 0.0484$$

the coupled natural frequencies (computed with eq.7.15) will be:

$$\left(\frac{\omega}{\omega_\alpha}\right)_1 = 0.7343, \quad \left(\frac{\omega}{\omega_\alpha}\right)_2 = 1.06747, \quad \omega_1 = 199.67 \quad Hz, \quad \omega_2 = 290.247 \quad Hz \qquad (7.31)$$

The vibration mode shapes calculated using eq. (7.17) are:

$$\left(\frac{h/c}{\alpha}\right)_1 = 0.6851, \quad \left(\frac{h/c}{\alpha}\right)_2 = -0.0981 \qquad (7.32)$$

The mode shapes are :

$$[\Phi] = \begin{bmatrix} \begin{Bmatrix} h/c \\ \alpha \end{Bmatrix}_1 & \begin{Bmatrix} h/c \\ \alpha \end{Bmatrix}_2 \end{bmatrix} = \begin{bmatrix} 0.6851\alpha_1 & -0.0981\alpha_2 \\ \alpha_1 & \alpha_2 \end{bmatrix} = \begin{bmatrix} 0.6851 & -0.0981 \\ 1 & 1 \end{bmatrix} \qquad (7.33)$$

where $\alpha_1 = \alpha_2 = 1$ has been assumed.

The generalised mass and stiffness matrices can be found as:

$$[M]=[\Phi]^T[m][\Phi]=\begin{bmatrix}0.5745 & 0\\ 0 & 0.0389\end{bmatrix} \tag{7.34}$$

$$[K]=[\Phi]^T[k][\Phi]=\begin{bmatrix}0.3098 & 0\\ 0 & 0.0443\end{bmatrix} \tag{7.35}$$

The location of the pivot point of the vibration mode are:

$$\begin{aligned} x_{pv1}/c &= a-\left(\frac{h/c}{\alpha}\right)_1 = 0.25-0.6851=-0.4351\\ x_{pv2}/c &= a-\left(\frac{h/c}{\alpha}\right)_2 = 0.25+0.0981=0.3481 \end{aligned} \tag{7.36}$$

The pivot of the first and second vibration mode lies in 0.4351 chord fore and 0.3481 chord aft of the leading edge respectively. The vibration mode shapes of the system is depicted in Fig. 7.11.

7.2.3. Flutter Analysis of the DLR Model

Flutter Analysis of the DLR Model will be carried out by State Space equation (5.15):

$$\left\{\overset{\bullet}{X}\right\}=[A]\{X\}+[B]\{u\} \tag{5.15}$$

where State Transition Matrices [A] and [B] are:

$$[A]=\begin{bmatrix}0 & 1 & 0 & 0\\ -\left(\frac{\omega}{\omega_\alpha}\right)_1^2 & 0 & 0 & 0\\ 0 & 0 & 0 & 1\\ 0 & 0 & -\left(\frac{\omega}{\omega_\alpha}\right)_2^2 & 0\end{bmatrix}=\begin{bmatrix}0 & 1 & 0 & 0\\ -(0.7343)^2 & 0 & 0 & 0\\ 0 & 0 & 0 & 1\\ 0 & 0 & -(1.0674)^2 & 0\end{bmatrix} \tag{7.37}$$

$$[B]=\begin{bmatrix}0 & 0 & 0 & 0\\ 0 & M_1^{-1} & 0 & 0\\ 0 & 0 & 0 & 0\\ 0 & 0 & 0 & M_2^{-1}\end{bmatrix}=\begin{bmatrix}0 & 0 & 0 & 0\\ 0 & (0.5745)^{-1} & 0 & 0\\ 0 & 0 & 0 & 0\\ 0 & 0 & 0 & (0.0389)^{-1}\end{bmatrix} \tag{7.38}$$

The initial value of the state vector {X} is the same with the previous one used for Isogai model.

In order to check the value of the coupled natural frequencies, the characteristic of the system is computed with zero dynamic pressure for some cycles of oscillation. The response of the system is shown in Fig. 7.12. In this computation the value of the time step $\Delta\tau = 0.0327$ is used, which corresponds to the time step $\Delta t = 0.0001203$ sec.

From equation (7.28) the natural frequencies can be found as:

$$\left(\frac{\omega}{\omega_\alpha}\right)_1 = 0.7334, \quad \left(\frac{\omega}{\omega_\alpha}\right)_2 = 1.0675$$

Fig. 7.12. represents the response of both mode shapes (i.e. the response of the generalized displacement with corresponding frequencies ω_1/ω_α and ω_2/ω_α).

Before the flutter calculation is performed, it is important to analyze or to validate the quality of the aerodynamic forces. For this purpose, steady and unsteady pressure distribution of the test case AGARD CT5 for NLR 7301 with the following data:

Mach number	M = 0.7
Reynolds number	Re = 2.14E+06 (based on chord)
Mean angle of attack	α0 = 2 deg
Amplitude angle of attack	α1 = 0.5 deg
Pitching axis	xp = 0.4c
Reduced frequency	k = 0.384 (based on chord)

has been chosen [92]. The steady and unsteady pressure distribution of the NLR 7301 airfoil for this test case are presented in Fig. 7.13. Comparison with the experimental results shows a good agreement of the numerical (the TSD+BL results) and the experimental results. The influence of the boundary layer for this test case can not be neglected and must be considered.

It is recommended by Schewe et. al. [87], that the MP 77 case in the experiment must be examined or simulated prior to flutter analysis step, in order to compare the lift between the experimental and the numerical result.

The flow and geometric parameters for the MP 77 case in experiment are as follows:

Mach number	M = 0.759
Reynolds number	Re = 1.7E+06 (based on chord)
Angle of attack	α0 = 1.25 deg (uncorrected).

The simulation was carried out with two different angle of attack (α0 = 0.74 and α0 = -0.5), in order to examine the influence of angle of attack in the pressure distribution. Fig. 7.14 represents the steady pressure distribution for this MP 77 case. It can be seen that the pressure distribution from the experiment can not be good simulated. With the angle of attack α0 = 0.74 the pressure distribution on the upper surface from the numerical result is more negative than from that from the experimental result. On the other hand the pressure distribution on the lower surface from the numerical result is more positive than that from the experimental result. The best agreement of the pressure distribution with the experimental result was obtained with the angle of attack α0 = -0.5 (particularly for the lower surface of the airfoil).

The steady lift coefficient of the NLR 7301 airfoil for various Mach numbers is presented in Fig. 7.15. The used angle of attack in simulation is –0.5 degrees instead of 1.25 as in the experiment, in order to obtain the closest lift coefficient with the experimental values. From Mach number 0.5 to 0.75 the steady lift coefficient of the experimental result is relatively flat. This result is questionable, because the lift coefficient becomes larger with the increasing Mach number within the subsonic range. Probably there is a change of angle of attack in the experiment because of the static aeroelastic effect. The rear-loading type of aerodynamic load causes the nose-down pitching moment, which makes the actual angle of attack smaller (due to the elasticity of the model). After the Mach number 0.75 the lift coefficient increases sharply, until a maximum value at the Mach number 0.8. Then the lift coefficient desccreases until Mach number 0.85. In the comparison to the experiment the steady lift coefficient from the TSD result increases monotonic from Mach number 0.5 to 0.75. Afterwards the lift coefficient decreases slowly from M = 0.75 to 0.8. After the Mach number 0.8 it decreases sharply. The influence of the boundary layer makes the lift smaller as can be seen from TSD+BL result in Fig. 7.15. The computation of the aerodynamic load with the TSD plus boundary layer could not be carried out for the Mach number higher than 0.825.

The simulation can not produce a convergence result. This is probably because of the buffeting phenomenon at the higher Mach number.

Fig. 7.16 shows the diagram of flutter speed index (V^*), flutter frequency (ω_f/ω_α), ratio of (h/c) to α and phase lag between the two modes versus Mach number. The flutter speed index will be compared with the experimental result from DLR Goettingen (conducted by Schewe et. al. [87]).

From Fig. 7.16a it can be seen that the flutter speed index V^* from the experimental result is relatively flat up to Mach number 0.75. Afterwards the V^* decreases sharply, until the Transonic Dip is reached at the Mach number 0.771 with $V^* = 0.202$. After the Dip the flutter speed index V^* increases again.

The flutter speed index from the calculation is relatively flat from Mach number 0.5 to 0.6. The calculated flutter speed indexes V^* at Mach number 0.5 are 0.281 from TSD result and 0.285 from TSD+BL result. As comparison the flutter speed index V^* from the experiment is 0.273 at Mach number 0.55. Afterwards V^* decreases slowly up to Mach 0.725. From M = 0.725 to 0.75 it increases slightly again and then it decreases again, until the Transonic Dip is reached. The Transonic Dip for this system with this method lies at M = 0.8125 with V^* = 0.152 (TSD result) and V^* = 0.164 (TSD+BL result). The deviation of the aerodynamics forces between the experimental and the numerical result, as shown in Fig. 7.15, causes the difference of the Transonic Dip characteristic (the Mach number and the V^*) between the experimental and numerical result. After the Dip the flutter speed index from the calculation increases up to M = 0.8375 (TSD) and M = 0.825 (TSD+BL).

The calculated neutral response of the system at Mach number 0.5 is shown in Fig. 7.17. At this Mach number it can be seen from Fig. 7.16c and d that the ratio of (h/c) to α is 0.32 with associated phase lag 36 degrees. The neutral response at M = 0.725 with $V^* = 0.205$ (TSD) and 0.210 (TSD+BL) is shown in Fig. 7.18. One can see from Fig. 7.16c and d that the ratio of (h/c) to α is 0.39 with phase lag 25 degrees (TSD) and 23 degrees (TSD+BL).

Comparison with the Fig. 7.17 reveals that the displacement ratio becomes larger and on the other hand the phase lag becomes smaller with the increasing Mach number.

The neutral response at M = 0.75 with $V^* = 0.208$ (TSD) and 0.216 (TSD+BL) is shown in Fig. 7.19. One can see from Fig. 7.16c and d that the displacement ratio is 0.383 (TSD) and 0.377 (TSD+BL) with phase lag 25.6 degrees (TSD) and 24.3 degrees (TSD+BL). Compared to Fig. 7.18 the ratio of (h/c) to α becomes little bit smaller and the phase lag becomes little bit larger.

The neutral response at the Dip M = 0.8125 is shown in Fig. 7.20 with $V^* = 0.152$ (TSD) and 0.164 (TSD+BL). One can see from Fig. 7.16c and d that the displacement ratio of (h/c) to α is 0.515 (TSD) and 0.59 (TSD+BL) with phase lag 13.7 degrees (TSD) and 10.1 degrees (TSD+BL). Comparison with the Fig. 7.17 reveals that the displacement ratio becomes larger and on the other hand the phase lag becomes smaller with the increasing Mach number. The neutral response at M = 0.825 (after the Dip) is presented in Fig. 7.21 with V^* = 0.177 (TSD) and 0.204 (TSD+BL). One can see from Fig. 7.16c. and d that the ratio of (h/c) to α is 0.51 (TSD) and 0.46 (TSD+BL) with phase lag 23 degrees (TSD) and 16 degrees (TSD+BL). The neutral response at M = 0.8375 is shown in Fig. 7.22 with $V^* = 0.196$ (TSD). The ratio of (h/c) to α is 0.49 (TSD) with phase lag 33 degrees (TSD). Compared to Fig. 7.20 the ratio of (h/c) to α becomes smaller and the phase lag becomes larger. From the response analysis one can conclude that the Transonic Dip occurs associated with the lowest phase lag and the largest displacement ratio between both of the modes.

The above flutter results have been partially published in Ref. [91].

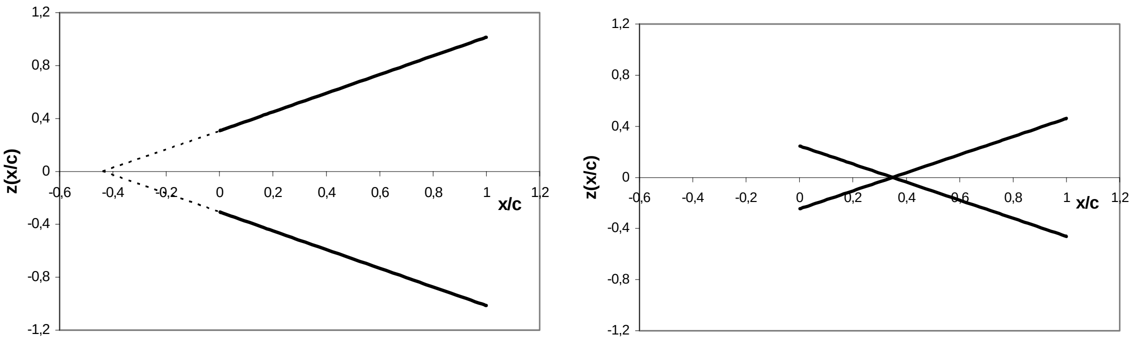

(a). 1st Mode (b). 2nd Mode

Fig. 7.11. Vibration Mode Shapes of the DLR Model

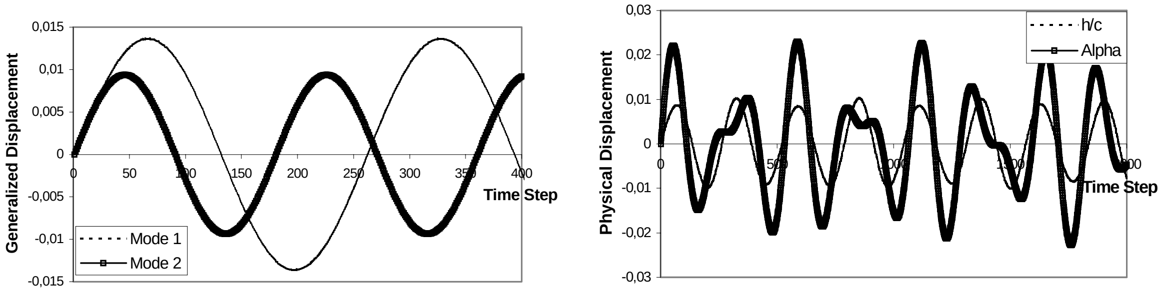

(a). Generalised response (b). Physical Response

Fig. 7.12 Response of the DLR Model at Zero Dynamic Pressure

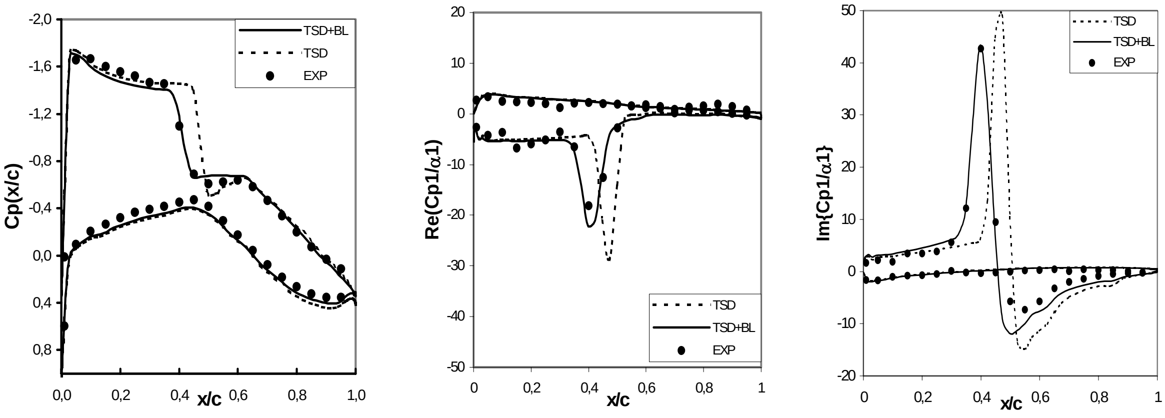

(a) Steady pressure (b) Real Part (c) Imaginary Part

Fig. 7.13. Steady and Unsteady Pressure Distribution of the DLR Model at M=0.7, Re=2.14E+06, α0=2.0, α1=0.5, k=0.384, xp=0.4c

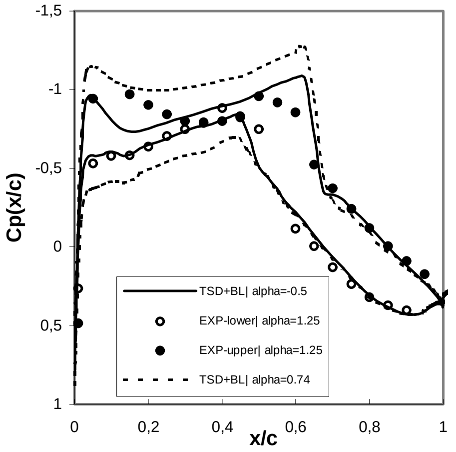

Fig.7.14. MP77 Case of DLR Model at M=0.759, Re=1.7E+06, α0=1.25 (uncorrected)

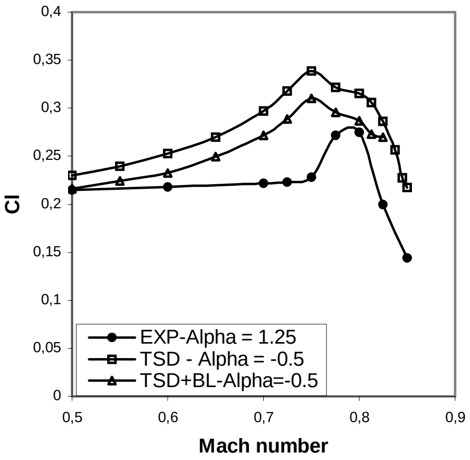

Fig. 7.15. Steady Lift of DLR Model for Various Mach Number

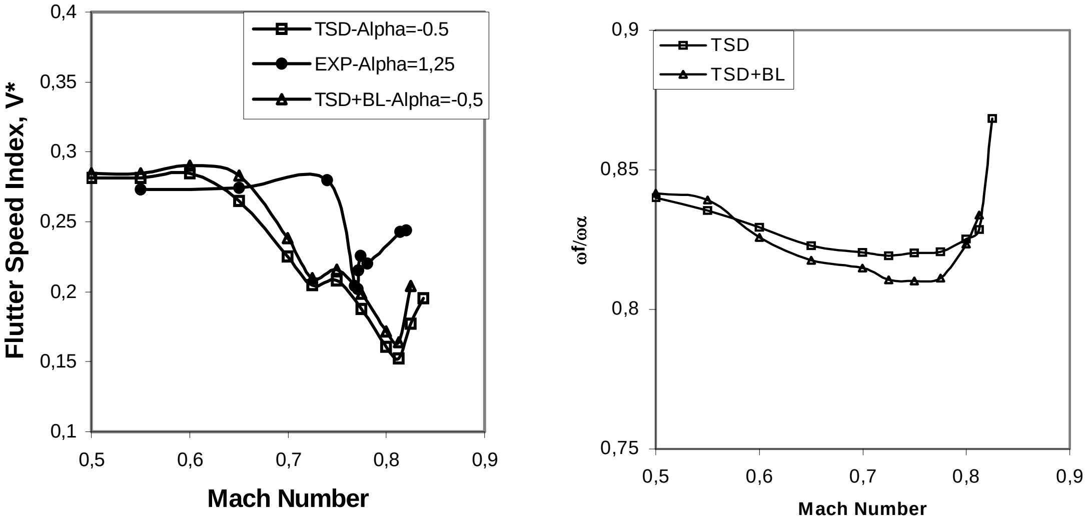

(a) Flutter Speed Index

(b) Flutter Frequency

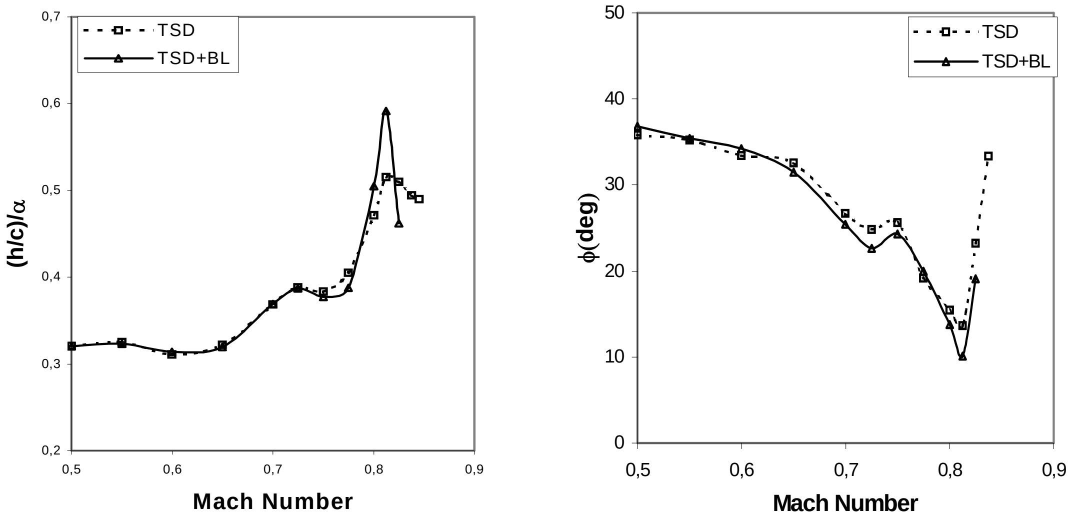

(c) Displacement Ratio

(d) Phase Lag

Fig. 7.16. Diagram of Flutter Speed Index, Flutter Frequency, Displacement Ratio and Phase Lag versus Mach number of DLR Model

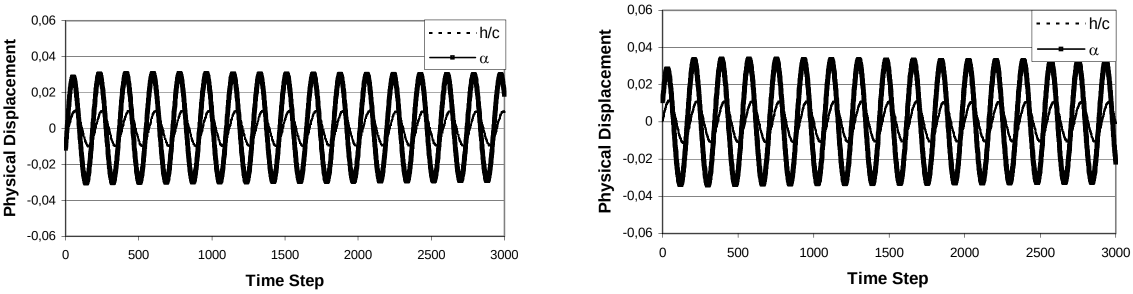

(a) TSD, M = 0.5, $V^* = 0.281$ (b) TSD+BL, M = 0.5, $V^* = 0.285$

Fig. 7.17. Neutral Response of DLR Model at Mach Number 0.5

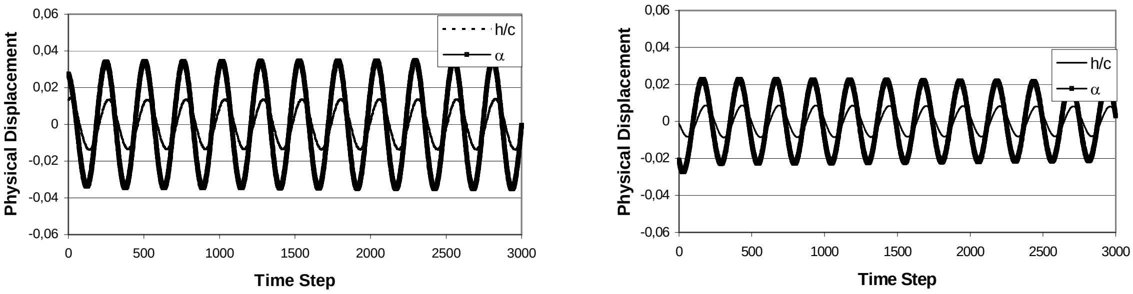

(a) TSD, M = 0.725, $V^* = 0.205$ (b) TSD+BL, M = 0.725, $V^* = 0.210$

Fig. 7.18. Neutral Response of DLR Model at Mach Number 0.725

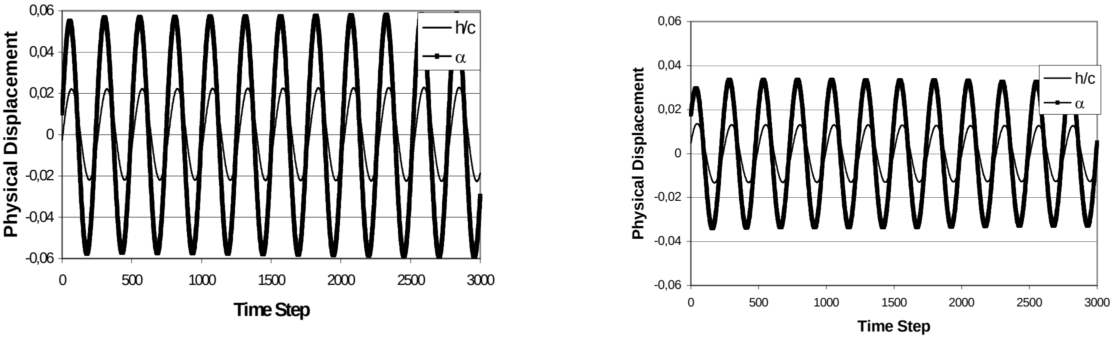

(a) TSD, M = 0.75, V* = 0.208 (b) TSD+BL, M = 0.75, V* = 0.216

Fig. 7.19. Neutral Response of DLR Model at Mach Number 0.75

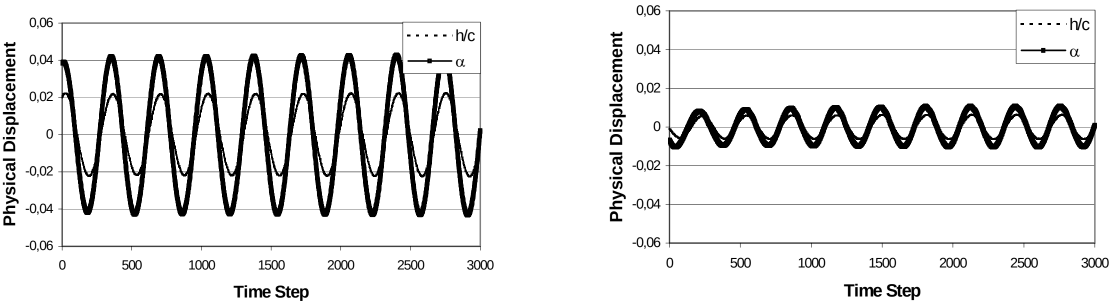

(a) TSD, M = 0.8125, V^* = 0.152 (b) TSD+BL, M = 0.8125, V^* = 0.164

Fig. 7.20. Neutral Response of DLR Model at the Dip (Mach = 0.8125)

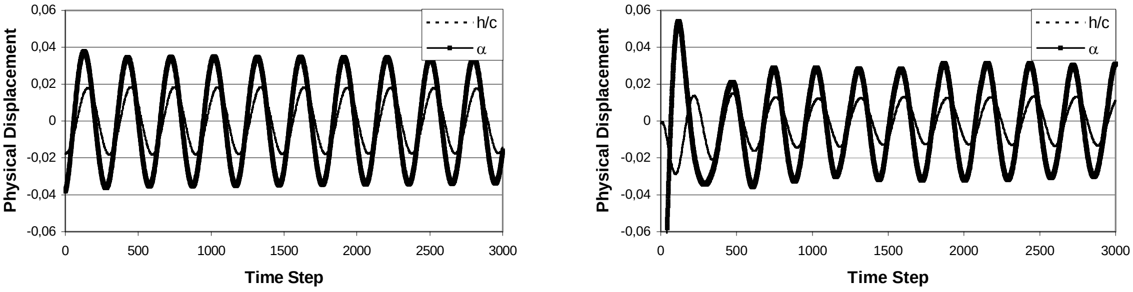

(a) TSD, M = 0.825, V^* = 0.177 (b) TSD+BL, M = 0.825, V^* = 0.204

Fig. 7.21. Neutral Response of DLR Model at Mach Number 0.825

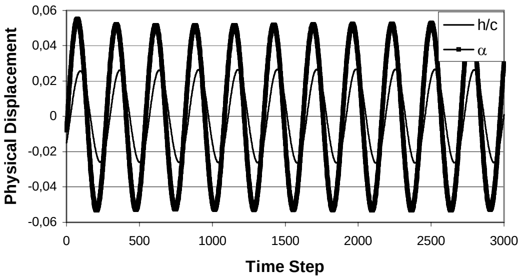

Fig. 7.22. Neutral Response of DLR Model at Mach Number 0.8375
(TSD, M = 0.8375, V^* = 0.196)

7.3. Transonic Dip of the AGARD Wing 445.6

In this sub chapter the flutter characteristic of the AGARD Wing 445.6 is computed for various Mach numbers, in order to examine the Transonic Dip phenomenon. The influence of the boundary layer in the flutter characteristic of the wing is also examined. The wing has been tested by Yates [88] in the wind tunnel TDT (Transonic Dynamic Tunnel) of NASA Langley. The wing is well-known as standard wing for aeroelastic simulation and dynamic response. The so-called ‘weak’ model 3 of this wing is selected as the basis model for the simulation of the Transonic Dip in this analysis. The number of the vibration mode shapes, which is involved in this simulation is only two modes (i.e. only the 1st bending and 1st torsion modes). The other mode shapes (with higher frequencies) is neglected, because only those two mode shapes are involved in flutter mechanism, as reported by Lee Rausch and Batina in Ref. [93]. Tables 7.3 and 7.4 and Fig. 7.23 represent the geometrical parameters and the structural data of the AGARD Wing 445.6.

Table 7.3. Geometrical Parameters of the AGARD Wing 445.6

Parameter		
Half span	s	2.5 ft
Root Chord	cr	1.833 ft
Taper Ratio	ct/cr	0.659
Aspect Ratio	AR	3.288
Sweep at ¼ Chord	φ_{LE}	45^o
Relative thickness	t/c	4%
Twist	θ	0.0^o

Table 7.4. Structural Data of the AGARD Wing 445.6

Parameter		
Profil		NACA 65A004
Steady angle of attack from Experiment	$\alpha 0$	0^o
Position of the elastic Axis (normalised with chord *c*)	a	0.5(from leading edge)
Frequency of the 1. Mode (Bending)	ω_1	9.6 Hz (60.3 rad/s)
Frequency of the 2. Mode (Torsion)	ω_2	38.16Hz (239.8 rad/s)
Ratio of Structure to Fluid density, ρ_m/ρ_∞	μ	225.82

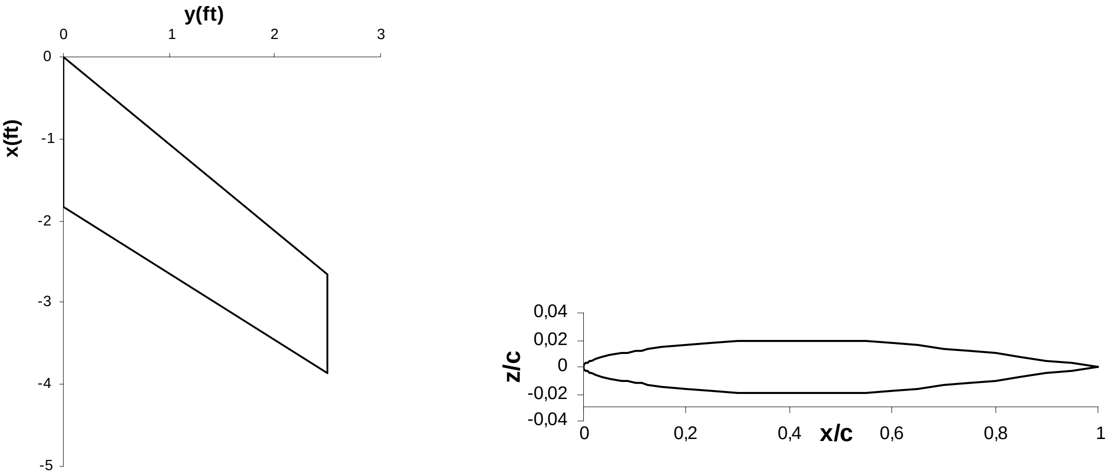

(a) Geometry (b) Airfoil

Fig. 7.23. Geometry of the AGARD Wing 445.6

In order to reduce the complexity of the flutter analysis, the Reynolds number and the ratio of structure to fluid density are assumed to be fixed for all Mach number. The Reynolds number for this simulation is 1.0E+06 (based on the root chord).

7.3.1. Modal Analysis of the AGARD Wing 445.6

The modal analysis of the AGARD Wing 445.6 was accomplished by Yates [88]. The two vibration mode shapes is presented in Fig. 7.24. The mode shapes was normalized, so that the value of the generalized mass matrix is equal to one.

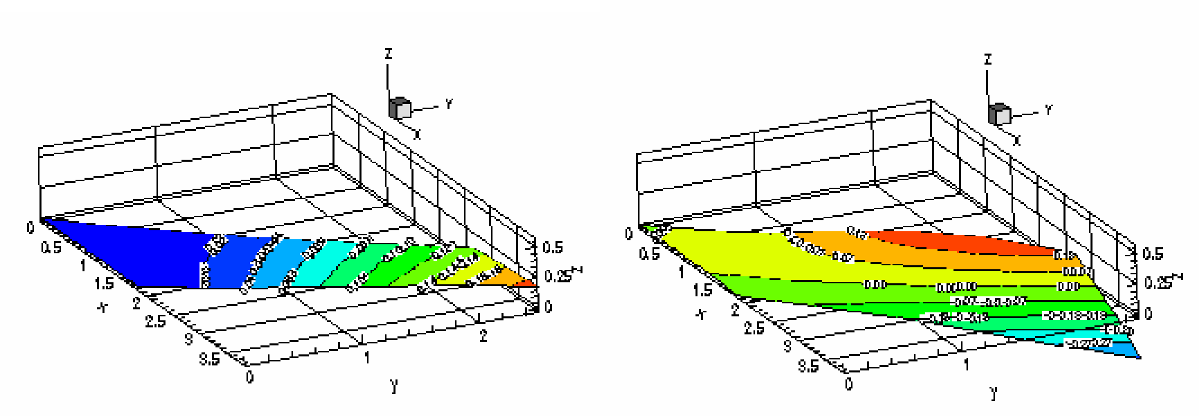

1st. Mode (Bending)
($\omega_1 = 9.6\ Hz,\ \omega_1/\omega_\alpha = 0.252$)

2nd Mode (Torsion)
($\omega_2 = 38.16\ Hz,\ \omega_2/\omega_\alpha = 1.0$)

Fig. 7.24. Vibration Mode Shapes of the AGARD Wing 445.6

In order to check the values of the coupled natural frequencies, response of the system is computed with zero dynamic pressure for some cycles of the oscillation. The Response system is shown in Fig. 7.25. In this computation the value of the time step $\Delta\tau = 0.277036388$ has been used. This is coresponded with $\Delta t = 0.00726$ sec. From equation (7.28) the natural frequencies can be found as:

$$\left(\frac{\omega}{\omega_\alpha}\right)_1 = 0.252, \quad \left(\frac{\omega}{\omega_\alpha}\right)_2 = 1.008$$

Fig. 7.25 represents the response of both mode shapes with zero dynamic pressure (i.e. the response of the generalized displacement with corresponded ω_1/ω_α und ω_2/ω_α).

7.3.2. Flutter Analysis of the AGARD Wing 445.6

The flutter analysis of the AGARD Wing 445.6 is accomplished by means of State Space equation (5.15):

$$\left\{\dot{X}\right\} = [A]\{X\} + [B]\{u\} \tag{5.15}$$

with the State Transition Matrices $[A]$ and $[B]$ are:

$$[A] = \begin{bmatrix} 0 & 1 & 0 & 0 \\ -\left(\frac{\omega}{\omega_\alpha}\right)_1^2 & 0 & 0 & 0 \\ 0 & 0 & 0 & 1 \\ 0 & 0 & -\left(\frac{\omega}{\omega_\alpha}\right)_2^2 & 0 \end{bmatrix} = \begin{bmatrix} 0 & 1 & 0 & 0 \\ -(0.2520)^2 & 0 & 0 & 0 \\ 0 & 0 & 0 & 1 \\ 0 & 0 & -(1.008)^2 & 0 \end{bmatrix} \tag{7.39}$$

$$[B]=\begin{bmatrix}0&0&0&0\\0&M_1^{-1}&0&0\\0&0&0&0\\0&0&0&M_2^{-1}\end{bmatrix}=\begin{bmatrix}0&0&0&0\\0&(1.0)^{-1}&0&0\\0&0&0&0\\0&0&0&(1.0)^{-1}\end{bmatrix} \tag{7.40}$$

The initial value of the state vector {X} is the same with the previous one used for Isogai model.

Before flutter analysis is carried out, the aerodynamics of the wing must be first examined. The steady pressure distribution of the AGARD Wing 445.6 for two Mach numbers (M=0.96 and 1.141) with zero angle of attack are presented in Fig. 7.26 and 7.27 for four sections along the span. Since the wing has a symmetrical airfoil and the angle of attack is zero, the wing does not produce a steady lift. It can be seen that the influence of the boundary layer into the pressure distribution is small. This is because there is no shock arises on the profile, which can lead a strong mutual interaction with the boundary layer.

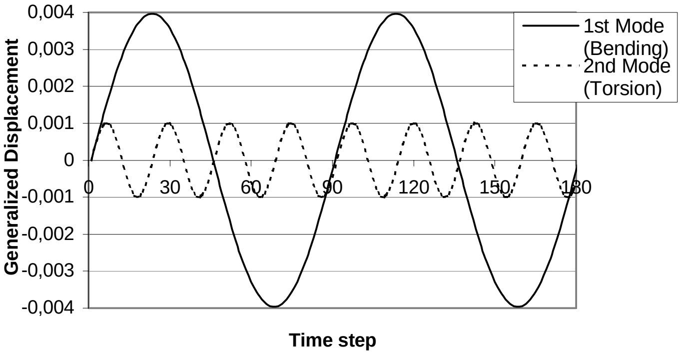

Fig. 7.25. Response of the AGARD Wing 445.6 at Zero Dynamic Pressure

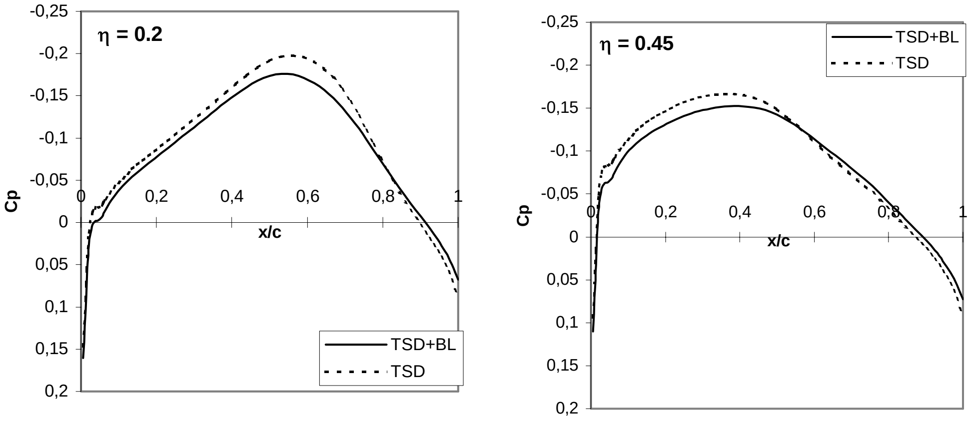

Fig. 7.26. Steady Pressure Distribution of the AGARD Wing 445.6
Mach = 0.96, α = 0.0, Re = 1.0E+06

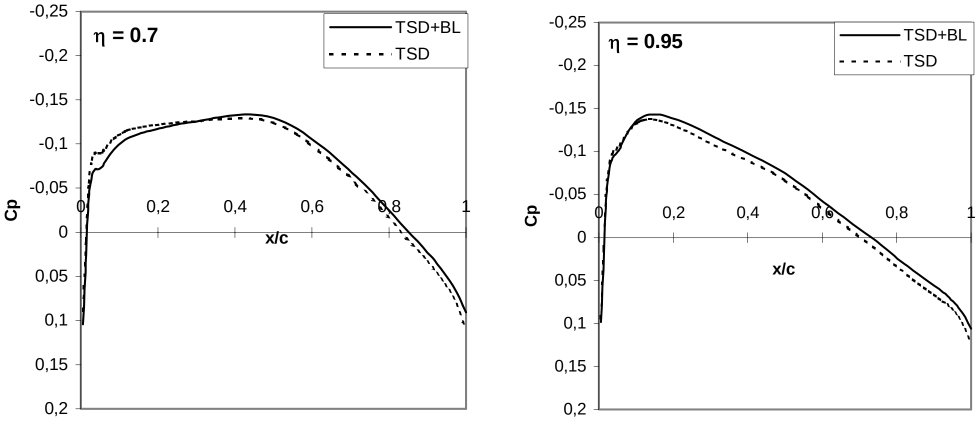

Fig. 7.26. Steady Pressure Distribution of the AGARD Wing 445.6 (continued)
Mach = 0.96, α = 0.0, Re = 1.0E+06

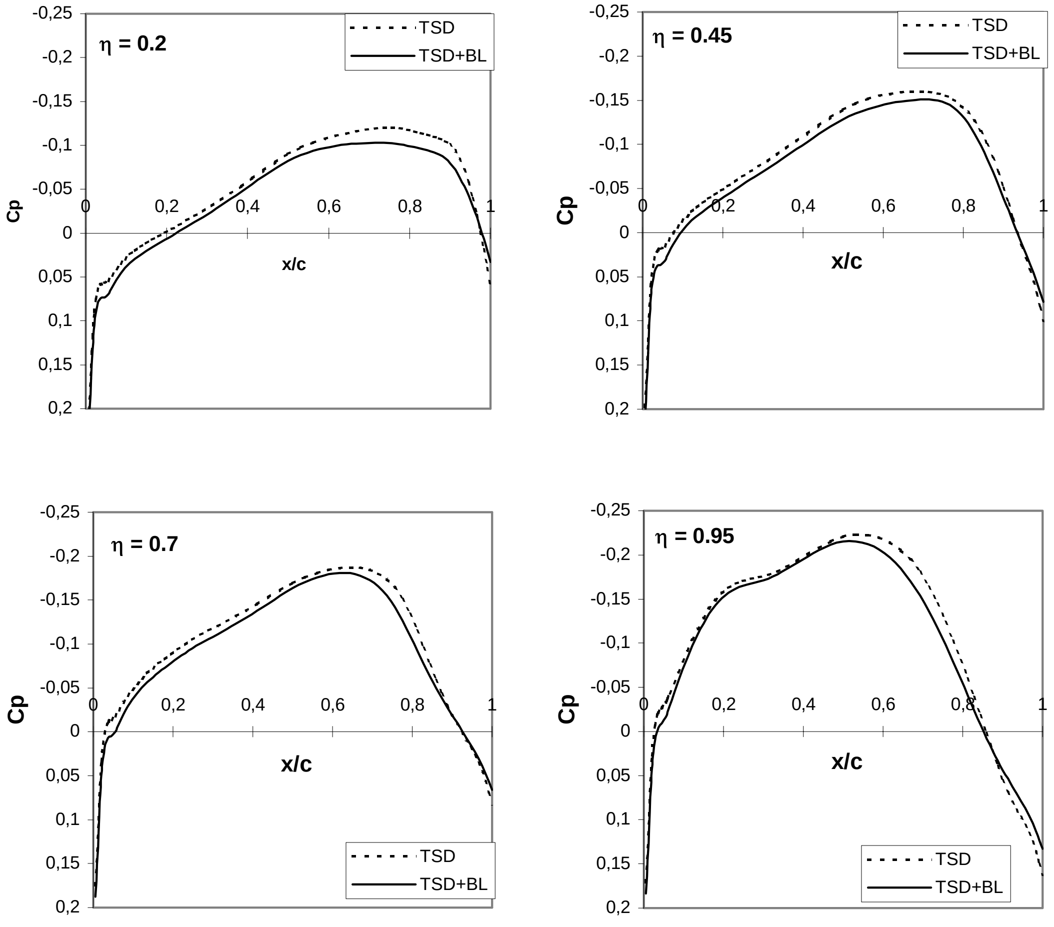

Fig. 7.27. Steady Pressure Distribution of the AGARD Wing 445.6
Mach = 1.141, α = 0.0, Re = 1.0E+06

Flutter analysis is then carried out for each Mach number. The response of the system is computed until a neutral response is found for each Mach number. This is carried out by starting the given speed (U_∞) and dynamic pressure ($0.5\rho_\infty U_\infty^2$) with low values and then increasing it step by step. Fig. 7.28 and Table 7.5 show the diagram of flutter speed index (V^*) and flutter frequency (ω_f/ω_α) versus Mach number.

The flutter speed index (V^*) is defined as:

$$V^* = \frac{V_f}{b\omega_\alpha \sqrt{\mu}} \tag{7.41}$$

where:

V_f = flutter speed
b = semi root chord
ω_α = uncoupled frequency of the torsion mode
μ = ratio of structural to fluid mass

The flutter speed index V^* and flutter frequency (ω_f/ω_α) will be compared with the results of Lee Rausch and Batina [93, 94] (with Euler and Navier Stokes equations, CFL3D code of NASA) and experimental values of Yates [88].

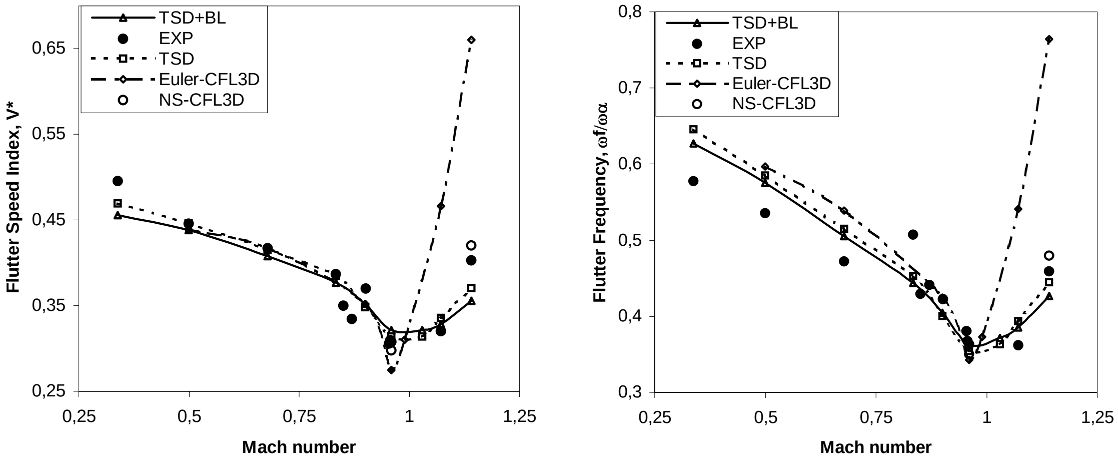

(a) Flutter Speed Index (b) Flutter Frequency

Fig. 7.28. Flutter Speed Index and Flutter Frequency v/s Mach Number of the AGARD Wing 445.6

Table 7.5a. Flutter Speed Index, V^* v/s Mach Number

Mach Number	TSD present	TSD+BL present	Euler [94]	Navier-Stokes [93]	EXP [88]
0.338	0.469	0.463	-	-	0.496
0.499	0.446	0.438	0.439	-	0.446
0.678	0.415	0.408	0.417	-	0.417
0.834	0.384	0.377	-	-	0.387
0.85	-	-	-	-	0.350
0.87	-	-	-	-	0.334
0.901	0.348	0.344	0.352	-	0.370
0.954	-	-	-	-	0.306
0.957	-	-	-	-	0.310
0.96	0.314	0.321	0.275	0.298	0.308
0.99	-	-	0.310	-	-
1.03	0.314	0.321	-	-	-
1.072	0.336	0.328	0.466	-	0.320
1.141	0.370	0.355	0.660	0.420	0.403

Table 7.5b. Flutter Frequency, (ω_f/ω_α) v/s Mach Number

Mach Number	TSD present	TSD+BL present	Euler [94]	Navier-Stokes [93]	EXP [88]
0.338	0.646	0.627	-	-	0.578
0.499	0.585	0.575	0.597	-	0.535
0.678	0.515	0.506	0.539	-	0.472
0.834	0.453	0.444	-	-	0.507
0.85	-	-	-	-	0.430
0.87	-	-	-	-	0.441
0.901	0.401	0.405	0.425	-	0.422
0.954	-	-	-	-	0.381
0.957	-	-	-	-	0.367
0.96	0.355	0.363	0.343	0.350	0.363
0.99	-	-	0.373	-	-
1.03	0.363	0.372	-	-	-
1.072	0.394	0.385	0.541	-	0.362
1.141	0.445	0.427	0.764	0.480	0.459

From Fig. 7.28 one can observe the followings:

- all numerical results can represent the Transonic Dip (the lowest flutter speed index, V^*) at Mach number 0.96.

- all numerical results agree with the experiment within the subsonic region.

- the deviation between Euler and the TSD is occurred after the Dip, whereby the flutter speed index of Euler result increases rapidly (more steeply than the TSD results)

- the influence of the boundary layer into the flutter result is small (compare between the TSD and the TSD+BL results in Fig. 7.28).

- the 1st mode shape seems to be dominant in the flutter mechanism (see Fig.7.28b). (notes: the frequency of 1st mode shape is $(\omega_1/\omega_\alpha) = 0.252$ and the 2nd mode shape is $(\omega_2/\omega_\alpha) = 1.0$)

Lee Rausch and Batina [93] used the Thin Layer Navier Stokes equations for the flutter analysis of this wing only for Mach number 0.96 and 1.141. This calculation serves for the confirmation of the inviscid results. It seems that all numerical and experimental result agree well at the Mach number 0.96. But at the Mach number 1.141 there is deviation between the experimental and numerical results. The Navier Stokes result seems a little bit over estimate, on the other hand the results of TSD and TSD+BL are under estimate compared to the experimental value.

The generalized response at the Mach number 0.96 and 1.141 (calculated with TSD and TSD+BL) is shown in Fig. 7.29 and 7.30 for various values of flutter speed index V^*. It seems that the generalized response is not so sensitive with the change of the flutter speed index (see Fig. 7.29a and c and Fig. 7.30a and c). The generalized response of the TSD and of the TSD+BL looks similar (not so different). This means that the influence of the boundary layer is not so significant for this case.

A part of these results has been presented in Ref. [95]

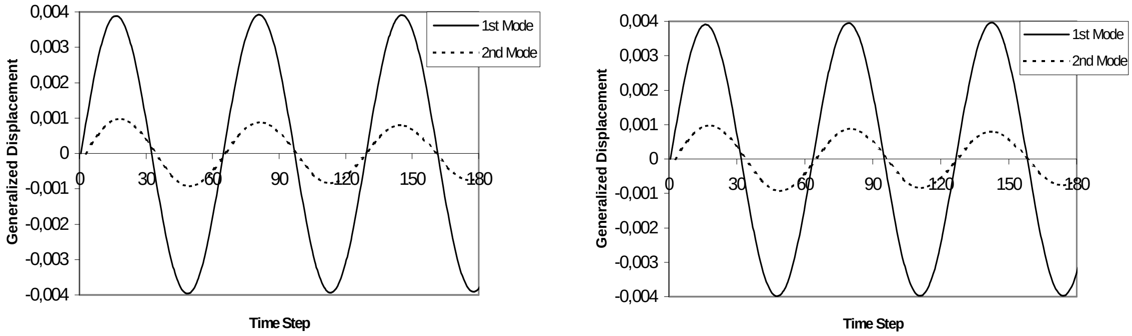

(a). TSD Result, $V^{*}= 0.314$ (b). TSD+BL Result, $V^{*}= 0.321$

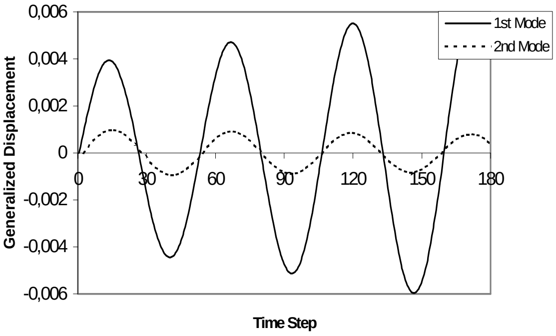

(c). TSD Result, $V^{*}= 0.769$

Fig. 7.29. Response of the AGARD Wing 445.6 at M=0.96

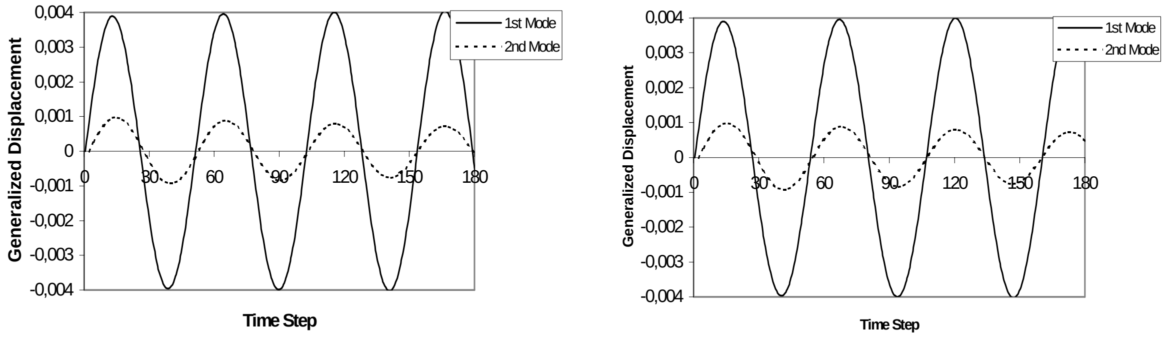

(a). TSD Result, $V^{*}= 0.370$ (b). TSD+BL Result, $V^{*}= 0.355$

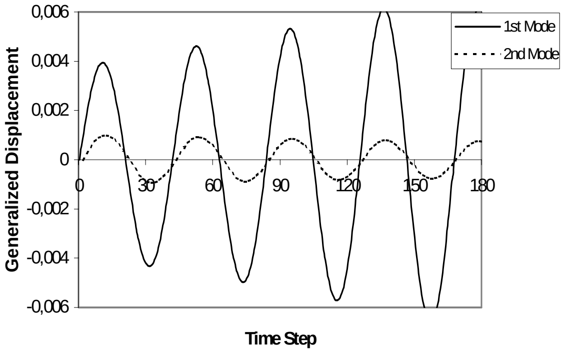

(c). TSD Result, $V^{*}= 0.769$

Fig. 7.30. Response of the AGARD Wing 445.6 at M=1.141

8. Summary and Recommendation

The goal of the present work is the development of a computer code, which is based on viscous – inviscid interaction method, which calculates steady and unsteady aerodynamic forces acting on airfoil and wing. The use of the code for the flutter calculation of airfoil and wing was also presented. The flow conditions were both laminar and turbulent, in the subsonic and particularly in the transonic regime.

The developed code consists of the following subroutines:

- Subroutine Inviscid:
    based on TSD, Euler and Small Disturbance Euler Equations
- Subroutine Viscous:
    - Integral Boundary Layer Equations:
        - Method proposed by Drela and Giles (laminar and turbulent)
        - Lag Entrainment Method proposed by Green et. al. (turbulent)
        - Method from Karman - Thwaites (laminar)
    - Differential Boundary Layer Equations:
        - Method proposed by Hamilton et. al. (laminar and turbulent)
    - Blasius Solution (laminar flat plate boundary layer)
    - Exponential 1/7 Law (turbulent flat plate boundary layer)
    - Transition from Laminar to Turbulent using the e^n Method

The coupling between the viscous and inviscid flow takes place in the boundary condition of the subroutine inviscid, where the influence of the boundary layer must be considered. The kinematics (tangential) boundary condition was updated with the displacement thickness (in form of the transpiration velocity or the gradient/slope of the surface). The coupling procedure is carried out with the direct and semi - inverse coupling for attached and separated flow respectively. The code was then used for flutter analysis of airfoils and wings. The flutter analysis is performed with State Transition Matrix technique in the time domain, which is efficient and can be solved accurately.

The following steps were performed in order to validate the developed computer code:

- Validating the developed computer code was performed first for checking the subroutines individually, i.e. the subroutine inviscid, subroutine viscous and transition prediction. From all simulations, that have been performed, it is shown that the individual subroutine supplies good results (see Chapter 6.1).
- After validating of the individual subroutines, the developed computer code was used for assessment of airfoils and wings under various flow conditions. The flow conditions represents symmetrical and asymmetrical flows, steady and unsteady flows, attached and separated flow. From all simulations, that have been performed, it is shown that the developed computer code could achieve the same quality (for some cases even better) with the values from the literature (see Chapter 6.2 and 6.3). During the simulation of separated flow it is shown that the developed code could supply good results comparable with the Navier Stokes equations with Baldwin Lomax turbulence model (see chapter 6.2.3.). Regarding the shock position, the shock position calculated by viscous - inviscid interaction method is mostly in front of the shock position calculated by Navier Stokes with Baldwin Lomax turbulence model (see Chapters 6.3.1 and 6.3.2) and for some cases is behind that of Navier Stokes results with Spalart Almaras turbulence model (see chapter 6.2 and 6.3).

Based on all performed aerodynamic simulations, the followings can be concluded:

- The influence of the boundary layer must be considered. With the inclusion of the boundary layer into the aerodynamic computation, the quality of the lift, drag and moment coefficient can be improved around approximately 10% (or even more for some cases) (see Chapter 6.2 and 6.3). But this improvement does not ensure automatically that the numerical results agree with the experiment data. The agreement between the numerical and the experimental result depends on some things, e.g.: the case to be examined, the quality of the experiment and the quality of the calculation method. For the cases with higher Reynolds numbers and without separation, a good agreement between the calculation and the experiment could be achieved. But the flow with separation is still a challenge for the aerodynamicists, in order to compute the characteristic of the flow (i.e. lift, drag and moments) accurately. The quality of experimental data depends on the measuring technique, the quality of the wind tunnel and the model. The quality of the calculation method is influenced by the assumption behind the governing equation, the numeric method and the solution technique.
- The unsteady flow with larger mean angle of attack, resulting from oscillatory motion, is particularly difficult to simulate, although the amplitude of the oscillation is small. The complexity of the unsteady flow could be not completely simulated with the viscous-inviscid interaction method. The influence of the boundary layer still represents a ‘linear’ relationship, i.e. due to the boundary layer the shock position shifts forward, the shock intensity becomes smaller and the global characteristic: lift, drag and moments become smaller. The pressure distribution of the viscous-inviscid interaction method does not show a reverse phase with the pressure distribution of the inviscid method.

The following steps were performed in validation of the flutter calculation method and application of the viscous-inviscid interaction method for flutter analysis:

- The developed flutter calculation method (with the inviscid aerodynamics model TSD) was validated with the classical test case of Isogais model, before the code was used for the computation of the flutter of another airfoil and wing. The flutter analysis result represents the ability of the developed flutter calculation method to capture the Transonic Dip, i.e. the lowest flutter speed in the transonic flow. The resulted flutter speed index v/s Mach number diagram showed that the developed flutter calculation method could supply the same quality with another method that has been published (see Chapter 7.1).
- The developed flutter calculation method (with the inviscid aerodynamics model TSD and the viscous-inviscid aerodynamics model TSD+BL) was used for the flutter analysis of the DLR 2D model and the AGARD wing 445.6. The flutter speed index v/s Mach number diagram for the DLR model showed that the deviation of the flutter speed between the calculation and the experiment lies in the determining of the aerodynamic forces. The deformation of the wind tunnel model because of the aerodynamic forces (static aeroelastic effect) causes this deviation (see Chapter 7.2). The flutter diagram of the AGARD wing 445.6 represents the agreement between the calculation and the experiment. Comparison with other numerical methods shows the same quality (see Chapter 7.3). The influence of the boundary layer on the flutter characteristic for the two cases is small (approximately 5% of the result by using the inviscid aerodynamics model).

In order to improve the viscous-inviscid interaction method, the followings are suggested:

- An improvement or an extension of the closure equations of the turbulent boundary layer in the integral boundary layer method, in order to be able to compute a massively separation.

- The simultaneous coupling between the viscous and the inviscid aerodynamic model should be examined. The closure equations should be kept the same, as they are applied in the direct and the semi inverse coupling, in order to know the difference between the both couplings technique.
- Because of the time restriction, the differential boundary layer method was not examined or elaborated intensively in this present work. As a further work this method should be examined, in order to recognize its deviation with the integral boundary layer method.
- A possibility for the improvement of the implementation of the 2D integral boundary layer method along the span is that the distribution of velocity is connected with the stream lines, in order to consider the three-dimensional effects. At the present work it was implemented in strip theory manner along the span without considering the stream lines of the flows.

The followings are suggested for the improvement of the flutter analysis:

- The flutter analysis with Euler and Euler plus boundary layer aerodynamics model should be performed. The boundary condition for aeroelastic coupling should be implemented by means of transpiration velocity concept (like the boundary layer coupling which is already implemented), in order to avoid the moving grid generation (because of the movement of the structure). This means: the movement of the structure is formulated as additional induced velocity; with this velocity the boundary condition of the aerodynamic model is updated.
- For validating the developed flutter analysis, which is developed in the time domain, an ‘apple to apple’ comparison with flutter analysis in the frequency domain should be carried out. Because of the time restriction this comparison could not be made in the present work.
- Deformation of the structure (due to aeroelastic effect) should be treated, in order to compute the aerodynamic forces of a flexible structure accurately.
- Extension of the developed flutter analysis for the investigation of flutter suppression or gust load alleviation should be continued by adding the state space formulation with control systems matrix.

References

[1] Laschka, B., ‘Zur Theorie der harmonisch schwingenden tragenden Fläche bei Unterschallanströmung’, Zeitschrift für Flugwissenschafften, 11, 1963

[2] Albano, E. and Rodden, W.P., ‘A Doublet-Lattice Method for Calculating the Lift Distributions on Oscillating Surfaces in Subsonic Flow’, AIAA Journal, 7(2) : 279-285, 1969

[3] Drela, M. and Giles, M.B., ‘Viscous-Inviscid Analysis of Transonic and Low Reynolds Number Airfoils‘; AIAA Journal, Vol. 25, No. 10, Oct. 1987

[4] Wolles; B.A., ‘Computational Viscid-Inviscid Interaction Modelling of the Flow about Aerofoils‘; PhD Thesis, University of Twente, The Netherlands, 1999

[5] Schlichting, H., ‘Boundary Layer Theory‘ ; Mac Graw Hill, New York, 1960

[6] Su, J., ‘Calculation of Compressible and Incompressible Viscous Flows by a Viscous Inviscid Splitting Finite Element Method’, Proceeding of 23rd ICAS Congress, Toronto, Canada, 8-13 Sept., 2002, pp. 171.1-171.8

[7] Le Balleur, J.C., ’New Possibilities of Numerical Viscous Inviscid Coupling for Viscous Flows with Massive Separation and for Inviscid Zonal Methods’, Conference on Computational Aeronautical Dynamics, Antibes, May 1989

[8] Rizzetta, D.P., ’Procedures for the Computation of Unsteady Transonic Flows Including Viscous Effect’, NASA CR – 166249, Jan 1982

[9] Houwink, R., ‘Unsteady Viscous Transonic Flow Computation using the LTRAN2-NLR Code Coupled with Green’s Lag Entrainment Method’, in Numerical and Physical Aspects of Aerodynamic Flows (Editor T. Cebeci) , Vol. II, Chapter 15, Springer Verlag, New York, 1984.

[10] Rizzetta, D.P. & Borland, C.J., ‘Unsteady Transonic Flow Over Wings Including Inviscid/Viscous Interaction’, AIAA Journal, vol. 21, March 1983, pp. 363-371

[11] Green, J.E., Weeks, D.J. and Brooman, J.W.F., ‘ Prediction of Turbulent Boundary Layers and Wakes in Compressible Flow by a Lag-Entrainment Method‘; R. & M. No. 3791, British Aeronautical Research Council, 1977

[12] Goldstein, S., ’On Laminar Boundary Layer Flow near a Position of Separation’, Quarterly Journal of Mechanics and Applied Mathematics, 1, 1948

[13] Chaterall, D. & Mangler, K., ’The Integration of the Two Dimensional Laminar Boundary Layer Equations Past the Point of Vanishing Skin Friction’, Journal of Fluid Mechanics, 26, Part I:163-182, 1966

[14] Carter, J.E., ‘A New Boundary Layer Interaction Technique for Separated Flows’, NASA TM 78690, June 1978

[15] Melnik, R.E. and Brook; J.W., The Computation of Viscid/Inviscid Interaction on Airfoils with Separated Flow‘; Third Symposium on Numerical and Physical Aspects of Aerodynamic Flows, California State University, 1985, pp.1-21 – 1-37

[16] Le Balleur, J.C. and Girodroux-Lavigne; P., ‘A Viscous-Inviscid Interaction Method for Computing Unsteady Transonic Separation‘; Third Symposium on Numerical and Physical Aspects of Aerodynamic Flows, California State University, 1985

[17] Zhiliang, L. and Voss, R., ‘DLR FP+VII Code Improvements and Computation of Unsteady Transonic Flows’, DLR IB 232 – 96 J 03, Institut für Aeroelastik –DLR, Göttingen, Germany, 1996.

[18] Veldman, A.E.P., ‘New, quasi-Simultaneous Method to Calculate Interacting Boundary Layer’, AIAA Journal, 19 (1):79-85, Jan 1981

[19] Houwink, R. and Veldman, A.E.P., ‘Steady and Unsteady Separated Flow Computation for Transonic Airfoil’, AIAA Paper 84-1618, June 1984

[20] Howlett, J.T., ‘Calculation of Unsteady Transonic Flows with Mild Separation by Viscous-Inviscid Interaction‘, NASA-TP-3197, NASA Langley Research Center, Jun 01, 1992

[21] Edwards, John W.,‘ Transonic Shock Oscillations and Wing Flutter Calculated with an Interactive Boundary Layer Coupling Method‘, NASA-TM-110284, NASA Langley Research Center (Hampton, VA United States), Aug 01, 1996

[22] Galpin, S.A., ‘The Application of a Time-Accurate Unstructured Euler Solver, Coupled with a Boundary Layer Solver for the Solution of Transonic Aeroelastic Problems on Complex Configurations’, Proceeding of 22nd Congress of ICAS, Haerogate, 2000, pp. 271.1-271.8

[23] Haase, W., Chaput, E., Elsholz, E., Leschziner, M., Müller, U.R., ‘ECARP : European Computational Aerodynamic Research Project : Validation of CFD Codes and Assessment of Turbulence Models’, Notes on Numerical Fluid Mechanics, Vieweg Verlag, Braunschweig, 1997

[24] Drela, M. and Mughal, B., ‘A Calculation Method for the 3D Boundary Layer Equations in Integral Form‘; AIAA Paper 93-0786, Reno Nevada, Jan.1993

[25] Van Dalsem, W.R. and Steger, J.L., ‘Finite Difference Simulation of Transonic Separated Flow Using a Full Potential – Boundary Layer Interaction Approach’, AIAA Paper 83-1689, July 1983

[26] Hamilton II, H.H., Millman, D.R. and Greendyke, R.B., ‘Finite Difference Solution of Laminar or Turbulent Boundary Layer Flow over Axisymmetric Bodies with Ideal Gas, CF4 or Equilibrium Air Chemistry’, NASA TP-3271, Dec. 1992

[27] Henke, H. H., ‘Progress of the Viscous-Coupled 3D Euler Method EUVISC and Its Aeroelastic Application‘, International Forum of Aeroelasticity and Structure Dynamics (IFASD) 2003, Amsterdam, The Netherland, 4-6, June 2003

[28] Lock, R.C. and Williams, B.R. ‚Viscous-Inviscid Interactions in External Aerodynamics, Progress on Aerospace Sciences, 24, pp. 51-171, 1987

[29] T. Cebeci and J. Cousteix; ‘Modeling and Computation of Boundary Layer Flow‘; Springer, Berlin, 1999

[30] Hoffman, K.A., ‘CFD for Engineers’, University of Texas at Austin, 1989

[31] Murman, E.M and Cole, J.D., ’Calculation of Plane Steady Transonic Flows’, AIAA Journal, Vol. 9, pp. 114-121, 1971

[32] Garabedian, P.R. and Korn, D., ’Analysis of Transonic Airfoil’, Communications on Pure and Applied Mathematics, Vol. 24, pp. 841-851, 1971

[33] Steger, J.L. and Lomax, H., ‘Transonic Flow about Two Dimensional Airfoils by Relaxation Procedures’, AIAA Journal, Vol. 10, pp.49-54, 1972

[34] Ballhaus, W.F. and Bailey, F.R., ‘Numerical Calculation of Transonic Flow About Swept Wings’, AIAA Paper 72-677, 1972

[35] Bailey, F.R. and Steger, J.L., ‘Relaxation Techniques for Three Dimensional Transonic Flow About Wings’, AIAA Paper 72-189, 1972

[36] Murman, E.M., ’Analysis of Embedded Shock Waves Calculated by Relaxation Methods’, AIAA Journal, Vol. 12, no.5, pp. 626-635, 1974

[37] Ballhaus, W.F. and Goorjian, P.M., ‘Implicite Finite Difference Computations of Unsteady Transonic Flows about Airfoil’, AIAA Journal, Vol. 15, Dec. 1977, pp. 1728-1735

[38] Borland,C.J., Rizzetta, D.P. and Yoshihara, H., ‘Numerical Simulation of 3D Unsteady Transonic Flow over Swept Wing’, AIAA Journal, Vol. 20, March 1982, pp. 340-347

[39] Ballhaus, W.F. and Steger, J.L., ‘Implicit Approximate Factorization Schemes for the Low Frequency Transonic Equations’, NASA TM X-73, 082, 1975

[40] Ballhaus, W.F, Jameson, A. and Albert, J., ‘Implicit Approximate Factorization Schemes for the Efficient Solution of Steady Transonic Flow Problems’, AIAA Journal, Vol. 16, No. 6, pp.573-579, June 1978

[41] Baker, T.J., ’Potential Flow Calculation by the Approximate Factorization Method’, Journal of Computational Physics, Vol. 42, pp. 1-19, 1981

[42] Steinhoff, J. and Jameson, A., ‘Multiple Solution of the Transonic Potential Flow Equations’, AIAA Journal, Vol. 20, pp. 1521-1525, 1982

[43] Salas, M., Jameson, A. and Melnik, R., ‘A Comparative Study of the Non Uniqueness Problem of the Potential Equation’, AIAA Paper 83-1888, 1983

[44] Hafez, M.M. and Lovel, D., ‘TSD Calculation including Entropy Correction’, Numerical & Physical Aspects of Aerodynamic Flows II (editor T. Cebeci), Springer Verlag, 1981

[45] Hafez, M.M. and Lovel, D., ‘Entropy and Vorticity Corrections for Transonic Flows’, AIAA Paper 83-1926, 1983

[46] Fuglsang, D. F. and Williams, M. H.; ,‘Non Isentropic Unsteady Transonic Small Disturbance Theory‘; AIAA Paper 85-0800, 1985

[47] Batina, J.T., ‘Efficient Algorithm for Solution of the Unsteady Transonic Small-Disturbance Equation’, Journal of Aircraft, Vol. 25, No.7, pp.598-605, 1988

[48] Batina, J.T., Seidel, D.A., Bland, S.R., Bennett, R.M., ‘Unsteady Transonic Flow Calculations for Realistic Aircraft Configurations’, Journal of Aircraft, Vol. 26, Jan. 1989, pp. 21-28; also as AIAA Paper 87-0850

[49] Batina, J.T., ‘A Finite Difference Approximate Factorization Algorithm for Solution of the Unsteady Transonic Small Disturbance Equation’, NASA TP 3129, Jan. 1992

[50] Mitterer, K. F., Maughmer, M. D., Silva, Walter A. and Batina, J. T., Improving CAP-TSD steady pressure solutions through airfoil slope modification , NASA-TM-110214 , NASA Langley Research Center (Hampton,VA United States), Aug 01, 1996

[51] Hung, H.; Gear, J.A. & Phillips, N.J.T., ’Transonic Flow Calculations using a dimensional Splitting Method’, ANZIAM Journal, 42 (E), pp C752-C773, 2000

[52] Ly, E. and Nakamichi, J., ‘Time–linearised Transonic Small Disturbance Code including Entropy and Vorticity Effects’, Proceeding of 23rd ICAS Congress, Toronto, Canada, 8-13 Sept., 2002, pp. 1-10

[53] Greco Jr., P.C. and Sheng, L.Y., ‘A Fast Viscous Correction Method Applied to Small Disturbance Potential Transonic Flows in the Frequency Domain’, Proceeding of 24th ICAS Congress, Yokohama, 29 Aug- 3 Sept. 2004.

[54] Steger, J.L. and van Dalsem, W.R., ’Basic Numerical Methods’, in Unsteady Transonic Aerodynamics (editor David Nixon), Progress in Astronautics & Aeronautics, Vol. 120, AIAA, 1989

[55] Sekar, W. K., ‘Viskose - Nichtviskose Interaktionsmethode zur Berechnung der Aerodynamik und Aeroelastik in Transsonische Anströmung’, Interner Bericht, 2004-08, Lehrstuhl für Fluid Mechanik, Technische Universität München, 2004

[56] Batina, J.T., ‘Unsteady Transonic Small-Disturbance Theory Including Entropy and Vorticity Effects’, Journal of Aircraft, Vol. 26, No. 6, June 1989

[57] Kreiselmaier, E. and Laschka, B., ‘Small Disturbance Euler Equations: Efficient and Accurate Tool for Unsteady Load Prediction’, Journal of. Aircraft, Vol. 37, No. 5, Sept.-Oct. 2000

[58] Roe, P.L., ‘Appoximate Riemann Solver, Parameter Vector and Difference Schemes’, Journal of Computational Physics, 43, 1981

[59] Yoon, S. and Jameson, A., ‘A Multigrid LU-SSOR Scheme for Approximate Newton-Iteration Applied to the Euler Equations, NASA-CR-17954, 1986

[60] Blazek, J., ‘Investigation of the Implicit LU-SSOR Scheme, Forschungsbericht DLR-FB 93-51, 1993

[61] Weishäupl, C. Laschka, B., ‘Calculations of Unsteady Aerodynamic Forces Using the Small Disturbance Euler Equations (SDEu)’, IFASD Forum, Madrid, 5-7 June 2001

[62] Weishäupl, C. and Laschka, B., ‘Small Disturbance Euler Simulations for Delta Wing Unsteady Flows due to Harmonic Oscillations’, Journal of. Aircraft, Vol. 41, No. 4, Jul.-Aug. 2004

[63] Allen, A., Weishäupl, C. and Laschka, B., ‚Eulerrechnungen an Flügeln kleiner Streckung’, DGLR 2004-053, Proceeding des DGLR Luft- und Raumfahrtkongresses, 2004

[64] Bisplinghoff, R.L., Ashley, H. and Halfman., R.L., ‘Aeroelasticity’, Addison-Wesley, New York, 1955

[65] Borland, C.J. and Rizzetta, D.P., ‘Nonlinear Transonic Flutter Analysis’, AIAA Journal, Vol.20, Nov. 1982, pp. 1606-1615

[66] Bennet, R.M., Batina, J.T., Cunningham, H.J.; ‘Wing Flutter Calculations with the CAP-TSD Unsteady Transonic Small Disturbance Program’, Journal of Aircraft Vol. 26 No. 9, 1989

[67] Skelton, R.E., ‘Dynamic Systems Control: Linear Systems Analysis and Synthesis’, John Wiley and Son, New York, 1988

[68] Viviand, H., ‘Numerical Solutions of Two Dimensional Reference Test Case’, in AGARD AR No. 211 : Test Case for Inviscid Flow Field Methods, NATO, Neuilly Sur Seine, France, 1985

[69] Warren, E.W. and Hassan, H.A.; ’Alternative to the e^n Method for Determining Onset of Transition’, AIAA Journal, Vol.36, No.1, pp111-113, 1998.

[70] Thibert, Grandjacques and Bateman, ‚NACA 0012 Airfoil‘ , in AGARD AR 138,’ Experimental Data Base for Computer Program Assessment’, London, May 1979.

[71] Sekar, W.K., Weishäupl, C. and Laschka, B.; ‚Flow Calculation around Airfoils using the TSD Equation and Viscous – Inviscid Interaction‘, in Indo German Conference 2001 (Bandung, Indonesien, 11. –13. Juli 2001) also in ‚Jurnal Sains dan Teknologi Aeronotika‘ (JSTA), Vol. 3 No. 3 Maret 2002, ISSN 1411-0555

[72] Cook, P.H., McDonald, M.A. and Firmin, M.C.P., ‘Aerofoil RAE 2822- Pressure Distribution, Boundary Layer and Wake Measurement’, in AGARD AR 138,’ Experimental Data Base for Computer Program Assessment’, London, May 1979.

[73] Holst, T.L., ‘Viscous Transonic Airfoil Workshop Compendium of Results’, Journal of Aircraft, Vol. 25, No. 12, Dec. 1988, pp.1073-1087

[74] Harris, C. D., „Two-Dimensional Aerodynamic Characteristics of the NACA 0012 Airfoil in the Langley 8-foot Transonic Pressure Tunnel“ , NASA TM-81927, 1981

[75] Cvrlje, T. ‘Instationäre Aerodynamik des Separationsvorgangs zwischen Träger und Orbiter’, Dissertation Technische Universität München, Germany, 2001.

[76] Prananta, B.B., ‘Physical & Numerical Aspects of Aeroelastic Simulations’, PhD Dissertation, TU Delft, The Netherlands, 1999

[77] Lorenz-Meyer, W. and Aulehla, F., ‘MBB Body of Revolution No. 3’, in AGARD AR 138,’ Experimental Data Base for Computer Program Assessment’, London, May 1979.

[78] Anonymous. RAMPANT User’s Manual. Fluent Inc., Centerra Resource Park, Lebanon, NH 03766, June 1997

[79] Djojodihardjo, H., Widodo, A.F., Priyono, E., Sekar, W.K., Weishäupl, C. and Laschka, B., ‘Transonic Flow Calculation of Axi-Symmetric Bodies using Slender Body Integral, Transonic Small Disturbance and Navier-Stokes Equations’, International Conference on Computational and Experimental Engineering and Sciences (ICCES) 2003, Corfu, Greece, 24-25 July 2003

[80] Landon, ‚Oscillatory and Pitching Oscillation‘, in AGARD Report no. 702, Compendium of Unsteady Aerodynamic Measurements, London, August 1982

[81] Zwaan, ‚LANN Wing, Pitching Oscillation‘, in AGARD Report no. 702, Compendium of Unsteady Aerodynamic Measurements - Addendum, London, August 1982

[82] Bennet, R.M. and Walker, C.E., ’Computational Test Cases for a Clipped Delta Wing with Pitching and Trailing-Edge Control Surface Oscillations’, NASA Langley, Virginia, March 1999

[83] Sekar, W.K., Weishäupl, C. and Laschka, B.; A Viscous – Inviscid Interaction Approach for Flow Calculation around Airfoils‘, in 3rd. Indo Taiwan Seminar, Bandung, Indonesia, 16. –18. December 2002

[84] Sekar, W. K., Weishäupl, C., and Laschka, B., ‘Comparison of Viscous-Inviscid Interaction Results using Two Inviscid Numerical Methods based on TSD and Euler Equations’, to be presented at Regional Conference on Aeronautical Science, Technology and Industry RC-ASTI 2004, Bandung Indonesia, 18-19 May 2004

[85] Pechloff, A. and Laschka; B., ‘Small Disturbance Navier-Stokes Method: Efficient Tool for Predicting Unsteady Air Loads’, Journal of Aircraft, Vol.43, No.1, 2006

[86] Isogai, K.; ‘Transonic Dip Mechanism of Flutter of a Sweptback Wing : Part II ‘, AIAA Journal Vol. 19 No. 9., 1981

[87] Schewe, G., Knipfer, A. , Mai, H. and Dietz, G., ‘Experimental and Numerical Investigation of Nonlinear Effects in Transonic Flutter’, DLR IB 232-2002 J 01, DLR Institut of Aeroelasticity, Göttingen, 2002

[88] Yates Jr.; E. C., ‘AGARD Standard Aeroelastic Configurations for Dynamic Response I – Wing 445.6’, AGARD R-765, 1985

[89] Davis, S.,’NACA 64A010 (NASA Ames model). Oscillatory pitching.’ in Compendium of Unsteady Aerodynamic Measurement, AGARD Report R-702, Neuilly-sur-Seine, 1982

[90] Alonso, J.J. and Jameson, A., ‘Fully Implicit Time Marching Aeroelastic Solutions’, AIAA Paper 94-0056, 1994

[91] Sekar, W.K., Laschka, B., ‘Calculation of Transonic Dip of Airfoils using Viscous-Inviscid Aerodynamic Interaction Method’, DGLR Kongress 2003, München, Germany, 17-20 Nov. 2003. Also published in Journal of Aerospace Science and Technology, Vol. 9, Nov. 2005

[92] Zwaan, ‚NLR 7301 supercritical airfoil. Oscillatory Pitching and Oscillating Flap‘, in AGARD Report no. 702, Copendium of Unsteady Aerodynamic Measurements, London, August 1982

[93] Lee-Rausch, E.M. and Batina, J.T., ‘Calculation of AGARD Wing 445.6 Flutter using Navier-Stokes Aerodynamics’, AIAA Paper No. 93-3476, AIAA 11th Aplied Aerodynamics Conference, Monterey, California, USA, 9-11 August 1993

[94] Lee-Rausch, E.M. and Batina, J.T., ‘Wing Flutter Boundary Prediction Using Unsteady Euler Method’, AIAA Paper 93-1422-CP, 1993

[95] Sekar, W.K., Weishäupl, C., and Laschka, B., ‘A Viscous-Inviscid Interaction for Aerodynamic and Aeroelastic Calculation’, to be presented at ICAS 2004, Yokohama Japan, 29 August –03 September 2004

Appendix 1. Numerical Methods

A1.1. The Runge-Kutta Method

The Runge-Kutta method is used to solve a 1st order linear differential equation numerically. In the Runge-Kutta method, an initial value (or a boundary value) of the function which must be solved at the starting point is needed in order to determine its value at the next point.

The procedure of Runge-Kutta method for solving of a 1st order linear differential equation can be written as follows:

The differential equation, which must be solved, has the following form:

$$\frac{dy}{dx} = f(x, y) \qquad (A1.1)$$

where $f(x,y)$ is a function of x and y.

The given initial value of y at the first point x_n is:

$$y(x_n) = y_n \qquad (A1.2)$$

The solution of eq. (A1.1) at the next point x_{n+1} is given by:

$$y_{n+1} = y_n + \frac{1}{6}\left(k_1 + 2k_2 + 2k_3 + k_4\right) \qquad (A1.3)$$

where:

$$\begin{aligned}
k_1 &= h\ f(x_n, y_n) \\
k_2 &= h\ f(x_n + \frac{h}{2}, y_n + \frac{k_1}{2}) \\
k_3 &= h\ f(x_n + \frac{h}{2}, y_n + \frac{k_2}{2}) \\
k_4 &= h\ f(x_n + h, y_n + k_3) \\
h &= x_{n+1} - x_n \qquad (A1.4)
\end{aligned}$$

For a simultaneous system of many 1st order differential equations the procedure of Runge-Kutta method becomes as follows:

The system of differential equations reads:

$$\begin{aligned}
\frac{dy}{dx} &= f(x, y, z, ...) \\
\frac{dz}{dx} &= g(x, y, z, ...) \qquad (A1.5) \\
. \quad & \quad .
\end{aligned}$$

where $f(x,y,z...)$ and $g(x,y,z...)$..., are functions of x, y,z...

The initial values of y, z... at the starting point x_n are:

$$\begin{aligned}
y(x_n) &= y_n \\
z(x_n) &= z_n \qquad (A1.6) \\
. \quad & \quad . \\
. \quad & \quad .
\end{aligned}$$

The solutions of eq. (A1.5) for the next point x_{n+1} are:

$$y_{n+1} = y_n + \frac{1}{6}\left(k_1 + 2k_2 + 2k_3 + k_4\right)$$

$$z_{n+1} = z_n + \frac{1}{6}\left(m_1 + 2m_2 + 2m_3 + m_4\right) \qquad (A1.7)$$

$$\begin{matrix} . & & . \\ \\ . & & . \end{matrix}$$

where:

$$k_1 = h\ f(x_n, y_n, z_n, ...)$$
$$k_2 = h\ f(x_n + \frac{h}{2}, y_n + \frac{k_1}{2}, z_n + \frac{m_1}{2}, ...)$$
$$k_3 = h\ f(x_n + \frac{h}{2}, y_n + \frac{k_2}{2}, z_n + \frac{m_2}{2}, ...)$$
$$k_4 = h\ f(x_n + h, y_n + k_3, z_n + m_3, ...)$$

$$m_1 = h\ g(x_n, y_n, z_n, ...)$$
$$m_2 = h\ g(x_n + \frac{h}{2}, y_n + \frac{k_1}{2}, z_n + \frac{m_1}{2}, ...)$$
$$m_3 = h\ g(x_n + \frac{h}{2}, y_n + \frac{k_2}{2}, z_n + \frac{m_2}{2}, ...)$$
$$m_4 = h\ g(x_n + h, y_n + k_3, z_n + m_3, ...)$$
$$h = x_{n+1} - x_n \qquad (A1.8)$$

A1.2. The Newton Iteration Method

The Newton iteration method is used if one would like to determine the roots of a function with iterative procedure. This method is quick and stable, if the derivative of the function is not singular.

The roots of a function F:

$$F(x) = 0 \qquad (A1.9)$$

will be solved iteratively.

From the 1st order Taylor series, the value of F at x_{n+1} can be computed as:

$$F(x_{n+1}) = F(x_n) + \left(\frac{dF}{dx}\right)_{x=x_n} (x_{n+1} - x_n) \qquad (A1.10)$$

where x_n is an initial guessed value of root x.

Taking the eq. (A1.10) equals to zero:

$$F(x_n) + \left(\frac{dF}{dx}\right)_{x=x_n} (x_{n+1} - x_n) = 0 \qquad (A1.11)$$

then x_{n+1} is found as:

$$x_{n+1} = x_n - \frac{F(x_n)}{\left(\frac{dF}{dx}\right)_{x=x_n}} \qquad (A1.12)$$

This procedure is repeated iteratively until a convergence value of x is obtained.

Appendix 2. Integral Boundary Layer Equations

A2.1. The Integral Momentum Equation

The integral boundary layer equations are derived from the Prandtl differential boundary layer equations.

The Prandtl differential boundary layer equations in 2D flow are as follows:

$$\frac{\partial \rho u^2}{\partial x} + \frac{\partial \rho u w}{\partial z} = -\frac{\partial p}{\partial x} + \frac{\partial \tau_{xz}}{\partial z} \qquad (A2.1)$$

$$0 = -\frac{\partial p}{\partial z} \qquad (A2.2)$$

$$\frac{\partial \rho u}{\partial x} + \frac{\partial \rho w}{\partial z} = 0 \qquad (A2.3)$$

with u and w are the components of the speed in the x and z directions.

The integration of the momentum equation (A2.1) within the boundary layer supplies:

$$\int_0^{\delta} \frac{\partial(\rho u^2 + p)}{\partial x} dz + \int_0^{\delta} \frac{\partial(\rho u w)}{\partial z} dz = \int_0^{\delta} \frac{\partial \tau_{xz}}{\partial z} dz \qquad (A2.4)$$

By introducing new variables displacement thickness δ^* and momentum thickness θ as:

$$\delta^* = \int_0^{\infty} \left(1 - \frac{\rho U}{\rho_e U_e}\right) dz \qquad \theta = \int_0^{\infty} \left(1 - \frac{U}{U_e}\right) \frac{\rho U}{\rho_e U_e} dz$$

one obtains the following equation:

$$\frac{\left(\delta - \delta^* - \theta\right)}{\rho_e U_e^2} \frac{\partial \rho_e U_e^2}{\partial x} - \frac{\partial \theta}{\partial x} - \frac{\partial \delta^*}{\partial x} + \frac{W_e}{U_e} = -\frac{\delta}{\rho_e U_e^2} \frac{\partial p}{\partial x} + \frac{\tau_w}{\rho_e U_e^2} \qquad (A2.5)$$

U_e and W_e are the components of the speed at the edge of the boundary layer in the x and z direction.

The term (W_e/U_e) is eliminated with the integration of the continuity equation (A2.3):

$$\int_0^{\delta} \frac{\partial \rho u}{\partial x} dz + \int_0^{\delta} \frac{\partial \rho w}{\partial z} dz = 0 \qquad (A2.6)$$

$$\frac{W_e}{U_e} = \frac{1}{\rho_e U_e} \frac{\partial \rho_e U_e \delta^*}{\partial x} - \frac{\delta}{\rho_e U_e} \frac{\partial \rho_e U_e}{\partial x} \qquad (A2.7)$$

Substituting eq. (A2.7) in eq. (A2.5) yields:

$$\frac{\left(\delta - \delta^* - \theta\right)}{U_e} \frac{\partial U_e}{\partial x} - \frac{\partial \theta}{\partial x} - \frac{\theta}{\rho_e U_e} \frac{\partial \rho_e U_e}{\partial x} = -\frac{\delta}{\rho_e U_e^2} \frac{\partial p}{\partial x} + \frac{\tau_w}{\rho_e U_e^2} \qquad (A2.8)$$

With the momentum equation at the edge of the boundary layer as:

$$-\frac{\partial p_e}{\partial x} = \frac{\partial \rho_e U_e^2}{\partial x} + \frac{\partial \rho_e U_e W_e}{\partial z} \qquad (A2.9)$$

one obtains the integral momentum equation as follows:

$$\frac{\partial \theta}{\partial x} + \frac{\left(\delta^* + 2\theta\right)}{U_e} \frac{\partial U_e}{\partial x} + \frac{\theta}{\rho_e} \frac{\partial \rho_e}{\partial x} = \frac{C_f}{2} \qquad (A2.10)$$

With the chain rule for the term ($\partial\rho_e/\partial x$) in eq. ($A$2.10) as:

$$\frac{\partial \rho_e}{\partial x} = \frac{\partial \rho_e}{\partial p_e} \frac{\partial p_e}{\partial x} = \frac{1}{\left(\partial p_e \middle/ \partial \rho_e \right)} \frac{\partial p_e}{\partial x} \qquad (A2.11)$$

and the isentropic relation: $\frac{\partial p}{\partial \rho} = a^2 \qquad (A2.12)$

and the Bernoulli equation:
$$-\frac{1}{\rho_e}\frac{\partial p_e}{\partial x}=U_e\frac{\partial U_e}{\partial x} \qquad (A2.13)$$

and the defined shape factor $H = \delta^{*}/\theta$, one obtains the integral momentum equation from (A2.10) as:
$$\frac{\partial\theta}{\partial x}=\frac{C_f}{2}-\left(H+2-M_e^2\right)\frac{\theta}{U_e}\frac{\partial U_e}{\partial x} \qquad (A2.14)$$

A2.2. The Shape Factor Equation of Drela and Giles Method

In order to obtain the shape factor equation, one begins from the momentum equation (A2.1). With the use of the continuity equation (A2.3), the momentum equation becomes:
$$\rho u\frac{\partial u}{\partial x}+\rho w\frac{\partial u}{\partial z}=-\frac{\partial p}{\partial x}+\frac{\partial \tau_{xz}}{\partial z} \qquad (A2.15)$$
Multiplying equation (A2.15) with *u* gives:
$$\rho u^2\frac{\partial u}{\partial x}+\rho uw\frac{\partial u}{\partial z}=-u\frac{\partial p}{\partial x}+u\frac{\partial \tau_{xz}}{\partial z} \qquad (A2.16)$$
The equation (A2.16) can be written with the use of the continuity equation as:
$$\frac{1}{2}\left(\frac{\partial \rho u^3}{\partial x}+\frac{\partial \rho u^2 w}{\partial z}\right)=-u\frac{\partial p}{\partial x}+u\frac{\partial \tau_{xz}}{\partial z} \qquad (A2.17)$$
Integration of the equation (A2.17) in the boundary layer gives:
$$\left[\int_0^\delta\frac{\partial\rho u^3}{\partial x}dz-\int_0^\delta U_e^2\frac{\partial\rho u}{\partial x}dz-2\int_0^\delta\rho uU_e\frac{\partial U_e}{\partial x}dz\right]+\left[\int_0^\delta U_e^2\frac{\partial\rho u}{\partial x}dz-\int_0^\delta U_e^2\frac{\partial\rho_e U_e}{\partial x}dz\right]+\int_0^\delta U_e^2\frac{\partial\rho_e U_e}{\partial x}dz+$$
$$\left[2\int_0^\delta u\frac{dp}{dx}dz+2\int\rho uU_e\frac{\partial U_e}{\partial x}dz\right]+\int\frac{\partial\rho u^2 w}{\partial z}dz=2\int_0^\delta u\frac{\partial\tau_{xz}}{\partial z}dz \qquad (A2.18)$$

With the definition of energy thickness θ^*, density thickness δ^{**}, dissipation coefficient C_d as:
$$\theta^*=\int_0^\infty\left(1-\frac{U^2}{U_e^2}\right)\frac{\rho U}{\rho_e U_e}dz \qquad \delta^{**}=\int_0^\infty\left(1-\frac{\rho}{\rho_e}\right)\frac{U}{U_e}dz \qquad C_d=\frac{1}{\rho_e U_e^3}\int_0^\infty\tau\frac{dU}{dz}dz$$
and the use of the Bernoulli equation (A2.13), equation (A2.18) becomes to:
$$-\frac{\partial\rho_e U_e^3\theta^*}{\partial x}-U_e^2\frac{\partial\rho_e U_e\delta^*}{\partial x}+\delta U_e^2\frac{\partial\rho_e U_e}{\partial x}-2\rho_e U_e^2\delta^{**}\frac{\partial U_e}{\partial x}+\rho_e U_e^2 W_e=2\rho_e U_e^3 C_d \qquad (A2.19)$$
W_e in the equation (A2.19) is eliminated using the equation (A2.7).
After division by $\rho_e U_e^3$ equation (A2.19) becomes to:
$$\frac{\partial\theta^*}{\partial x}+\frac{\theta^*}{\rho_e U_e^3}\frac{\partial\rho_e U_e^3}{\partial x}+2\frac{\delta^{**}}{U_e}\frac{\partial U_e}{\partial x}=2C_d \qquad (A2.20)$$
The derivative of ρ_e in the equation (A2.20) will be eliminated with the Bernoulli equation (A2.13) and the isentropic relation (A2.12).
With the defined shape factors H^* and H^{**} as:
$$H^*=\frac{\theta^*}{\theta}, \qquad H^{**}=\frac{\delta^{**}}{\theta}$$

then equation (A2.20) becomes to:
$$\frac{\partial H^*}{\partial x}+\left(3-M_e^2\right)\frac{H^*}{U_e}\frac{\partial U_e}{\partial x}+\frac{\theta^*}{\theta^2}\frac{\partial\theta}{\partial x}+\frac{2H^{**}}{U_e}\frac{\partial U_e}{\partial x}=2\frac{C_d}{\theta} \qquad (A2.21)$$

The term ($\partial\theta/\partial x$) in equation (A2.21) is eliminated using the momentum equation (A2.14) in order to obtain the shape factor equation as follows:

$$\frac{\partial H^*}{\partial x} = 2\frac{C_d}{\theta} - \frac{H^*}{\theta}\frac{C_f}{2} - \left(\frac{2H^{**}}{H^*} + 1 - H\right)\frac{H^*}{U_e}\frac{\partial U_e}{\partial x} \qquad (A2.22)$$

A2.3. The Shape Factor Equation of the Greens Method

In order to obtain the shape factor equation, Green defined a variable which called Entrainment coefficient as:

$$C_E = \frac{1}{U}\frac{d}{dx}\left[U(\delta - \delta^*)\right] \qquad (A2.23)$$

The shape factor equation can be derived as follows:

Defining the incompressible shape factor $\overline{H}$ as: $\overline{H} = \frac{1}{\theta}\int_0^\infty \frac{\rho}{\rho_e}\left(1 - \frac{U}{U_e}\right)dz$

and the mass flow shape factor H_1 as: $H_1 = \frac{\delta - \delta^*}{\theta}$

Multiplying the derivative of the shape factor $\overline{H}$ with respect to x with the momentum thickness as:

$$\theta\frac{d\overline{H}}{dx} = \theta\frac{d\overline{H}}{dH_1}\frac{dH_1}{dx} = \frac{d\overline{H}}{dH_1}\left[\theta\frac{d}{dx}\frac{\left(\delta - \delta^*\right)}{\theta}\right] \qquad (A2.24)$$

Subtitution of eq. (A2.23) into eq. (A2.24) gives:

$$\theta\frac{d\overline{H}}{dx} = \frac{d\overline{H}}{dH_1}\left[C_E - H_1\frac{\theta}{U_e}\frac{dU_e}{dx} - H_1\frac{d\theta}{dx}\right] \qquad (A2.25)$$

With the help of the incompressible integral momentum equation, i.e. eq. (A2.14) with M_e equals zero, one obtains from equation (A2.25) the following shape factor equation:

$$\frac{d\overline{H}}{dx} = \frac{1}{\theta}\frac{d\overline{H}}{dH_1}\left[C_E - H_1\left\{\frac{C_f}{2} - \left(H + 1\right)\frac{\theta}{U_e}\frac{dU_e}{dx}\right\}\right] \qquad (A2.26)$$

Appendix 3. Modification of the Integral Boundary Layer Equations

A modification of the integral momentum equation to be applied in inverse boundary layer calculation method will be presented. The modification is carried out for the integral boundary layer equations based on the Greens Lag Entrainment mehod.

A variable mass flow in the boundary layer is defined:

$$\overline{m} = \rho_e U_e \delta^* \qquad (A3.1)$$

The derivative of the mass flow in x direction is:

$$\frac{d\overline{m}}{dx} = U_e H\theta \frac{\partial \rho_e}{\partial x} + \rho_e H\theta \frac{\partial U_e}{\partial x} + \rho_e U_e H \frac{\partial \theta}{\partial x} + \rho_e U_e \theta \frac{\partial H}{\partial x} \qquad (A3.2)$$

$$\frac{1}{\overline{m}} \frac{d\overline{m}}{dx} = \frac{1}{\rho_e} \frac{\partial \rho_e}{\partial x} + \frac{1}{U_e} \frac{\partial U_e}{\partial x} + \frac{1}{\theta} \frac{\partial \theta}{\partial x} + \frac{1}{H} \frac{\partial H}{\partial x} \qquad (A3.3)$$

With the assumption of small disturbances:

$$\frac{\rho_e}{\rho_\infty} = 1 - M_\infty^2 \phi_x \qquad \frac{U_e}{U_\infty} = 1 + \phi_x \qquad (A3.4)$$

and the relationship between H and $\overline{H}$:

$$H = \left(\overline{H} + 1\right)\left(1 + \frac{\gamma - 1}{2} r M_e^2\right) - 1 \qquad (A3.5)$$

the derivative of ρ_e, U_e and H with respect to x become:

$$\frac{1}{\rho_e} \frac{\partial \rho_e}{\partial x} = - \frac{M_\infty^2 \phi_{xx}}{1 - M_\infty^2 \phi_x} \qquad (A3.6)$$

$$\frac{1}{U_e} \frac{\partial U_e}{\partial x} = \frac{\phi_{xx}}{1 + \phi_x} \qquad (A3.7)$$

$$\frac{\partial H}{\partial x} = \left(1 + \frac{\gamma - 1}{2} r M_e^2\right) \frac{d\overline{H}}{dx} + (\gamma - 1) r M_e (\overline{H} + 1) \frac{dM_e}{dx} \qquad (A3.8)$$

where the derivative of M_e with respect to x is given by:

$$\frac{dM_e}{dx} = M_\infty \left[1 + \frac{\gamma - 1}{2} M_\infty^2\right] \frac{1}{U_e} \frac{dU_e}{dx} \qquad (A3.9)$$

With the help of the integral momentum equation (A2.14), the equation (A3.3) becomes to:

$$\frac{1}{\overline{m}} \frac{d\overline{m}}{dx} = \frac{1}{\theta} \frac{C_f}{2} + \frac{R_1}{H} \frac{d\overline{H}}{dH_1} \left[\frac{1}{\theta}\left(C_E - \frac{C_f H_1}{2}\right)\right] +$$

$$\frac{\phi_{xx}}{1 + \phi_x} \left[-(H + 2 - M_e^2) + H_1 (H + 1) \frac{d\overline{H}}{dH_1} \frac{R_1}{H} + \frac{1}{H} (\gamma - 1) r M_e M_\infty R_2 (\overline{H} + 1) + 1 - \frac{(1 + \phi_x) M_\infty^2}{1 - M_\infty^2 \phi_x} \right]$$

$$(A3.10)$$

where R_1 and R_2 are given by:

$$R_1 = 1 + \frac{(\gamma - 1)}{2} r M_e^{\ 2} \qquad R_2 = 1 + \frac{(\gamma - 1)}{2} M_\infty^{\ 2}$$

In the direct method the value of the outer velocity [$\phi_{xx}/(1+\phi_x)$] in the equation (A3.10) is given by the inviscid model and the value of the mass flow is calculated from equation (A3.10). In the inverse method the situation is oppositely. The values of the outer velocity will be calculated with the estimated value of the mass flow. Therefore the procedure of the inverse method must be carried out by an iteration process.

From the equation (A3.10) one obtains the outer velocity (see also eq. (A3.7)) as follows:

$$\frac{\phi_{xx}}{1+\phi_x}=\frac{1}{U_v}\frac{dU_v}{dx}=\frac{\dfrac{-1}{\overline{m}}\dfrac{d\overline{m}}{dx}+\dfrac{1}{H\theta}R_1\dfrac{d\overline{H}}{dH_1}\left(C_E-\dfrac{C_f H_1}{2}\right)+\dfrac{C_f}{2\theta}}{(H+1)\left\{1-\dfrac{R_1}{H}\left[\dfrac{(\gamma-1)rM_eM_\infty R_2}{R_1^2}+H_1\dfrac{d\overline{H}}{dH_1}\right]\right\}-M_e^2+\dfrac{(1+\phi_x)M_\infty^2}{1-M_\infty^2\phi_x}} \qquad (A3.11)$$

The index *v* in outer velocity *U* shows that the velocity is calculated from viscous aerodynamic model.

The shape factor equation for inverse method can be found via elimination of the outer velocity in the equation (3.50) (see Chapter 3.2.3.) with the equation (A3.11):

$$\frac{d\overline{H}}{dx}=\frac{\dfrac{d\overline{H}}{dH_1}\left\{\dfrac{1}{\theta}\left(C_E-\dfrac{C_f H_1}{2}\right)\left[1-\dfrac{R_1(\gamma-1)rM_eM_\infty R_2}{HR_1^2}\right]-H_1\left(\dfrac{1}{\overline{m}}\dfrac{d\overline{m}}{dx}-\dfrac{C_f}{2\theta}\right)\right\}}{\left\{1-\dfrac{R_1}{H}\left[\dfrac{(\gamma-1)rM_eM_\infty R_2}{R_1^2}+H_1\dfrac{d\overline{H}}{dH_1}\right]-\dfrac{M_e^2}{(H+1)}+\dfrac{(1+\phi_x)M_\infty^2}{(1-M_\infty^2\phi_x)(H+1)}\right\}} \qquad (A3.12)$$

The entrainment coefficient equation for inverse method can be found also via elimination of the outer velocity in the equation (3.51) with the equation (A3.11):

$$\frac{dC_E}{dx}=\frac{F}{\theta}\left\{\frac{R_3}{H+H_1}\left[(C_\tau)^{1/2}_{EQ0}-\lambda C_\tau^{1/2}\right]+\left(\frac{\theta}{U_e}\frac{dU_e}{dx}\right)_{EQ}\right\}-F\left(1+0.075M_e{}^2\frac{R_1}{1+0.1M_e{}^2}\right)\phi_{xx} \qquad (A3.13)$$

where R_3 is given by (see also Chapter 3.2.4.):

$$R_3=2.8 \qquad if \quad \overline{H}\le 2.4 \qquad (a)$$

$$R_3=\frac{0.15}{\left(1-\dfrac{C_2}{2}\right)0.08\left(1-\eta^*\right)} \qquad if \quad \overline{H}>2.4 \qquad (b)$$

Appendix 4. Goldstein's Singularity

By solving the integral boundary layer equations with direct method a singular value of the boundary layer parameters exists if the flow exhibits separation. This singular value is called as Goldstein's Singularity. This phenomenon can be described clearly with the following mathematical analysis.

A4.1. Goldstein's Singularity in the Drela and Giles Method

As basis equations are the integral momentum boundary layer equation (A2.14) and the shape factor equation (A2.22):

$$\frac{\partial\theta}{\partial x}=\frac{C_f}{2}-\left(H+2-M_e^2\right)\frac{\theta}{U_e}\frac{\partial U_e}{\partial x} \qquad (A2.14)$$

$$\frac{\partial H^*}{\partial x}=2\frac{C_d}{\theta}-\frac{H^*}{\theta}\frac{C_f}{2}-\left(\frac{2H^{**}}{H^*}+1-H\right)\frac{H^*}{U_e}\frac{\partial U_e}{\partial x} \qquad (A2.22)$$

Because of $\theta = \delta^*/H$ then equation (A2.14) can be formulated as:

$$\frac{1}{H}\frac{\partial\delta^*}{\partial x}-\frac{\delta^*}{H^2}\frac{\partial H}{\partial x}=\frac{C_f}{2}-\left(H+2-M_e^2\right)\frac{\theta}{U_e}\frac{\partial U_e}{\partial x} \qquad (A4.1)$$

Applying chain rule for the derivative of H as function of M_e and H_k , then equation (A4.1) becomes to:

$$\frac{1}{H}\frac{\partial\delta^*}{\partial x}-\frac{\delta^*}{H^2}\left[\frac{\partial H}{\partial H_k}\frac{\partial H_k}{\partial x}+\frac{\partial H}{\partial M_e^2}\frac{\partial M_e^2}{\partial x}\right]=\frac{C_f}{2}-\left(H+2-M_e^2\right)\frac{\theta}{U_e}\frac{\partial U_e}{\partial x} \qquad (A4.2)$$

$$\frac{\partial\delta^*}{\partial x}=\theta\left[\frac{\partial H}{\partial H_k}\frac{\partial H_k}{\partial x}+\frac{\partial H}{\partial M_e^2}\frac{\partial M_e^2}{\partial x}\right]+H\frac{C_f}{2}-H\left(H+2-M_e^2\right)\frac{\theta}{U_e}\frac{\partial U_e}{\partial x} \qquad (A4.3)$$

Equation (A2.22) can be written in another form as:

$$\frac{\partial H_k}{\partial x}=\frac{1}{\left(\partial H^*/\partial H_k\right)}\left[2\frac{C_d}{\theta}-\frac{H^*}{\theta}\frac{C_f}{2}-\left(\frac{2H^{**}}{H^*}+1-H\right)\frac{H^*}{U_e}\frac{\partial U_e}{\partial x}\right] \qquad (A4.4)$$

Substituting eq. (A4.4) into the eq. (A4.3), one can obtain the following equation:

$$\frac{\partial\delta^*}{\partial x}=\frac{\left(\partial H/\partial H_k\right)}{\left(\partial H^*/\partial H_k\right)}\left[2C_d-H^*\frac{C_f}{2}-H^*\left(\frac{2H^{**}}{H^*}+1-H\right)\frac{\theta}{U_e}\frac{\partial U_e}{\partial x}\right]+$$

$$\left[H\frac{C_f}{2}-H\left(H+2-M_e^2\right)\frac{\theta}{U_e}\frac{\partial U_e}{\partial x}+\theta\frac{\partial H}{\partial M_e^2}\frac{\partial M_e^2}{\partial x}\right] \qquad (A4.5)$$

Equation (A4.5) shows that the value of the displacement thickness becomes singular, if the derivative $\partial H^*/\partial H_k$ equals to zero.

A4.2. Goldstein's Singularity in the Greens Lag Entrainment Method

As the starting point is the equation (A4.1):

$$\frac{1}{H}\frac{\partial\delta^*}{\partial x}-\frac{\delta^*}{H^2}\frac{\partial H}{\partial x}=\frac{C_f}{2}-\left(H+2-M_e^2\right)\frac{\theta}{U_e}\frac{\partial U_e}{\partial x} \qquad (A4.1)$$

The derivative from H to x direction in the equation (A4.1) is eliminated with the equation (A3.8) and resulted:

$$\frac{1}{H}\frac{\partial\delta^*}{\partial x}-\frac{\delta^*}{H^2}\left[\left(1+\frac{\gamma-1}{2}rM_e^2\right)\frac{d\overline{H}}{dx}+(\gamma-1)rM_e(\overline{H}+1)\frac{dM_e}{dx}\right]=\frac{C_f}{2}-\left(H+2-M_e^2\right)\frac{\theta}{U_e}\frac{\partial U_e}{\partial x} \qquad (A4.6)$$

With the help of the equations (A2.26) and (A3.9) the derivatives of $\overline{H}$ and M_e with respect to x direction in the equation (A4.6) are eliminated and from this results the derivative of the displacement thickness can be obtained as:

$$\frac{d\delta^*}{dx}=\frac{HC_f}{2}+\left(1+\frac{\gamma-1}{2}rM_e^2\right)\frac{d\overline{H}}{dH_1}\left[\left(C_E-H_1\frac{C_f}{2}\right)+H_1(H+1)\frac{\theta}{U_e}\frac{dU_e}{dx}\right]+$$

$$\frac{\theta}{U_e}\frac{dU_e}{dx}\left[\left(\overline{H}+1\right)(\gamma-1)rM_eM_\infty\left(1+\frac{\gamma-1}{2}M_\infty^2\right)-H(H+2-M_e^2)\right] \qquad (A4.7)$$

The equation (A4.7) becomes singular if $\frac{d\overline{H}}{dH_1}$ is singular.